frontiers | Research Topics

Imaging-based methods for fracture risk assessment

Edited by
Egon Burian, Nico Sollmann and
Julio Carballido-Gamio

Published in
Frontiers in Endocrinology

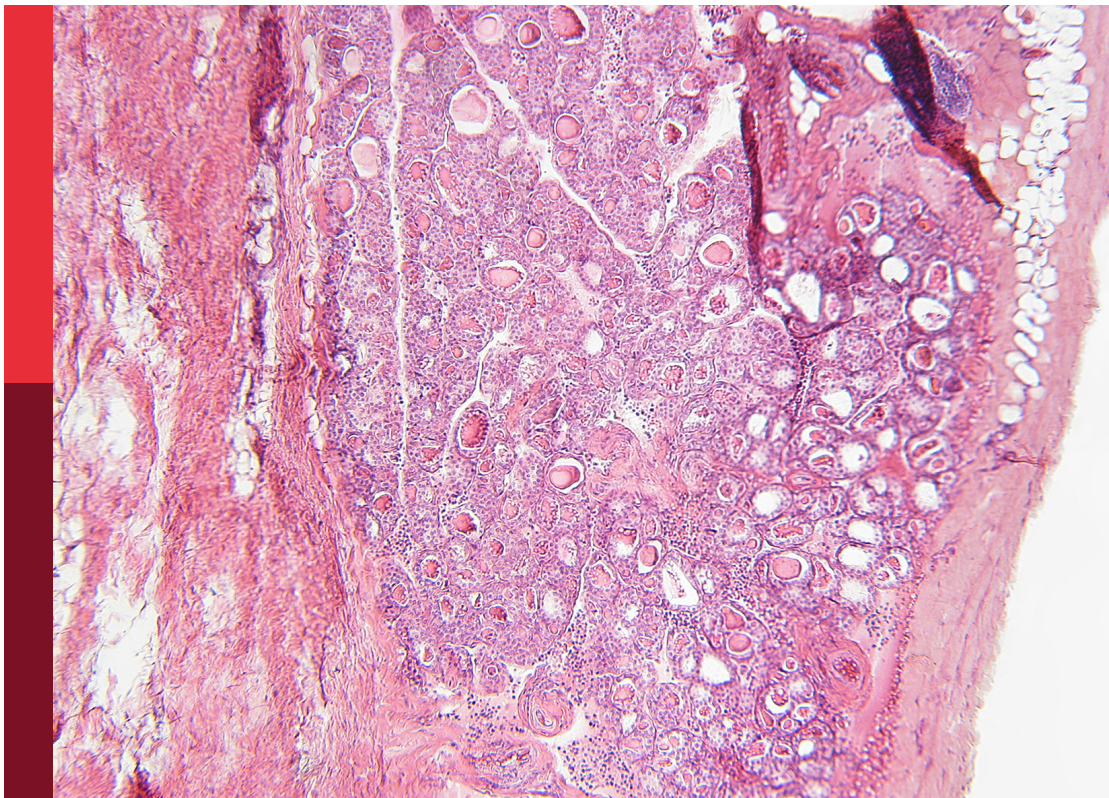

ISSN 1664-8714
ISBN 978-2-8325-6729-6
DOI 10.3389/978-2-8325-6729-6

Generative AI statement
Any alternative text (Alt text) provided alongside figures in the articles in this ebook has been generated by Frontiers with the support of artificial intelligence and reasonable efforts have been made to ensure accuracy, including review by the authors wherever possible. If you identify any issues, please contact us.

About Frontiers

Frontiers is more than just an open access publisher of scholarly articles: it is a pioneering approach to the world of academia, radically improving the way scholarly research is managed. The grand vision of Frontiers is a world where all people have an equal opportunity to seek, share and generate knowledge. Frontiers provides immediate and permanent online open access to all its publications, but this alone is not enough to realize our grand goals.

Frontiers journal series

The Frontiers journal series is a multi-tier and interdisciplinary set of open-access, online journals, promising a paradigm shift from the current review, selection and dissemination processes in academic publishing. All Frontiers journals are driven by researchers for researchers; therefore, they constitute a service to the scholarly community. At the same time, the *Frontiers journal series* operates on a revolutionary invention, the tiered publishing system, initially addressing specific communities of scholars, and gradually climbing up to broader public understanding, thus serving the interests of the lay society, too.

Dedication to quality

Each Frontiers article is a landmark of the highest quality, thanks to genuinely collaborative interactions between authors and review editors, who include some of the world's best academicians. Research must be certified by peers before entering a stream of knowledge that may eventually reach the public - and shape society; therefore, Frontiers only applies the most rigorous and unbiased reviews. Frontiers revolutionizes research publishing by freely delivering the most outstanding research, evaluated with no bias from both the academic and social point of view. By applying the most advanced information technologies, Frontiers is catapulting scholarly publishing into a new generation.

What are Frontiers Research Topics?

Frontiers Research Topics are very popular trademarks of the *Frontiers journals series*: they are collections of at least ten articles, all centered on a particular subject. With their unique mix of varied contributions from Original Research to Review Articles, Frontiers Research Topics unify the most influential researchers, the latest key findings and historical advances in a hot research area.

Find out more on how to host your own Frontiers Research Topic or contribute to one as an author by contacting the Frontiers editorial office: frontiersin.org/about/contact

Imaging-based methods for fracture risk assessment

Topic editors

Egon Burian — Zurich University Hospital, Switzerland

Nico Sollmann — Ulm University Medical Center, Germany

Julio Carballido-Gamio — University of Colorado Anschutz Medical Campus, United States

Citation

Burian, E., Sollmann, N., Carballido-Gamio, J., eds. (2025). *Imaging-based methods for fracture risk assessment*. Lausanne: Frontiers Media SA.

doi: 10.3389/978-2-8325-6729-6

Table of contents

frontiers | Frontiers in Endocrinology

TYPE Editorial
PUBLISHED 06 August 2025
DOI 10.3389/fendo.2025.1668924

OPEN ACCESS

EDITED AND REVIEWED BY
Alberto Falchetti,
Ospedale Santa Maria della Misericordia di Udine, Italy

*CORRESPONDENCE
Egon Burian
Egon.burian@usz.ch

RECEIVED 18 July 2025
ACCEPTED 23 July 2025
PUBLISHED 06 August 2025

CITATION
Burian E, Sollmann N and Carballido-Gamio J (2025) Editorial: Imaging-based methods for fracture risk assessment.
Front. Endocrinol. 16:1668924.
doi: 10.3389/fendo.2025.1668924

Editorial: Imaging-based methods for fracture risk assessment

Egon Burian[1,2]*, Nico Sollmann[3,4,5,6] and Julio Carballido-Gamio[7]

[1]Department of Diagnostic and Interventional Radiology, University Hospital of Zurich, Zurich, Switzerland, [2]Faculty of Medicine, University of Zurich, Zurich, Switzerland, [3]Department of Diagnostic and Interventional Radiology, University Hospital Ulm, Ulm, Germany, [4]Department of Nuclear Medicine, University Hospital Ulm, Ulm, Germany, [5]Department of Diagnostic and Interventional Neuroradiology, School of Medicine and Health, Technical University of Munich (TUM) Klinikum Rechts der Isar, Technical University of Munich, Munich, Germany, [6]Technical University of Munich (TUM)-Neuroimaging Center, TUM Klinikum Rechts der Isar, Technical University of Munich, Munich, Germany, [7]Department of Radiology, University of Colorado, Aurora, CO, United States

KEYWORDS

fracture, imaging - computed tomography, bone mineral density, MRI, proton density fat fraction

Editorial on the Research Topic
Imaging-based methods for fracture risk assessment

Fragility fractures represent a significant global health burden and can arise from osteoporosis (1). While areal bone mineral density (aBMD) derived from dual-energy X-ray absorptiometry (DXA) has long been the diagnostic standard, approximately 50% of fractures occur in individuals with aBMD above the osteoporotic threshold, underscoring limitations of DXA-derived aBMD in capturing the multifaceted nature of bone fragility (2–5). This necessitates a shift towards comprehensive imaging techniques and/or parameters that offer deeper insights into bone quality such as microarchitecture and biomechanical factors. This Research Topic explored recent advancements, persistent challenges, and future directions in this evolving field.

Conventional DXA provides a two-dimensional (2D) projection, simplifying bone geometry and material properties, but with measurements confounded by bone size (2). However, extracting sophisticated structural information from existing DXA scans could enhance its utility. The “Minimal Model” (MM) of hip structure, derived from DXA Hip Structural Analysis (HSA) variables like Femoral Neck Width (FNW), Sigma, and Delta, offers crucial biomechanical insights beyond simple aBMD. Zhao et al. demonstrated that the MM significantly improved hip fracture discrimination (area under the curve [AUC] = 0.838) compared to BMD alone (AUC = 0.781) in Chinese adults, with increases in FNW, Sigma, and Delta independently associated with higher hip fracture risk. This study indicated that detailed structural geometry, even from 2D imaging, might provide superior predictive power.

Quantitative computed tomography (QCT) offers three-dimensional (3D) volumetric imaging, enabling separate analysis of cortical and trabecular bone and measuring volumetric BMD (vBMD) without projection errors (2, 4). Furthermore, QCT enables assessments of bone shape and cortical bone thickness, and estimates of bone strength

through finite element analysis (FEA) (6). However, the spatial resolution of QCT scans at the proximal femur and spine is not enough to visualize trabecular bone microarchitecture and its higher radiation dose and required FEA expertise limit its routine clinical use. Leveraging routine CT scans, Hounsfield Units (HU) are emerging as a valuable metric for osteoporosis assessments. Chen et al. showed that anterior column HU values were significantly lower in osteoporotic vertebral compression fractures (OVCFs) and correlated strongly with DXA T-scores (r = 0.643) and aBMD (r = 0.656). Crucially, anterior column HU demonstrated the highest correlation with vertebral compression degrees (r=0.727) and superior predictive ability for severe OVCFs (grade 3), with an optimal cutoff of 59.07 HU (AUC = 0.913). This opportunistic approach provided a localized bone quality assessment that could directly inform clinical decisions like short-term absolute bed rest post-fracture.

Chemical shift encoding-based water-fat separation MRI (CSE-MRI) is a non-invasive, radiation-free tool for assessing bone and muscle composition (5, 7, 8). Stohldreier et al. investigated 6-month changes in proton density fat fraction (PDFF) and T2* of paraspinal muscles (PSM) and vertebral bone marrow (VBM; T11-L4) as predictive biomarkers for incidental VCFs. They found that PDFF significantly increased in both PSM and VBM in patients who subsequently developed VCFs, even when opportunistic CT-based BMD remained unchanged. This suggests fatty degeneration is a crucial, early biomarker for bone fragility, challenging sole reliance on BMD Decreasing PSM T2* was also identified as a risk factor. This innovative MRI application shifts assessment from purely structural to detecting metabolic and compositional changes, potentially enabling earlier risk stratification.

Image-based biomechanical approaches, particularly FEA, aim to directly assess bone strength by simulating fracture-inducing forces. FE models, constructed from DXA or QCT data, estimate stress and strain distributions via computational modeling to predict bone strength and fracture loads (9, 10). In this regard, DXA-based FEA is accessible and comes at low radiation exposure, but relies on simplified 2D geometry. QCT-based FEA offers detailed 3D insights but incurs higher costs and radiation as well as expertise. Despite theoretical superiority, biomechanical models still face significant barriers to clinical integration. Key challenges include: (1) accurate material property characterization: current imaging struggles to quantify non-mineral components (collagen, water) crucial for bone toughness and viscoelasticity, leading to incomplete material data for FE models (Luo et al.); (2) modeling bone anisotropy: most FE models use simplified isotropic assumptions, overlooking bone's directional strength variations, which limits accuracy in simulating multi-directional fall forces (Luo et al.); and (3) realistic fall simulations: real-world falls are unpredictable, influenced by random triggers and complex individual-specific muscle reflexes that are difficult to accurately replicate in simulations. These fundamental scientific and engineering hurdles necessitate continued research in advanced imaging, material science, and computational modeling for FEA to reach its full clinical potential.

Fracture risk extends beyond bone integrity, involving soft tissues and systemic health. Ahmed Mohamed et al. conducted a meta-analysis that revealed that preoperative thoracolumbar fascia injury (TLFI), diagnosed by MRI, may be a frequently overlooked complication in OVCFs (28% incidence) that significantly increases residual back pain post-percutaneous vertebral augmentation (odds ratio = 4.79). This highlights the need for a holistic assessment, including soft tissue integrity, for comprehensive pain management.

Furthermore, bone fragility is intertwined with systemic diseases. Jin et al. demonstrated that in patients with Parkinson's disease (PD), hip fractures mediate the association between osteoporosis and mortality, emphasizing aggressive osteoporosis and fall management in this vulnerable population. The work by Abate et al. in liver transplant patients also identified transplant-specific factors like rejection episodes and low aBMD as critical for predicting long-term bone fragility progression. Such studies advocate for a multidisciplinary approach to fracture prevention, integrating imaging with broader clinical contexts.

The field of fracture risk assessment is transforming, moving beyond BMD to embrace sophisticated imaging techniques and parameters that capture bone quality and tissue composition. Advanced techniques like DXA-based structural analysis, localized CT-based HU measurements with opportunistic vBMD assessments, and MRI-derived biomarkers have potential to enhance predictive accuracy. The development of personalized nomograms for specific patient cohorts further exemplifies a shift towards tailored interventions. However, considerable challenges persist, including the need for robust validation in larger and diverse populations, standardization of imaging protocols, and improved computational efficiency for complex biomechanical models. Future research must prioritize hybrid and multi-modal approaches, leveraging artificial intelligence and machine learning for automated analysis and seamless clinical integration. The ultimate goal is to develop accurate, generalizable, reproducible, and user-friendly tools that can be seamlessly integrated into routine clinical workflows, fostering a holistic vision for musculoskeletal health and leading to more effective and personalized fracture prevention strategies worldwide.

Author contributions

EB: Writing – original draft. NS: Writing – review & editing. JC: Writing – review & editing.

Conflict of interest

The authors declare that the research was conducted in the absence of any commercial or financial relationships that could be construed as a potential conflict of interest.

Generative AI statement

The author(s) declare that no Generative AI was used in the creation of this manuscript.

Publisher's note

References

1. Compston JE, McClung MR, Leslie WD. Osteoporosis. *Lancet*. (2019) 393:364–76. doi: 10.1016/S0140-6736(18)32112-3

2. Loffler MT, Sollmann N, Mei K, Valentinitsch A, Noel PB, Kirschke JS, et al. X-ray-based quantitative osteoporosis imaging at the spine. *Osteoporos Int*. (2020) 31:233–50. doi: 10.1007/s00198-019-05212-2

3. Sollmann N, Loffler MT, Kronthaler S, Bohm C, Dieckmeyer M, Ruschke S, et al. MRI-based quantitative osteoporosis imaging at the spine and femur. *J Magn Reson Imaging: JMRI*. (2020) 54(1):12–35. doi: 10.1002/jmri.27260

4. Link TM. Osteoporosis imaging: state of the art and advanced imaging. *Radiology*. (2012) 263:3–17. doi: 10.1148/radiol.12110462

5. Sollmann N, Kirschke JS, Kronthaler S, Boehm C, Dieckmeyer M, Vogele D, et al. Imaging of the osteoporotic spine - quantitative approaches in diagnostics and for the prediction of the individual fracture risk. *Rofo*. (2022) 194:1088–99. doi: 10.1055/a-1770-4626

6. Wang MC, Kiapour A, Massaad E, Shin JH, Yoganandan N. A guide to finite element analysis models of the spine for clinicians. *J Neurosurg Spine*. (2024) 40:38–44. doi: 10.3171/2023.7.SPINE23164

7. Burian E, Subburaj K, Mookiah MRK, Rohrmeier A, Hedderich DM, Dieckmeyer M, et al. Texture analysis of vertebral bone marrow using chemical shift encoding-based water-fat MRI: a feasibility study. *Osteoporos Int*. (2019) 30:1265–74. doi: 10.1007/s00198-019-04924-9

8. Burian E, Becherucci EA, Junker D, Sollmann N, Greve T, Hauner H, et al. Association of cervical and lumbar paraspinal muscle composition using texture analysis of MR-based proton density fat fraction maps. *Diagnost (Basel)*. (2021) 11. doi: 10.3390/diagnostics11101929

9. Dieckmeyer M, Rayudu NM, Yeung LY, Loffler M, Sekuboyina A, Burian E, et al. Prediction of incident vertebral fractures in routine MDCT: Comparison of global texture features, 3D finite element parameters and volumetric BMD. *Eur J Radiol*. (2021) 141:109827. doi: 10.1016/j.ejrad.2021.109827

10. Greve T, Rayudu NM, Dieckmeyer M, Boehm C, Ruschke S, Burian E, et al. Finite element analysis of osteoporotic and osteoblastic vertebrae and its association with the proton density fat fraction from chemical shift encoding-based water-fat MRI - A preliminary study. *Front Endocrinol (Lausanne)*. (2022) 13:900356. doi: 10.3389/fendo.2022.900356

frontiers | Frontiers in Pediatrics

TYPE Case Report
PUBLISHED 20 January 2025
DOI 10.3389/fped.2024.1505766

OPEN ACCESS

EDITED BY
Nico Sollmann,
Ulm University Medical Center, Germany

REVIEWED BY
Mel Mupparapu,
University of Pennsylvania, United States
Frederick Singer,
Saint John's Health Center, United States

*CORRESPONDENCE
Dimitri Ceroni
✉ dimitri.ceroni@hcuge.ch

RECEIVED 08 October 2024
ACCEPTED 31 December 2024
PUBLISHED 20 January 2025

CITATION
Paris E, De Marco G, Vazquez O, Boudabbous S, Steiger C, Dayer R and Ceroni D (2025) Polyostotic fibrous dysplasia with epiphyseal involvement of the proximal femur in a child: a case report and review of the literature.
Front. Pediatr. 12:1505766.
doi: 10.3389/fped.2024.1505766

Polyostotic fibrous dysplasia with epiphyseal involvement of the proximal femur in a child: a case report and review of the literature

Elio Paris[1], Giacomo De Marco[2], Oscar Vazquez[2], Sana Boudabbous[3], Christina Steiger[2], Romain Dayer[2] and Dimitri Ceroni[2]*

[1]Faculty of Medicine, University of Geneva, Geneva, Switzerland, [2]Pediatric Orthopedic Unit, Pediatric Surgery Service, Geneva University Hospital, Geneva, Switzerland, [3]Radiology Department, Geneva University Hospital, Geneva, Switzerland

Fibrous dysplasia (FD) is a benign medullary fibro-osseous anomaly that compromises the mechanical strength of bones, especially the long bones that bear strong mechanical stresses. It can lead to an inability to remodel immature bone into mature lamellar bone, resulting in inappropriate bone alignment in response to mechanical stresses. This case study describes a rare case of polyostotic FD presenting with an epiphyseal lesion of the proximal femoral head in its weight-bearing zone, accompanied by an unconventional femoral malrotation. The present case leads us to recommend that clinicians should not underestimate the occurrence of other deformities, such as the retrotorsion or flexion deformities that can compromise bone structure and the hip's biomechanics. Finally, the involvement of the epiphysis is probably more common than usually thought, introducing an additional complexity since juxta-articular lesions in weight-bearing joints may collapse, compromising articular congruence and function. To minimise this risk, bone scintigraphy and MRI should play a critical role in the patient's workup, evaluation, prognosis and follow-up.

KEYWORDS

fibrous dysplasia, proximal femur, pediatric, case report, epiphysis

1 Introduction

Fibrous dysplasia (FD) is a benign, non-hereditary, genetic bone disorder presenting as either an isolated skeletal lesion (its monostotic form) or affecting multiple bones (its polyostotic form) (1). The disease's incidence is estimated to be from 1 in 5,000 to 1 in 10,000 (2). FD is sometimes associated with single or multiple endocrinopathies, precocious puberty and cutaneous hyperpigmentation in McCune–Albright syndrome (3). Radiographically, it usually appears as a well-defined radiolucent medullary lesion that is irregular, mildly expansive and characterised by a hazy opacity typically described as "ground-glass" (4); it is usually designated as type IA according to the Lodwick classification (5). On long bones, FD can cause expansion of the bone edges, with cortical thinning and endosteal scalloping. The diaphysis is usually involved, but the metaphysis can also be affected (4). In very rare instances of the disease's polyostotic form, the epiphysis may be involved, especially in children (3, 6–10). These changes are usually visible on plain radiographs, but computed tomography and

magnetic resonance imaging (MRI) are regularly performed to better investigate the tumour matrix and tumour expansion. This case study describes a rare case of polyostotic FD presenting with an epiphyseal lesion of the proximal femoral head in its weight-bearing zone, accompanied by an unconventional femoral malrotation.

2 Case report

A 10.5-year-old child underwent fixation surgery in a regional hospital for a pathological diaphyseal fracture of the left femur. A closed reduction of the fracture was performed and subsequently stabilised using two flexible retrograde intramedullary nails. After hardware removal, he was referred to our hospital centre at the age of 12 for a follow-up on his suspected fibrous dysplasia. On clinical examination, there was no leg length discrepancy, and no "café au lait" spots were noted on his skin. The patient tested positively during an anterior impingement (the FADIR test), with a severe restriction in internal rotation at his left hip related to his femoral retroversion.

X-ray images of the left femur revealed various radiolucent lesions in the diaphysis, with sclerotic edges, scalloping and a ground-glass appearance (Figure 1a). The patient's plain radiographs showed no coxa vara or shepherd's crook deformities but revealed an increased sagittal radius of curvature and retrotorsion of the proximal femur (Figure 1b). The patient's growth plates were still open at the level of the proximal and distal femur.

FIGURE 1
X-ray images of the left femur after removal of osteosynthetic materials: the frontal coronal plane image revealed a variety of radiolucent lesions in the diaphysis, with sclerotic edges, scalloping and a "ground-glass" appearance (a) sagittal plain radiographs showed an increased sagittal radius of curvature and retrotorsion of the proximal femur (b).

Whole body MRI confirmed the diagnosis of polyostotic FD, displaying FD foci in the left femur, right tibia, left fibula, left calcaneus, both iliac wings, maxillary bone, and the sphenoid wing (Figure 2). The lesions on the left femur were in the proximal epiphysis, the proximal metaphysis and along the diaphysis. MRI demonstrated a low signal intensity in T1-weighted images (Figure 3a) and a high signal intensity in fat-suppressed T2-weighted images, also showing strong gadolinium enhancement (Figure 3b) without diffusion restriction (Figure 2b). There was no significant bone marrow or soft tissue enhancement. At the femoral head, the lesion was juxta-articular, with no subchondral bone collapse. Scintigraphy, added to assess skull involvement, confirmed the polyostotic hyperfixation and demonstrated an unknown parasymphyseal involvement of the mandible with an extension into its right branch (Figure 4). Finally, blood tests enabled us to exclude endocrine dysfunctions.

Timeline:

- Occurrence of a pathological fracture of the left femur in August 2023
- Closed reduction of the femoral fracture and stabilization by elastic intramedullary nailing in August 2023.
- Removal of osteosynthesis material in March 2024.
- Patient referred to our institution for further treatment in April 2024.
- Additional radiographic assessment between April and June 2024 (scintigraphy, bone scan, MRI, and echography of the genital tract).
- Blood analysis: April 2024.

3 Discussion

FD is a pathological condition that leads to an inability to remodel immature bone into mature lamellar bone, resulting in inappropriate bone alignment in response to mechanical stresses (6). Histologically, fibroblast proliferation will result in excessive fibrous tissue replacing normal calcium hydroxyapatite in the osteoid matrix (11). As previously noted, FD is classified into two types: the monostotic form affects a single bone, while polyostotic FD is characterised by the involvement of multiple bones. Polyostotic FD is frequently accompanied by manifestations of syndromes such as McCune–Albright syndrome (3) or Mazabraub syndrome (12), where it is associated with endocrine abnormalities and overproduction of melatonin in the skin (3) or with intramuscular myxomas (12), respectively. Most endocrinopathies present during FD revolve around hyperthyroidism, hyperparathyroidism, acromegaly, diabetes mellitus, and Cushing syndrome.

FD is the result of a mutation in the guanine-nucleotide alpha stimulating-GNAS gene. It seems to be recognised that the chronological timing of the mutation's appearance is responsible for a somatic mosaicism that determines the extent of the disease and its clinical manifestations (13). Mutations that occur at early stages of embryogenesis typically result in the widespread distribution of bone lesions (1). Conversely, mutations occurring

10.3389/fped.2024.1505766

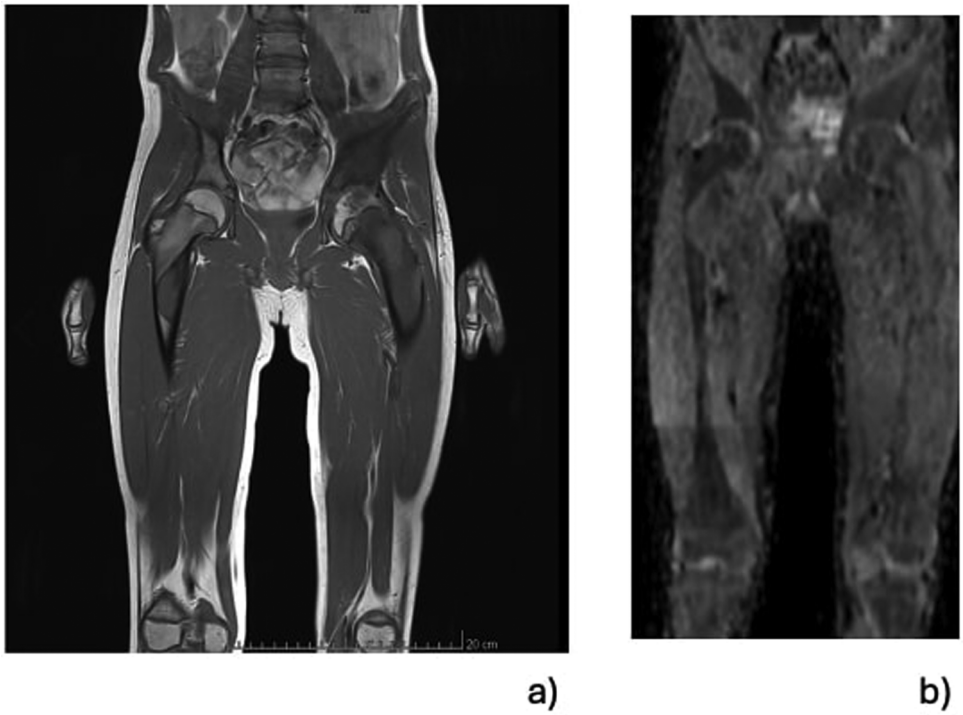

FIGURE 2
Selected total-body MRI at the level of the pelvis and both femurs using low signal intensity on T1-weighted images and demonstrating the foci of FD affecting the epiphysis, the femoral neck, the diaphyseal regions of the left femur and the same hip's acetabulum. A lesion is visible in the subtrochanteric region of the right femur **(a)**. There was a high signal intensity without diffusion restriction on the fat-suppressed T2-weighted images enhanced with gadolinium **(b)**.

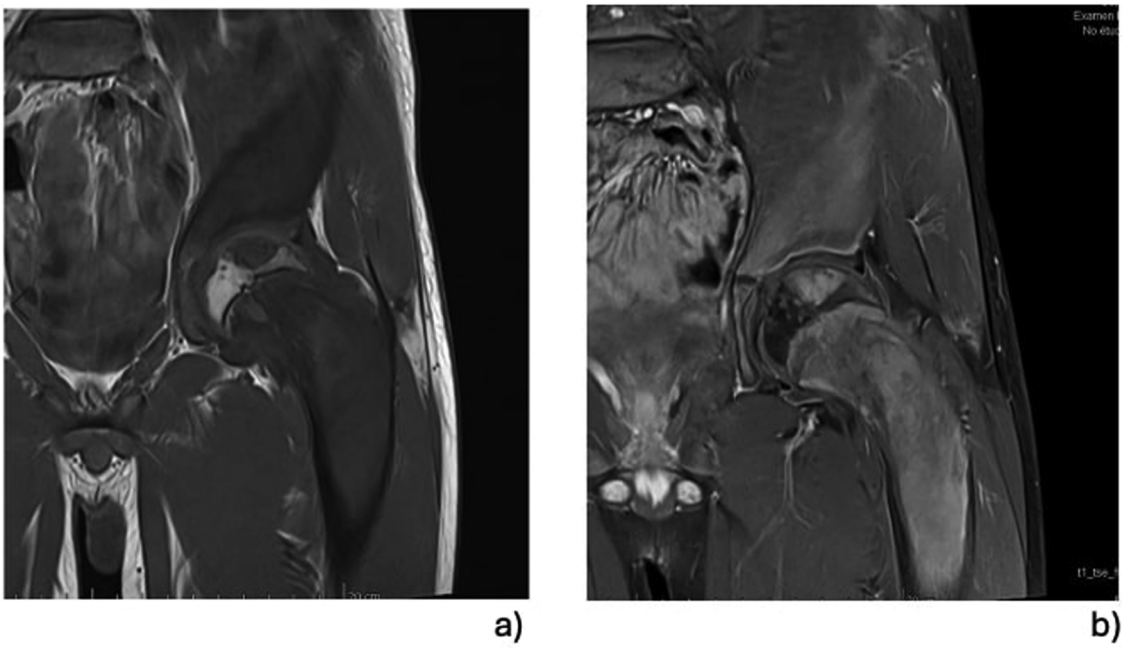

FIGURE 3
MRI focusing on left proximal femur lesions: the focus of the FD of the proximal epiphysis and the significant involvement of the femoral neck can be seen precisely. The examination did not demonstrate transphyseal diffusion of the FD, and the lesions seemed not to originate from the epiphyseal growth plate. All the lesions were characterised by a low signal intensity on T1-weighted images **(a)**, but these were significantly better in the T1-weighted images enhanced with gadolinium **(b)**.

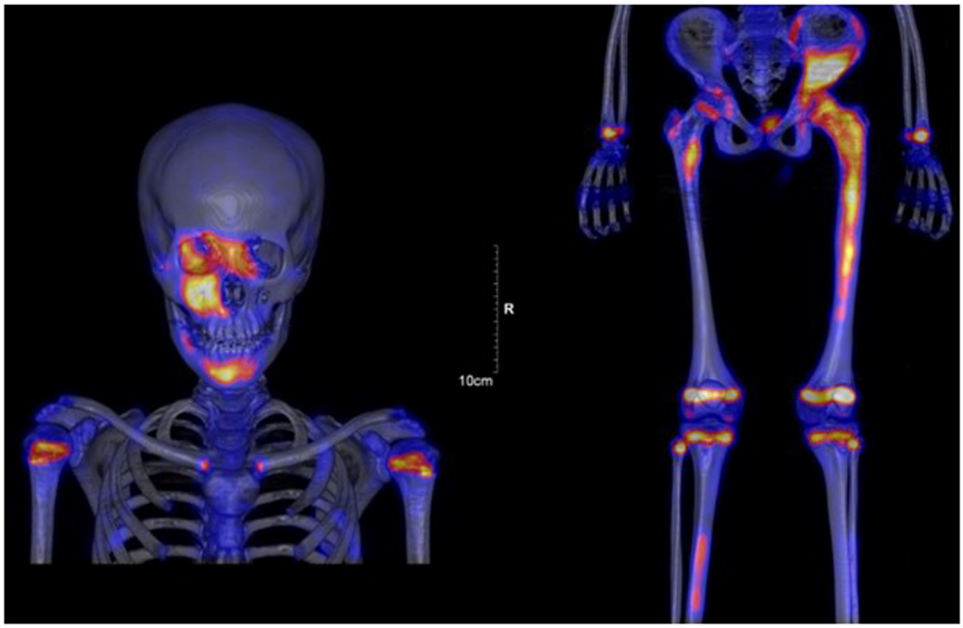

FIGURE 4
Scintigraphy confirmed polyostotic hyperfixation and demonstrated an unknown parasymphyseal involvement of the mandible with extension into its right branch.

at later stages of embryogenesis result in a more localised distribution (1). The involvement of a gene mutation is why FD cannot occur spontaneously and why the monostotic form of FD never progresses to the polyostotic form (1).

As a rule, when either monostotic or polyostotic FD occurs in long bones, such as the tibia, femur or humerus, it typically affects the diaphysis or metaphysis. Several authors have postulated that FD bone lesions usually spare the epiphysis (3, 14–16), and, when present, epiphyseal involvement depends, above all, on the patient's age. In fact, the literature suggests that diaphyseal and metaphyseal lesions can expand with growth and could even result in the involvement of the epiphysis after physeal closure in adults (7, 14–17). On the contrary, however, cases of FD with epiphyseal involvement before puberty are quite rare since only seven cases were found in previous reports involving paediatric populations (3, 6–10). Nixon and Condon postulated that FD in children might originate from a fibro-osseous aberration occurring in the epiphyseal growth plate, with a subsequent bidirectional extension into the epiphysis and the metaphysis (10). According to them, the lesion's extension across the epiphyseal growth plate supports this hypothesis (10).

Involvement of the proximal femoral epiphysis, as in our patient, has been described only in 2 cases in the paediatric population, even in polyostotic forms of FD (8). The present case is rich in information and leads to several realisations. Firstly, it confirms that the risk of a pathological fracture in FD patients varies according to the patient's age, with a major predisposition to fractures of the femur. Fractures are most prevalent between the ages of 6 and 10, and peak incidence is estimated to be 0.4 fractures per FD patient per year (1). Secondly, our case demonstrated that multiplanar proximal femoral deformity can occur in patients with FD. Typically, it is now recognised that femurs affected with FD in their proximal third will develop coxa vara deformities, leading to the characteristic "shepherd's crook" deformity (18–22). In our patient, the deformity occurred in the sagittal plane (a proximal femoral flexion deformity) and in the horizontal plane (a proximal femoral retrotorsion). Moreover, it is interesting to note that the above-cited deformities are recognised as generating femoroacetabular impingement. Thus, even though almost one-third of femurs affected by FD develop a typical coxa vara deformity, it also appears important to look out for deformities in all three planes and, thus, for clinical signs of femoroacetabular impingement. Thirdly, our case did not validate the pathophysiological hypothesis which suggests that FD may originate from a fibro-osseous aberration in the epiphyseal growth plate, with a subsequent extension into both the epiphysis and metaphysis. Instead, we have the impression that the distribution of lesions is random, with a predominance of diaphyseal and metaphyseal locations. This highlights the importance of doing a full radiological work-up using MRI to rule-out the presence and characteristics of multiple foci of bone lesions. Due to their insignificant appearance, one could imagine that epiphyseal lesions might be overlooked and underdiagnosed. Hence, patients with polyostotic FD should be systematically investigated for epiphyseal lesions (10), since epiphyseal lesions due to FD are structurally weak and introduce additional complexity since they can induce serious deformities into the articular surface. Indeed, juxta-articular

lesions in weight-bearing joints can collapse leading to a loss of proper joint congruence.

Further radiological monitoring also remains essential because cystic changes are occasionally seen in FD lesions, with secondary transformations into aneurysmal bone cysts (9, 10, 23, 24). Even worse, FD lesions can degenerate into high-grade sarcoma, with an incidence of 0.5% in monostotic FD and 4% in McCune–Albright syndrome (24, 25). The most common forms of malignant degeneration, in decreasing order of frequency, are osteosarcoma, fibrosarcoma and chondrosarcoma. MRI is also crucial for assessing bone and soft tissue invasion and for guiding a percutaneous biopsy for a final diagnosis.

It is very common for general physician to be the first specialist consulted for FD, whatever its form, even though some children with McCune–Albright because of their non-orthopedic symptoms, such as skin pigmentation or precocious puberty. Patients' monostotic lesions are very frequently diagnosed incidentally on radiographs taken for unrelated symptoms and they must be referred to an orthopedic specialist, even if they are asymptomatic. Thus, radiological investigations, particularly bone scintigraphy and MRI, play a critical role in the identification, prognostic evaluation, and follow-up of osseous complications in paediatric patients with polyostotic FD.

4 Conclusion

Polyostotic fibrous dysplasia (FD) is a benign medullary fibro-osseous anomaly that compromises the mechanical strength of bones, especially the long bones that bear strong mechanical stresses. As a result, these may inappropriately align, particularly at the proximal femur. Deformities typically occur in the femur's frontal plane, ranging from the coxa vara deformity to the well-known "shepherd's crook" deformity. The present case leads us to recommend that clinicians should not underestimate the occurrence of other deformities, such as the retrotorsion or flexion deformities that can compromise bone structure and the hip's biomechanics. Finally, the involvement of the epiphysis is probably more common than usually thought, introducing an additional complexity since juxta-articular lesions in weight-bearing joints may collapse, compromising articular congruence and function. In order to minimise this risk, bone scintigraphy and MRI should play a critical role in the patient's workup, evaluation, prognosis and follow-up.

Data availability statement

The original contributions presented in the study are included in the article/Supplementary Material, further inquiries can be directed to the corresponding author.

Ethics statement

The studies involving humans were approved by commission cantonale d'éthique de la recherche sur l'être humain (CCER). The studies were conducted in accordance with the local legislation and institutional requirements. Written informed consent for participation in this study was provided by the participants' legal guardians/next of kin. Written informed consent was obtained from the individual(s), and minor(s)' legal guardian/next of kin, for the publication of any potentially identifiable images or data included in this article.

Author contributions

EP: Data curation, Writing – original draft, Writing – review & editing. GD: Writing – review & editing. OV: Writing – review & editing. SB: Data curation, Investigation, Supervision, Writing – original draft. CS: Writing – review & editing. RD: Writing – review & editing. DC: Investigation, Supervision, Writing – original draft, Writing – review & editing.

Funding

The author(s) declare financial support was received for the research, authorship, and/or publication of this article. Open access funding by University of Geneva.

Conflict of interest

The authors declare that the research was conducted in the absence of any commercial or financial relationships that could be construed as a potential conflict of interest.

Generative AI statement

The author(s) declare that no Generative AI was used in the creation of this manuscript.

Publisher's note

References

1. Kushchayeva YS, Kushchayev SV, Glushko TY, Tella SH, Teytelboym OM, Collins MT, et al. Fibrous dysplasia for radiologists: beyond ground glass bone matrix. *Insights Imaging*. (2018) 9(6):1035–56. doi: 10.1007/s13244-018-0666-6

2. Tafti D, Cecava ND. Fibrous dysplasia. In: *StatPearls*. Treasure Island, FL: StatPearls Publishing (2024). Available online at: http://www.ncbi.nlm.nih.gov/books/NBK532947/ (cited July 29, 2024).

3. Albright F, Butler A, Hampton A, Smith P. Syndrome characterized by osteitis fibrosa disseminate, areas of pigmentation and endocrine dysfunction, with precocious puberty in females: report of 5 cases. *N Engl J Med*. (1937) 216:727–46. doi: 10.1056/NEJM193704292161701

4. Lädermann A, Stern R, Ceroni D, De Coulon G, Taylor S, Kaelin A. Unusual radiologic presentation of monostotic fibrous dysplasia. *Orthopedics*. (2008) 31(3):282. doi: 10.3928/01477447-20080301-25

5. Lodwick GS, Wilson AJ, Farrell C, Virtama P, Dittrich F. Determining growth rates of focal lesions of bone from radiographs. *Radiology*. (1980) 134(3):577–83. doi: 10.1148/radiology.134.3.6928321

6. Fukui T, Kawamoto T, Hitora T, Yamagami Y, Akisue T, Yamamoto T. Polyostotic fibrous dysplasia with epiphyseal involvement in long bones: a case report. *Case Rep Orthop*. (2013) 2013:715402. doi: 10.1155/2013/715402

7. Harris WH, Dudley HR, Barry RJ. The natural history of fibrous dysplasia. An orthopaedic, pathological, and roentgenographic study. *J Bone Joint Surg Am*. (1962) 44:207–33. doi: 10.2106/00004623-196244020-00001

8. Nixon GW, Condon VR. Epiphyseal involvement in polyostotic fibrous dysplasia. A report of two cases. *Radiology*. (1973) 106(1):167–70. doi: 10.1148/106.1.167

9. Takechi R, Shinozaki T, Fukuda T, Yanagawa T, Takagishi K. Involvement of the proximal tibial epiphysis by monostotic fibrous dysplasia. *Clin Imaging*. (2009) 33(2):154–7. doi: 10.1016/j.clinimag.2008.09.014

10. Burdiles A, Marín R, Klaber I, Solar A, Calderón M, Jara F, et al. Polyostotic fibrous dysplasia (McCune-Albright) with rare multiple epiphyseal lesions in association with aneurysmal bone cyst and pathologic fracture. *Radiol Case Rep*. (2021) 16(9):2719–25. doi: 10.1016/j.radcr.2021.06.017

11. Kaloostian SW, Vartanian TK, Ordookhanian C, Vartanian T, Kaloostian PE. Concomittant fibrous dysplasia with aneurysmal bone cyst formation within the skull, humerus and rib. *J Surg Case Rep*. (2018) 2018(7):rjy180. doi: 10.1093/jscr/rjy180

12. Mazabraud A, Semat P, Roze R. [Apropos of the association of fibromyxomas of the soft tissues with fibrous dysplasia of the bones]. *Presse Med (1893)*. (1967) 75(44):2223–8.

13. Chapurlat RD, Orcel P. Fibrous dysplasia of bone and McCune–Albright syndrome. *Best Pract Res Clin Rheumatol*. (2008) 22(1):55–69. doi: 10.1016/j.berh.2007.11.004

14. Daves M, Yardley J. Fibrous dysplasia of bone. *Am J Med Sci*. (1957) 234(5):590–606. doi: 10.1097/00000441-195711000-00009

15. Fairbank H. Fibrocystic disease of bone. *J Bone and Joint Surg B*. (1950) 32-B(3):403–23. doi: 10.1302/0301-620X.32B3.403

16. Warrick C. Polyostotic fibrous dysplasia, Albright's syndrome, a review of the literature and report of four male cases, two of which were associated with precocious puberty. *J Bone and Joint Surg B*. (1949) 31-B(2):175–83. doi: 10.1302/0301-620X.31B2.175

17. Latham PD, Athanasou NA, Woods CG. Fibrous dysplasia with locally aggressive malignant change. *Arch Orthop Trauma Surg*. (1992) 111(3):183–6. doi: 10.1007/BF00388097

18. Breck LW. Treatment of fibrous dysplasia of bone by total femoral plating and hip nailing. A case report. *Clin Orthop Relat Res*. (1972) 82:82–3. doi: 10.1097/00003086-197201000-00011

19. Funk FJ, Wells RE. Hip problems in fibrous dysplasia. *Clin Orthop Relat Res*. (1973) 90:77–82.

20. Connolly JF. Shepherd's crook deformities of polyostotic fibrous dysplasia treated by osteotomy and zickel nail fixation. *Clin Orthop Relat Res*. (1977) 123:22–4.

21. Freeman BH, Bray EW, Meyer LC. Multiple osteotomies with zickel nail fixation for polyostotic fibrous dysplasia involving the proximal part of the femur. *J Bone Joint Surg Am*. (1987) 69(5):691–8. doi: 10.2106/00004623-198769050-00009

22. Enneking WF, Gearen PF. Fibrous dysplasia of the femoral neck. Treatment by cortical bone-grafting. *J Bone Joint Surg Am*. (1986) 68(9):1415–22. doi: 10.2106/00004623-198668090-00015

23. Diercks RL, Sauter AJ, Mallens WM. Aneurysmal bone cyst in association with fibrous dysplasia. A case report. *J Bone Joint Surg Br*. (1986) 68-B(1):144–6. doi: 10.1302/0301-620X.68B1.3941131

24. Montalti M, Alberghini M, Ruggieri P. Secondary aneurysmal bone cyst in fibrous dysplasia of the proximal femur. *Orthopedics*. (2009) 32(5):363. doi: 10.3928/01477447-20090501-10

25. Mattei TA, Mattei JA, Ramina R, Aguiar PH. Fibrous dysplasia in combination with aneurysmal bone cyst presenting as a subarachnoid haemorrhage. *Neurol Sci*. (2005) 26(3):178–81. doi: 10.1007/s10072-005-0458-x

frontiers | Frontiers in Endocrinology

TYPE Review
PUBLISHED 06 February 2025
DOI 10.3389/fendo.2025.1510010

OPEN ACCESS

EDITED BY
Nico Sollmann,
Ulm University Medical Center, Germany

REVIEWED BY
Alan C. Seifert,
Icahn School of Medicine at Mount Sinai, United States
Juliana Ebling Brondani,
Federal University of Minas Gerais, Brazil

*CORRESPONDENCE
Jiang Du
jiangdu@ucsd.edu

†These authors have contributed equally to this work

RECEIVED 12 October 2024
ACCEPTED 15 January 2025
PUBLISHED 06 February 2025

CITATION
Shin SH, Chae HD, Suprana A, Jerban S, Chang EY, Shi L, Sah RL, Pettus JH, Woods GN and Du J (2025) UTE MRI technical developments and applications in osteoporosis: a review.
Front. Endocrinol. 16:1510010.
doi: 10.3389/fendo.2025.1510010

UTE MRI technical developments and applications in osteoporosis: a review

Soo Hyun Shin[1†], Hee Dong Chae[1,2†], Arya Suprana[1,3†], Saeed Jerban[1], Eric Y. Chang[1,4], Lingyan Shi[3], Robert L. Sah[3], Jeremy H. Pettus[5], Gina N. Woods[5] and Jiang Du[1,3,4*]

[1]Department of Radiology, University of California, San Diego, San Diego, CA, United States, [2]Department of Radiology, Seoul National University Hospital, Seoul, Republic of Korea, [3]Department of Bioengineering, University of California, San Diego, San Diego, CA, United States, [4]Radiology Service, Veterans Affairs San Diego Healthcare System, San Diego, CA, United States, [5]Department of Medicine, University of California, San Diego, San Diego, CA, United States

Osteoporosis (OP) is a metabolic bone disease that affects more than 10 million people in the USA and leads to over two million fractures every year. The disease results in serious long-term disability and death in a large number of patients. Bone mineral density (BMD) measurement is the current standard in assessing fracture risk; however, the majority of fractures cannot be explained by BMD alone. Bone is a composite material of mineral, organic matrix, and water. While bone mineral provides stiffness and strength, collagen provides ductility and the ability to absorb energy before fracturing, and water provides viscoelasticity and poroelasticity. These bone components are arranged in a complex hierarchical structure. Both material composition and physical structure contribute to the unique strength of bone. The contribution of mineral to bone's mechanical properties has dominated scientific thinking for decades, partly because collagen and water are inaccessible using X-ray based techniques. Accurate evaluation of bone requires information about its components (mineral, collagen, water) and structure (cortical porosity, trabecular microstructure), which are all important in maintaining the mechanical integrity of bone. Magnetic resonance imaging (MRI) is routinely used to diagnose soft tissue diseases, but bone is "invisible" with clinical MRI due to its short transverse relaxation time. This review article discusses using ultrashort echo time (UTE) sequences to evaluate bone composition and structure. Both morphological and quantitative UTE MRI techniques are introduced. Their applications in osteoporosis are also briefly discussed. These UTE-MRI advancements hold great potential for improving the diagnosis and management of osteoporosis and other metabolic bone diseases by providing a more comprehensive assessment of bone quantity and quality.

KEYWORDS

UTE, MRI, contrast mechanism, quantitation, osteoporosis

Introduction

Osteoporosis (OP) is a progressive bone disease that is characterized by low bone mass and structural deterioration (1). Fractures are among the most dramatic sequelae. OP affects more than 10 million people in the USA and causes more than two million fractures, with an annual cost estimated at about $19 billion (2). The need for focused preventive strategies has become a major public health priority.

The current standard technique for assessing bone fracture is dual-energy X-ray absorptiometry (DXA), which can only provide information on bone mineral density (BMD) (3). However, the majority of fractures cannot be explained by BMD alone. Bone is a composite material consisting of, by volume, mineral (~43%), organic matrix (~35%), and water (~22%) (4, 5). While bone mineral provides stiffness and strength (6), collagen provides ductility and the ability to absorb energy before fracturing (7), and water contributes to viscoelasticity and poroelasticity (8). These bone components are arranged in a complex hierarchical structure (9). Both material composition and physical structure contribute to the unique strength of bone. The contribution of mineral to bone's mechanical properties has dominated scientific thinking; however, accurate evaluation of bone requires information about its components (mineral, collagen, water) and structure (cortical porosity, trabecular microstructure), which are all important in maintaining the mechanical integrity of bone (10).

Unfortunately, no single modality can evaluate all bone components and structures. DXA can only measure areal BMD without information about bone collagen, water, and bone microstructure. Computed tomography (CT) can measure volumetric BMD and capture bone structure without information about bone collagen and water (11). Conventional CT has a spatial resolution that is too low to evaluate cortical porosity. High-resolution peripheral quantitative CT (HR-pQCT) can assess bone porosity but cannot resolve smaller pores (e.g., pores with diameters less than 83 μm) (12, 13). Micro CT (μCT) is the reference standard for evaluating cortical porosity but cannot be used for *in vivo* applications (14). Magnetic resonance imaging (MRI) is routinely used to diagnose soft tissue diseases, but bone is "invisible" with clinical MRI due to its short transverse relaxation time (15, 16). This review paper aims to summarize the recent developments in ultrashort echo time (UTE) MRI techniques for direct imaging of bone.

Materials and methods

This narrative review was conducted to synthesize the most relevant advancements and applications of UTE MRI, particularly focusing on the authors' contributions and other key studies in the field. The UTE-type sequences include two-dimensional (2D) and 3D UTE (15–28) zero echo time (ZTE) (25–36), pointwise encoding time reduction with radial acquisition (PETRA) (37–39), Cartesian variable TE (vTE) (40), water- and fat-suppressed proton projection MRI (WASPI) (41), sweep imaging with Fourier transformation (SWIFT) (42), hybrid acquisition-weighted stack of spirals (AWSOS) (43), ramped hybrid encoding (RHE) (44), and Looping Star (45). A simple search on Pubmed shows more than 600 papers on direct imaging of bone using the various UTE-type sequences. It is difficult to summarize all the published articles in this review. The selection of articles was primarily guided by the authors' expertise and their understanding of the pivotal developments in UTE MRI research.

In conventional MRI, bone produces near zero signal, leading most clinicians to rely on plain radiography or CT as the primary modality for bone evaluation. The lack of detectable signals can be mainly attributed to the bone's short mean apparent transverse relaxation time (T2) or apparent transverse relaxation time (T2*) components. T2 or T2* relaxation time refers to the time constant that describes the rate at which excited protons lose phase coherence due to interactions with surrounding tissues in MRI, with short T2* values indicating a rapid decay of transverse magnetization. Long T2* tissues retain a detectable signal level at the time of the measurement of the MR signal, allowing them to remain visible in conventional pulse sequences. In contrast, short T2* tissues such as bone, tendons, ligaments, and menisci lose most of their signal before spatial encoding, resulting in undetectable signals during signal acquisition, making these tissues appear dark or "invisible" on conventional MRI scans.

For simplicity, T2* values can be categorized into five groups: <0.01 ms (supershort), 0.01–1 ms (ultrashort), 1–10 ms (short), 10–100 ms (intermediate), and 100–4000 ms (long) (16). Echo time (TE) is the interval between the delivery of the RF pulse and the measurement of the MR signal. It determines the time the system waits before measuring the signal. A general rule is that the effective TE should match the T2* of the tissue for optimal detectability. Recent advances in hardware have enabled gradient-recalled echo (GRE) sequences with much reduced TEs to capture signals from short T2 tissues. However, conventional sequences, such as fast spin echo (FSE) and GRE, cannot produce echo times shorter than 1 ms on clinical MRI systems. Therefore, tissues with ultrashort T2 values, such as bone, require specialized techniques for effective signal detection.

Recently, a group of UTE-type sequences, including 2D and 3D UTE, ZTE, PETRA, vTE, WASPI, SWIFT, AWSOS, RHE, and Looping Star sequences, with nominal TEs of 0.1 ms or less have been developed to directly image short-T2 tissues (15–45). While a short TE is essential for imaging bone, it alone is insufficient due to the low proton density in bone (i.e., ~22% water by volume in normal bone). Effective suppression of long-T2 signals is crucial for achieving high-contrast images of bone. Quantitative UTE imaging can provide valuable insights into bone structure and components. In the next section, we will review technical developments in morphological and quantitative UTE imaging of bone. Their applications in osteoporosis will also be briefly discussed.

Results

Part I: technical developments in morphological UTE MRI

With the UTE technique, bone signal with an ultrashort transverse relaxation time can be captured. However, UTE MRI is

primarily T1-weighted with negative contrast between bone and neighboring musculoskeletal tissues, such as muscle and marrow fat, which have far higher proton densities than that of bone. A key issue for high contrast morphological imaging of bone is the efficient suppression of long T2 signals from surrounding muscle and marrow fat (46). Different contrast mechanisms have been developed for this purpose.

UTE with echo subtraction

One basic approach to enhancing contrast in UTE imaging is subtracting two images acquired at distinct echo times (TEs). In the dual-echo UTE imaging technique with echo subtraction, bone contrast is acquired by subtracting a second echo image from a first echo image which is equivalent to T2 bandpass filtering (19). Signals from long T2 tissues experience minimal decay by the time of the second echo, while the signal from bone undergoes significant decay by the time of the second echo. As a result, long T2 tissues show a high signal in the second echo, while bone shows a signal void. Subtraction of the second echo image from the first echo image leads to suppression of long T2 signals, leaving bone signal minimally unaffected, creating high contrast for cortical bone. Rescaled subtraction (46), where the first UTE free induction decay (FID) image is scaled down prior to subtraction to lower signal from long-T2 tissues in the first compared to the second echo, works more efficiently in creating high positive contrast for short-T2 species, especially cortical bone, which has a much lower mobile proton density than surrounding muscle or fat. Figure 1 shows an example of 3D dual-echo UTE imaging with rescaled subtraction applied to the tibia of a healthy volunteer. Conventional 3D UTE imaging provides a relatively high signal but negative contrast for the tibia (Figure 1A). Regular echo subtraction presents a positive contrast between bone and muscle, but a negative contrast between cortical bone and fat, as fat also has a short T2* (Figure 1C). The contrast between bone and fat/muscle increases using the rescaled subtraction technique (Figures 1D–F). However, subtraction techniques are sensitive to patient motion, which can cause misalignment between the source images and result in artifacts.

UTE with long T2 saturation

Preparation pulses can be employed to selectively suppress signals from long T2 components, improving contrast by allowing better visualization of short T2 tissues (47–49). In UTE imaging with long T2 saturation, saturation pulses are used to suppress the signals from long T2 tissues, such as muscle and bone marrow fat, which typically produce higher signals than bone. For example, a 90° pulse with a relatively long duration and a low amplitude can flip the longitudinal magnetization of long T2 tissues into the transverse plane, where a large spoiling gradient can subsequently dephase the transverse magnetization (48). In comparison, bone magnetization is barely excited by this long saturation pulse as the decay rate of bone exceeds the excitation rate. Therefore, a long 90° pulse can be used with a large spoiling gradient to suppress long T2 tissues, leaving bone to be subsequently detected by UTE data acquisition. T2 selective RF excitation (TELEX) can be used to increase bone contrast (47). Dual-band long-T2 suppression pulses further improve the suppression of signals from muscle and fat (49). However, residual signals from muscle and marrow fat due to B1 and B0 inhomogeneities may still compromise bone contrast.

UTE with off-resonance saturation

Off-resonance saturation with subtraction can generate contrast for short T2 components by utilizing the broader absorption line shape of short T2 tissues, such as bone, compared to long T2 tissues like muscle or fat, making them more sensitive to off-resonance RF radiation (50). UTE imaging with off-resonance saturation contrast (UTE-OSC) employs a high-power saturation pulse placed a few kHz off the water peak to preferentially saturate signals from bone, leaving long T2 muscle and fat signals largely unaffected (50). Subtraction of UTE images with off-resonance saturation from basic UTE images can effectively suppress signals from muscle and fat, creating high bone contrast.

UTE with adiabatic inversion

One limitation of saturation techniques that utilize hard RF pulses is their sensitivity to B0 and B1 inhomogeneities, making

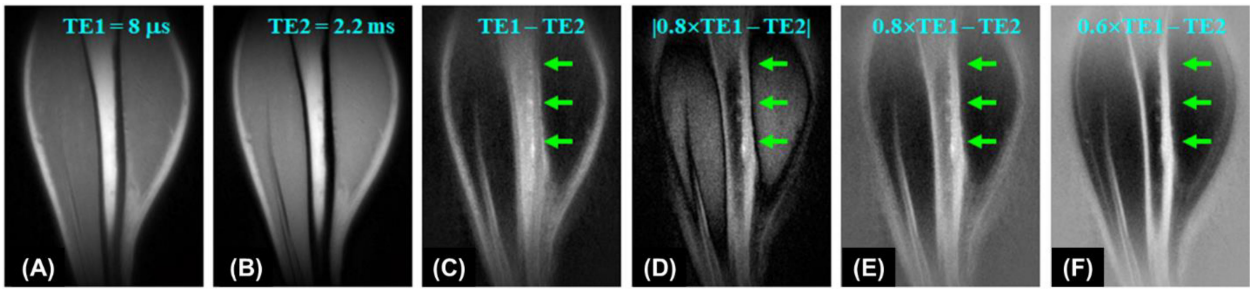

FIGURE 1
3D UTE imaging of the tibia of a volunteer with dual TEs of 8 μs **(A)** and 2.2 ms **(B)**. Subtraction of the second echo (TE = 2.2 ms) from the first one (TE = 8 μs) shows limited contrast for cortical bone due to a high signal from marrow fat **(C)**. Higher bone contrast is achieved by scaling down the first echo UTE image by a factor of 0.8 and using absolute pixel intensity in the subtraction image **(D)**. Bone contrast can be further enhanced by allowing negative signal intensity in long-T_2 tissues **(E, F)**. From Ref. (46), with permission.

them less robust compared to adiabatic inversion (18). The adiabatic inversion recovery UTE (IR-UTE) contrast mechanism employs a long adiabatic inversion pulse to invert the longitudinal magnetizations of long-T2 water (e.g., muscle) and long-T2 fat (18, 21, 24, 51). The duration of the adiabatic inversion pulse is much longer than bone T2* (18). As a result, the longitudinal magnetizations of muscle and marrow fat are fully inverted, while the bone magnetization is not inverted but largely saturated by the long adiabatic inversion pulse (51). The UTE data acquisition starts at an inversion time (TI) adjusted so that the inverted long T2 magnetizations approach the null points, leaving the uninverted bone magnetization being selectively detected by UTE data acquisition. The adiabatic inversion pulse has a relatively broad spectral bandwidth, thereby insensitive to B1 and B0 inhomogeneities. The IR-UTE technique allows uniform inversion of long T2 magnetizations, providing robust high contrast imaging of bone (18, 21). Figure 2 shows representative IR-UTE images of cortical bone in the forearm, which is depicted with excellent image contrast but invisible with conventional clinical FSE sequences.

UTE with double adiabatic inversion

A single inversion pulse can reduce the signal from fat and long T2* components (such as muscle) by up to 80% (21). However, using dual inversion pulses allows for the complete nulling of both, providing more effective signal suppression (52–54). The double adiabatic inversion recovery UTE sequence (double-IR-UTE) employs two identical adiabatic inversion pulses (duration of ~6 ms) with the same center frequency to sequentially invert the longitudinal magnetizations of long T2 species, followed by multispoke UTE data acquisition (55). The two adiabatic inversion pulses are applied with pre-defined inversion times TI1, which is the time between the centers of the two adiabatic inversion pulses, and TI2, which is the time from the center of the second adiabatic inversion pulse to the center spoke of the multispoke acquisition. Robust long T2 suppression can be achieved by timing the center spoke at the null point. Long T2 transverse magnetizations acquired before the null point are of opposite polarity to those acquired after the nulling point, leading to cancellation in the regridding process during image reconstruction and, therefore, efficient suppression of long T2 signals from muscle and marrow fat. Bone magnetization is not inverted but saturated by the two long adiabatic inversion pulses, recovers after the second TI2, and is subsequently detected by UTE data acquisition. The advantage of double-IR-UTE is the robust suppression of long T2 tissues with a broad range of T1s, such as fat and muscle, which can be nulled simultaneously using specific combinations of TI1 and TI2. The double-IR-UTE sequence is insensitive to inhomogeneities in the B1 and B0 fields due to the use of adiabatic inversion pulses with relatively broad spectral bandwidths. Figure 3 shows double-IR-UTE imaging of the knee joint in a healthy volunteer, which shows high signal from short-

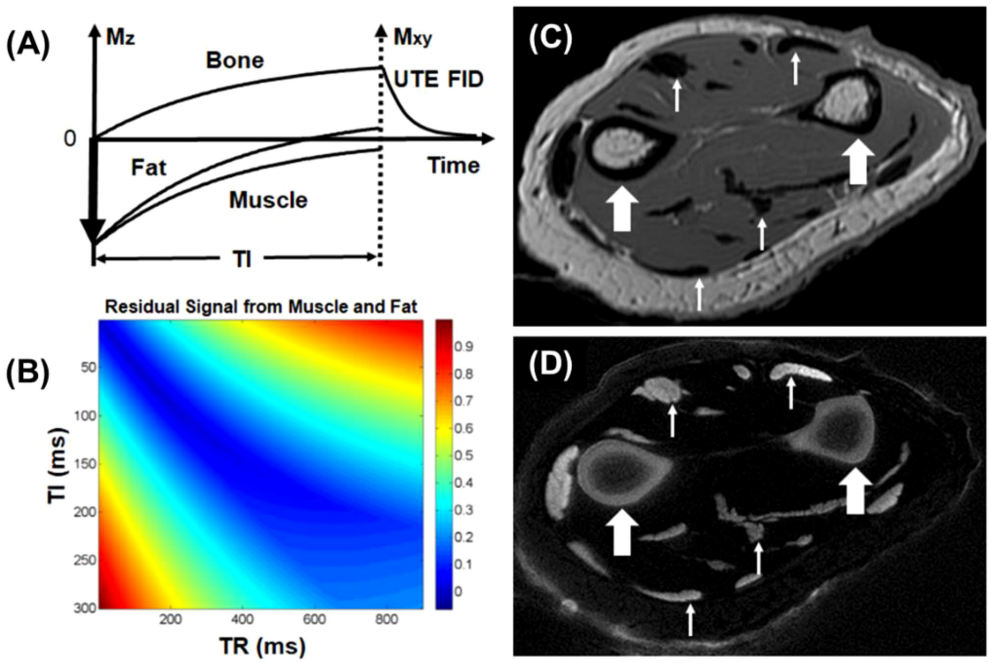

FIGURE 2
The IR-UTE sequence inverts the longitudinal magnetizations of long T2 muscle and fat with a long adiabatic inversion pulse (duration = 8.64 ms) **(A)**. The longitudinal magnetization of bone is largely saturated, recovers during TI, and is subsequently detected by the UTE data acquisition **(B)**. Clinical FSE imaging of the forearm shows pure signal void for cortical bone (thick arrows), tendons, and aponeuroses (thin arrows) **(C)**. The IR-UTE sequence shows high signal and contrast for cortical bone (thick arrows) and other short T2 tissues (thin arrows) **(D)**. From Ref. (21), with permission.

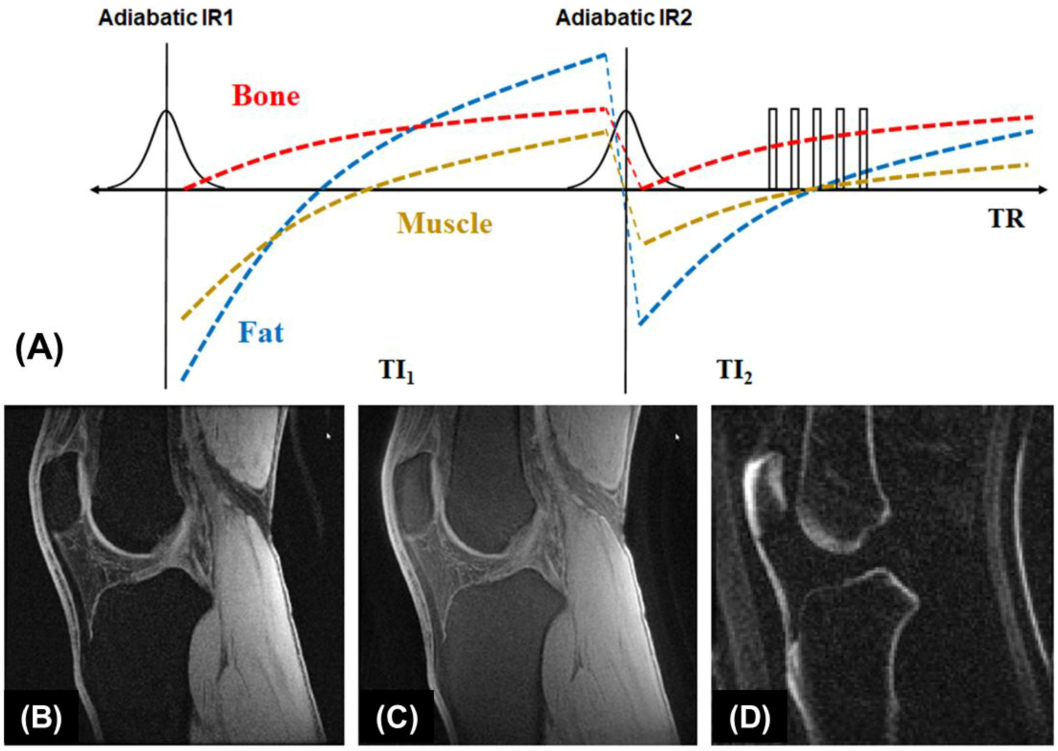

FIGURE 3
The double-IR-UTE sequence employs two identical adiabatic inversion pulses for simultaneous suppression of long T2 muscle and fat with different T1s, followed by 3D UTE data acquisition to produce high contrast imaging of bone **(A)**. The knee joint of a 31-year-old volunteer was subject to clinical GRE **(B)**, fat-saturated UTE **(C)**, and double-IR-UTE **(D)** imaging. The double-IR-UTE sequence shows excellent suppression of muscle and fat, providing high contrast for the patellar tendon and cortical bone **(D)**. From Ref. (55), with permission.

and ultrashort-T2 species, such as the patellar tendon and cortical bone.

UTE with relaxation-parameter contrast

UTE data acquisition can be combined with relaxation-parameter contrast (56). UTE with relaxation parameter contrast and subtraction exploits the sensitivity of bone proton magnetization to both T2 and RF pulse duration. Excitation pulse parameters are selected to determine the extent of concurrent relaxation and excitation. The RF pulse duration and amplitude can be changed to adjust the relaxation dependence of bone contrast. To selectively detect signals from magnetization within a specific range of T2 values, two RF pulse durations are chosen so that the sensitivity transition between them brackets the range of interest. Two UTE datasets with similar imaging parameters but different RF excitation pulses are acquired. Bone contrast is created by subtraction of the two UTE images, as shown in Figure 4.

UTE with dual-RF and dual-echo (DURANDE)

The 3D DURANDE UTE sequence and bone-selective image reconstruction have been proposed for rapid bone imaging (57). This technique acquires two dual-echo UTE datasets following short and long RF pulses, with encoding gradients varying continuously along the entire pulse train to halve the total imaging time. The DURANDE UTE sequence employs two rectangular RF pulses (RF1 and RF2), differing in duration and amplitude but having the same pulse area applied alternately in successive TR periods along the entire pulse train. Two echoes at a short TE and a long TE are collected from the beginning of the gradient ramp-up within each TR. As a result, four echoes are produced and combined via a view-sharing approach to generate two independent k-space datasets during image reconstruction. Accelerated UTE bone imaging can be achieved by using the sparsity of bone voxels in the corresponding subtraction images.

Short TR adiabatic inversion recovery UTE MRI of trabecular bone

In STAIR-UTE, 3D IR-UTE data are acquired with a short TR and a high flip angle within specific absorption rate (SAR) limits for clinical imaging (58–60). The short TR and TI combination is selected to achieve robust suppression of long-T2 muscle and marrow fat regardless of their different T1 values. Multiple spokes are acquired for efficient volumetric imaging of cortical and trabecular bone (60). The STAIR-UTE sequence is more efficient than other UTE or ZTE techniques, such as the spectral presaturation with IR UTE (SPIR-UTE), in selective imaging of trabecular bone (61). Figure 5 shows STAIR-UTE images of the spine and SPIR-UTE images of the fingers. The SPIR-UTE images showed T_2* values of 2.42 ± 0.56 for the capitate, which is much longer than the T_2* of 0.31 ± 0.01 ms for the trabecular bone of the

10.3389/fendo.2025.1510010

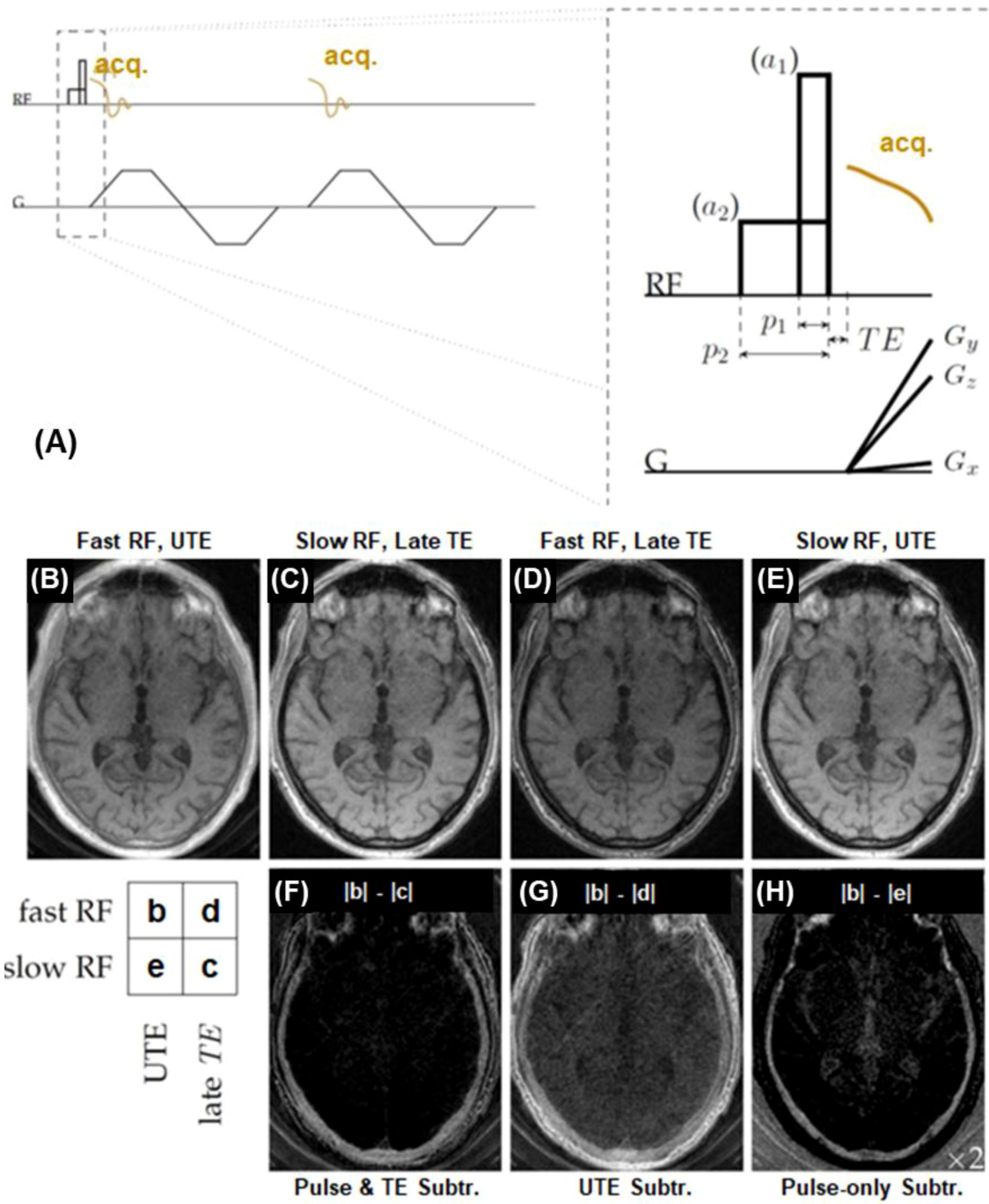

FIGURE 4
Bone imaging with the relaxation-parameter contrast mechanism, which is based on two hard RF pulses with different durations but equal pulse areas to generate T_2-selective excitation **(A)**. The contrast mechanism can be combined with single or dual-echo UTE data acquisition using two RF amplitudes (a_1 and a_2) and pulse durations (p_1 and p_2) with equal pulse areas. An example is shown on a volunteer's skull, including UTE with a short RF pulse of 24.47 μT and a TE of 34 μs **(B)**, UTE with a long RF pulse of 1.53 μT and a TE of 2.0 ms **(C)**, UTE with a short RF pulse and a longer TE of 2.0 ms **(D)**, and UTE with a long RF pulse and a TE of 34 μs **(E)**. The difference image (|b|-|c|) **(F)** depicts cortical bone more specifically than the conventional UTE subtraction difference image (|b|-|d|) **(G)**, and captures more bone signal than the pulse-only difference image (|b|−|e|) **(H)**. From Ref. (56), with permission.

spine measured on STAIR-UTE images (60, 61), or the T_2* value of ~0.3 ms for the cortical bone (62). The much longer T_2* values suggest that SPIR-UTE imaging of the trabecular bone is subject to significant long-T2 signal contamination. In comparison, STAIR-UTE-measured T_2* values for the trabecular bone are close to those measured for cortical bone, suggesting that bone marrow fat is completely suppressed and only signal from trabeculae is selectively detected in STAIR-UTE imaging (60).

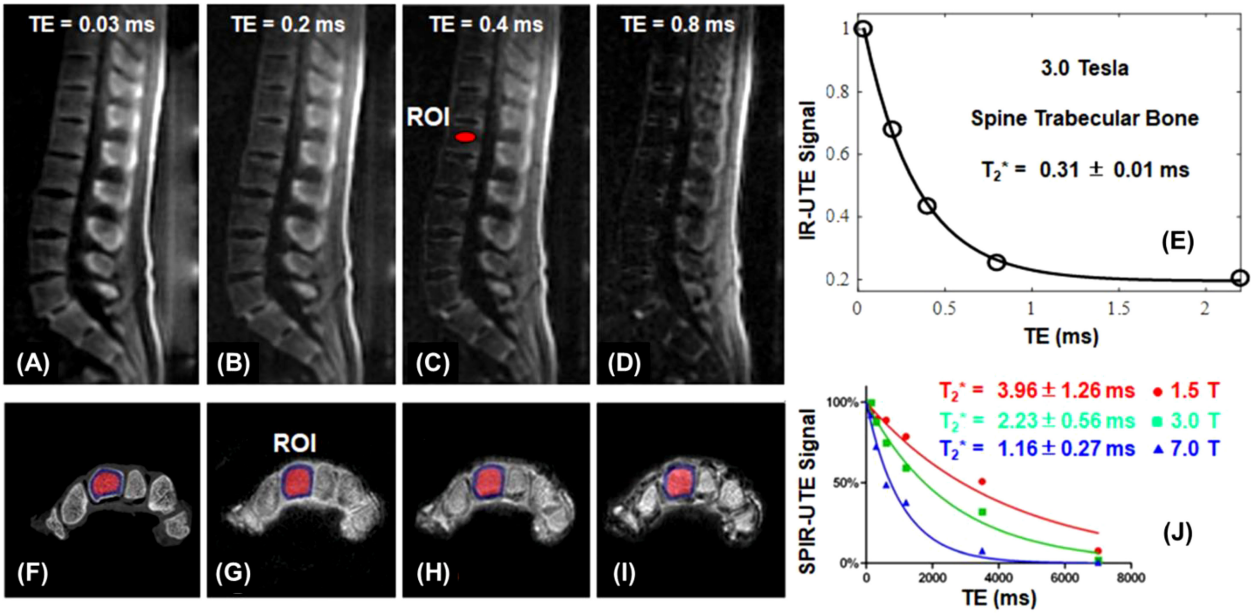

FIGURE 5
STAIR-UTE imaging of trabecular bone in the spine of a 36-year-old male volunteer with TEs of 0.032 ms **(A)**, 0.2 ms **(B)**, 0.4 ms **(C)**, and 0.8 ms **(D)** at 3T, and the single-component T_2* fitting **(E)**. μCT **(F)** and SPIR-UTE imaging of trabecular bone in the fingers at 1.5 T **(G)**, 3.0 T **(H)**, 7.0 T **(I)**, and the corresponding single component T_2* fitting **(J)**. STAIR-UTE imaging of trabecular bone in the spine shows a short-T_2* of 0.31 ± 0.01 ms at 3.0 T, while SPIR-UTE imaging of trabecular bone in the fingers shows short-T_2* values of 1.16 ± 0.27 ms at 7.0 T, 2.23 ± 0.56 ms at 3.0 T, and 3.96 ± 1.26 ms at 1.5 T, respectively. From Refs. (60, 61), with permission.

UTE on the fat peak for trabecular bone imaging

Past research has focused on high resolution imaging of marrow to indirectly detect trabecular microstructure (5, 63, 64). Two major challenges exist: the high susceptibility at the marrow/bone interface and the multiple fat peaks, both of which significantly reduce T_2*, leading to low marrow signal (misclassified as bone) and overestimation of trabecular volume. UTE is insensitive to T_2* shortening. However, UTE employs non-Cartesian radial sampling, which is sensitive to chemical shift artifacts (65). UTE imaging on the fat peak resolves this issue (66). Bone is off-resonance in fat-centered imaging, but it has a much lower signal than marrow, and the off-resonance artifact is negligible. Figure 6 shows UTE and clinical GRE imaging of a trabecular bone sample from a 65-year-old male donor. UTE on the water peak shows strong chemical shift artifacts, which are significantly reduced in UTE imaging on the fat peak. Trabecular bone thickness is overestimated at longer TEs (e.g., TE = 1.1, 2.2, 3.3, or 4.4 ms) or with the clinical GRE sequence. UTE imaging on the fat peak is expected to perform even better in older

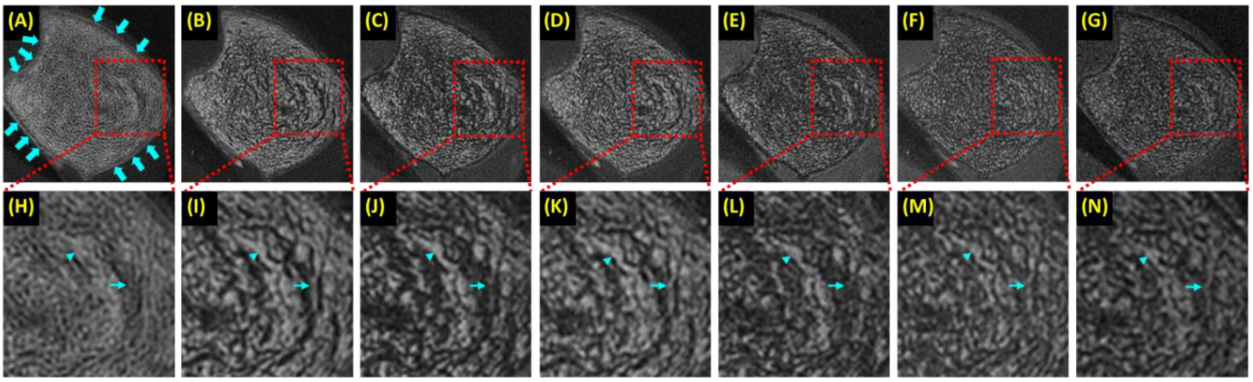

FIGURE 6
A trabecular bone specimen imaged with 3D UTE on the water peak at TE of 0.03 ms **(A)** and on the fat peak at TEs of 0.03 ms **(B)**, 1.1 ms **(C)**, 2.2 ms **(D)**, 3.3 ms **(E)**, and 4.4 ms **(F)**, and clinical 3D GRE at TE of 4.4 ms **(G)**, with the zoomed regions indicated with the red dashed-line boxes shown in the second row **(H-N)**. UTE images on the water peak show significant chemical shift artifacts, manifesting as blurred trabecular bone structure and ringing artifacts [arrows in **(A)**]. The more significant fat signal loss was observed at longer TEs **(C-F, J-M)** due to the strong susceptibility between bone/marrow interface and at TEs of 1.1 ms **(C, J)** and 3.3 ms **(E, L)** due to fat/water signal cancellation, with both leading to overestimation of trabecular thickness. From Ref. (66) with permission.

osteoporotic or diabetic patients who typically have a higher fat fraction in the marrow.

ZTE MRI of cortical bone

ZTE employs a short rectangular pulse excitation followed by readout gradient flat-top sampling to minimize the effective TE (29). A small flip angle (1-2°) is typically used to minimize the dead-time gap, which causes a spherical void in the center of k-space. A variety of approaches have been developed to address this k-space gap and associated low frequency artifacts in the reconstructed images (33). The repetition time (TR) is minimized to speed up data acquisition. Higher receiver bandwidths (62.5-83.3 kHz) are recommended to mitigate chemical shift artifacts. Bias field correction, contrast inversion, and background segmentation are employed for CT-like bone contrast (34–36). The principal difference between ZTE and UTE sequences is the temporal order of setting the spatial encoding gradient and RF excitation (33). UTE offers the freedom to adjust TE, a feature not possible in ZTE imaging. UTE also allows high flip angles, a significant advantage in direct bone imaging using the STAIR contrast mechanism (60). On the other hand, the ZTE sequence acquires k-space data after the readout gradients are fully ramped up, avoiding fidelity issues introduced by gradient ramping (33). ZTE has a shorter effective TE and can detect signal from shorter T2 species. ZTE can be applied in many of the same applications and with many of the same magnetization preparation methods as UTE.

Other UTE-type sequences for bone imaging

Many other UTE-type sequences have been developed for bone imaging. These sequences can be combined with each of the above contrast mechanisms for high-contrast imaging of bone. For example, adiabatic inversion recovery-based preparations can be combined with ZTE (29–36), vTE (40), AWSOS (43), RHE (44), and PETRA (37–39) sequences for high contrast imaging of cortical bone and other short-T_2 tissues, respectively. On-resonance long-T_2 suppression or off-resonance short-T_2 saturation can be applied to SWIFT, PETRA, WASPI, RHE, and ZTE sequences to create short-T_2 contrast. For example, SWIFT with off-resonance saturation has been used to image the interface between cartilage and subchondral bone (67). A systematic study of the above contrast mechanisms combined with ZTE, vTE, WASPI, SWIFT, AWSOS, PETRA, RHE, and Looping Star sequences remains to be investigated, and their SNR and CNR efficiency remains to be compared.

Part II: technical development in quantitative UTE imaging

Quantitative UTE MRI techniques have been developed to evaluate bone MR relaxation properties such as T1 and T2* relaxation times, and tissue properties such as total water proton density (TWPD), bound water proton density (BWPD), pore water proton density (PWPD), macromolecular proton density (MMPD), magnetization transfer ratio (MTR), susceptibility, and perfusion (24–26).

Bone T1 relaxation time

T1 relaxation is a fundamental MR tissue property and describes how fast the longitudinal magnetization recovers to the steady state. Many T1 measurement techniques have been combined with UTE acquisitions to provide accurate T1 measurements of bone, such as saturation recovery UTE (18), inversion recovery UTE (68), UTE with variable repetition time (UTE-VTR) (69), and UTE with variable flip angle (UTE-VFA) methods (70). The UTE-VTR method is sensitive to B1 inhomogeneity. The actual flip angle imaging (AFI) method has been widely used for 3D B1 mapping (71). By combining UTE and AFI techniques, it is possible to use a pair of interleaved UTE acquisitions with a short TR (e.g., 20 ms) and a longer TR (e.g., 100 ms) to produce accurate B1 mapping for bone (69). Furthermore, combining UTE-VTR and UTE-AFI (UTE-AFI-VTR) provides accurate T1 mapping for bone with B1 correction. A short T1 of ~250 ms was reported for cortical bone (69).

Bone T2* relaxation time

Bone water exists as pore water residing in the macroscopic pores and as loosely bound water attached to the organic matrix (72). UTE sequences can detect pore water with a longer T_2* of ~3 ms and loosely bound water with an ultrashort T_2* of ~0.3 ms (62, 73–76). IR-UTE or STAIR-UTE allows partial inversion and nulling of pore water with longer T2*, leaving bound water with ultrashort T2* to be selectively imaged (21, 60, 77). Figure 7 shows single- and bi-component fitting of UTE and IR-UTE images of a bovine cortical bone sample (77). Excellent bi-component fitting was achieved to show the existence of two distinct water components: bound water with a short T_2* of 0.26 ms (72.4% by volume) and pore water with a longer T_2* of 1.56 ms (27.6%). The IR-UTE images show a single component with T_2* ~0.31 ms, suggesting that pore water is efficiently suppressed and bound water selectively imaged (77).

UTE-MT modeling of MMF and exchange rates

There is another group of protons, collagen backbone protons, which have extremely short T2* relaxation times and are invisible with UTE sequences. UTE magnetization transfer (UTE-MT) modeling can measure collagen backbone proton fraction and exchange rates between water and collagen protons (73–75, 78–83). Figure 8 shows UTE-MT imaging of a bovine bone sample. Excellent two-pool MT modeling and MT parameters mapping were achieved using a Gaussian lineshape (79). The lower half of this bone sample shows increased variations in UTE image signal intensity and MT parameters, suggesting an abnormality that needs further investigation.

UTE mapping of water and collagen protons

UTE sequences can be used to map TWPD, BWPD, PWPD, and MMPD (20–23, 25, 76, 84–91). TWPD can be estimated by comparing the UTE MRI signal of bone with an external reference with known proton density (20, 21, 76, 84–88). BWPD can be measured with IR-UTE or STAIR-UTE, which efficiently suppresses pore water (21, 23, 60). PWPD can be quantified by subtracting

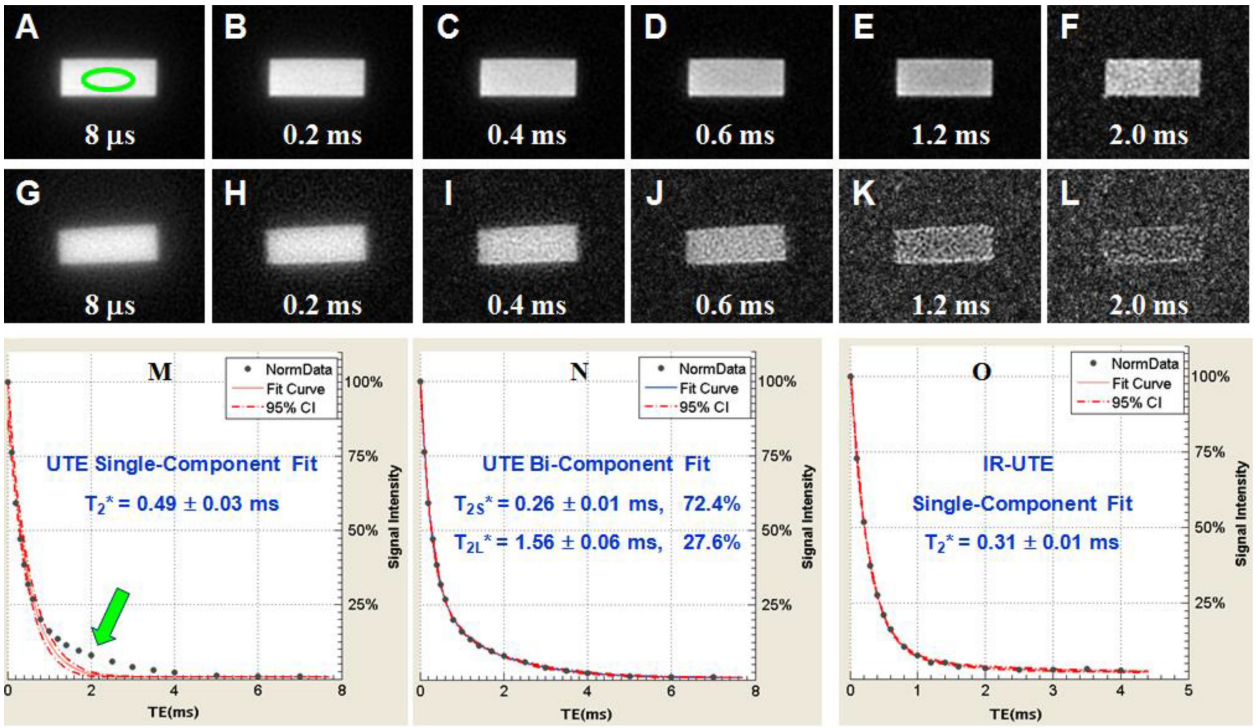

FIGURE 7
UTE imaging of a sectioned bovine cortical bone with TEs of 8 µs to 2 ms **(A-F)**, IR-UTE with TEs of 8 µs to 2 ms **(G-L)**. Single- **(M)** and bi-component **(N)** fitting suggest two components: bound water with a short T_2*~0.26 ms and pore water with a T_2* ~1.56 ms. IR-UTE images show one component with a T_2* of ~0.31 ms **(O)**, consistent with bound water imaging. From Ref. (77) with permission.

bound water from total water. MMPD can be quantified by combining total water proton density with macromolecular fraction (MMF) (91). Figure 9 shows 3D mapping of TWPD, BWPD, PWPD, and MMPD for tibial midshaft of a 35-year-old healthy female, a 76-year-old female with osteopenia, and a 57-year-old female with OP, respectively (91). The OP patient has higher PWPD but lower MMF and MMPD, consistent with increased porosity and loss of mineral/collagen.

UTE quantitative susceptibility mapping

Susceptibility is an important material property. QSM techniques can estimate calcium and iron accumulation in the brain (92). Bone susceptibility is more challenging to measure due to the lack of signal. UTE can detect phase evolution in cortical and trabecular bone. The phase changes with increasing TEs can be used to evaluate bone susceptibility using various algorithms such as Morphology Enabled Dipole Inversion (MEDI) (93). UTE with QSM (UTE-QSM) provides information about bone susceptibility, which is indirectly related to bone mineral (93–98). Figure 10 shows UTE-QSM and µCT-measured volumetric BMD (vBMD) of a human bone sample, with an excellent linear correlation between QSM and vBMD (n=9). UTE-QSM can reliably evaluate vBMD in cortical bone. Similar results are also observed for trabecular bone.

UTE perfusion

There is a close association between bone perfusion and bone remodeling and fracture repair (99–102). Increased cortical bone turnover and inflammation are also associated with increased blood flow (99). There is a strong correlation between bone perfusion and BMD (101, 102). However, the nature of bone makes it difficult to

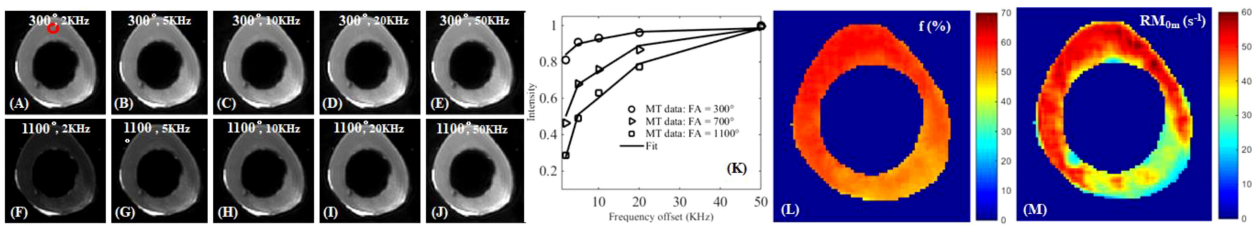

FIGURE 8
UTE-MT imaging of cortical bone with an MT power of 300° and frequency offsets of 2 kHz **(A)**, 5 kHz **(B)**, 10 kHz **(C)**, 20 kHz **(D)**, 50 kHz **(E)**, and 1100° and 2 kHz **(F)**, 5 kHz **(G)**, 10 kHz **(H)**, 20 kHz **(I)**, 50 kHz **(J)**, and two-pool fitting **(K)** with maps of macromolecular fraction [MMF or f; **(L)**] and exchange rate [RM_{0m}; **(M)**]. From Ref. (79) with permission.

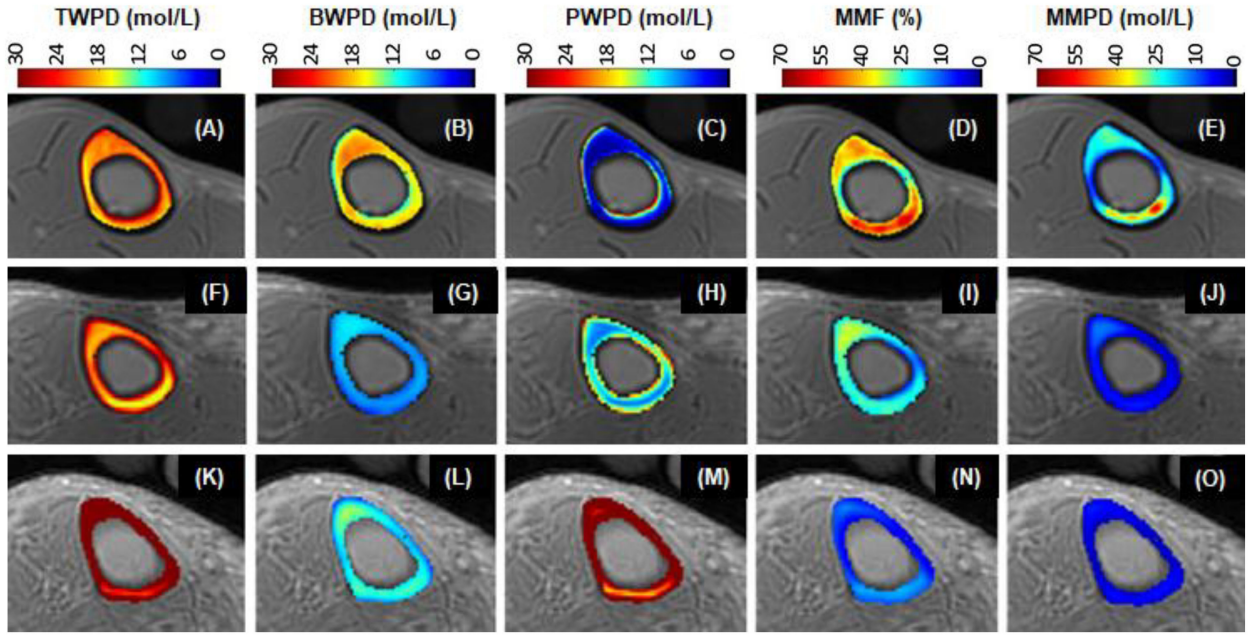

FIGURE 9
UTE maps of TWPD **(A, F, K)**, BWPD **(B, G, L)**, PWPD **(C, H, M)**, MMF **(D, I, N)**, and MMPD **(E, J, O)** of a 35-year-old healthy (1st row), a 76-year-old osteopenia (2nd row), and a 57-year-old OP (3rd row) females. The OP patient has the highest PWPD but the lowest MMF and MMPD. From Ref. (91) with permission.

investigate perfusion. The techniques applicable to many soft tissues are difficult or impossible to apply to bone. For example, dynamic contrast-enhanced MRI (DCE-MRI) can be used to study perfusion in various tissues and organs. The technique employs fast T1-weighted images to capture signal changes induced by exogenous intravascular nondiffusible gadolinium-based contrast agents as a function of time. Conventional DCE-MRI can study perfusion in the marrow of trabecular bone (103), but cannot study perfusion in cortical bone due to the lack of detectable signal. Dynamic UTE imaging has been developed to evaluate perfusion in cortical bone (104, 105). A recent study reported dynamic 2D UTE imaging of the tibial midshaft of a 38-year-old healthy volunteer and found ~20% signal enhancement after intravenous gadolinium contrast injection (105). Kinetic analysis demonstrated a K^{tran} of 0.23 ± 0.09 min^{-1} and K_{ep} of 0.58 ± 0.11 min^{-1} for the tibial midshaft of this volunteer. DCE-UTE can potentially be used to evaluate bone remodeling and fracture recovery.

Other UTE-type sequences for bone quantification

Bone components (water, collagen, mineral) and microstructure (cortical porosity, trabecular structure) can be qualified by many other UTE-type sequences such as ZTE (25–36), PETRA (37–39), vTE (40), WASPI (41), and SWIFT (42). For example, WASPI has been used to image bone water and the solid matrix of bone (106). SWIFT has been shown to be able to identify the presence and extent of dental caries and fine structures of the teeth, including cracks and accessory canals (107). Furthermore,

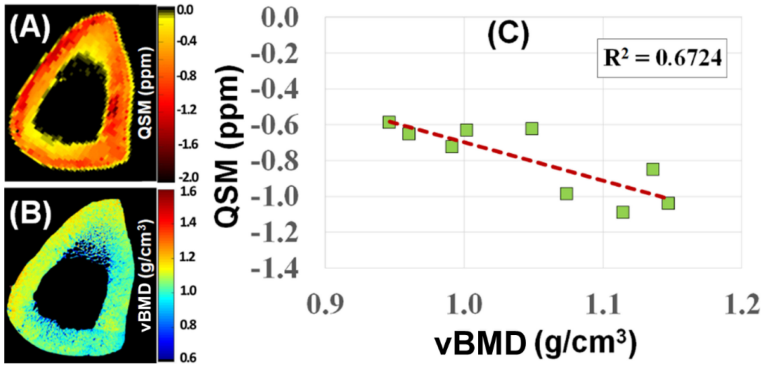

FIGURE 10
UTE-QSM **(A)** and μCT volumetric BMD (vBMD) **(B)** maps of a human cortical bone sample. A negative correlation (R^2 = 0.6724) was observed between QSM and vBMD (n=9) **(C)**. From Ref. (98) with permission.

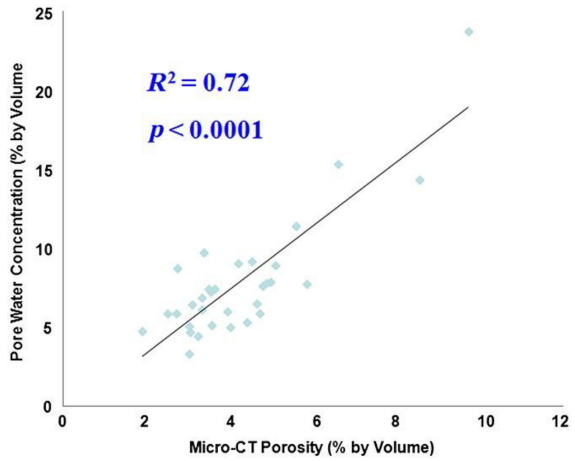

FIGURE 11
Correlation between UTE-measured pore water concentration and µCT-measured porosity in cadaveric human cortical bone samples (n = 32). A high correlation (R^2 = 0.72; P < 0.0001) was observed between UTE pore water concentration and µCT porosity, suggesting that UTE sequences can reliably access pore water in cortical bone using a clinical MR scanner. From Ref. (77) with permission.

solid-state 31P MRI can be achieved with UTE-type sequences by focusing on the 31P peak (108). 31P UTE MRI can map phosphorus content, assess bone mineral density, and differentiate between mature and newly remodeled bone (108, 109).

Part III: applications in OP

UTE-measured pore water to assess cortical porosity

UTE MRI can be used to measure pore water concentration in cortical bone (23, 76, 84–88). A recent study showed a high correlation (R^2 = 0.72; P < 0.0001) between µCT porosity and pore water concentration in 32 cadaveric human cortical bone samples (Figure 11) (77). Water residing in the microscopic pores of cortical bone is expected to behave more like "free" water with much longer T2* relaxation time than water bound to the organic matrix. Therefore, separating pore water from bound water is easy, allowing accurate pore water mapping without requiring ultrahigh spatial resolution to resolve the small pores. This is confirmed by the high correlation with an R^2 of 0.72 between µCT porosity and pore water concentration in cortical bone. µCT porosity is consistently lower than pore water content assessed by UTE MRI. Pore water content in cortical bone is also significantly correlated with its mechanical properties (110–112). In another study, UTE MRI, µCT, and histomorphometry were performed on tibial samples from 11 donors. UTE-measured pore water content showed significant correlations (R^2>0.25) with histomorphometry-based lacunae and small Haversian canals, which are below the detectable range of µCT at 9 µm. The µCT-based porosity showed strong correlations with histomorphometric porosity and pore size when considering all pores or only large pores (R>0.70, P<0.01). Correlations were poor when considering only small pores in histomorphometric analyses (R<0.3) (88). Therefore, pore water in smaller pores can be detected by UTE MRI but not by µCT imaging.

UTE measured bound water to assess bone organic matrix density

UTE MRI can map bound water in cortical and trabecular bone (21, 23, 60). Bound water is a surrogate of bone organic matrix density and negatively correlates with bone mineral density, as shown in Figure 12 (113). It is also reported that bound water in human cortical bone decreases with age, although osteonal remodeling throughout life with only modest changes in tissue mineral density or ash fraction with age after skeletal maturation (114). Bound water and bone density are directly correlated with human cortical bone's material strength (72, 84, 111, 112).

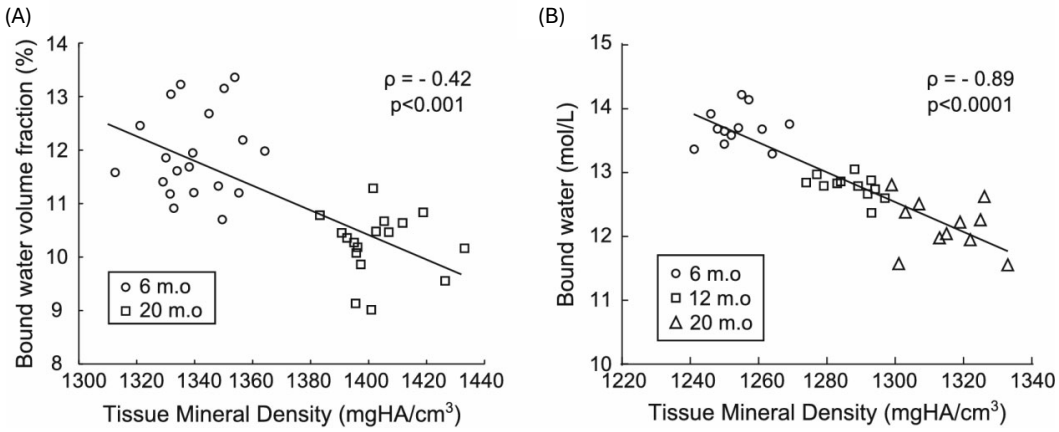

FIGURE 12
Bound water decreases as mineralization increases in rodents throughout life, as evidenced in mice **(A)** and rats **(B)**, where bound water was calculated as the volume fraction of the bone tissue volume (%) or as the concentration of protons (mol/L) in the bone tissue volume in which µCT determined the latter. Spearman's rank correlation was performed to calculate the correlation coefficient (ρ). From Ref. (113) with permission.

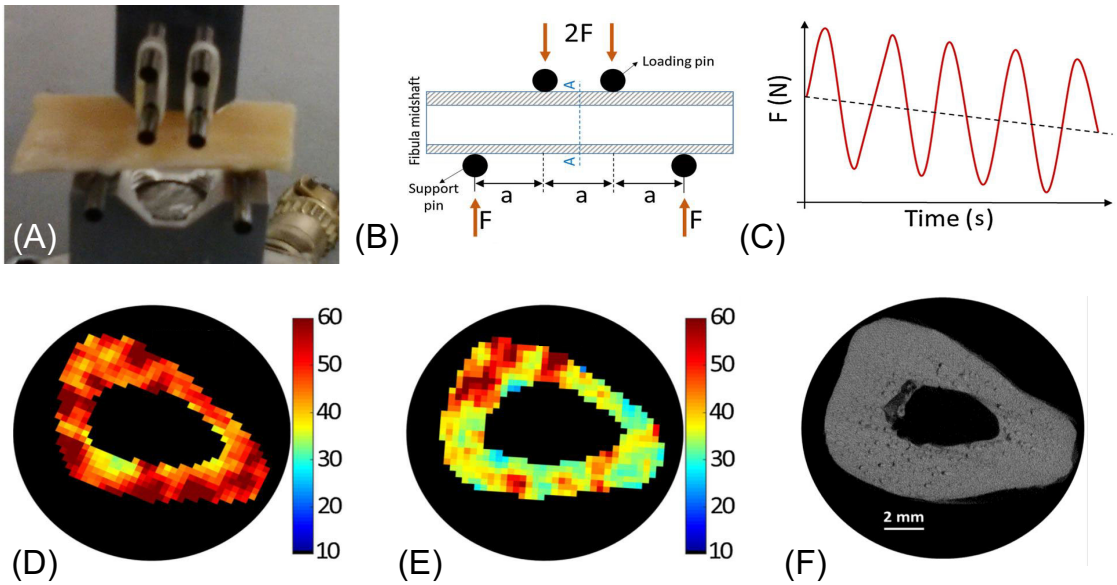

FIGURE 13
A representative 4-point bending setup and force-time diagram **(A-C)**, as well as MMF maps before **(D)** and after **(E)** loading with marked changes but little change in μCT image and porosity map **(F)**. From Ref. (73) with permission.

UTE-MT measures to assess bone mechanical properties

UTE-MT can indirectly assess collagen backbone protons, providing information about cortical porosity and mechanical properties (73, 81–83). A recent study reported a moderate to strong negative correlation between UTE magnetization transfer ratio (MTR) and μCT porosity (R^2 = 0.46–0.51), while a moderate positive correlation was observed between MTR and yield stress (R^2 = 0.25–0.30) and failure stress (R^2 = 0.31–0.35).A weak positive correlation (R^2 = 0.09–0.12) between MTR and Young's modulus at all off-resonance saturation frequencies was also observed (115). UTE-MT measured MTR provides quantitative information on cortical bone and is sensitive to μCT porosity and biomechanical function. MMF derived from UTE-MT imaging can assess mechanical failures after bone stress injury, which is difficult to evaluate using other techniques (83). In another study (73), fibular samples (n=14) were subject to cyclic loading using a 4-point bending setup (Figure 13). Loading was applied to reduce bone stiffness by 20%. Then, bone samples were imaged with UTE MRI and μCT before and after loading. MMF from two-pool UTE-MT modeling decreased by 12% on average, while μCT porosity measured at 6 μm voxel size showed no significant change. A representative sample is shown in Figure 13, with averaged MMF decreasing from 63% to 55% (p=0.0001), but no detectable changes in μCT porosity (73).

UTE biomarkers for comprehensive assessment of bone and fracture risk

In recent years, many studies have shown that UTE MRI can provide markers of cortical bone porosity, morphologic structure, mineralization, and osteoid density, which are useful measures of bone health (20–23, 76, 84–91, 116–120). In a recent study, Jones et al. reported UTE MRI of 15 participants with OP and 19 without OP (117). The OP group showed elevated pore water (11.6 mol/L vs. 9.5 mol/L; P = 0.007) and total water densities (21.2 mol/L vs. 19.7 mol/L; P = 0.03), and lower cortical bone thickness (4.8 mm vs. 5.6 mm; P < 0.001) and ^{31}P density (6.4 mol/L vs. 7.5 mol/L; P = 0.01) than the non-OP group, respectively. Meanwhile, there was no evidence of a difference in bone water (BW) or ^{31}P-to-BW concentration ratio. Furthermore, pore and total water densities were inversely associated with DXA and HR-pQCT measured BMD (P < 0.001) (117). In another study, Jerban et al. investigated the differences in water and collagen contents in tibial cortical bone between female osteopenia (OPe) patients, osteoporosis (OPo) patients, and young participants (Young) using a clinical 3T scanner (91). They found MMF, BWPD, and MMPD were significantly lower in OPo patients than in the young group, whereas T1, TWPD, and PWPD were significantly higher in OPo patients. The largest OPo/Young average percentage differences were found in MMF (41.9%), PWPD (103.5%), and MMPD (64.0%), with PWPD significantly higher (50.7%), while BWPD significantly lower (16.4%) in OPe than the Young group on average. Meanwhile, MMF was significantly lower (27%) in OPo patients compared with OPe group (91). As a result, UTE-MRI measured TWPD, PWPD, and MMF were recommended to evaluate individuals with OPe and OPo. Manhard et al. also demonstrated the feasibility of quantitatively mapping bound and pore water *in vivo* in human cortical bone with practical human MR imaging constraints (84). Jacobson et al. reported a comprehensive set of UTE MRI biomarkers to assess cortical bone. They found the

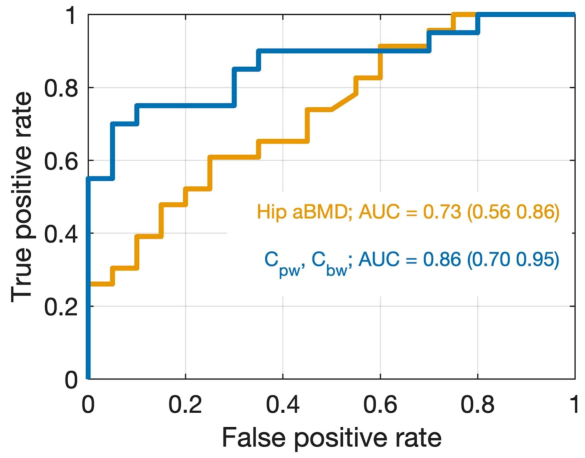

FIGURE 14
Receiver operating characteristic (ROC) curves for discriminating between non-fracture and distal radius fracture cases using two logistic regression models. The model in orange uses only hip BMD as a predictor which was the best model found without the inclusion of UTE MRI data. The model in blue uses both C_{pw} and C_{bw} as predictors, which was the best overall model. Although the 95% CIs of the AUCs overlap, the data are trending toward the conclusion that the UTE MRI better discriminates Fx from Non-Fx patients than does DXA in the present study. From Ref. (121) with permission.

UTE MRI-derived porosity index and signal-intensity-based estimated BMD correlated with the HR-pQCT variables (porosity: $r = 0.73$, $p = 0.006$; BMD: $r = 0.79$, $p = 0.002$) (120).

UTE MRI has also been used to assess fracture risk. In a recent study, Nyman et al. quantified bound water concentration (C_{bw}) and pore water concentration (C_{pw}) in the radius and tibia as predictors of bone fragility (121). Maps of C_{bw} and C_{pw} were acquired from the uninjured distal third radius of 20 patients who experienced a fragility fracture of the distal radius (Fx) and 20 healthy controls (Non-Fx), and from the tibia mid-diaphysis of 30 women with clinical OP (low T-scores) and 15 women without OP (normal T-scores). They found C_{bw} was significantly lower ($p = 0.0018$) and C_{pw} was higher ($p = 0.0022$) in the Fx group than in the Non-Fx group. The area-under-the-receiver operator characteristics curve (AUC with 95% confidence intervals) was 0.73 (0.56, 0.86) for hip BMD (best predictors without MRI) and 0.86 (0.70, 0.95) for the combination of C_{bw} and C_{pw} (best predictors overall), as shown in Figure 14. Meanwhile, C_{bw} was significantly lower ($p = 0.0005$) in women with OP (23.8 ± 4.3 ^{1}H mol/L) than in women without OP (29.9 ± 6.4 ^{1}H mol/L). They also found that it was C_{bw}, not C_{pw}, which was sensitive to bone-forming osteoporosis medications over 12 months. Their results are largely consistent with the study by Gallant et al. (122), who found the hydroxyl groups on raloxifene provided a possible explanation for the therapeutic effect of raloxifene, a Food and Drug Administration (FDA)-approved agent that is designed to treat bone loss, decrease fracture risk, and improve bone mechanical properties. The benefits of raloxifene treatment are essentially independent of bone mass changes and are mediated by an increase in matrix-bound water as measured by UTE MRI. The study suggests a cell-independent mechanism that can be utilized for novel pharmacological approaches to enhancing bone strength (122).

Contrast-enhanced UTE to monitor fracture repair

Bone is highly vascularized. Perfusion plays an important role in the growth and development of bone as well as in disease and healing (99–102). Reduced perfusion is observed in the trabecular bone of patients with OP (98). It is believed that decreased osseous vascularity contributes to increased fracture risk (123). Reduced perfusion occurs in synchrony with reduced BMD in vertebral trabecular bone (124). UTE can be used to evaluate bone perfusion (104, 105). There is an extensive enhancement in blood vessels due to fracture of the tibial plateau two days after injury, with specific enhancement of the periosteum distinguished from that of blood vessels, as shown in Figure 15 (104). Even without contrast enhancement, UTE can detect callus formation from a 22-year-old male with a fractured tibia examined 3 weeks after injury (125).

Discussion

UTE-MRI techniques offer significant advancements in assessing cortical and trabecular bone properties, providing valuable insights beyond traditional imaging methods, such as DXA, CT, HR-pQCT, ultrasound, and conventional MRI (24–26). High signal and contrast can be created for cortical and trabecular bone through a series of contrast mechanisms outlined in this review article. Techniques like ZTE MRI offer a radiation-free alternative for generating CT-like bone contrast. A series of quantitative UTE MRI techniques are also introduced. The ability to quantify total, bound, and pore water content has shown strong correlations with bone microstructure, mechanical properties, and age-related changes, making them promising biomarkers for evaluating fracture risk and osteoporosis. More advanced techniques, such as UTE-QSM and UTE-MT (72, 73, 77–83, 92–98, 126–128), enable us to evaluate bone mineral content and organic matrix density. Dynamic UTE imaging provides information about bone perfusion and modeling and can be used to monitor fracture healing (104, 105).

The UTE MRI techniques may provide new opportunities in assessing bone properties and fracture risk in not only osteoporosis but also other metabolic diseases such as osteopenia, osteomalacia, Paget's disease, hypophosphatasia, chronic kidney disease–mineral and bone disorder, diabetes, etc. For example, type 2 diabetes (T2D) is characterized by normal or high BMD but impaired bone strength (129–131). Animal and specimen studies indicate that brittle behavior in T2D bone is primarily due to a substantial reduction in collagen capacity for deformation (132–138). High glucose levels lead to the creation of advanced glycation end-products (AGEs), which cause non-enzymatic crosslinking, thereby increasing brittleness of the otherwise elastic collagen fibers and reducing bone toughness (132–138). Quantitative magnetization transfer MRI has been extensively studied to probe extracellular matrix (ECM) and measure the crosslinking of collagen and other polymers (139–141). UTE-MT modeling can

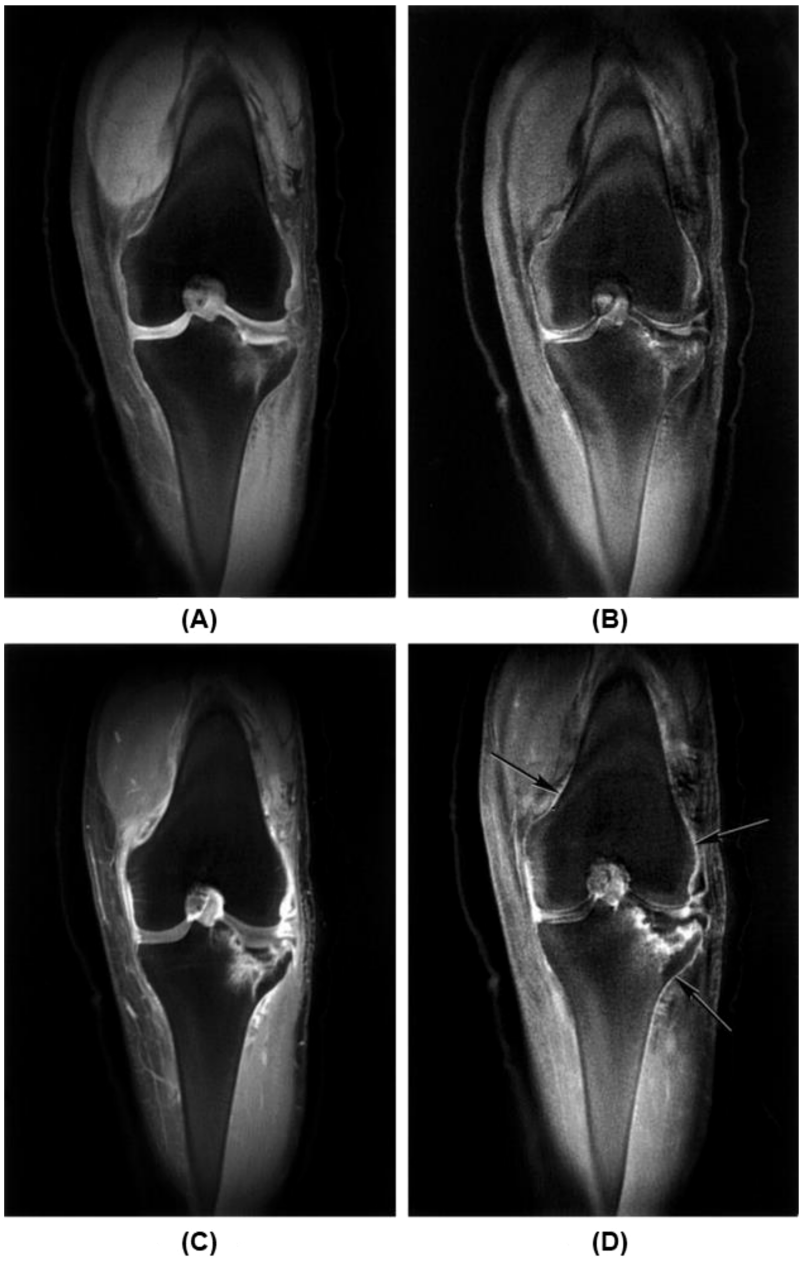

FIGURE 15
Fracture of tibial plateau 2 days after injury is seen with coronal fat-suppressed UTE (TR/TE=500/0.08 ms) **(A)** and echo subtraction (TE=0.08 minus TE=17.7 ms) **(B)** images before enhancement and the corresponding images **(C, D)** after enhancement, with extensive enhancement in blood vessels in **(C)** and specific enhancement of the periosteum in **(D)**. From Ref. (104) with permission.

measure collagen backbone proton fraction and exchange rates between water and collagen protons (73, 78–83). The exchange rates can be used to assess collagen crosslinking and potentially explain the impaired bone strength in T2D (137, 142).

This review has several limitations. First, the review summarized solid-state 1H UTE techniques. 31P UTE MRI techniques and their applications were only briefly mentioned without systematic discussion. Second, the review only discussed applications in OP. The UTE MRI techniques can also be applied to other metabolic bone diseases.

Conclusion

With a decade of technical development, the advanced UTE-type MRI sequences allow direct imaging of bone with high signal and contrast. Quantitative UTE MRI techniques can assess all the major components of bone, including water, collagen, and mineral. Advanced UTE techniques can map different bone water components (total water, bound water, and pore water) and evaluate bone perfusion. UTE sequences can also assess bone microstructure, including cortical porosity and trabecular structure.

UTE MRI can map phosphorus content, assess bone mineral density, and differentiate between mature and newly remodeled bone. In summary, UTE MRI provides a comprehensive package to assess all bone components (mineral, collagen, water) and microstructure (cortical porosity, trabecular microstructure) using a single modality for improved detection of bone deficits, with potential advantages over conventional X-ray based techniques which can only assess bone mineral. Further research is needed to establish the clinical significance of these UTE-type MRI techniques.

Author contributions

SS: Conceptualization, Data curation, Formal analysis, Investigation, Methodology, Software, Validation, Visualization, Writing – original draft, Writing – review & editing. H-DC: Conceptualization, Data curation, Formal analysis, Investigation, Methodology, Software, Validation, Visualization, Writing – original draft, Writing – review & editing. AS: Investigation, Methodology, Validation, Writing – original draft, Writing – review & editing. SJ: Investigation, Methodology, Software, Validation, Visualization, Writing – original draft, Writing – review & editing, Conceptualization, Data curation, Formal analysis. EC: Conceptualization, Data curation, Formal analysis, Investigation, Methodology, Software, Validation, Visualization, Writing – original draft, Writing – review & editing. LS: Validation, Writing – original draft, Writing – review & editing. RS: Validation, Writing – original draft, Writing – review & editing. JP: Validation, Writing – original draft, Writing – review & editing. GW: Validation, Writing – original draft, Writing – review & editing. JD: Conceptualization, Data curation, Formal analysis, Funding acquisition, Investigation, Methodology, Project administration, Resources, Software, Supervision, Validation, Visualization, Writing – original draft, Writing – review & editing.

Funding

The author(s) declare financial support was received for the research, authorship, and/or publication of this article. The authors acknowledge grant support from the National Institutes of Health (NIH) (1R01 AR062581, 1R01 AR068987, R01AR075825, R01AR079484, and K01AR080257), the VA Clinical Science Research & Development Service (I01BX005952), and GE Healthcare. The authors declare that this study received funding from GE Healthcare. The funder was not involved in the study design, collection, analysis, interpretation of data, the writing of this article or the decision to submit it for publication.

Conflict of interest

The authors declare that the research was conducted in the absence of any commercial or financial relationships that could be construed as a potential conflict of interest.

Generative AI statement

The author(s) declare that no Generative AI was used in the creation of this manuscript.

Publisher's note

References

1. LeBoff MS, Greenspan SL, Insogna KL, Lewiecki EM, Saag KG, Singer AJ, et al. The clinician's guide to prevention and treatment of osteoporosis. *Osteoporos Int.* (2022) 33:2049–102. doi: 10.1007/s00198-021-05900-y

2. Williams SA, Daigle SG, Weiss R, Wang Y, Arora T, Curtis JR. Economic burden of osteoporosis-related fractures in the US medicare population. *Ann Pharmacother.* (2021) 55:821–9. doi: 10.1177/1060028020970518

3. Genant HK, Cooper C, Poor G, Reid I, Ehrlich G, Kanis J, et al. Interim report and recommendations of the World Health Organization task-force for osteoporosis. *Osteoporos Int.* (1999) 10:295–64. doi: 10.1007/s001980050224

4. American Society for Bone and Mineral Research ASBMR Bone Curriculum (2004). Available online at: http://depts.washington.edu/bonebio/ASBMRed/ASBMRed.html (Accessed August 04, 2024).

5. Wehrli FW, Song HK, Saha PK, Wright AC. Quantitative MRI for the assessment of bone structure and function. *NMR BioMed.* (2006) 19:731–64. doi: 10.1002/nbm.v19:7

6. Turner CH. Bone strength: current concepts. *Ann NY Acad Sci.* (2006) 1068:429–46. doi: 10.1196/annals.1346.039

7. Viquet-Carrin S, Garnero P, Delmas PD. The role of collagen in bone strength. *Osteoporosis Int.* (2006) 17:319–36. doi: 10.1007/s00198-005-2035-9

8. Cowin SC. Bone poroelasticity. *J Biomechanics.* (1999) 32:217–38. doi: 10.1016/S0021-9290(98)00161-4

9. Ritchie RO, Buehler MJ, Hansma P. Plasticity and toughness in bone. *Phys Today.* (2009) 62:41–7. doi: 10.1063/1.3156332

10. Seeman E, Delmas PD. Bone quality – the material and structural basis of bone strength and fragility. *N Engl J Med.* (2006) 354:2250–61. doi: 10.1056/NEJMra053077

11. Schreiber JJ, Anderson PA, Hsu WK. Use of computed tomography for assessing bone mineral density. *Neurosurg Focus.* (2014) 37:E4. doi: 10.3171/2014.5.FOCUS1483

12. Nishiyama KK, Macdonald HM, Buie HR, Hanley DA, Boyd SK. Postmenopausal women with osteopenia have higher cortical porosity and thinner cortices at the distal radius and tibia than women with normal aBMD. *J Bone Miner Res.* (2010) 25:882–90. doi: 10.1359/jbmr.091020

13. Burghardt AJ, Kazakia GJ, Ramachandran S, Link TM, Majumdar S. Age and gender related differences in the geometric properties and biomechanical significance of intra-cortical porosity in the distal radius and tibia. *J Bone Miner Res.* (2010) 25:983–93. doi: 10.1359/jbmr.091104

14. Cooper D, Turinsky A, Sensen C, Hallgrimsson B. Effect of voxel size on 3D micro-CT analysis of cortical bone porosity. *Calcif Tissue Int.* (2007) 80:211–9. doi: 10.1007/s00223-005-0274-6

15. Du J, Bydder GM. Qualitative and quantitative ultrashort-TE MRI of cortical bone. *NMR BioMed.* (2013) 26:489–506. doi: 10.1002/nbm.v26.5

16. Du J, Bydder GM. Introduction to MRI of Short- and Ultrashort-T_2 Tissues. In: Du J, Bydder GM, editors. *MRI of Short- and Ultrashort-T_2 Tissues: Making the Invisible Visible.* Switzerland: Springer (2024). p. 3–10.

17. Conolly S, Nishimura D, Macovski A, Glover G. Variable-rate selective excitation. *J Magn Reson.* (1988) 78:440–58. doi: 10.1016/0022-2364(88)90131-X

18. Robson MD, Gatehouse PD, Bydder M, Bydder GM. Magnetic resonance: an introduction to ultrashort TE (UTE) imaging. *J Comput Assist Tomogr*. (2003) 27:825–46. doi: 10.1097/00004728-200311000-00001

19. Rahmer J, Bornert P, Groen J, Bos C. Three-dimensional radial ultrashort echo-time imaging with T2 adapted sampling. *Magn Reson Med*. (2006) 55:1075–82. doi: 10.1002/mrm.20868

20. Techawiboonwong A, Song HK, Leonard MB, Wehrli FW. Cortical bone water: *in vivo* quantification with ultrashort echo-time MR imaging. *Radiology*. (2008) 248:824–33. doi: 10.1148/radiol.2482071995

21. Du J, Carl M, Bydder M, Takahashi A, Chung CB, Bydder GM. Qualitative and quantitative ultrashort echo time (UTE) imaging of cortical bone. *J Magn Reson*. (2010) 207:304–11. doi: 10.1016/j.jmr.2010.09.013

22. Horch RA, Nyman JS, Gochberg DF, Dortch RD, Does MD. Characterization of 1H NMR signal in human cortical bone for magnetic resonance imaging. *Magn Reson Med*. (2010) 64:680–7. doi: 10.1002/mrm.22459

23. Manhard MK, Uppuganti S, Granke M, Gochberg DF, Nyman JS, Does MD. MRI-derived bound and pore water concentrations as predictors of fracture resistance. *Bone*. (2016) 87:1–10. doi: 10.1016/j.bone.2016.03.007

24. Ma Y, Jang H, Jerban S, Chang EY, Chung CB, Bydder GM, et al. Making the invisible visible-ultrashort echo time magnetic resonance imaging: Technical developments and applications. *Appl Phys Rev*. (2022) 9:041303. doi: 10.1063/5.0086459

25. Ma Y, Jerban S, Jang H, Chang D, Chang EY, Du J. Quantitative ultrashort echo time (UTE) magnetic resonance imaging of bone: an update. *Front Endocrinol (Lausanne)*. (2020) 11:567417. doi: 10.3389/fendo.2020.567417

26. Jerban S, Ma Y, Chang EY, Chung CB, Bydder GM, Du J. A UTE-Based Biomarker Panel in Osteoporosis. In: Du J, Bydder GM, editors. *MRI of Short- and Ultrashort-T_2 Tissues: Making the Invisible Visible*. Switzerland: Springer (2024). p. 427–39.

27. Carl M, Bydder GM, Du J. UTE imaging with simultaneous water and fat signal suppression using a time-efficient multi-spoke inversion recovery pulse sequence. *Magn Reson Med*. (2016) 76:577–82. doi: 10.1002/mrm.25823

28. Carl M, Jang H, Ma Y, Fung M, Du J. Chapter 4: Three-Dimensional Ultrashort Echo Time (3D UTE) Imaging. In: Du J, Bydder GM, editors. *MRI of Short- and Ultrashort-T_2 Tissues: Making the Invisible Visible*. Switzerland: Springer Nature (2024). p. 29–52.

29. Weiger M, Pruessmann KP, Hennel F. MRI with zero echo time: hard versus sweep pulse excitation. *Magn Reson Med*. (2011) 66:379–89. doi: 10.1002/mrm.22799

30. Seifert AC, Li C, Wilhelm MJ, Wehrli SL, Wehrli FW. Towards quantification of myelin by solid-state MRI of the lipid matrix protons. *Neuroimage*. (2017) 163:358–67. doi: 10.1016/j.neuroimage.2017.09.054

31. Jang H, Carl M, Ma Y, Searleman AC, Jerban S, Chang EY, et al. Inversion recovery zero echo time (IR-ZTE) imaging for direct myelin detection in human brain: a feasibility study. *Quant Imaging Med Surg*. (2020) 10:895–906. doi: 10.21037/qims.2020.04.13

32. Weiger M, Froidevaus R, Baadsvik EL, Brunner DO, Rosler MB, Pruessmann KP. Advances in MRI of the myelin bilayer. *NeuroImage*. (2020) 217:116888. doi: 10.1016/j.neuroimage.2020.116888

33. Weiger M, Pruessmann KP. Zero echo time (ZTE) MRI. In: Du J, Bydder GM, editors. *MRI of Short- and Ultrashort-T_2 Tissues: Making the Invisible Visible*. Switzerland: Springer (2024). p. 53–66.

34. Breighner RE, Endo Y, Konin GP, Gulotta LV, Koff MF, Potter HG. Technical developments: zero echo time imaging of the shoulder: enhanced osseous detail by using MR imaging. *Radiology*. (2018) 286:960–6. doi: 10.1148/radiol.2017170906

35. Breighner RE, Potter HG. CT-like Contrast for Bone Imaging with ZTE-MRI. In: Du J, Bydder GM, editors. *MRI of Short- and Ultrashort-T_2 Tissues: Making the Invisible Visible*. Switzerland: Springer (2024). p. 549–59.

36. Lu A, Gorny KR, Ho M-L. Zero TE MRI for craniofacial bone imaging. *AJNR Am J Neuroradiol*. (2019) 40:1562–6. doi: 10.3174/ajnr.A6175

37. Grodzki DM, Jakob PM, Heismann B. Ultrashort echo time imaging using pointwise encoding time reduction with radial acquisition (PETRA). *Magn Reson Med*. (2012) 67:510–8. doi: 10.1002/mrm.23017

38. Li C, Magland JF, Zhao X, Seifert AC, Wehrli FW. Selective *in vivo* bone imaging with long-T suppressed PETRA MRI. *Magn Reson Med*. (2017) 77:989–97. doi: 10.1002/mrm.26178

39. Grodzki DM. Pointwise encoding time reduction with radial acquisition (PETRA) MRI. In: Du J, Bydder GM, editors. *MRI of Short- and Ultrashort-T_2 Tissues: Making the Invisible Visible*. Switzerland: Springer (2024). p. 67–76.

40. Hager B, Juras V, Zaric O, Szomolanyi P, Trattnig S, Deligianni X. The variable echo time (vTE) sequence. In: Du J, Bydder GM, editors. *MRI of Short- and Ultrashort-T_2 Tissues: Making the Invisible Visible*. Switzerland: Springer (2024). p. 107–18.

41. Wu Y, Chesler DA, Glimcher ML, Garrido L, Wang J, Jiang HJ, et al. Multinuclear solid state three dimensional MRI of bone and synthetic calcium phosphates. *Proc Nat Acad Sci USA*. (1999) 96:1574–8. doi: 10.1073/pnas.96.4.1574

42. Idiyatullin D, Corum C, Park JY, Garwood M. Fast and quiet MRI using a swept radiofrequency. *J Magn Reson*. (2006) 181:342–9. doi: 10.1016/j.jmr.2006.05.014

43. Qian Y, Williams A, Chu CR, Boada FE. High-resolution ultrashort echo time (UTE) imaging on human knee with AWSOS sequence at 3.0 T. *J Magn Reson Imaging*. (2012) 35:204–10. doi: 10.1002/jmri.22639

44. Jang H, Shin SH, Carl M, Ma Y, Du J. Ramped hybrid encoding. In: Du J, Bydder GM, editors. *MRI of Short- and Ultrashort-T_2 Tissues: Making the Invisible Visible*. Switzerland: Springer (2024). p. 77–90.

45. Wiesinger F, Menini A, Solana AB. Looping star. *Magn Reson Med*. (2019) 81:57–68. doi: 10.1002/mrm.27440

46. Du J, Bydder M, Takahashi AM, Carl M, Chung CB, Bydder GM. Short T2 contrast with three-dimensional ultrashort echo time imaging. *Magn Reson Imaging*. (2011) 29:470–82. doi: 10.1016/j.mri.2010.11.003

47. Sussman MS, Pauly JM, Wright GA. Design of practical T2-selective RF excitation (TELEX) pulses. *Magn Reson Med*. (1998) 40:890–9. doi: 10.1002/mrm.1910400615

48. Larson PE, Gurney PT, Nayak K, Gold GE, Pauly JM, Nishimura DG. Designing long-T2 suppression pulses for ultrashort echo time imaging. *Magn Reson Med*. (2006) 56:94–103. doi: 10.1002/mrm.20926

49. Li C, Magland JF, Rad HS, Song HW, Wehrli FW. Comparison of optimized soft-tissue suppression schemes for ultra-short echo time (UTE) MRI. *Magn Reson Med*. (2012) 68:680–9. doi: 10.1002/mrm.23267

50. Du J, Takahashi A, Bydder M, Chung CB, Bydder GM. Ultrashort TE imaging with off-resonance saturation contrast (UTE-OSC). *Magn Reson Med*. (2009) 62:527–31. doi: 10.1002/mrm.22007

51. Larson PE, Conolly SM, Pauly JM, Nishimura DG. Using adiabatic inversion pulses for long-T2 suppression in ultrashort echo time (UTE) imaging. *Magn Reson Med*. (2007) 58:952–61. doi: 10.1002/mrm.21341

52. Du J, Takahashi A, Bae WC, Chung CB, Bydder GM. Dual inversion recovery, ultrashort echo time (DIR UTE) imaging: creating high contrast for short-T2 species. *Magn Reson Med*. (2010) 63:447–55. doi: 10.1002/mrm.22257

53. Bae W, Dwek JR, Znamirowski R, Statum S, Hermida JC, D'Lima DD, et al. Ultrashort echo time MR imaging of osteochondral junction of the knee at 3 T: Identification of anatomic structures contributing to signal intensity. *Radiology*. (2009) 254:837–45. doi: 10.1148/radiol.09081743

54. Du J, Carl M, Bae WC, Statum S, Chang EY, Bydder GM, et al. Dual inversion recovery ultrashort echo time (DIR-UTE) imaging and quantification of the zone of calcified cartilage (ZCC). *Osteoarthritis Cartilage*. (2013) 21:77–85. doi: 10.1016/j.joca.2012.09.009

55. Ma YJ, Zhu Y, Lu X, Carl M, Chang EY, Du J. Short T2 imaging using a 3D double adiabatic inversion recovery prepared ultrashort echo time cones (3D DIR-UTE-Cones) sequence. *Magn Reson Med*. (2018) 79:2555–63. doi: 10.1002/mrm.26908

56. Johnson EM, Vyas U, Ghanouni P, Pauly KB, Pauly JM. Improved cortical bone specificity in UTE MR Imaging. *Magn Reson Med*. (2017) 77:684–95. doi: 10.1002/mrm.26160

57. Lee H, Zhao X, Song HK, Zhang R, Bartlett SP, Wehrli FW. Rapid dual-RF, dual-echo, 3D ultrashort echo time craniofacial imaging: A feasibility study. *Magn Reson Med*. (2019) 81:3007–16. doi: 10.1002/mrm.27625

58. Ma Y, Jang H, Wei Z, Cai Z, Xue Y, Chang EY, et al. Myelin imaging in human brain using a short repetition time adiabatic inversion recovery prepared ultrashort echo time (STAIR-UTE) MRI sequence in multiple sclerosis. *Radiology*. (2020) 297:392–404. doi: 10.1148/radiol.2020200425

59. Ma Y, Jang H, Wei Z, Wu M, Chang EY, Corey-Bloom J, et al. Brain ultrashort T2 component imaging using a short TR adiabatic inversion recovery prepared dual-echo ultrashort TE sequence with complex echo subtraction (STAIR-dUTE-ES). *J Magn Reson*. (2021) 323:106898. doi: 10.1016/j.jmr.2020.106898

60. Ma Y, Chen Y, Li L, Cai Z, Zhao W, Jerban S, et al. Trabecular bone imaging using a 3D adiabatic inversion recovery prepared ultrashort echo time cones sequence at 3T. *Magn Reson Med*. (2020) 83:1640–51. doi: 10.1002/mrm.28027

61. Wurnig MC, Calcagni M, Kenkel D, Vich M, Weiger M, Andreisek G, et al. Characterization of trabecular bone density with ultra-short echo-time MRI at 1.5, 3.0, and 7.0 T - comparison with micro-computed tomography. *NMR BioMed*. (2014) 27:1159–66. doi: 10.1002/nbm.v27.10

62. Biswas R, Bae W, Diaz E, Masuda K, Chung CB, Bydder GM, et al. Ultrashort echo time (UTE) imaging with bi-component analysis: bound and free water evaluation of bovine cortical bone subject to sequential drying. *Bone*. (2012) 50:749–55. doi: 10.1016/j.bone.2011.11.029

63. Majumdar S. Magnetic resonance imaging of trabecular bone structure. *Top Magn Reson Imaging*. (2002) 13:323–34. doi: 10.1097/00002142-200210000-00004

64. Chang G, Deniz CM, Honig S, Rajapakse CS, Egol K, Regatte RR, et al. Feasibility of three-dimensional MRI of proximal femur microarchitecture at 3 tesla using 26 receive elements without and with parallel imaging. *J Magn Reson Imaging*. (2014) 40:229–38. doi: 10.1002/jmri.24345

65. Bydder M, Carl M, Bydder GM, Du J. MRI chemical shift artifact produced by center-out radial sampling of k-space: A potential pitfall in clinical diagnosis. *Quant Imaging Med Surg*. (2021) 11:3677–83. doi: 10.21037/qims-21-115

66. Jerban S, Moazamian D, Mohammadi HS, Ma Y, Jang H, Namiranian B, et al. More accurate trabecular bone imaging using UTE MRI at the resonance frequency of fat. *Bone*. (2024) 184:117096. doi: 10.1016/j.bone.2024.117096

67. Rautiainen J, Salo EN, Tiitu V, Finnila MAJ, Aho OM, Saarakkala S, et al. Assessment of human tibial cartilage-bone interface in osteoarthritis using SWIFT. In: *Proceedings of ISMRM 21st Annual Meeting*. Salt Lake City, Utah, USA: International Society of Magnetic Resonance in Medicine (ISMRM) (2013). P0434.

68. Wei Z, Ma Y, Jang H, Yang W, Du J. To measure T1 of short T2 species using an inversion recovery prepared three-dimensional ultrashort echo time (3D IR-UTE) method: a phantom study. *J Magn Reson*. (2020) 314:106725. doi: 10.1016/j.jmr.2020.106725

69. Ma YJ, Lu X, Carl M, Zhu Y, Szeverenyi NM, Bydder GM, et al. Accurate T1 mapping of short T2 tissues using a three-dimensional ultrashort echo time cones actual flip angle imaging-variable repetition time (3D UTE-Cones AFI-VTR) method. *Magn Reson Med*. (2018) 80:598–608. doi: 10.1002/mrm.27066

70. Ma YJ, Zhao W, Wan L, Guo T, Searleman A, Jang H, et al. Whole knee joint T1 values measured *in vivo* at 3T by combined 3D ultrashort echo time cones actual flip angle and variable flip angle methods. *Magn Reson Med*. (2019) 81:1634–44. doi: 10.1002/mrm.27510

71. Yarnykh VL. Actual flip-angle imaging in the pulsed steady state: a method for rapid three-dimensional mapping of the transmitted radiofrequency field. *Magn Reson Med*. (2007) 57:192–200. doi: 10.1002/mrm.21120

72. Nyman JS, Ni Q, Nicolella DP, Wang X. Measurements of mobile and bound water by nuclear magnetic resonance correlate with mechanical properties of bone. *Bone*. (2008) 42:193–9. doi: 10.1016/j.bone.2007.09.049

73. Jerban S, Ma YJ, Nazaran A, Dorthe EW, Cory E, Carl M, et al. Detecting stress injury (fatigue fracture) in fibular cortical bone using quantitative ultrashort echo time-magnetization transfer (UTE-MT): an *ex vivo* study. *NMR BioMed*. (2018) 31:e3994. doi: 10.1002/nbm.v31.11

74. Xue Y, Ma Y, Wu M, Jerban S, Wei Z, Chang EY, et al. Quantitative 3D ultrashort echo time magnetization transfer (3D UTE-MT) imaging for evaluation of knee cartilage degeneration *in vivo*. *J Magn Reson Imaging*. (2021) 54:1294–302. doi: 10.1002/jmri.27659

75. Zhang X, Ma Y, Wei Z, Wu M, Ashir A, Jerban S, et al. Macromolecular fraction (MMF) from 3D ultrashort echo time cones magnetization transfer (3D UTE-Cones-MT) imaging predicts meniscal degeneration and knee osteoarthritis. *Osteoarthr Cartil*. (2021) 29:1173–80. doi: 10.1016/j.joca.2021.04.004

76. Li C, Seifert AC, Rad HS, Bhagat YA, Rajapakse CS, Sun W, et al. Cortical bone water concentration: dependence of MR imaging measures on age and pore volume fraction. *Radiology*. (2014) 272:796–806. doi: 10.1148/radiol.14132585

77. Chen J, Grawn S, Shao H, D'Lima D, Bydder GM, Du J. Evaluation of bound and pore water in cortical bone using ultrashort echo time (UTE) magnetic resonance imaging. *NMR BioMed*. (2015) 28:1754–62. doi: 10.1002/nbm.3436

78. Hodgson RJ, Evans R, Wright P, Grainger AJ, O'connor PJ, Helliwell P, et al. Quantitative magnetization transfer ultrashort echo time imaging of the Achilles tendon. *Magn Reson Med*. (2011) 65:1372–6. doi: 10.1002/mrm.22715

79. Ma Y, Carl M, Chang EY, Du J. Quantitative magnetization transfer ultrashort echo time imaging using a time-efficient 3D multispoke cones sequence. *Magn Reson Med*. (2018) 79:692–700. doi: 10.1002/mrm.26716

80. Ma Y, Shao H, Chang EY, Du J. UTE magnetization transfer (UTE-MT) imaging and modeling: magic angle independent biomarkers of tissue properties. *NMR BioMed*. (2016) 29:1546–52. doi: 10.1002/nbm.v29.11

81. Ma Y, Tadros AS, Du J, Chang EY. Quantitative two-dimensional ultrashort echo time magnetization transfer (2D UTE-MT) imaging of cortical bone. *Magn Reson Med*. (2017) 79:1941–9. doi: 10.1002/mrm.26846

82. Zhu Y, Cheng X, Ma Y, Wong JH, Xie Y, Du J, et al. Rotator cuff tendon assessment using magic-angle insensitive 3D ultrashort echo time cones magnetization transfer (UTE-Cones-MT) imaging and modeling with histological correlation. *J Magn Reson Imaging*. (2018) 48:160–8. doi: 10.1002/jmri.25914

83. Jerban S, Ma Y, Wan L, Searleman AC, Jang H, Sah RL, et al. Collagen proton fraction from ultrashort echo time magnetization transfer (UTE-MT) MRI modeling correlates significantly with cortical bone porosity measured with micro-computed tomography (μCT). *NMR BioMed*. (2019) 32:e4045. doi: 10.1002/nbm.4045

84. Manhard MK, Horch RA, Gochberg DF, Nyman JS, Does MD. *In vivo* quantitative MR imaging of bound and pore water in cortical bone. *Radiology*. (2015) 277:221–30. doi: 10.1148/radiol.2015140336

85. Chen J, Grogan SP, Shao H, D'Lima D, Bydder GM, Wu Z, et al. Evaluation of bound and pore water in cortical bone using ultrashort-TE MRI. *NMR Biomed*. (2015) 28:1754–62. doi: 10.1002/nbm.3436

86. Jerban S, Ma Y, Jang H, Namiranian B, Le N, Shirazian H, et al. Water proton density in human cortical bone obtained from ultrashort echo time (UTE) MRI predicts bone microstructural properties. *Magn Reson Imaging*. (2020) 67:85–9. doi: 10.1016/j.mri.2020.01.004

87. Jerban S, Ma Y, Li L, Jang H, Wan L, Guo T, et al. Volumetric mapping of bound and pore water as well as collagen protons in cortical bone using 3D ultrashort echo time cones MR imaging techniques. *Bone*. (2019) 127:120–8. doi: 10.1016/j.bone.2019.05.038

88. Jerban S, Ma Y, Wong JH, Nazaran A, Searleman A, Wan L, et al. Ultrashort echo time magnetic resonance imaging (UTE-MRI) of cortical bone correlates well with histomorphometric assessment of bone microstructure. *Bone*. (2019) 123:8–17. doi: 10.1016/j.bone.2019.03.013

89. Rajapakse CS, Bashoor-Zadeh M, Li C, Sun W, Wright AC, Wehrli FW. Volumetric cortical bone porosity assessment with MR imaging: validation and clinical feasibility. *Radiology*. (2015) 276:526–35. doi: 10.1148/radiol.15141850

90. Jerban S, Ma Y, Dorthe EW, Kakos L, Le N, Alenezi S, et al. Assessing cortical bone mechanical properties using collagen proton fraction from ultrashort echo time magnetization transfer (UTE-MT) MRI modeling. *Bone Rep*. (2019) 11:100220. doi: 10.1016/j.bonr.2019.100220

91. Jerban S, Ma Y, Wei Z, Shen M, Ibrahim Z, Jang H, et al. Ultrashort echo time MRI detects significantly lower collagen but higher pore water in the tibial cortex of female patients with osteopenia and osteoporosis. *J Bone Miner Res*. (2024) 39:707–16. doi: 10.1093/jbmr/zjae053

92. Wang Y, Liu T. Quantitative susceptibility mapping (QSM): Decoding MRI data for a tissue magnetic biomarker. *Magn Reson Med*. (2015) 73:82–101. doi: 10.1002/mrm.25358

93. Dimov AV, Liu Z, Spincemaille P, Prince MR, Du J, Wang Y. Bone quantitative susceptibility mapping using a chemical species-specific R2* signal model with ultrashort and conventional echo data. *Magn Reson Med*. (2018) 79:121–8. doi: 10.1002/mrm.26648

94. Jang H, Lu X, Carl M, Searleman AC, Jerban S, Ma Y, et al. True phase quantitative susceptibility mapping using continuous single point imaging: a feasibility study. *Magn Reson Med*. (2019) 81:1907–14. doi: 10.1002/mrm.27515

95. Lu X, Ma Y, Chang EY, He Q, Searleman A, von Drygalski A, et al. Simultaneous quantitative susceptibility mapping (QSM) and R2* for high iron concentration quantification with 3D ultrashort echo time sequences: An echo dependence study. *Magn Reson Med*. (2018) 79:2315–22. doi: 10.1002/mrm.27062

96. Lu X, Jang H, Ma Y, Chang EY, Du J. Ultrashort echo time quantitative susceptibility mapping (UTE-QSM) of highly concentrated magnetic nanoparticles: a comparison study about different sampling strategies. *Molecules*. (2019) 24:1143. doi: 10.3390/molecules24061143

97. Jang H, von Drygalski A, Wong J, Zhou JY, Aguero P, Lu X, et al. Ultrashort echo time quantitative susceptibility mapping (UTE-QSM) for detection of hemosiderin deposition in hemophilic arthropathy: a feasibility study. *Magn Reson Med*. (2020) 84:3246–55. doi: 10.1002/mrm.28388

98. Jerban S, Lu X, Jang H, Ma Y, Namiranian B, Le N, et al. Significant correlations between human cortical bone mineral density and quantitative susceptibility mapping (QSM) obtained with 3D Cones ultrashort echo time magnetic resonance imaging (UTE-MRI). *Magn Reson Imaging*. (2019) 62:104–10. doi: 10.1016/j.mri.2019.06.016

99. McCarthy I. The physiology of bone blood flow: a review. *J Bone Joint Surg*. (2006) 88:4–9. doi: 10.2106/00004623-200611001-00002

100. Colleran PN, Wilkerson MK, Bloomfield SA, Sura LJ, Turner RT, Delp MD. Alternations in skeletal perfusion with simulated microgravity: a possible mechanicsm for bone remodeling. *J Appl Physiol*. (2000) 89:1046–54. doi: 10.1152/jappl.2000.89.3.1046

101. Otter MW, Qin YX, Rubin CT, McLeod KJ. Does bone perfusion/reperfusion initiate bone remodeling and the stress fracture syndrome? *Med Hypotheses*. (1999) 53:363–8. doi: 10.1054/mehy.1998.0782

102. Vogt MT, Cauley JA, Kuller LH, Nevitt MC. Bone mineral density and blood flow to the lower extremities: the study of osteoporotic fractures. *J Bone Miner Res*. (1997) 12:283–9. doi: 10.1359/jbmr.1997.12.2.283

103. Wang YX, Griffith JF, Kwok AWL, Leung JCS, Yeung DKW, Ahuja AT, et al. Reduced bone perfusion in proximal femur of subjects with decreased bone mineral density preferentially affects the femoral neck. *Bone*. (2009) 45:711–5. doi: 10.1016/j.bone.2009.06.016

104. Robson MD, Gatehouse PD, So PW, Bell JD, Bydder GM. Contrast enhancement of short T2 tissues using ultrashort TE (UTE) pulse sequences. *Clin Radiol*. (2004) 59:720–6. doi: 10.1016/j.crad.2003.09.025

105. Wan L, Wu M, Sheth V, Shao H, Jang H, Bydder GM, et al. Evaluation of cortical bone perfusion using dynamic contrast enhanced ultrashort echo time (UTE) imaging: a feasibility study. *Quant Imaging Med Surg*. (2019) 9:1383–93. doi: 10.21037/qims.2019.08.05

106. Cao H, Ackerman JL, Hrovat MI, Graham L, Glimcher MJ, Wu Y. Quantitative bone matrix density measurement by water- and fat-suppressed proton projection MRI (WASPI) with polymer calibration phantoms. *Magn Reson Med*. (2008) 60:1433–43. doi: 10.1002/mrm.21771

107. Idiyatullin D, Corum C, Moeller S, Prasad HS, Garwood M, Nixdorf DR. Dental magnetic resonance imaging: making the invisible visible. *J Endod*. (2011) 37:745–52. doi: 10.1016/j.joen.2011.02.022

108. Robson MD, Gatehouse PD, Bydder GM, Neubauer S. Human imaging of phosphorus in cortical and trabecular bone *in vivo*. *Magn Reson Med*. (2004) 51:888–92. doi: 10.1002/mrm.20055

109. Seifert AC, Wehrli FW. Solid-state quantitative 1H and 31P MRI of cortical bone in humans. *Curr Osteoporos Rep*. (2016) 14:77–86. doi: 10.1007/s11914-016-0307-2

110. Nyman JS, Does MD. Bound water and pore water in osteoporosis. In: Du J, Bydder GM, editors. *MRI of Short- and Ultrashort-T_2 Tissues: Making the Invisible Visible*. Switzerland: Springer (2024). p. 409–20.

111. Horch RA, Gochberg DF, Nyman JF, Does MD. Non-invasive predictors of human cortical bone mechanical properties: T(2)-discriminated H NMR compared with high resolution X-ray. *PloS One*. (2011) 6:e16359. doi: 10.1371/journal.pone.0016359

112. Bae WC, Chen PC, Chung CB, Masuda K, DLima D, Du J. Quantitative ultrashort echo time (UTE) MRI of human cortical bone: correlation with porosity and biomechanical properties. *J Bone Miner Res*. (2012) 27:848–57. doi: 10.1002/jbmr.1535

113. Granke M, Does MD, Nyman JS. The role of water compartments in the material properties of cortical bone. *Calcif Tissue Int*. (2015) 97:292–307. doi: 10.1007/s00223-015-9977-5

114. Currey JD, Brear K, Zioupos P. The effects of ageing and changes in mineral content in degrading the toughness of human femora. *J Biomech*. (1996) 29:257–60. doi: 10.1016/0021-9290(95)00048-8

115. Chang EY, Bae WC, Shao H, Biswas R, Li S, Chen J, et al. Ultrashort echo time magnetization transfer (UTE-MT) imaging of cortical bone. *NMR BioMed*. (2015) 28:873–80. doi: 10.1002/nbm.v28.7

116. Hong AL, Ispiryan M, Padalkar MV, Jones BC, Batzdorf AS, Shetye SS, et al. MRI-derived bone porosity index correlates to bone composition and mechanical stiffness. *Bone Rep*. (2019) 11:100213. doi: 10.1016/j.bonr.2019.100213

117. Jones BC, Lee H, Cheng CC, Mukaddam M, Song HK, Snyder PJ, et al. MRI quantification of cortical bone porosity, mineralization, and morphologic structure in postmenopausal osteoporosis. *Radiology*. (2023) 307:e221810. doi: 10.1148/radiol.221810

118. Jerban S, Ma Y, Wei Z, Jang H, Chang EY, Du J. Quantitative magnetic resonance imaging of cortical and trabecular bone. *Semin Musculoskelet Radiol*. (2020) 24:386–401. doi: 10.1055/s-0040-1710355

119. Abbasi-Rad S, Saligheh Rad H. Quantification of human cortical bone bound and free water *in vivo* with ultrashort echo time MR imaging: a model-based approach. *Radiology*. (2017) 83:862–72. doi: 10.1148/radiol.2016160780

120. Jacobson AM, Zhao X, Sommer S, Sadik F, Warden SJ, Newman C, et al. A comprehensive set of ultrashort echo time magnetic resonance imaging biomarkers to assess cortical bone health: a feasibility study at clinical field strength. *Bone*. (2024) 181:117031. doi: 10.1016/j.bone.2024.117031

121. Nyman JS, Ketsiri T, Louie EA, Harkins KD, Manhard MK, Gochberg DF, et al. Toward the use of MRI measurements of bound and pore water in fracture risk assessment. *Bone*. (2023) 176:116863. doi: 10.1016/j.bone.2023.116863

122. Gallant MA, Brown DM, Hammond M, Wallace JM, Du J, Deymier-Black AC, et al. Bone cell-independent benefits of raloxifene on the skeleton: a novel mechanism for improving bone material properties. *Bone*. (2014) 61:191–200. doi: 10.1016/j.bone.2014.01.009

123. Biffar A, Sourbron S, Dietrich O, Schmidt G, Ingrisch M, Reiser MF, et al. Combined diffusion-weighted and dynamic contrast-enhanced imaging of patients with acute osteoporotic vertebral fractures. *Eur J Radiol*. (2010) 76:298–303. doi: 10.1016/j.ejrad.2010.05.020

124. Zhu J, Zhang L, Wu X, Xiong Z, Qiu Y, Hua T, et al. Reduction of longitudinal vertebral blood perfusion and its likely causes: a quantitative dynamic contrast-enhanced MR imaging study of a rat osteoporosis model. *Radiology*. (2017) 282:369–80. doi: 10.1148/radiol.2016152006

125. Reichert ILH, Robson MD, Gatehouse PD, He T, Chappell KE, Holmes J, et al. Magnetic resonance imaging of cortical bone with ultrashort TE pulse sequences. *Magn Reson Imaging*. (2005) 23:611–8. doi: 10.1016/j.mri.2005.02.017

126. Diaz E, Chung CB, Bae WC, Statum S, Znamirowski R, Bydder GM, et al. Ultrashort echo time spectroscopic imaging (UTESI): an efficient method for quantifying bound and free water. *NMR BioMed*. (2012) 25:161–8. doi: 10.1002/nbm.v25.1

127. Du J, Diaz E, Carl M, Bae W, Chung C, Bydder GM. Ultrashort echo time imaging with bicomponent analysis. *Magn Reson Med*. (2012) 67:645–9. doi: 10.1002/mrm.23047

128. Jerban S, Lu X, Dorthe EW, Alenezi S, Ma Y, Kakos L, et al. Correlation of cortical bone microstructural and mechanical properties with water proton fractions obtained from ultrashort echo time (UTE) MRI tricomponent T2* model. *NMR BioMed*. (2020) 33:e4233. doi: 10.1002/nbm.v33.3

129. Schwartz A, Sellmeyer D, Ensrud K, Cauley JA, Tabor HK, Schreiner PJ, et al. Older women with diabetes have an increased risk of fracture: a prospective study. *J Clin Endocrinol Metab*. (2001) 86:32–8. doi: 10.1210/jcem.86.1.7139

130. Botella Martínez S, Varo Cenarruzabeitia N, Escalada San Martin J, Calleja Canelas A. The diabetic paradox: Bone mineral density and fracture in type 2 diabetes. *Endocrinol Nutr*. (2016) 63:495–501. doi: 10.1016/j.endoen.2016.10.010

131. Hofbauer LC, Busse B, Eastell R, Ferrari S, Frost M, Müller R, et al. Bone fragility in diabetes: novel concepts and clinical implications. *Lancet Diabetes Endocrinol*. (2022) 10:207–20. doi: 10.1016/S2213-8587(21)00347-8

132. Goldin A, Beckman JA, Schmidt AM, Creager MA. Advanced glycation end products: sparking the development of diabetic vascular injury. *Circulation*. (2006) 114:597–605. doi: 10.1161/CIRCULATIONAHA.106.621854

133. Poundarik AA, Wu PC, Evis Z, Sroga GE, Ural A, Rubin M, et al. A direct role of collagen glycation in bone fracture. *J Mech Behav BioMed Mater*. (2015) 52:120–30. doi: 10.1016/j.jmbbm.2015.08.012

134. Saito M, Mori S, Mashiba T, Komatsubara S, Marumo K. Collagen maturity, glycation induced-pentosidine, and mineralization are increased following 3-year treatment with incadronate in dogs. *Osteoporosis Int*. (2008) 19:1343–54. doi: 10.1007/s00198-008-0585-3

135. Ogawa N, Yamaguchi T, Yano S, Yamauchi M, Yamamoto M, Sugimoto T, et al. The combination of high glucose and advanced glycation end-products (AGEs) inhibits the mineralization of osteoblastic MC3T3-E1 cells through glucose-induced increase in the receptor for AGEs. *Hormone Metab Res*. (2007) 39:871–5. doi: 10.1055/s-2007-991157

136. Valcourt U, Merle B, Gineyts E, Viguet-Carrin S, Delmas PD, Garnero P, et al. Non-enzymatic glycation of bone collagen modifies osteoclastic activity and differentiation. *J Biol Chem*. (2007) 282:5691–703. doi: 10.1074/jbc.M610536200

137. Saito M, Fujii K, Mori Y, Marumo K. Role of collagen enzymatic and glycation induced cross-links as a determinant of bone quality in spontaneously diabetic WBN/Kob rats. *Osteoporos Int*. (2006) 17:1514–23. doi: 10.1007/s00198-006-0155-5

138. Campbell GM, Tiwari S, Picke A-K, Hofbauer C, Rauner M, Morlock MM, et al. Effects of insulin therapy on porosity, non-enzymatic glycation and mechanical competence in the bone of rats with type 2 diabetes mellitus. *Bone*. (2016) 91:186–93. doi: 10.1016/j.bone.2016.08.003

139. Fishbein KW, Gluzband YA, Kaku M, Ambia-Sobhan H, Shapses SA, Yamauchi M, et al. Effects of formalin fixation and collagen cross-linking on T2 and magnetization transfer in bovine nasal cartilage. *Magnetic Resonance Med*. (2007) 57:1000–11. doi: 10.1002/mrm.21216

140. Ho LC, Sigal IA, Jan N-J, Yang X, van der Merwe Y, Yu Y, et al. Non-invasive MRI assessments of tissue microstructures and macromolecules in the eye upon biomechanical or biochemical modulation. *Sci Rep*. (2016) 6:32080. doi: 10.1038/srep32080

141. Gochberg DF, Fong PM, Gore JC. Studies of magnetization transfer and relaxation in irradiated polymer gels - interpretation of MRI-based dosimetry. *Phys Med Biol*. (2001) 46:799. doi: 10.1088/0031-9155/46/3/314

142. Nishad Fathima M, Baias M, Blumich B, Blumich B, Ramasamim T. structure and dynamics of water in native and tanned collagen fibers: Effect of crosslinking. *Int J Biol Macromol*. (2010) 47:590–6. doi: 10.1016/j.ijbiomac.2010.08.003

frontiers | Frontiers in Endocrinology

TYPE Original Research
PUBLISHED 20 February 2025
DOI 10.3389/fendo.2025.1467825

OPEN ACCESS

EDITED BY
Julio Carballido-Gamio,
University of Colorado Anschutz Medical Campus, United States

REVIEWED BY
Po-hung Wu,
University of California, San Francisco, United States
Gabby Joseph,
University of California, San Francisco, United States

*CORRESPONDENCE
Ejigayehu G. Abate
Abate.ejigayehu@mayo.edu

RECEIVED 21 July 2024
ACCEPTED 02 January 2025
PUBLISHED 20 February 2025

CITATION
Abate EG, McKenna A, Yang L, Ball CT and Kearns AE (2025) Five-year evaluation of bone health in liver transplant patients: developing a risk score for predicting bone fragility progression beyond the first year.
Front. Endocrinol. 16:1467825.
doi: 10.3389/fendo.2025.1467825

Five-year evaluation of bone health in liver transplant patients: developing a risk score for predicting bone fragility progression beyond the first year

Ejigayehu G. Abate[1*], Amanda McKenna[1], Liu Yang[2], Colleen T. Ball[3] and Ann E. Kearns[4]

[1]Division of Endocrinology, Mayo Clinic, Jacksonville, FL, United States, [2]Department of Transplantation, Mayo Clinic, Jacksonville, FL, United States, [3]Division of Clinical Trials and Biostatistics, Mayo Clinic, Jacksonville, FL, United States, [4]Division of Endocrinology, Diabetes, Metabolism and Nutrition, Department of Medicine, Mayo Clinic, Rochester, MN, United States

Introduction: Liver transplant (LT) recipients have a substantial risk of bone loss and fracture. An individual's risk is highest before and within the first year after transplantation and returns to baseline in some patients but not all. We aim to identify risk factors for bone loss and fracture beyond the first year LT and to create a risk-scoring tool to aid clinicians in identifying those at high risk for bone loss and fracture.

Methods: We conducted a retrospective review of 264 liver transplant recipients between 2011 and 2014, who were followed in our transplant clinic for an additional five years. Clinical records were evaluated at the one-year post-LT visit and subsequently on an annual basis for up to five years.

Results: Over a median follow-up of 3.6 years post-liver transplantation, 40 out of 264 patients experienced disease progression, defined as worsening bone mineral density (BMD), initiation of osteoporosis treatment, or a new fracture. Factors associated with BMD progression included female sex, Caucasian race, new fractures, number of acute rejection events requiring treatment, and lower dual energy X-ray absorptiometry (DXA) scores after the first year post-LT. A risk model was developed using multivariable analysis, with a risk score based on BMD categories. The concordance index was 0.771, indicating good discrimination between those who progressed and those who did not. Risk categories were defined as low (0-4 points), medium (5 points), and high (6-9 points) based on model coefficients. The probability of progression-free survival at two years post-LT was 96.7% for low-risk, 83.1% for medium-risk, and 59.1% for high-risk groups.

Conclusion: We developed a simple, clinically applicable risk score that predicts bone disease progression beyond the first year after LT. This tool may help guide appropriate bone health follow-up, although prospective validation is necessary.

KEYWORDS

liver transplant, transplant related bone disease, osteoporosis, bone risk factors, fractures, post liver transplant related bone loss, glucocorticoid induced osteoporosis

Introduction

Liver transplantation has been an accepted treatment for end-stage liver disease for over 40 years. Advancements in pre-transplant liver disease management, operative techniques, and reduction in dose and duration of glucocorticoid therapy in most patients after LT have improved longevity. With this improvement in survival, there is a need to understand and manage the longer term consequences of LT to enhance quality of life. Over the past two decades, 40-60% of liver transplant recipients have experienced transplant-related bone disorders, a prevalence that has remained unchanged despite advances in transplant care (1–4).

Significant bone loss and fracture, occurring in 13-56% f cases, are predominantly observed in the period before liver transplantation (pre-LT) and within the first-year post-transplant post-LT, with prevalence rates of 13-56% and 14-60% respectively (3–5). The cause is multifactorial, including excess alcohol use, malnutrition, sarcopenia, cholestatic liver disease, hyperbilirubinemia, hyponatremia, vitamin D deficiency, and hypogonadism which tend to improve after transplantation. Additional variables affecting post-LT bone loss include exposure to high-dose glucocorticoid (GC) within the first few months of transplant for immunosuppression, and reduced mobility due to the impact of GC on muscle and bone, to mention a few (6–8). For this reason, Liver Society practice guidelines, American association for study of Liver diseases and American Society for transplantation, and the European clinical practice guidelines include bone densitometry in all patients undergoing LT evaluation (9, 10).

The long-term impact of liver transplantation on bone health remains inadequately understood. While some studies suggest that bone density may stabilize or improve after the first-year post-transplant in most individuals, this recovery is inconsistent (8–10). A subset of patients continues to experience persistent bone loss and an increased risk of fractures. Bone loss progression is commonly assessed through dual-energy X-ray absorptiometry (DXA), while fracture risk is evaluated using radiographic imaging and clinical diagnosis. However, the mechanisms driving these varied outcomes are unclear and require further investigation to enhance our understanding and management of bone health in LT patients beyond the first year post-LT.

Bone histomorphometry, a technique for assessing bone micro-architecture, demonstrates uncoupling of bone remodeling both before and shortly after liver transplantation, marked by decreased bone formation and increased bone resorption (11, 12). Additional studies suggest that bisphosphonates, which reduce bone resorption, can mitigate early post-transplant bone loss. However, while short-term benefits are evident, long-term data remain limited (13, 14). Although bone remodeling often normalizes within four months, some patients continue to face elevated fracture risk, and no clear guidelines exist for monitoring beyond the first year. Furthermore, current fracture assessment tools, including DXA, have limitations in this population (2–4). Our study aims to identify clinical characteristics and BMD values at one-year post-LT that predict progression of bone disease in five years. Based on our findings, we developed a scoring system to identify patients requiring closer monitoring through clinical screening and bone density assessments.

Abbreviations: LT, Liver transplant; BMD, Bone mineral density; DXA, dual-energy X-ray absorptiometry; MELD, Model for End-Stage Liver Disease.

Materials and methods

Study design and participants

The study was approved by the institution review board. The cohort included all adult LT recipients from January 2011 through June 2014 who had bone mineral density performed at 1 year post transplant visit. Exclusion criteria were a prior transplant, multiorgan transplant, lack of BMD test results within 1-year post-LT, death within 1 year post transplant, or receiving medication for osteoporosis (Figure 1).

Data on biochemistry, the model of end stage liver disease (MELD), bone mineral density (BMD) as measured by DXA result, demography, and clinical endpoints were extracted from participants' medical records. BMD measured by dual energy x-ray absorptiometry (DXA-GE) are routinely performed at lumbar spine, total hip and femoral neck. Our primary outcome was progression of skeletal fragility after the first-year post LT, defined as transitioning to the subsequent worse BMD diagnosis (osteopenia or osteoporosis), receiving treatment for osteoporosis, or having a new fracture.

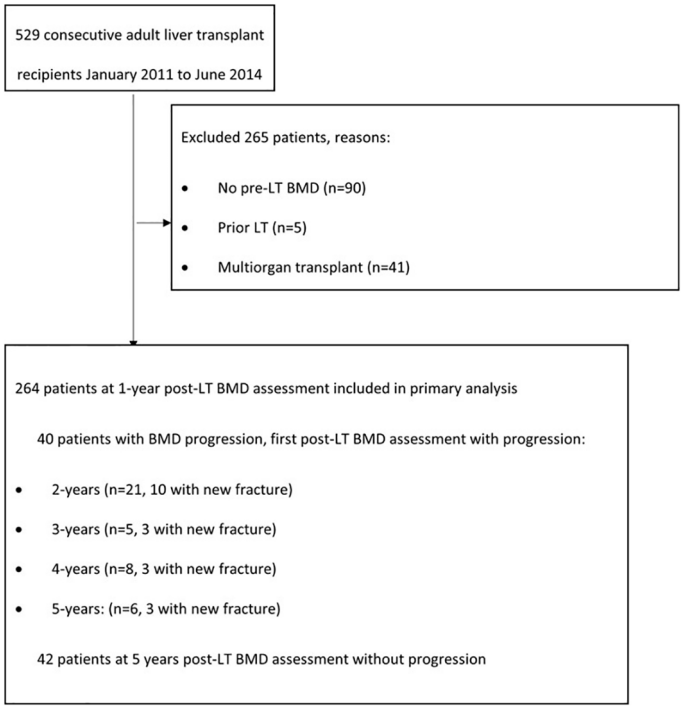

FIGURE 1
Patient flow diagram.

Data collection and BMD data

All patients had DXA scans performed at our facility, and serial comparisons were available. All patients had BMD of the lumbar spine, total hip, and femoral neck measured by DXA using a GE Lunar iDXA (General ElectricCross-calibration of the multiple scanners is routinely performed with a phantom; to provide accurate longitudinal assessment of BMD. BMD results were classified using the World Health Organization diagnostic criteria, defined as osteoporosis if T score is -2.5 or lower, osteopenia if T score is between -1 to -2.4, and normal if T score -1 or higher. Review of electronic medical record documentation including clinical notes and imaging was performed for subjects at one year post LT. Fractures were considered fragility related if occurred from a fall of standing height or from low energy injury reported confirmed in the clinical history. If the cause of the fracture was uncertain, the patient was reported not to have a fracture. We obtained the number of any rejections occurring within the first year of post-LT by review of transplant follow-up notes. Most patients did not have rejection. Bone loss progression was defined as having one or more of the following: Transitioned from normal BMD at 1-year post-LT to osteopenia or osteoporosis, transitioned from osteopenia at 1-year post-LT to osteoporosis, received treatment for osteoporosis after 1-year post-LT, or had a new fracture after 1-year post-LT. BMD classification was based on the lowest BMD T score available for the corresponding clinical visit (Table 1).

Immunosuppression

The immunosuppressive regimen protocol following LT is mycophenolate mofetil (CellCept) (for 2 months), prednisone (taper completed by 4 months), and tacrolimus indefinitely. If the patient has high-risk hepatocellular carcinoma, mycophenolate mofetil will be stopped as early as day 21 post LT, and the patient will remain only on tacrolimus. If the patient has renal insufficiency, mycophenolate is continued as maintenance therapy along with tacrolimus to reduce tacrolimus levels to avoid further decline in kidney function. Patients with moderate to severe acute cellular rejection receives intravenous (IV) methylprednisolone 1 gram every other day for a total of 3 doses. Patients then undergo repeat liver biopsy, and if the biopsy indicates persistent moderate rejection, treatment with another cycle of IV methylprednisolone is given. Patients receive thymoglobulin if organ rejection persists. Patients receive a higher dose of tacrolimus maintenance therapy for mild acute cellular rejection. The protocol of immunosuppression did not change during the study period.

Statistical analysis

Associations of patient characteristics with bone loss progression after the 1-year post LT visit were evaluated using Cox proportional hazards regression models, where hazard ratios (HRs) and 95% confidence intervals (CIs) were estimated. Patients

10.3389/fendo.2025.1467825

TABLE 1 Patient characteristics.

	N	n (%) or median (IQR)
Pre-transplant information		
Female sex	264	88 (33.3%)
Race		
Caucasian	264	222 (84.1%)
African American	264	23 (8.7%)
Other	264	14 (5.3%)
Not reported	264	5 (1.9%)
Body mass index (kg/m2)	264	27.8 (24.9, 32.1)
Primary liver disease	264	
Cirrhosis, Type C		88 (33.3%)
Alcoholic cirrhosis		42 (15.9%)
Cirrhosis, fatty liver (Nash)		33 (12.5%)
Cirrhosis, cryptogenic idiopathic		30 (11.4%)
Alcoholic cirrhosis with hepatitis C		17 (6.4%)
Cirrhosis, autoimmune		11 (4.2%)
Primary biliary cirrhosis		10 (3.8%)
Cirrhosis, other		4 (1.5%)
Primary sclerosing cholangitis		12 (4.5%)
Metabolic disease		8 (3.0%)
All other diagnoses		9 (3.4%)
MELD score	264	18 (11, 25)
History of prednisone use	261	15 (5.7%)
Information collected at 1st annual follow-up visit		
Age (years)	264	60 (54, 66)
Fractures	264	
No fractures		204 (77.3%)
Pre-transplant fracture, no new fracture in 1st year post-LT		21 (8.0%)
New fracture in 1st year post-LT with or without history of		39 (14.8%)
pre-transplant fracture		
Total prednisone dose in 1st year post-LT	264	1.10 (1.10, 1.10)
Number of rejections in 1st year post-LT	264	
0		217 (82.2%)
1		35 (13.3%)
2		10 (3.8%)
3		2 (0.8%)
Tacrolimus use in 1st year post-LT	254	232 (91.3%)
Mycophenolate in 1st year post-LT	253	33 (13.0%)
Sirolimus use in 1st year post-LT	264	8 (3.0%)
Lowest BMD T score at 1st annual follow-up	264	-1.60 (-2.20, -0.90)
Spine T score	256	-0.40 (-1.30, 0.40)
Femoral neck T score	263	-1.50 (-2.00, -0.75)
Total hip T score	263	-1.10 (-1.70, -0.30)

without bone loss progression were censored at the last available BMD assessment prior to any graft failure. To create a scoring algorithm that classifies patients based on their risk of bone loss progression after their first annual post-LT BMD assessment, a multivariable Cox proportional hazards regression model was developed using a backward selection approach, with a focus on reduction in the Akaike Information Criterion (AIC). The multivariable Cox proportional hazards regression model was developed by including variables with $p \leq 0.20$ from the univariable analysis. Variables were removed one at a time, based on the largest p-value, until no further reduction in the Akaike Information Criterion (AIC) was observed (Table 2). The BMD measurement at 1 year post-LT was selected over pre-LT BMD to identify predictors associated with the 1-year post-LT DXA assessment, independent of pre-transplant values, and the closer proximity of the BMD at 1 year Post-LT visit.

The risk score model was constructed using factors known at one-year post-LT, with points assigned based on variables with $p \leq 0.20$. The scoring system included the following: sex (+1 point if female), race (+2 points if not African American), fracture history (+2 points for new fractures post-transplant or +1 point for pre-transplant fractures), number of rejections (+2 points for ≥2 rejections or +1 point for 1 rejection), and lowest BMD T-score (+2 points if $T \leq -2.5$ or +1 point if $T > -2.4$ and < -1.0) (Table 3). The point values for the risk score were determined by rounding each model coefficient to the nearest integer (e.g., female sex had a coefficient of 0.828, rounded to 1; non-African American race had a coefficient of 1.870, rounded to 2). This simplification was done to create an easy-to-use risk scoring system (Supplementary Table 1).

The risk score was calculated by summing the points for the included variables, resulting in a plausible score range of 0-9. To evaluate the discriminatory ability of the risk score in predicting bone loss progression, we estimated the concordance index and corresponding 95% confidence intervals (CIs) using bootstrap methods (Table 2). Concordance index is a measure of the model's ability to discriminate between those who progressed and those who didn't with consideration of the time-to-event and censoring. The concordance index was 0.76 in our cohort. The risk score was categorized into three groups: low (0-4 points), medium (5 points), and high (6-9 points) risk of skeletal fragility progression.

We assessed the performance of the risk score by plotting Kaplan-Meier estimates of progression-free survival according to

10.3389/fendo.2025.1467825

TABLE 2 Associations with BMD progression after 1 year post-liver transplant visit.

	N	No. of events	Single variable analysis		Multivariable model	
			HR (95% CI)	P	HR (95% CI)	P
Pre-transplant information						
Sex						
Male	176	16	1.00 (reference)		1.00 (reference)	
Female	88	24	2.89 (1.54-5.45)	.001	2.29 (1.20-4.38)	0.012
Race						
African American	23	5	1.00 (reference)		1.00 (reference)	
White/Other/Unknown	241	35	6.37 (0.86-47.11)	.070	6.47 (0.85-49.11)	0.071
Body mass index (-5 kg/m2)			1.23 (0.90-1.70)	.20		
30 kg/m2 or higher	87	11	1.00 (reference)			
< 30 kg/m2	177	29	1.16 (0.58-2.34)			
Primary liver disease						
Cirrhosis, Type C (yes vs. no)	88	11	0.84 (0.42-1.69)	.62		
Alcoholic cirrhosis (yes vs. no)	42	8	1.47 (0.67-3.19)	.34		
Cirrhosis, fatty liver (Nash) (yes vs. no)	33	6	1.06 (0.44-2.53)	.90		
Cirrhosis, cryptogenic idiopathic (yes vs. no)	30	7	1.41 (0.62-3.21)	.41		
MELD score (+15)			1.50 (0.87-2.26)	.17		
18 or less	138	18	1.00 (reference)			
More than 18	126	22	1.22 (0.65-2.27)			
Information collected at 1 year post LT visit						
Age (+10 years)			1.26 (0.86-1.83)	.24		
60 years or younger	132	19	1.00 (reference)			
Older than 60 years	132	21	1.04 (0.56-1.94)			
Fractures						
No fractures	204	20	1.00 (reference)		1.00 (reference)	
Pre-transplant fracture, no new fracture in 1st year post-LT	21	5	2.04 (0.76-5.45	.16	2.03 (0.74-5.56)	.17
New fracture in 1st year post-LT with or without history of pre-transplant fracture	39	15	4.94 (2.52-9.68	<.001	4.48 (2.22-9.05)	<.001
Total prednisone dose in 1st year post-LT (+0.5)			1.06 (0.97-1.15)	.18		
1.1 or less	201	24	1.00 (reference)			
More than 1.1	63	16	2.45 (1.30-4.63)			
No. of rejections in 1st year post-LT (+1)			1.76 (1.12-2.76)	.014	1.74 (1.07-2.84)	0.026
0	217	28	1.00 (reference)			
1	35	8	2.25 (1.02-5.00)			
2 or more	12	4	2.71 (0.95-7.74)			
Tacrolimus use in 1st year post-LT (yes vs. no/unk)						
No/Unknown	32	7	1.00 (reference)			
Yes	232	33	0.55 (0.24-1.24)	.15		

(Continued)

TABLE 2 Continued

	N	No. of events	Single variable analysis		Multivariable model	
			HR (95% CI)	P	HR (95% CI)	P
Mycophenolate in 1st year post-LT						
No/Unknown	231	36	1.00 (reference)			
Yes	33	4	1.05 (0.37-2.97)	.92		
Sirolimus use in 1st year post-LT						
No/Unknown	256	37	1.00 (reference)			
Yes	8	3	2.52 (0.78-8.21)	.12		
Lowest BMD T score at 1-year post-LT follow-up (-1)	75	11	1.81 (1.24-2.64)	.002	1.69 (1.12-2.55)	0.012
-1.0 or higher		11	1.00 (reference)			
Between -2.5 to and -1.0	153	19	0.95 (0.45-1.99)			
-2.5 or lower	36	10	3.03 (1.28-7.17)			
Spine T score at 1-year post-LT follow-up (-1)			1.30 (1.00-1.69)	.046		
Femoral neck T score at 1-year post-LT follow-up (-1)			1.65 (1.13-2.41)	.010		
Total hip T score at 1-year post-LT follow-up (-1)			1.62 (1.16-2.27)	.004		

BMD, bone mineral density; HR, hazard ratio; CI, confidence interval; LT, liver transplant.
BMD progression was defined as having one or more of the following: transitioned to a worse diagnosis (osteopenia or osteoporosis) based on the lowest BMD T score, received treatment for osteoporosis, or had a new fracture. Patients were censored at the last available BMD assessment prior to graft failure. The multivariable Cox proportional hazards regression model included variables with P≤0.20 from single variable analysis removing one variable at a time based on the largest P value until there was no longer a reduction in the Akaike Information Criterion. Prior to starting the backward selection procedure, some variables were removed from the model due to high correlation. Prednisone dose was not included due to the correlation with the number of rejections (Spearman correlation = 0.74). The only BMD T-score included in the multivariable model prior to backward selection was the lowest T score at 1-year post-LT follow-up. The concordance index for the multivariable model was 0.771 (95% bootstrap CI 0.696-0.867) (15). For body mass index, MELD score, age at 1 year follow-up, total prednisone dose, number of rejections, and lowest bone mineral density T score, unadjusted HRs and 95% CIs were presented for categorized versions of the variables to ease interpretation, but the continuous versions of the variables were used for calculating P values and for consideration in the multivariable model.
The number in parathesis Indicate the unit increase (+) or decrease (-) in the predictor variable associated with the reported Hazard Ratio. For example, Age (+10 years) signifies that the HR corresponds to a 10-year increase in age.

risk score categories. Median follow-up time was calculated using the reverse Kaplan-Meier method, with patients who experienced progression censored at the time of progression (Figure 2, Table 4). All analyses were conducted using R version 4.0.3 (R Foundation for Statistical Computing, Vienna, Austria).

Results

Our cohort included 264 patients who underwent LT at our institution, with bone mineral density testing available at their 1-year post LT visit met the criteria for analysis. Table 1 describes the characteristics of the cohort including bone mineral density results extracted from their medical records. At one year post LT, the median age was 60 years (IQR 54 to 66 years), 88 (33.3%) were female, 47 (17.8%) had one or more rejections within the first year after LT. The cohort consisted of diverse liver disease as the cause for transplant. 39 (14.8%) had a fracture in the first year after LT, and median lowest BMD T score from the spine, femoral neck, or total hip was -1.60 (IQR -2.20 to -0.90). Fractures were predominantly in the spine (thoracic and vertebral spine).

After 1 year LT visit, 40/264 patients experienced bone loss progression over a median follow-up period of 3.6 years post-LT bone density (IQR 1.0 to 3.6 years), with 21 patients progressing by year 2 post LT visit (Figure 1). There were 42 patients who completed 5-year post LT follow-up visits without progression. The remaining 182 patients either had graft failure requiring a second liver transplant (N=24) or were lost to follow-up prior to the 5-year post LT visit. Among those who progressed, the majority were within 2 years of LT (n=21) and 10/21 had new fractures which was not evident in the pre or immediate post-transplant period (Figure 1). Eight out of the 10 patients had multiple fractures predominantly in the spine. Clinical characteristics of those who progress include female sex which were 2.89 times more likely to progress than male counterparts, Caucasians or those who identified as others were 6 times more likely to progress than African Americans, those with new fracture at 1 year post LT regardless of history of pre transplant fracture were 5 times more likely to progress than those who did not have reported fracture, patients with one or more episodes of organ rejection were over 2 times likely to progress than those who did not have rejection and low hip DXA scan were also likely to progress. Based on this significant data, we identified female sex, Caucasian race, history of fracture before transplant and within 12 months post LT, organ rejection of 2 or more episodes, and low BMD in osteoporosis range as a significant variable to play a role in progression of bone loss.

Due to the limited number of patients who developed bone loss progression and the strong correlations between some of the factors, the use of multivariable analysis to predict bone loss progression was

10.3389/fendo.2025.1467825

TABLE 3 Risk score development for predicting BMD progression after 1 year post liver transplant visit.

Variable in model	Model Coefficient	Points
Sex		
Male	Reference	0
Female	0.828	1
Race		
African American	Reference	0
White race, other race, or unknown race	1.870	2
Fractures		
No fractures	Reference	0
Pre-transplant fracture, no new fracture in 1st year post-LT	0.707	1
New fracture in 1st year post-LT with or without history of pre-transplant fracture	1.430	2
No. of rejections in 1st year post-LT, continuous	0.555	
No. of rejections, categories		
0		0
1		1
2 or more		2
Lowest BMD T score at 1-year post-LT follow-up, continuous	-0.524	
Lowest BMD T score at 1-year post-LT follow-up categories		
-1.0 or higher		0
Between -2.5 to and -1.0		1
-2.5 or lower		2

The number of points for the simplified score were determined by rounding the model coefficient up to the nearest integer. For the number of rejections, only 1 patient had more than 2 rejections so those with 2 or more rejections were combined into the same category. The lowest T-score was categorized based on common clinical diagnostic criteria. The risk score is calculated by summing the number of points with a plausible range of 0 to 9. The concordance index for the score created using the model coefficients and the simplified risk score was 0.771 and 0.761, respectively.

challenging. We considered any variable with a $P \leq 0.20$ from single variable analysis in our model, excluding prednisone dose due to its correlation with the number of rejections. The lowest BMD T score at 1-year post-LT was the only BMD measurement considered in the model. The remaining factors under consideration were included in a multivariable Cox proportional hazards regressions model. Using a backward elimination approach, one variable at a time was removed from the model based on the highest P value until there was no longer a reduction in the AIC. The final multivariable model included 5 factors, sex, race, fracture history, number of rejections within one-year post-LT, and the lowest BMD T score at 1-year post-LT (concordance index = 0.771, 95% CI 0.696-0.867).

To create the risk score, each model coefficient was rounded up to the nearest integer and these individual scores were summed to create a score that ranges from 0 to 9 (Table 3). After reviewing the observed proportion of patients who developed bone loss progression by the

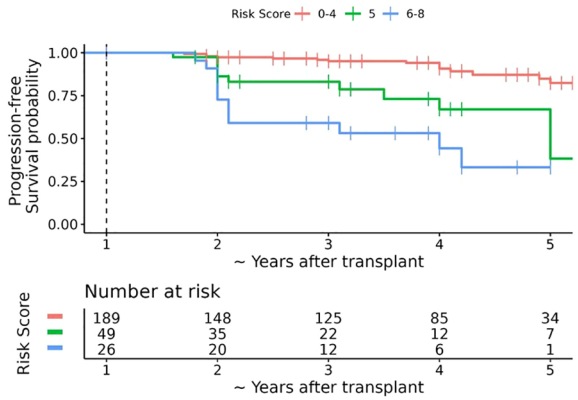

FIGURE 2
Kaplan-Meier estimates of progression-free survival after 1 year post-transplant bone mineral density (BMD) assessment according to simplified risk score. The dashed vertical line represents the date of the first annual BMD assessment (baseline timepoint). The horizontal axis represents the number of years after the first annual BMD assessment plus 1 year; for ease of interpretation the horizontal axis is labelled as the approximate number of years after transplant. Over a median follow-up of ~ 3.6 years post-transplant (interquartile range ~3 to ~ 5 years post-transplant), 40 patients experienced bone loss progression, 20 of which occurred within 18 months after 1 year post-LT BMD assessment. The overall probability of progression-free survival at ~2.5, ~3.5, and ~4.5 years post-transplant was 90.3% (95% CI 86.3% to 94.4%), 87.1% (95% CI 82.4% to 92.0%), and 78.1% (95% CI 60.0% to 79.6%), respectively.

2-year post LT visit according to the risk score (Supplementary Table 1), we combined the risk scores into 3 risk categories: low risk 0-4, medium risk 5, and high risk 6-9. The probability of progression-free survival by the 2-year post LT visit was 96.7% (93.8% to 99.6%), 83.1% (71.6% to 96.5%), and 59.1% (41.7% to 83.7%) for the low, medium, and high-risk categories, respectively (Table 4, Figure 2).

Discussion

Our findings shows that certain characteristics identified as risk factors for osteoporosis and fractures in the non-transplant population are also significant for bone health changes in post LT patients. Specifically, female gender, Caucasian race/ethnicity, and a history of previous fractures were identified as important risk

TABLE 4 Kaplan-meier estimates of the probability (%) of progression-free survival after the 1 year post liver transplant visit.

Years after 1 year post LT visit	Simplified Risk Score		
	0-4	5	6-8
1.5 (~2.5 years after transplant)	96.7 (93.8-99.6)	83.1 (71.6-96.5)	59.1 (41.7-83.7)
2.5 (~3.5 years after transplant)	95.1 (91.7-98.7)	73.1 (57.9-92.3)	53.2 (35.5-79.7)
3.5 (~4.5 years after transplant)	87.1 (80.3-94.6)	67.0 (50.2-89.5)	33.2 (15.2-72.7)

Progression was defined as having one or more of the following: transitioned to a worse diagnosis (osteopenia or osteoporosis) based on the lowest BMD T score, received treatment for osteoporosis, or had a new fracture.

factors (14, 16). Refinement in risk assessment for this population comes from our identification of liver transplant (LT)-related factors associated with skeletal health deterioration. Specifically, a higher number of rejection episodes and low bone density in the hip were significant factors.

Our study agrees with previous work that most fractures occur early, before transplant or within the first 1-2 years of transplant (13, 14). In contrast to prior studies, we did not observe any association between the type of liver disease (alcohol, Non-alcoholic liver disease, hepatitis c) and progression of bone disease (14, 17). However, we did not look at those with cholestatic liver disease separately due to our small number of patients in the cohort.

In contrast to prior studies, our study highlights the importance of recognizing the risk factors for bone loss and fracture after the first year of transplant unique to liver transplant recipients. More specifically, similar to the non-transplant population, females at any time were more likely to progress than their male counterparts. Women have lower bone mass at any point compared to men, so it was not surprising to discover that the most significant effect of liver disease on the bone was higher in women than men. Prior studies have questioned the validity of BMD in predicting bone disease in those receiving liver transplants (2). In this study, we found that BMD is essential in the risk stratification of patients at high risk for progression in conjunction with other clinical factors identified in this study. BMD at 1-year post LT was also helpful in predicting those who are likely to progress. We noted that patients with BMD at any site (spine, femoral neck, or total hip) in the osteoporosis range at 1-year post LT were three times more likely to progress compared to those with normal BMD (T score >-1) at any site. In addition, a one standard deviation (SD) decrease in the total hip BMD at 1-year post LT was strongly associated with BMD progress after the first annual post-LT follow-up. A change in BMD by one standard deviation change in the femoral neck and spine was also trending towards a positive prediction of progression, although not significant (Table 2).

Furthermore, ethnic variation in peak bone mass is likely to explain the race differences noted in our study rather than the mere impact of transplant alone. African Americans generally have been shown to have a higher bone mineral density at baseline than white Americans, and fracture rate also appears to be lower in AA at any skeletal sites compared to whites in nontransplant patients (16). We are not aware of any known differences in the mechanism of bone loss between AA and Caucasians other than the fact that AA may have higher bone mass at baseline than Caucasians but whether the rate of loss is different between the two groups is unknown. Unique to our transplant cohort, we noticed that although Caucasians had a higher risk for progression than African Americans, a higher proportion in the AA group 5/23 (22%) progressed versus 35/241 (14%) Caucasians. The number of African American LT population was low but carried a concerning trend of disease progression raising the possibility that perhaps the rate of bone loss can be higher in AA population and may need close follow-up. Future studies may help understand potential race differences in how organ failure and transplantation affect different ethnic groups.

Glucocorticoid use, mycophenolate, and Tacrolimus use were not associated with progression risk, in keeping with the concept that bone disease in transplant patients is a unique entity caused by multifactorial pathways rather than explained by immunosuppression alone. High glucocorticoid (GC) use is typically limited to the first 4-6 months post-LT and discontinued in most individuals. GC is known to affect the bone by uncoupling bone resorption and bone formation, resulting in increased bone resorption by inhibiting gonadal steroids, increased urinary calcium excretion by inhibiting intestinal and renal calcium reabsorption, and secondary hyperparathyroidism and reduced bone formation by inhibiting type I collagen, osteocalcin, insulin-like growth factors, and bone matrix proteins, receptor activator for nuclear factor kappa B ligand (RANK-L (18, 19). The effect of GC on the bone goes well beyond the withdrawal of GC, and the GC effect on the bone is apparent even in lower doses (19, 20).

Our study shows that frequent organ rejection (>2) episodes rather than GC use may be an important clinical tool that can differentiate those with long-term effects on the bone from those with low rejection episodes. Our study noted that a higher number of rejections (>2 episodes) was associated with a significantly high risk of bone progression. Those with a higher rejection frequency in the first year of transplant may have received a higher dose of steroid than those with less frequent rejection events and are overall sicker. In addition, the finding may be in part explained by the GC effect on various organs, and GC-sparing therapies such as calcineurin inhibitor (Tacrolimus) may have a favorable effect on bone health GC asserts a direct effect on reducing osteoblast replication, differentiation, and lifespan resulting in a decline in bone formation. 33/232 (14%) of patients using Tacrolimus in first-year post-LT progressed, whereas only 4/33 (12%) patients using mycophenolate progressed. Though the findings were insignificant, the trend was that those on Tacrolimus had half the probability of progressing HR 0.55 (0.24-1.24) compared to those not on Tacrolimus. Prior studies have shown that early glucocorticoid withdrawal improves bone mass recovery (21–24). Calcineurin inhibitors (cyclosporine A (CsA) and Tacrolimus) are GC-sparing immunosuppressants that have been instrumental in reducing GC use. The effects of cyclosporine A (CsA) on bone health are unclear, though it generally appears to increase bone resorption and lead to bone loss. In contrast, tacrolimus is associated with less bone loss, likely due to reduced glucocorticoid (GC) use rather than direct effects on bone cells (13, 22). Glucocorticoids, mycophenolate, tacrolimus, and liver disease type were not significantly linked to increased bone disease progression, suggesting that bone disease in transplant patients has unique, multifactorial causes. Pre-transplant fracture notably was associated with BMD progression, with 38% (15 of 39) of patients with pre-transplant fractures experiencing progression—five times higher than those without fractures. Even without new post-transplant fractures, these patients had twice the risk of BMD progression, observed in 5 of 21 patients, emphasizing pre-transplant fractures as a key factor in post-transplant bone disease.

Long-term follow-up of LT patients beyond the first year should include fracture risk assessment through a comprehensive clinical history of known fracture risk factors. Particular attention should be given to patients who have received high doses of glucocorticoids for frequent rejections in the early post-transplant years. Clinicians should make every effort to obtain adequate clinical history and, when in doubt, obtain spine imaging to evaluate for asymptomatic fracture.

Prior studies have shown that the risk of asymptomatic vertebral fracture in pre-LT recipients was as high as 56% (2, 25). The study underscores the importance of pre- or within one year of LT fracture assessment by spine imaging to evaluate for radiographic evidence of fracture or clinical history suggestive of fractures such as height loss and kyphosis.

Currently, there are no standardized guidelines for the optimal interval between bone mineral density (BMD) testing or for the management of patients with liver transplant (LT)-related bone disease. Based on our findings, we propose that patients with a clinical risk score greater than five should be considered for additional spine imaging, such as plain radiographs of thoracic and lumbar spine, to evaluate for asymptomatic fractures, or should be considered for early treatment intervention. Prospective studies are needed to further validate the efficacy of this risk tool in guiding patient selection for treatment.

This study has several limitations, largely due to its retrospective design. First, we did not account for comorbidities or medications that may impact bone density, such as thiazide diuretics for hypertension or conditions such as type 2 diabetes. Additionally, because the study relied on retrospective chart reviews, not all relevant medical information was consistently recorded, particularly for patients managed by external institution (21, 22, 26).

Not unexpectedly, the presence of fracture at any time (pre-LT and within 1-year post-LT) is one of the strongest predictors of 5-year disease progression compared to those that did not fracture. The presence of a new fracture in the first-year post-LT visit, regardless of prior fracture, was highly correlated with disease progression ($p < 0.001$).

Moreover, patients who received treatment for osteoporosis after the first year post-LT were classified as having "bone loss progression," based on the assumption that treatment initiation reflects a clinical decision prompted by observed bone loss or increased risk. While it is possible that some patients may have started treatment as a preventive measure, we lacked sufficient data to differentiate between those treated for active bone loss and those treated prophylactically. Further studies should aim to clarify this distinction.

Conclusion

We developed a risk-scoring tool to enable clinicians to identify individuals with the highest risk of deterioration in bone health, defined as time to decline to the subsequent worse diagnosis (osteopenia and osteoporosis) based on the lowest BMD T score, received treatment for osteoporosis or had a new fracture. The BMD progression risk score is an easy-to-calculate scoring system based on information collected at the one-year follow-up assessment after a liver transplant. This tool though an encouraging start, will require prospective validation.

Data availability statement

The raw data supporting the conclusions of this article will be made available by the authors, without undue reservation.

Ethics statement

The studies involving humans were approved by Mayo clinic Florida institution review board. The studies were conducted in accordance with the local legislation and institutional requirements. Written informed consent for participation was not required from the participants or the participants' legal guardians/next of kin in accordance with the national legislation and institutional requirements.

Author contributions

EA: Conceptualization, Data curation, Formal analysis, Funding acquisition, Investigation, Methodology, Project administration, Resources, Software, Supervision, Validation, Visualization, Writing – original draft, Writing – review & editing. AM: Conceptualization, Data curation, Formal analysis, Investigation, Methodology, Project administration, Resources, Software, Validation, Visualization, Writing – original draft, Writing – review & editing. LY: Conceptualization, Data curation, Formal analysis, Funding acquisition, Investigation, Methodology, Resources, Supervision, Validation, Visualization, Writing – original draft, Writing – review & editing. CB: Conceptualization, Data curation, Formal analysis, Funding acquisition, Investigation, Methodology, Resources, Software, Validation, Writing – original draft, Writing – review & editing. AK: Conceptualization, Data curation, Formal analysis, Funding acquisition, Investigation, Methodology, Project administration, Resources, Software, Supervision, Validation, Visualization, Writing – original draft, Writing – review & editing.

Funding

The author(s) declare financial support was received for the research, authorship, and/or publication of this article. Statistical support provided by Mayo Clinic.

Conflict of interest

The authors declare that the research was conducted in the absence of any commercial or financial relationships that could be construed as a potential conflict of interest.

Publisher's note

Supplementary material

The Supplementary Material for this article can be found online at: https://www.frontiersin.org/articles/10.3389/fendo.2025.1467825/full#supplementary-material

References

1. Cohen A, Sambrook P, Shane E. Management of bone loss after organ transplantation. *J Bone Miner Res*. (2004) 19:1919–32. doi: 10.1359/jbmr.040912

2. Krol CG, Dekkers OM, Kroon HM, Rabelink TJ, van Hoek B, Hamdy NA. No association between BMD and prevalent vertebral fractures in liver transplant recipients at time of screening before transplantation. *J Clin Endocrinol Metab*. (2014) 99:3677–85. doi: 10.1210/jc.2014-1469

3. Krol CG, Dekkers OM, Kroon HM, Rabelink TJ, van Hoek B, Hamdy NA. Longitudinal changes in BMD and fracture risk in orthotopic liver transplant recipients not using bone- modifying treatment. *J Bone Miner Res*. (2014) 29:1763–9. doi: 10.1002/jbmr.2214

4. Abate EG, Vega MV, Rivas AM, Meek S, Yang L, Ball CT, et al. Evaluation of factors associated with fracture and loss of bone mineral density within 1 year after liver transplantation. *Endocr Pract*. (2021) 27:426–32. doi: 10.1016/j.eprac.2020.10.008

5. Butin S, Griffoul I, Espitalier F, Salame E, Mulleman D, Goupille P. High incidence of vertebral osteoporotic fracture within the first year after liver transplantation. *Clin Exp Rheumatol*. (2017) 35(6):913–8.

6. Chiu YC, Liao PS, Chou YT, Lin CL, Hung CH, Lin CC, et al. The incidence and risk factors of hip fracture after liver transplantation (LT): A nationwide population-based study. *BioMed Res Int*. (2019) 2019:5845709. doi: 10.1155/2019/5845709

7. Danford CJ, Trivedi HD, Bonder A. Bone health in patients with liver diseases. *J Clin Densitom*. (2020) 23:212–22. doi: 10.1016/j.jocd.2019.01.004

8. Bergmann PJ. Change in bone density and reduction in fracture risk: A meta-regression of published trials. *J Bone Miner Res*. (2019) 34:1976. doi: 10.1002/jbmr.3835

9. Martin P, DiMartini A, Feng S, Brown R Jr., Fallon M. Evaluation for liver transplantation in adults: 2013 practice guideline by the American Association for the Study of Liver Diseases and the American Society of Transplantation. *Hepatology*. (2014) 59:1144–65. doi: 10.1002/hep.26972

10. Guichelaar MM, Malinchoc M, Sibonga J, Clarke BL, Hay JE. Bone metabolism in advanced cholestatic liver disease: analysis by bone histomorphometry. *Hepatology*. (2002) 36:895–903. doi: 10.1053/jhep.2002.36357

11. Guichelaar MM, Malinchoc M, Sibonga JD, Clarke BL, Hay JE. Bone histomorphometric changes after liver transplantation for chronic cholestatic liver disease. *J Bone Miner Res*. (2003) 18:2190–9. doi: 10.1359/jbmr.2003.18.12.2190

12. Vedi S, Ninkovic M, Garrahan NJ, Alexander GJ, Compston JE. Effects of a single infusion of pamidronate prior to liver transplantation: a bone histomorphometric study. *Transpl Int*. (2002) 15:290–5. doi: 10.1111/j.1432-2277.2002.tb00167.x

13. Bodingbauer M, Wekerle T, Pakrah B, Roschger P, Peck-Radosavljevic M, Silberhumer G, et al. Prophylactic bisphosphonate treatment prevents bone fractures after liver transplantation. *Am J Transplant*. (2007) 7:1763–9. doi: 10.1111/j.1600-6143.2007.01844.x

14. Vedi S, Greer S, Skingle SJ, Garrahan NJ, Ninkovic M, Alexander GA, et al. Mechanism of bone loss after liver transplantation: A histomorphometric analysis. *J Bone Miner Res*. (1999) 14:281–7. doi: 10.1359/jbmr.1999.14.2.281

15. Harrell FE, Lee KL, Mark DB. Tutorial in Biostatistics: Multivariable prognostic models: issues in developing models, evaluating assumptions and adequacy, and measuring and reducing errors. *Stat Med*. (1996) 15:361–87. doi: 10.1002/(SICI)1097-

16. Looker AC, Melton LJ3rd, Borrud LG, Shepherd JA. Lumbar spine bone mineral density in US adults: demographic patterns and relationship with femur neck skeletal status. *Osteoporos Int*. (2012) 23:1351–60. doi: 10.1007/s00198-011-1693-z

17. Bouxsein ML, Eastell R, Lui LY, Wu LA, de Papp AE, Grauer A, et al. Change in bone density and reduction in fracture risk: A meta-regression of published trials. *J Bone Miner Res*. (2019) 34:632–42. doi: 10.1002/jbmr.3641

18. Stein E, Ebeling P, Shane E. Post-transplantation osteoporosis. *Endocrinol Metab Clin North Am*. (2007) 36:937–63. doi: 10.1016/j.ecl.2007.07.008

19. Buckley L, Guyatt G, Fink HA, Cannon M, Grossman J, Hansen KE, et al. 2017 American college of rheumatology guideline for the prevention and treatment of glucocorticoid- induced osteoporosis. *Arthritis Rheumatol*. (2017) 69:1521–37. doi: 10.1002/art.40137

20. van Staa TP. The pathogenesis, epidemiology and management of glucocorticoid- induced osteoporosis. *Calcif Tissue Int*. (2006) 79:129–37. doi: 10.1007/s00223-006-0019-1

21. Feller RB, McDonald JA, Sherbon KJ, McCaughan GW. Evidence of continuing bone recovery at a mean of 7 years after liver transplantation. *Liver Transpl Surg*. (1999) 5:407–13. doi: 10.1002/(ISSN)1527-6473a

22. Goffin E, Devogelaer JP, Lalaoui A, Depresseux G, De Naeyer P, Squifflet JP, et al. Tacrolimus and low-dose steroid immunosuppression preserves bone mass after renal transplantation. *Transpl Int*. (2002) 15:73–80. doi: 10.1111/j.1432-2277.2002.tb00133.x

23. Guichelaar MM, Kendall R, Malinchoc M, Hay JE. Bone mineral density before and after OLT: long-term follow-up and predictive factors. *Liver Transpl*. (2006) 12:1390–402. doi: 10.1002/(ISSN)1527-6473

24. Mart i G, Gomez R, Jodar E, Loinaz C, Moreno E, Hawkins E. Long-term follow-up of bone mass after orthotopic liver transplantation: effect of steroid withdrawal from the immunosuppressive regimen. *Osteoporos Int*. (2002) 13:147–50. doi: 10.1007/s001980200006

25. Monegal A, Navasa M, Guanabens N, Peris P, Pons F, Martinez de Osaba MJ, et al. Bone disease after liver transplantation: a long-term prospective study of bone mass changes, hormonal status and histomorphometric characteristics. *Osteoporos Int*. (2001) 12:484–9. doi: 10.1007/s001980170094

26. Nightingale S, McEwan-Jackson FD, Hawker GA, Macarthur C, Khambalia AZ, Lo L, et al. Corticosteroid exposure not associated with long-term bone mineral density in pediatric liver transplantation. *J Pediatr Gastroenterol Nutr*. (2011) 53:326–32. doi: 10.1097/MPG.0b013e3182258656

frontiers | Frontiers in Endocrinology

TYPE Original Research
PUBLISHED 03 March 2025
DOI 10.3389/fendo.2025.1549068

OPEN ACCESS

EDITED BY
Egon Burian,
Zurich University Hospital, Switzerland

REVIEWED BY
Fabio Zecca,
University of Cagliari, Italy
Falko Ensle,
University Hospital Zürich, Switzerland

*CORRESPONDENCE
Yannick Stohldreier
Yannick.Stohldreier@med.uni-muenchen.de

†These authors have contributed equally to this work and share last authorship

RECEIVED 20 December 2024
ACCEPTED 17 February 2025
PUBLISHED 03 March 2025

CITATION
Stohldreier Y, Leonhardt Y, Ketschau J, Gassert FT, Makowski MR, Kirschke JS, Feuerriegel GC, Braun P, Schwaiger BJ, Karampinos DC, Hesse N and Gersing AS (2025) Longitudinal assessment of changes in muscle composition using proton density fat fraction and T2* in patients with and without incidental vertebral compression fractures. *Front. Endocrinol.* 16:1549068. doi: 10.3389/fendo.2025.1549068

Longitudinal assessment of changes in muscle composition using proton density fat fraction and T2* in patients with and without incidental vertebral compression fractures

Yannick Stohldreier[1]*, Yannik Leonhardt[2], Jannik Ketschau[2], Florian T. Gassert[2], Marcus R. Makowski[2], Jan S. Kirschke[3], Georg C. Feuerriegel[2], Philipp Braun[2], Benedikt J. Schwaiger[3], Dimitrios C. Karampinos[2], Nina Hesse[4†] and Alexandra S. Gersing[1,2†]

[1]Department of Neuroradiology, Ludwig Maximilians University Hospital, Ludwig Maximilians University (LMU) Munich, Munich, Germany, [2]Department of Diagnostic and Interventional Radiology, Klinikum Rechts Der Isar, School of Medicine, Technical University of Munich, Munich, Germany, [3]Department of Neuroradiology, Klinikum Rechts Der Isar, School of Medicine, Technical University of Munich, Munich, Germany, [4]Department of Radiology, Ludwig Maximilians University Hospital, Ludwig Maximilians University (LMU) Munich, Munich, Germany

Objective: Chemical shift encoded-based water-fat separation magnetic resonance imaging (CSE-MRI) is an emerging noninvasive tool for the assessment of bone and muscle composition. This study aims to examine both the predictive value and the longitudinal change of proton density fat fraction (PDFF) and T2* in the paraspinal muscles (PSM) in patients with and without the development of an incidental vertebral compression fracture (VCFs) after 6 months of follow-up.

Methods: Patients (N=56) with CT and 3T CSE-MRI of the lumbar spine at baseline and CSE-MRI at 6 months follow-up were included in this retrospective study. Patients who, on average, developed an incidental VCF one year after baseline MRI (VCF: N=14, 9 males, 66.8 ± 7.9 years) were frequency matched by age and sex to patients without VCFs (non-VCF) at baseline and follow-up (non-VCF: N=42, 27 males, 64.6 ± 13.3 years). Mean PDFF, T2*, and cross-sectional area (CSA) values from the autochthonous PSM of the thoracolumbar spine (T11-L4) and opportunistic CT-based bone mineral density (BMD) measurements were obtained for each individual. The associations between baseline measurements, longitudinal changes in PDFF, T2*, CSA of the PSM and the occurrence of VCFs at follow-up were evaluated using linear and logistic multivariable regression models. ROC analyses were used to assess cutoff values for predicting the development of VCFs.

Results: No significant difference in PDFF of the PSM was found between the VCF and non-VCF group at baseline (VCF/non-VCF 8.5 ± 13.8% vs. 5.0 ± 4.6%; p=0.53). In multivariable linear regression models adjusted for sex, age and

baseline BMD, PDFF values of the PSM increased significantly over 6 months in the VCF group (2.4 ± 2.8% vs. -1.0 ± 2.3%, p<0.001), while T2* values of the PSM showed a significant decrease (p ≤ 0.01). ROC analyses identified a PDFF increase of 0.2% in the PSM as the optimal cutoff value to distinguish between patients with and without VCF (AUC 0.86, 95% CI [0.74-0.98], p<0.001).

Conclusion: Longitudinal PDFF-based assessment of the PSM composition may be a useful indicator for the prediction of the development of vertebral compression fractures.

KEYWORDS

incidental vertebral compression fractures, magnetic resonance imaging, muscle, spine, proton density fat fraction, chemical shift encoded MRI, bone mineral density

1 Introduction

In our aging society, osteoporosis is a significant health issue with insufficiency fractures of vertebrae being linked to increased mortality rates and a substantial economic burden (1–4). Early detection and reliable assessment of osteoporosis are crucial for preventing vertebral fractures. Dual-energy x-ray absorptiometry (DXA) and quantitative CT (qCT) are currently the diagnostic reference standard for the assessment of osteoporosis. However, qCT offers more precise bone mineral density (BMD) measurements compared to DXA, while at the same time resulting in higher radiation exposure of the patient (5). Reduced BMD is the major risk factor for incidental vertebral compression fractures (VCF) (6). Osteoporosis and bone loss are closely linked to sarcopenia and poor muscle strength through endocrine pathways (7). Both are independently established risk factors for vertebral fractures (8–11). Bone marrow is composed of various cell types within a trabecular bone matrix and its composition is influenced by several metabolic and external factors (12). Increased fat content is part of the pathophysiology of osteoporosis in the spine and is driven by enhanced proliferation of mesenchymal stem cells into adipocytes (13–15). A radiation free approach for fat quantification is proton density fat fraction (PDFF) mapping via chemical-shift encoding-based water-fat MRI (CSE-MRI) (16). The PDFF technique has shown to be a reliable measurement tool for fat quantification in different tissues and several previous studies have demonstrated a negative correlation between the BMD and PDFF of the vertebral bone marrow (17–24). The advantage of CSE-MRI over spatially limited measurement methods, such as single voxel proton magnetic resonance spectroscopy (MRS), is that the heterogeneous composition of the bone marrow and PSM as well as the cross-sectional area (CSA) of the PSM can be assessed simultaneously. In clinical practice, CSE-MRI can easily be integrated into routine MR imaging protocols. A recent study reported an increase of PDFF over one year within the vertebral bodies before an incidental fracture occurred while the BMD remained unchanged, indicating that PDFF could be used as a predictive biomarker for bone health (25). Fat infiltration may be influenced by external stress factors, such as myelotoxic chemotherapy, or by metabolic disorders like diabetes (26–28). Additionally, a correlation of fat infiltration of the vertebral bone marrow and the paraspinal muscles (PSM) was previously reported (29). CT- and MRI-based fat quantifications in previous studies have also demonstrated an inverse correlation between fat infiltration of the PSM and reduced muscle strength as well as spinal instability (30, 31). CSE-MRI also allows for the assessment of T2*. In vertebral bodies, T2* is linked to the osseous microarchitecture, showing an inverse correlation with BMD (29, 32).

The aim of this study is to investigate the relationship between the occurrence of vertebral compression fractures (VCF) and PDFF and T2* measurements of the PSM and the vertebral bone marrow in the lumbar region.

Abbreviations: AUC, Area under the curve; BMD, Bone mineral density; CSA, Cross-sectional area; CSE-MRI, Chemical shift encoded-based Water-Fat Separation Magnetic Resonance Imaging; HU, Hounsfield units; ICC, Intraclass correlation coefficient; L, Lumbar vertebra; MDCT, Multi-Slice Detector Computer Tomography; MRS, Single Voxel Proton Magnetic Resonance Spectroscopy; PDFF, Proton Density Fat Fraction; PSM, Paraspinal muscle; RMSCV, Root mean square coefficient of variation; ROC, Receiver operating characteristics; T, Thoracic vertebra; VCF, Vertebral compression fracture.

2 Materials and methods

2.1 Study design and patient selection

The study was approved by the local institutional review committee (Ethics Commission of the Medical Faculty, Technical University of Munich, Germany; Ethics proposal number 2022-433-S-SR). All patients gave written and informed consent prior to their participation in the study according to the Declaration of Helsinki. Between January 2018 and June 2021, a total of 200

patients underwent MRI protocol of the abdomen including a multi-echo gradient-echo sequence of the thoracolumbar spine and a CT including the lumbar spine from which opportunistic BMD measurements were derived as part of their clinical routine (33, 34). Exclusion criteria for MR imaging included pregnancy, presence of metal implants, and general contraindications for MR imaging (e.g., pacemakers). The 6 months follow-up CSE-MR images of all these patients were screened for newly detected vertebral compression fractures, which had not been present in the previous MR and CT scans. Patients with an incidental vertebral compression fracture (VCF) were retrospectively included, provided the fracture showed no signs of malignancy (e.g., osseous metastasis) or was caused by high-energy trauma. In total, 14 patients met all criteria and were enrolled in our study. These patients were frequency matched for age and sex in a 1:3 ratio to patients without VCF.

The medical treatment history of all enrolled patients was reviewed. None of them had undergone chemotherapy or osteoporosis treatment before or during the study. The follow-up MRI was performed 4.5 ± 2.4 months after the baseline MRI. The occurrence of a VCF was determined in an additional MRI 13.0 ± 8.5 months after baseline. The CT examinations were performed within 1 month of the baseline MR imaging.

2.2 Magnetic resonance imaging and measurements

MR images, including the lumbar spine, were acquired by two 3T-MRI systems (both Elition, Phillips Healthcare and Ingenia, Phillips Healthcare). Patients were placed in a supine position with a 16-channel anterior torso coil array and an inbuilt posterior 12-channel coil array. The imaging sessions included CSE-MRI for PDFF and T2* measurement, axial and coronal T2-TSE sequences, as well as axially acquired T1-weighted sequences with spectral fat saturation with and without contrast administration. For PDFF and T2* measurements, an axial six-echo 3D multi-echo gradient-echo sequence was employed, capturing all echoes in a single TR using bipolar gradients. The imaging parameters were as follows: repetition time (TR)/first echo time (TE1)/echo time step (ΔTE) = 7.8/1.35/1.1ms, field of view (FOV) = 300 x 400 x 150 mm^3, acquisition voxel size = 2 x 3 x 6 mm^3, reconstruction voxel size = 1.13 x 1.13 x 6 mm^3, receiver bandwidth = 1678 Hz/pixel, frequency direction = anterior/posterior (A/P), 1 average, scan time = 9.3 s. To minimize T1 bias effects, a flip angle of 3° was utilized (35). Complex multi-echo gradient-echo images were processed using the fat quantification routine provided by the vendor (mDixon Quant, Philips Healthcare). After phase correction, a complex-based water-fat decomposition was performed, incorporating a single T2* correction and a pre-calibrated fat spectrum considering the multiple peaks in the fat spectrum. A seven-peak fat spectrum model was employed. PDFF maps were computed as the ratio of fat signal over the sum of fat and water signals, and PDFF and T2* maps were extracted (36, 37). Besides PDFF maps, T2* maps were utilized to assess the muscle and bone composition of the participants.

Segmentation of the thoracolumbar vertebral bone marrow and PSM were performed manually by F.T.G. and Y.L. (3 and 4 years of experience in musculoskeletal imaging) on the PDFF and T2* maps using the IDS7 PACS (Sectra AB, Linkoeping, Sweden). The fractures were classified by two board-certified radiologists (B.J.S. and A.S.G., both with 12 years of experience in musculoskeletal imaging) by evaluating the involvement of the posterior column, superior and/or inferior endplate and deformity (crush, biconcave, wedge) of the vertebra. Fractures were classified with the Genant classification (38). B.J.S. and A.S.G. also ensured, in conjunction with the clinical history, that no morphological indications of malignant fractures were present in any of the sequences. Cylindrical ROIs were placed in axial PDFF and T2* maps in the center of the thoracic vertebrae (T) 11 to the lumbar vertebrae (L) 4, and the mean PDFF and T2* values were obtained for each vertebra (Figure 1). No ROIs were placed into fractured vertebrae at the six months follow-up. Beginning at T11, five consecutive slices on both sides were segmented in the PSM as illustrated in Figure 1 and

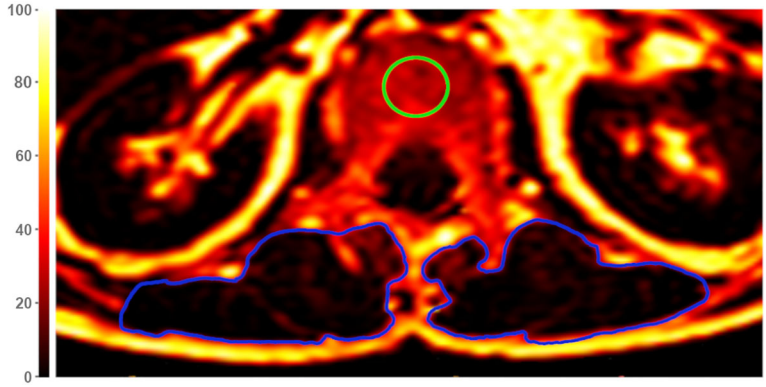

FIGURE 1
Exemplary axial Proton Density Fat Fraction (PDFF)-map at height of lumbar vertebra 1 (L1). For measurements of vertebral PDFF and T2*, regions of interest (ROIs) were placed in the center of each vertebra (green circle). Muscle PDFF, T2*, and cross-sectional area (CSA) were measured by segmentation of the paraspinal muscle (PSM) on both sides (blue circles). The color scale indicates PDFF values in [%].

values were averaged. Furthermore, the CSA values of each slice were noted for both sides and averaged. The longitudinal change of PDFF, T2* and CSA in the PSM and the change of PDFF and T2* in the vertebral bone marrow was calculated as the difference between the follow-up and the baseline values.

To evaluate the intrareader reproducibility of PDFF, T2*, and BMD values, a random sample of 10 subjects was selected and reanalyzed after 8 weeks by the same radiologists Y.L. and G.C.F. F.T.G. independently analyzed a random sample of 10 subjects after a 6 months interval from the initial review to evaluate inter-reader reproducibility.

2.3 Computed tomography and BMD measurement

All included patients received CT images using a dual-layer dual-energy CT (IQon Spectral CT, Phillips Healthcare, Amsterdam) or a multi-slice detector CT (MDCT) (Phillips iCT 256, Phillips Healthcare). The patients were positioned in supine position and scans obtained in craniocaudal direction. The scanning parameters followed routine clinical protocols: collimation of 0.9 mm, pixel spacing of 0.4/0.3 mm, pitch factor of 0.8/0.9, tube voltage of 120 kV, and a modulated tube current ranging from 125 to 250 mAs.

The trabecular bone of the entire vertebral bodies from L1 to L4 was manually segmented using the IDS7 PACS (Sectra AB, Linkoeping, Sweden) by a radiologists G.C.F. in the axial plane, excluding cortical bone. The mean Hounsfield Unit (HU) value for each non-fractured vertebra was calculated, and the average HU value for each patient was determined by averaging the mean HU values of the vertebrae. Fractured or degenerative altered vertebrae (i.e., vertebrae exhibiting osteoarthritic changes such as osteophytes, endplate sclerosis, reduced vertebral height, or vertebrae with vertebra-/kyphoplasty) were excluded from HU measurement. The HU units were used in a previously described and tested conversion equation to calculate the BMD of the lumbar vertebrae: 0.928 g/cm^3 × HU + 4.5 g/cm 3 for the IQon Spectral CT and 0.855 g/cm^3 × HU + 1.172 g/cm^3 for the Philips iCT 256 (39). Osteoporosis was defined as a BMD less than 80 mg/cm^3, while osteopenia was defined as a BMD ranging from 80 to 120 mg/cm^3 (40).

2.4 Statistical analysis

Statistical analysis was performed by Y.S. with RStudio Build 764 and R version 4.4.0 (R Foundation for Statistical Computing, Vienna, Austria). All tests were performed with a two-sided significance level of $\alpha = 0.05$. Metric variables are presented as mean ± standard deviation. Shapiro-Wilk test was used to assess the distribution of data. Group comparisons for normally distributed metric variables were assessed for equal variances using the Bartlett Test. If variances were equal, the two-sample t-test was utilized; otherwise, the Welch test was employed. For non-normally distributed metric data, equal variances were examined with the Fligner-Killeen Test. With equal variances, the Wilcoxon rank sum exact test/Mann-Whitney U test was applied; otherwise, Mood's median test was used for group comparisons. Categorial data was compared using Fisher's Exact test if the sample size in a group was less than 5, otherwise the Chi-squared test was performed. In order to distinguish patients with and without VCFs, ROC curves were generated to evaluate the longitudinal PDFF cutoff values of the vertebral bone marrow and PSM based on sensitivity and specificity. For each ROC curve the optimal cutoff value with the highest Youden Index was selected. In addition to calculating the AUC, we determined the 95% confidence interval with p-value. Multivariable logistic and linear regression models were calculated to explore the association between VCFs and PDFF by adjusting for sex, age and BMD.

Intra- and inter-reader reproducibility of T2*, PDFF, CSA and BMD values were evaluated by computing the intraclass correlation coefficient (ICC) and the root mean square coefficient of variation (RMSCV) of the difference between the measurements performed by the readers.

3 Results

Fourteen patients (66.8 ± 7.9 years, 9 males) with incidental VCFs (Figure 2) were frequency matched with patients without VCFs in a 1:3 ratio (n = 42, 64.6 ± 13.3 years, 27 males). Among VCF patients, six were osteopenic and two were osteoporotic, whereas in the non-VCF group, 17 were osteopenic and two were osteoporotic at baseline. No significant association was detected between osteopenic/osteoporotic patients and the development of VCFs (p = 0.40).

Descriptive statistics of MRI data of PDFF, T2*, and CSA analyses for patients with and without VCFs at baseline and follow-up are listed in Table 1. When assessing PSM parameters, there were no significant differences between the VCF and non-VCF groups in terms of baseline PDFF (VCF/non-VCF 8.5 ± 13.8% vs. 5.0 ± 4.6%, p = 0.53). Additionally, CSA (VCF/non-VCF 13.0 ± 4.5 cm^2 vs. 13.4 ± 3.4 cm^2, p = 0.44) showed no significant difference between both groups. While the PDFF of the PSM increased significantly in patients with VCF over time, the PDFF in the non-VCF decreased significantly over 6 month (VCF/non-VCF 2.4 ± 2.8% vs.-1.0 ± 2.3%; p < 0.001, Figure 3; Table 2). The analysis of T2* relaxation time of the PSM at baseline showed no significant difference between the VCF and non-VCF group (Table 1). However, at follow-up, the T2* relaxation time of the PSM was significantly higher in the non-VCF group compared to the VCF group (follow-up T2* VCF/non-VCF 26.5 ± 4.1 ms vs. 29.5 ± 2.4 ms, p = 0.02). The VCF group experienced a significantly higher longitudinal decrease in T2* in the PSM over time (VCF/non-VCF -3.3 ± 2.7 ms vs. -0.4 ± 2.2 ms, p = 0.01, Figure 3; Table 2).

VCF group showed a significant increase in vertebral bone marrow PDFF over time (7.9 ± 7.0% vs. -2.6 ± 5.4%, p < 0.001, Figure 3; Table 2). However, no significant differences in PDFF of the vertebral bone marrow were observed between the VCF and non-VCF group, neither at baseline nor at follow-up (Table 1). The mean T2* value of the vertebral bone marrow was significantly higher in patients with VCFs (baseline T2* VCF/non-VCF 10.9 ±

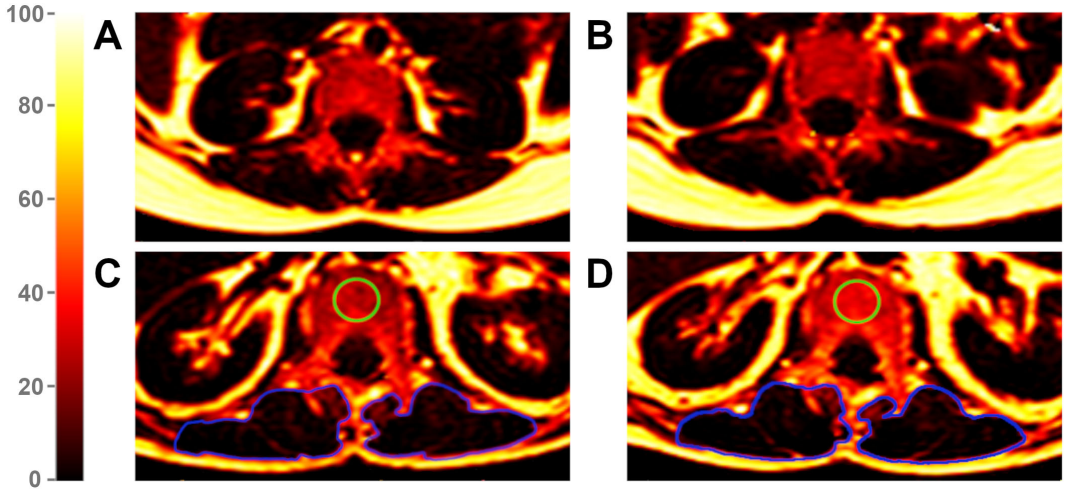

FIGURE 2
Proton Density Fat Fraction (PDFF) maps of a patient without vertebral compression fracture (VCF) at baseline **(A)** and follow-up **(B)** and of a patient with VCF at baseline **(C)** and follow-up **(D)**. The green region of interest (ROI) illustrates an exemplary measurement of the vertebral bone marrow in a VCF patient, visually highlighting an increase in fat infiltration from baseline **(C)** to follow-up **(D)**. The blue ROIs mark the paraspinal muscles. Due to an average PDFF change of 2.4% in PSM from baseline **(C)** to follow-up **(D)** among VCF patients, changes in color remain subtle. The color scale indicates PDFF values in [%].

3.2 ms vs. 8.1 ± 2.4 ms, p = 0.01), suggesting an initially slightly lower BMD. Indeed, BMD was lower among VCF patient, but the difference was not statistically significant (VCF/non-VCF 115.7 ± 37.9 mg/cm³ vs. 136.6 ± 45.6 mg/cm³, p = 0.12).

Multivariable linear regression analysis, adjusted for gender, age, and BMD, revealed an average increase in PDFF of the PSM of 3.5% from baseline to follow-up (95% CI [1.8 – 5.3]; p < 0.001) in patients who developed VCF compared to patients without VCF. The change in CSA of the PSM (82.6 cm², 95% CI [-177.8 - 343.0]; p = 0.52) did not significantly differ between the groups. Multivariable logistic regression model, adjusted for gender, age, and BMD, suggested that increasing PDFF of the PSM (OR = 2.21, 95% CI [1.38 - 4.73]; p < 0.01) and vertebral bone marrow over 6 months (OR = 1.49, 95% CI [1.19 - 2.14]; p < 0.01) are significant risk factors for the development of VCF. In the same model, decreasing T2* of the PSM was also identified as a risk factor for the development of a VCF (OR = 1.89, 95% CI [1.28 - 3.33]; p < 0.01). In contrast, changes in T2* of the vertebral bone marrow (OR = 0.97, 95% CI [0.69 - 1.32]; p = 0.87) and changes in CSA of the PSM over 6 months (OR = 1.00, 95% CI [0.99 – 1.00]; p = 0.50) do not pose a risk factor for the development of VCF.

Moreover, ROC analysis (Figure 4) showed that a PDFF change of 0.2% in the PSM (AUC 0.86, 95% CI [0.74 - 0.98], specificity 0.73, sensitivity 0.90, Youden Index = 0.63, p < 0.001) can significantly differentiate VCF from non-VCF patients.

The intrareader as well as the interreader agreement for T2* (ICC for both 0.98, 95% CI [0.96 - 0.99]), PDFF (ICC for both 0.98 [95% CI, 0.96 - 0.99]), CSA (ICC for both 0.98, 95% CI [0.96 - 0.99])

TABLE 1 Descriptive analyses between patients with (VCF) and without (non-VCF) vertebral compression fractures for baseline and follow-up. The values are listed as mean ± standard deviation.

	Baseline			Follow-Up		
	VCF group	Non-VCF group	*P*-value	VCF group	Non-VCF group	*P*-value
Vertebral bone marrow PDFF of T11 - L4 (%)	41.0 ± 12.2	46.8 ± 9.6	0.07 [b]	44.8 ± 14.4	43.8 ± 11.5	0.83 [b]
PDFF of the paraspinal muscle (%)	8.5 ± 13.8	5.0 ± 4.6	0.53 [c]	11.4 ± 16.6	4.6 ± 4.1	**0.04** [c]
Vertebral bone marrow T2* of T11 - L4 (ms)	10.9 ± 3.2	8.1 ± 2.4	**0.01** [b]	11.7 ± 5.7	9.0 ± 2.6	0.16 [c]
T2* of the paraspinal muscle (ms)	29.9 ± 4.5	30.0 ± 2.9	0.93 [d]	26.5 ± 4.1	29.5 ± 2.4	**0.02** [c]
CSA of the average right and left paraspinal muscle (cm²)	13.0 ± 4.5	13.4 ± 3.4	0.44 [c]	14.9 ± 4.5	13.3 ± 3.6	0.26 [b]

[a] Mood's median test.
[b] Two-sample t-test.
[c] Wilcoxon rank sum test/Mann-Whitney U test.
[d] Welch t-test.
PDFF, Proton Density Fat Fraction; VCF, vertebral compression fracture; CSA, cross-sectional area.
Statistically significant p-values (p ≤ 0.05) are highlighted in bold.

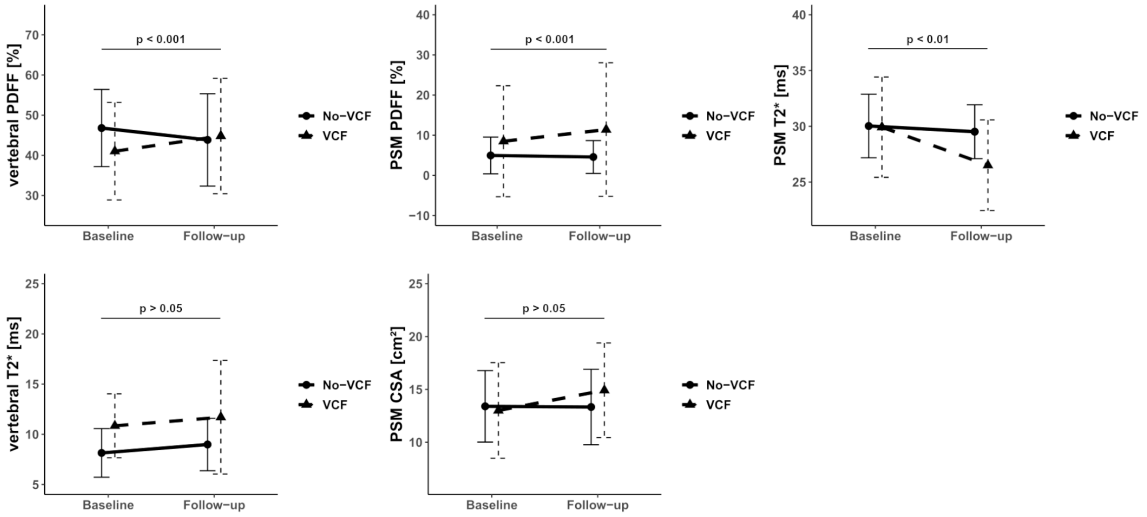

FIGURE 3
Median of Proton Density Fat Fraction (PDFF), T2* and CSA in the vertebral bone marrow and paraspinal muscle (PSM) grouped by vertebral compression fracture (VCF) status at baseline and at 6-month follow-up. The p-values refer to the change of the respective value from baseline to follow-up between patients with and without VCF.

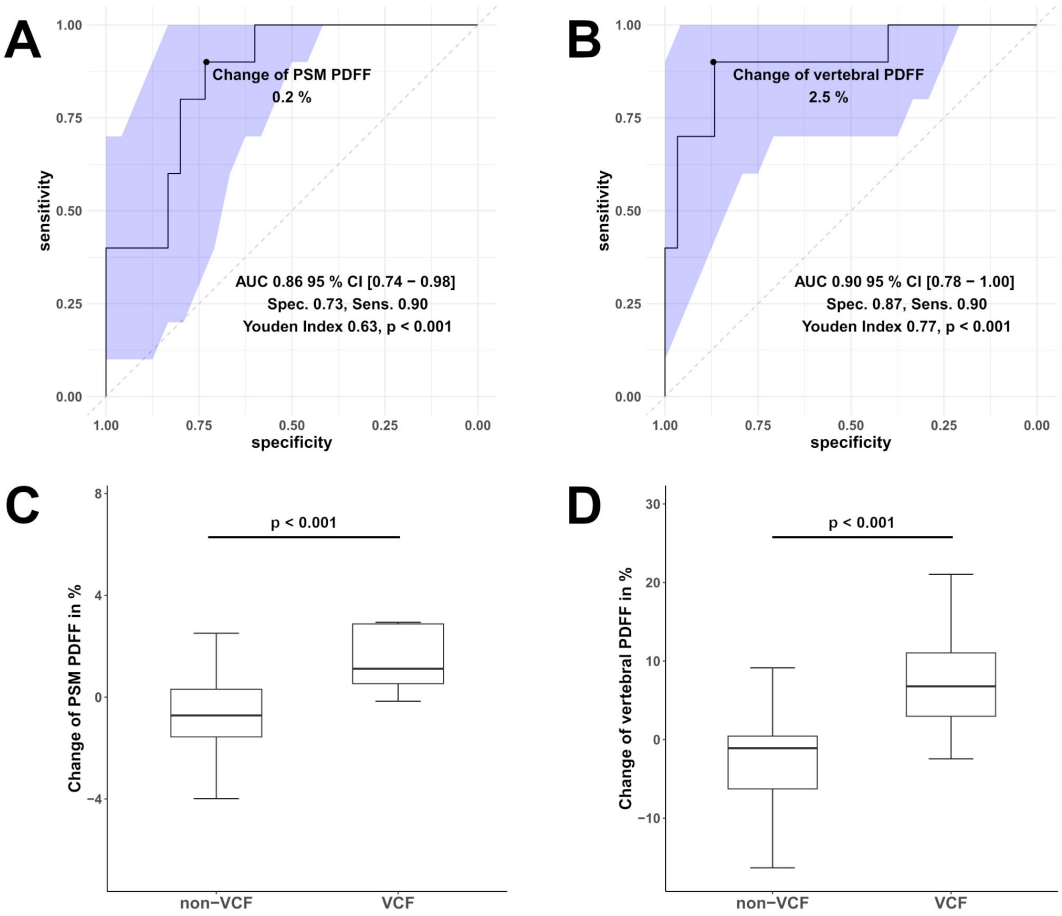

FIGURE 4
Receiver operating characteristic (ROC) curves of the change in Proton Density Fat Fraction (PDFF) in the paraspinal muscle (PSM, **(A)**) and vertebral bone marrow PDFF **(B)** were used to differentiate between patients with vertebral compression fracture (VCF) and without (non-VCF). The blue area illustrates the 95% confidence interval (CI) of the area under the curve (AUC). Additionally, boxplot **(C)** represents the median longitudinal change of PDFF in the PSM, and boxplot **(D)** shows the change of vertebral bone marrow PDFF between individuals who experienced VCF and those who did not. Respectively, the difference in in the change of PDFF PSM and vertebral bone marrow PDFF was significant (for both $p < 0.001$).

10.3389/fendo.2025.1549068

TABLE 2 Descriptive analyses for the change of Proton Density Fat Fraction (PDFF), T2* and muscle cross-sectional area (CSA) in the vertebral bone marrow and paraspinal muscle (PSM) between patients with (VCF) and without (non-VCF) vertebral compression fractures.

	VCF group	non-VCF group	P-value
Change in PDFF over 6 months of the paraspinal muscle (%)	2.4 ± 2.8	-1.0 ± 2.3	**<0.001** [c]
Change in T2* over 6 months of the paraspinal muscle (ms)	-3.3 ± 2.7	-0.4 ± 2.2	**0.01** [b]
Change in vertebral bone marrow PDFF of T11 - L4 over 6 months (%)	7.9 ± 7.0	-2.6 ± 5.4	**< 0.001** [b]
Change in vertebral bone marrow T2* of T11 - L4 over 6 months (ms)	0.4 ± 3.1	0.5 ± 2.1	0.93 [b]
Change in CSA over 6 months of the paraspinal muscle (cm^2)	0.6 ± 6.7	-0.1 ± 1.6	0.26 [a]

[a] Mood's median test.
[b] Two-sample t-test.
[c] Wilcoxon rank sum test/Mann-Whitney U test.
[d] Welch t-test.
PDFF, Proton Density Fat Fraction; VCF, vertebral compression fracture; CSA, cross-sectional area. The values are listed as mean ± standard deviation.
Statistically significant p-values ($p \leq 0.05$) are highlighted in bold.

and BMD (ICC intrareader 0.99, 95% CI [0.98 – 0.99] and interreader 0.99, 95% CI [0.97–0.99]) measurements were excellent. Intra- and interrater reproducibility, assessed by calculating the RMSCV, also demonstrated excellent agreement for T2* (RMSCV intrarater 0.8% and interrater 0.9%), PDFF (RMSCV intrarater 0.9% and interrater 0.8%), CSA (RMSCV intrarater 0.7% and interrater 0.8%) and BMD (RMSCV intrarater 0.4% and interrater 0.5%) measurements.

4 Discussion

This study assessed the associations between the occurrence of incidental VCFs and the longitudinal changes in PDFF, T2* and CSA of the PSM and vertebral bone marrow in the thoracolumbar region. Although no significant baseline difference in BMD was observed, the increase in PDFF in the PSM and vertebral bone marrow was significantly higher in patients who developed a VCF compared to those without VCF.

The marked increase in PSM PDFF within six months indicates a rapid fatty degeneration, potentially linked to the occurrence of VCFs. The CSA of the PSM showed a marginal increase in these patients, however this change did not reach statistical significance. Several studies have investigated the impact of elevated muscle PDFF on both muscle function and bone health. Fatty infiltration of the PSM has been associated with severe back pain and structural abnormalities in the lumbar spine, such as reduced disc height and decreased muscle strength (31, 41). In relation to bone health, the PDFF of the erector spinae, multifidus, and psoas muscles has been shown to be significantly higher in osteopenic patients (42).

Our findings, consistent with previously published studies, demonstrated an increase in PDFF within the vertebral bone marrow among individuals with VCFs, whereas BMD showed no significant differences. Although an inverse correlation between vertebral bone marrow PDFF and BMD has been well established (17–21), a recent study reported an increase in PDFF in vertebral bone marrow prior to incidental fractures, while BMD remained unchanged. This finding underscores the potential predictive value of PDFF over BMD in forecasting the occurrence of VCFs (25). Additionally, elevated fat content in the vertebral bone marrow has been linked to reduced bone quality and the presence of osteoporosis (29, 43). Postmenopausal women, a population at higher risk for osteoporotic vertebral fractures, exhibited significantly higher PDFF in the vertebral bone marrow compared to premenopausal women (44). Furthermore, insulin resistance is associated with increased vertebral bone marrow PDFF and a heightened risk of fractures. This suggests fatty vertebral infiltration may serve as an additional risk factor for fractures in patients with pathological glucose metabolism (45–47).

Age, physical inactivity, muscle atrophy, and reduced BMD are known risk factors for VCFs (6, 8–11). These factors are also linked to fatty infiltration in bone and muscle (18–21, 31, 48, 49). Muscle atrophy weakens spinal stability, leading to more mechanical stress and eventually, results in inactivity (50). We hypothesize that these factors interact in a vicious cycle: muscle atrophy reduces physical activity, promoting fatty muscle infiltration, thereby further reinforcing inactivity. In addition, muscle communicates with bone through various endocrinologic pathways influencing bone turnover and, consequently, BMD (7, 51). In our study, regression models demonstrated that PDFF of the PSM and vertebral bone marrow were significantly elevated in VCF patients, independent of age, gender, and baseline BMD. Unfortunately, no data on physical activity is available, which limits our ability to fully explore its role in the observed findings. Including physical activity metrics in future studies could provide valuable insights into the interplay between muscle function and fracture risk.

To the best of our knowledge, a decrease in T2* in skeletal muscle has not yet been described in patients with VCF or osteoporosis. T2* values are influenced by factors such as metabolic state, blood volume, ischemia, and physical activity (52–55). A T2* decrease reflects magnetic field inhomogeneity. In older adults muscle tissue accumulates dense bodies containing iron and lipids, causing disturbance in the magnetic field (56). In the VCF group, increased fatty infiltration in the PSM may have contributed to greater magnetic field inhomogeneities, measurable as T2* decay.

No significant differences were found in BMD and vertebral bone marrow T2* values between the VCF and non-VCF groups, which reflects the fact that both parameters are primarily surrogates for the calcified trabecular bone components. These measures may not necessarily detect subtle changes indicative of bone health deterioration, ultimately leading to VCFs. As PDFF of both vertebral bone marrow and muscle successfully differentiated between the two groups in our study, these parameters may

represent more reliable predictors of bone pathologies. On a microscopic level, bone consists of bone trabeculae and bone marrow. These two tissue types create inhomogeneities in the magnetic field, which also result in the shortening of the effective transverse relaxation time, detectable through T2* measurements (57, 58). T2* of vertebral bone marrow has been shown to negatively correlate with BMD. This suggests that a reduction in bone trabeculae increases magnetic field homogeneity within the vertebral bodies, resulting in longer T2* times (59). This correlation has been confirmed at the microstructural level using T2* mapping, where higher T2* values were associated with reduced trabecular density and increased trabecular spacing, indicating greater bone fragility (32).

An important limitation of this study is the small sample size of patients with VCFs. Hence, certain statistically significant differences may not have been detected. Another limitation of this study is the low resolution of the PDFF and T2* maps, which was necessary in order to cover a large field of view in both groups. Notably, T2* mapping within skeletal muscle might be more accurately estimated with higher spatial resolution. The low resolution employed in this study may account for the observed T2* decay in PSM among VCF patients as PDFF increases, potentially due to increased averaging of field inhomogeneity effects. The segmentations of the maps were time consuming, however the assessment of PSM through automated segmentations could be facilitated in the future by using automatic deep learning techniques (60, 61). Additionally, a longer follow-up period may reveal more pronounced changes in e.g. CSA or age, providing further insight into their role in VCF development and potentially revealing their predictive value. Lastly, PDFF changes may have emerged as a consequence of factors such as pain-related muscle inactivity and fat atrophy following a fracture, limiting their predictive validity.

In conclusion, the PDFF of the PSM increased over a 6 month period in patients with VCFs. This change was also detected within the vertebral bone marrow, which is consistent with previous studies. ROC modeling revealed an excellent discrimination between VCF development when choosing a cutoff value of 0.23% for the change in PDFF PSM. Our findings suggest that the longitudinal assessment of PDFF of the PSM and vertebral bone marrow may serve as useful indicator for musculoskeletal health and may enable the prediction of incidental vertebral compression fractures.

Data availability statement

The raw data supporting the conclusions of this article will be made available by the authors, without undue reservation.

Ethics statement

The studies involving humans were approved by the Ethics Commission of the Medical Faculty, Technical University of Munich, Germany (Ethics proposal number 2022-433-S-SR). The studies were conducted in accordance with the local legislation and institutional requirements. The participants provided their written informed consent to participate in this study.

Author contributions

YS: Data curation, Formal Analysis, Investigation, Methodology, Resources, Validation, Visualization, Writing – original draft, Writing – review & editing. YL: Conceptualization, Data curation, Investigation, Methodology, Project administration, Writing – review & editing. JK: Data curation, Investigation, Writing – review & editing. FG: Data curation, Investigation, Validation, Writing – review & editing. MM: Funding acquisition, Resources, Writing – review & editing. JSK: Methodology, Validation, Writing – review & editing. GF: Data curation, Investigation, Writing – review & editing. PB: Visualization, Writing – review & editing. BS: Validation, Writing – review & editing. DK: Methodology, Resources, Validation, Writing – review & editing. NH: Investigation, Supervision, Writing – original draft, Writing – review & editing. AG: Conceptualization, Funding acquisition, Methodology, Project administration, Resources, Supervision, Writing – original draft, Writing – review & editing.

Funding

The author(s) declare that financial support was received for the research, authorship, and/or publication of this article. This work was supported by the German Society of Musculoskeletal Radiology.

Conflict of interest

The authors declare that the research was conducted in the absence of any commercial or financial relationships that could be construed as a potential conflict of interest.

Generative AI statement

The author(s) declare that no Generative AI was used in the creation of this manuscript.

Publisher's note

References

1. Lippuner K, Grifone S, Schwenkglenks M, Schwab P, Popp AW, Senn C, et al. Comparative trends in hospitalizations for osteoporotic fractures and other frequent diseases between 2000 and 2008. *Osteoporos Int*. (2012) 23:829–39. doi: 10.1007/s00198-011-1660-8

2. Hadji P, Hardtstock F, Wilke T, Joeres L, Toth E, Möckel L, et al. Estimated epidemiology of osteoporosis diagnoses and osteoporosis-related high fracture risk in Germany: a German claims data analysis. *Arch Osteoporos*. (2020) 15:127. doi: 10.1007/s11657-020-00800-w

3. Heyde CE, Roth A, Putzier M. Osteoporotic vertebral body fractures. *Orthopadie (Heidelb)*. (2023) 52:808–17. doi: 10.1007/s00132-023-04433-y

4. Borgström F, Karlsson L, Ortsäter G, Norton N, Halbout P, Cooper C, et al. Fragility fractures in Europe: burden, management and opportunities. *Arch Osteoporos*. (2020) 15:59. doi: 10.1007/s11657-020-0706-y

5. Hernlund E, Svedbom A, Ivergård M, Compston J, Cooper C, Stenmark J, et al. Osteoporosis in the European Union: medical management, epidemiology and economic burden. A report prepared in collaboration with the International Osteoporosis Foundation (IOF) and the European Federation of Pharmaceutical Industry Associations (EFPIA). *Arch Osteoporos*. (2013) 8:136. doi: 10.1007/s11657-013-0136-1

6. Group TEPOS, O'Neill T. The relationship between bone density and incident vertebral fracture in men and women*. *J Bone Mineral Res*. (2009) 17:2214–21. doi: 10.1359/jbmr.2002.17.12.2214

7. Gielen E, Dupont J, Dejaeger M, Laurent MR. Sarcopenia, osteoporosis and frailty. *Metabolism*. (2023) 145:155638. doi: 10.1016/j.metabol.2023.155638

8. Alajlouni D, Tran T, Bliuc D, Blank RD, Cawthon PM, Orwoll ES, et al. Muscle strength and physical performance improve fracture risk prediction beyond garvan and FRAX: the osteoporotic fractures in men (MrOS) study. *J Bone Miner Res*. (2022) 37:411–9. doi: 10.1002/jbmr.4483

9. Alajlouni D, Bliuc D, Tran T, Eisman JA, Nguyen TV, Center JR. Decline in muscle strength and performance predicts fracture risk in elderly women and men. *J Clin Endocrinol Metab*. (2020) 105:411–419. doi: 10.1210/clinem/dgaa414

10. Sonnenfeld MM, Pimentel FL, Nasser EJ, Pompei LM, Fernandes CE, Steiner ML. Performance of the fracture risk assessment tool associated with muscle mass measurements and handgrip to screen for the risk of osteoporosis in young postmenopausal women. *Rev Bras Ginecol Obstet*. (2022) 44:32–9. doi: 10.1055/s-0041-1741408

11. Vendrami C, Shevroja E, Gonzalez Rodriguez E, Gatineau G, Elmers J, Reginster JY, et al. Muscle parameters in fragility fracture risk prediction in older adults: A scoping review. *J Cachexia Sarcopenia Muscle*. (2024) 15:477–500. doi: 10.1002/jcsm.13418

12. Karampinos DC, Ruschke S, Dieckmeyer M, Diefenbach M, Franz D, Gersing AS, et al. Quantitative MRI and spectroscopy of bone marrow. *J Magn Reson Imaging*. (2018) 47:332–53. doi: 10.1002/jmri.25769

13. Fazeli PK, Horowitz MC, MacDougald OA, Scheller EL, Rodeheffer MS, Rosen CJ, et al. Marrow fat and bone–new perspectives. *J Clin Endocrinol Metab*. (2013) 98:935–45. doi: 10.1210/jc.2012-3634

14. Rosen CJ, Bouxsein ML. Mechanisms of disease: is osteoporosis the obesity of bone? *Nat Clin Pract Rheumatol*. (2006) 2:35–43. doi: 10.1038/ncprheum0070

15. Zhao LJ, Jiang H, Papasian CJ, Maulik D, Drees B, Hamilton J, et al. Correlation of obesity and osteoporosis: effect of fat mass on the determination of osteoporosis. *J Bone Miner Res*. (2008) 23:17–29. doi: 10.1359/jbmr.070813

16. Reeder SB, Hu HH, Sirlin CB. Proton density fat-fraction: a standardized MR-based biomarker of tissue fat concentration. *J Magn Reson Imaging*. (2012) 36:1011–4. doi: 10.1002/jmri.23741

17. Orcel T, Chau HT, Turlin B, Chaigneau J, Bannier E, Otal P, et al. Evaluation of proton density fat fraction (PDFF) obtained from a vendor-neutral MRI sequence and MRQuantif software. *Eur Radiol*. (2023) 33:8999–9009. doi: 10.1007/s00330-023-09798-4

18. Li GW, Xu Z, Chen QW, Tian YN, Wang XY, Zhou L, et al. Quantitative evaluation of vertebral marrow adipose tissue in postmenopausal female using MRI chemical shift-based water-fat separation. *Clin Radiol*. (2014) 69:254–62. doi: 10.1016/j.crad.2013.10.005

19. Kühn JP, Hernando D, Meffert PJ, Reeder S, Hosten N, Laqua R, et al. Proton-density fat fraction and simultaneous R2* estimation as an MRI tool for assessment of osteoporosis. *Eur Radiol*. (2013) 23:3432–9. doi: 10.1007/s00330-013-2950-7

20. Justesen J, Stenderup K, Ebbesen EN, Mosekilde L, Steiniche T, Kassem M. Adipocyte tissue volume in bone marrow is increased with aging and in patients with osteoporosis. *Biogerontology*. (2001) 2:165–71. doi: 10.1023/A:1011513223894

21. Schwartz AV. Marrow fat and bone: review of clinical findings. *Front Endocrinol (Lausanne)*. (2015) 6:40. doi: 10.3389/fendo.2015.00040

22. Kiefer LS, Fabian J, Lorbeer R, Machann J, Storz C, Kraus MS, et al. Inter- and intra-observer variability of an anatomical landmark-based, manual segmentation method by MRI for the assessment of skeletal muscle fat content and area in subjects from the general population. *Br J Radiol*. (2018) 91:20180019. doi: 10.1259/bjr.20180019

23. Hu HH, Kan HE. Quantitative proton MR techniques for measuring fat. *NMR Biomed*. (2013) 26:1609–29. doi: 10.1002/nbm.v26.12

24. Kim HJ, Cho HJ, Kim B, You MW, Lee JH, Huh J, et al. Accuracy and precision of proton density fat fraction measurement across field strengths and scan intervals: A phantom and human study. *J Magn Reson Imaging*. (2019) 50:305–14. doi: 10.1002/jmri.26575

25. Leonhardt Y, Ketschau J, Ruschke S, Gassert FT, Glanz L, Feuerriegel GC, et al. Associations of incidental vertebral fractures and longitudinal changes of MR–based proton density fat fraction and T2* measurements of vertebral bone marrow. *Front Endocrinol*. (2022) 13. doi: 10.3389/fendo.2022.1046547

26. Gassert FG, Kranz J, Gassert FT, Schwaiger BJ, Bogner C, Makowski MR, et al. Longitudinal MR-based proton-density fat fraction (PDFF) and T2* for the assessment of associations between bone marrow changes and myelotoxic chemotherapy. *Eur Radiol*. (2023) 34(4)2437–2444. doi: 10.1007/s00330-023-10189-y

27. Harada S, Gersing AS, Stohldreier Y, Dietrich O, Lechner A, Seissler J, et al. Associations of gestational diabetes and proton density fat fraction of vertebral bone marrow and paraspinal musculature in premenopausal women. *Front Endocrinol (Lausanne)*. (2023) 14:1303126. doi: 10.3389/fendo.2023.1303126

28. Patsch JM, Li X, Baum T, Yap SP, Karampinos DC, Schwartz AV, et al. Bone marrow fat composition as a novel imaging biomarker in postmenopausal women with prevalent fragility fractures. *J Bone Miner Res*. (2013) 28:1721–8. doi: 10.1002/jbmr.1950

29. Gassert FT, Glanz L, Boehm C, Stelter J, Gassert FG, Leonhardt Y, et al. Associations between bone mineral density and longitudinal changes of vertebral bone marrow and paraspinal muscle composition assessed using MR-based proton density fat fraction and T2* Maps in patients with and without osteoporosis. *Diagnostics*. (2022) 12:2467. doi: 10.3390/diagnostics12102467

30. Beasley LE, Koster A, Newman AB, Javaid MK, Ferrucci L, Kritchevsky SB, et al. Inflammation and race and gender differences in computerized tomography-measured adipose depots. *Obes (Silver Spring)*. (2009) 17:1062–9. doi: 10.1038/oby.2008.627

31. chlaeger S, Inhuber S, Rohrmeier A, Dieckmeyer M, Freitag F, Klupp E, et al. Association of paraspinal muscle water-fat MRI-based measurements with isometric strength measurements. *Eur Radiol*. (2019) 29:599–608. doi: 10.1007/s00330-018-5631-8

32. Leonhardt Y, Gassert FT, Feuerriegel G, Gassert FG, Kronthaler S, Boehm C, et al. Vertebral bone marrow T2* mapping using chemical shift encoding-based water-fat separation in the quantitative analysis of lumbar osteoporosis and osteoporotic fractures. *Quant Imaging Med Surg*. (2021) 11:3715–25. doi: 10.21037/qims-20-1373

33. Löffler MT, Sollmann N, Mei K, Valentinitsch A, Noël PB, Kirschke JS, et al. X-ray-based quantitative osteoporosis imaging at the spine. *Osteoporos Int*. (2020) 31:233–50. doi: 10.1007/s00198-019-05212-2

34. Leonhardt Y, May P, Gordijenko O, Koeppen-Ursic VA, Brandhorst H, Zimmer C, et al. Opportunistic QCT bone mineral density measurements predicting osteoporotic fractures: A use case in a prospective clinical cohort. *Front Endocrinol (Lausanne)*. (2020) 11:586352. doi: 10.3389/fendo.2020.586352

35. Karampinos DC, Yu H, Shimakawa A, Link TM, Majumdar S. T_1-corrected fat quantification using chemical shift-based water/fat separation: application to skeletal muscle. *Magn Reson Med*. (2011) 66:1312–26. doi: 10.1002/mrm.22925

36. Yu H, McKenzie CA, Shimakawa A, Vu AT, Brau AC, Beatty PJ, et al. Multiecho reconstruction for simultaneous water-fat decomposition and T2* estimation. *J Magn Reson Imaging*. (2007) 26:1153–61. doi: 10.1002/jmri.21090

37. Eggers H, Brendel B, Duijndam A, Herigault G. Dual-echo Dixon imaging with flexible choice of echo times. *Magn Reson Med*. (2011) 65:96–107. doi: 10.1002/mrm.22578

38. Grigoryan M, Guermazi A, Roemer FW, Delmas PD, Genant HK. Recognizing and reporting osteoporotic vertebral fractures. *Eur Spine J*. (2003) 12 Suppl 2:S104–12. doi: 10.1007/s00586-003-0613-0

39. Löffler MT, Jacob A, Valentinitsch A, Rienmüller A, Zimmer C, Ryang YM, et al. Improved prediction of incident vertebral fractures using opportunistic QCT compared to DXA. *Eur Radiol*. (2019) 29:4980–9. doi: 10.1007/s00330-019-06018-w

40. The American College of Radiology. ACR–SPR–SSR Practice Parameter for the Performance of Quantitative Computed Tomography (QCT) Bone Mineral Density (2023). Available online at: https://www.acr.org/-/media/ACR/Files/Practice-Parameters/qct.pdf (Accesed May 17, 2024).

41. Teichtahl AJ, Urquhart DM, Wang Y, Wluka AE, Wijethilake P, O'Sullivan R, et al. Fat infiltration of paraspinal muscles is associated with low back pain, disability, and structural abnormalities in community-based adults. *Spine J*. (2015) 15:1593–601. doi: 10.1016/j.spinee.2015.03.039

42. Zhao Y, Huang M, Serrano Sosa M, Cattell R, Fan W, Li M, et al. Fatty infiltration of paraspinal muscles is associated with bone mineral density of the lumbar spine. *Arch Osteoporos*. (2019) 14:99. doi: 10.1007/s11657-019-0639-5

43. Gassert FT, Kufner A, Gassert FG, Leonhardt Y, Kronthaler S, Schwaiger BJ, et al. MR-based proton density fat fraction (PDFF) of the vertebral bone marrow

differentiates between patients with and without osteoporotic vertebral fractures. *Osteoporos Int*. (2022) 33:487–96. doi: 10.1007/s00198-021-06147-3

44. Sollmann N, Dieckmeyer M, Schlaeger S, Rohrmeier A, Syvaeri J, Diefenbach MN, et al. Associations between lumbar vertebral bone marrow and paraspinal muscle fat compositions-an investigation by chemical shift encoding-based water-fat MRI. *Front Endocrinol (Lausanne)*. (2018) 9:563. doi: 10.3389/fendo.2018.00563

45. Zhu L, Xu Z, Li G, Wang Y, Li X, Shi X, et al. Marrow adiposity as an indicator for insulin resistance in postmenopausal women with newly diagnosed type 2 diabetes - an investigation by chemical shift-encoded water-fat MRI. *Eur J Radiol*. (2019) 113:158–64. doi: 10.1016/j.ejrad.2019.02.020

46. Vestergaard P. Discrepancies in bone mineral density and fracture risk in patients with type 1 and type 2 diabetes–a meta-analysis. *Osteoporos Int*. (2007) 18:427–44. doi: 10.1007/s00198-006-0253-4

47. Palermo A, D'Onofrio L, Buzzetti R, Manfrini S, Napoli N. Pathophysiology of bone fragility in patients with diabetes. *Calcif Tissue Int*. (2017) 100:122–32. doi: 10.1007/s00223-016-0226-3

48. Peng H, Hu B, Xie LQ, Su T, Li CJ, Liu Y, et al. A mechanosensitive lipolytic factor in the bone marrow promotes osteogenesis and lymphopoiesis. *Cell Metab*. (2022) 34:1168–82.e6. doi: 10.1016/j.cmet.2022.05.009

49. Atherton PJ, Greenhaff PL, Phillips SM, Bodine SC, Adams CM, Lang CH. Control of skeletal muscle atrophy in response to disuse: clinical/preclinical contentions and fallacies of evidence. *Am J Physiol Endocrinol Metab*. (2016) 311:E594–604. doi: 10.1152/ajpendo.00257.2016

50. Jiang XY, Tang ZY, Liu BW, Lu SY, Pan DG, Jiang H, et al. Enhancing fracture risk indication: The impact of bone load index and muscle fat infiltration on vertebral compression fracture. *Exp Gerontol*. (2025) 199:112654. doi: 10.1016/j.exger.2024.112654

51. Kirk B, Feehan J, Lombardi G, Duque G. Muscle, bone, and fat crosstalk: the biological role of myokines, osteokines, and adipokines. *Curr Osteoporos Rep*. (2020) 18:388–400. doi: 10.1007/s11914-020-00599-y

52. Varghese J, Scandling D, Joshi R, Aneja A, Craft J, Raman SV, et al. Rapid assessment of quantitative T1, T2 and T2* in lower extremity muscles in response to maximal treadmill exercise. *NMR Biomed*. (2015) 28:998–1008. doi: 10.1002/nbm.v28.8

53. Jacobi B, Bongartz G, Partovi S, Schulte AC, Aschwanden M, Lumsden AB, et al. Skeletal muscle BOLD MRI: from underlying physiological concepts to its usefulness in clinical conditions. *J Magn Reson Imaging*. (2012) 35:1253–65. doi: 10.1002/jmri.23536

54. Vandenborne K, Walter G, Ploutz-Snyder L, Dudley G, Elliott MA, De Meirleir K. Relationship between muscle T2* relaxation properties and metabolic state: a combined localized 31P-spectroscopy and 1H-imaging study. *Eur J Appl Physiol*. (2000) 82:76–82. doi: 10.1007/s004210050654

55. Meyer RA, Towse TF, Reid RW, Jayaraman RC, Wiseman RW, McCully KK. BOLD MRI mapping of transient hyperemia in skeletal muscle after single contractions. *NMR Biomed*. (2004) 17:392–8. doi: 10.1002/nbm.v17:6

56. Schwenzer NF, Martirosian P, Machann J, Schraml C, Steidle G, Claussen CD, et al. Aging effects on human calf muscle properties assessed by MRI at 3 Tesla. *J Magn Reson Imaging*. (2009) 29:1346–54. doi: 10.1002/jmri.21789

57. Chavhan GB, Babyn PS, Thomas B, Shroff MM, Haacke EM. Principles, techniques, and applications of T2*-based MR imaging and its special applications. *Radiographics*. (2009) 29:1433–49. doi: 10.1148/rg.295095034

58. Karampinos DC, Ruschke S, Dieckmeyer M, Eggers H, Kooijman H, Rummeny EJ, et al. Modeling of T2* decay in vertebral bone marrow fat quantification. *NMR Biomed*. (2015) 28:1535–42. doi: 10.1002/nbm.v28.11

59. Wu HZ, Zhang XF, Han SM, Cao L, Wen JX, Wu WJ, et al. Correlation of bone mineral density with MRI T2* values in quantitative analysis of lumbar osteoporosis. *Arch Osteoporos*. (2020) 15:18. doi: 10.1007/s11657-020-0682-2

60. Agosti A, Shaqiri E, Paoletti M, Solazzo F, Bergsland N, Colelli G, et al. Deep learning for automatic segmentation of thigh and leg muscles. *Magma*. (2022) 35:467–83. doi: 10.1007/s10334-021-00967-4

61. Kreher R, Hinnerichs M, Preim B, Saalfeld S, Surov A. Deep-learning-based segmentation of skeletal muscle mass in routine abdominal CT scans. *In Vivo*. (2022) 36:1807–11. doi: 10.21873/invivo.12896

frontiers | Frontiers in Endocrinology

TYPE Review
PUBLISHED 04 March 2025
DOI 10.3389/fendo.2025.1538460

OPEN ACCESS

EDITED BY
Nico Sollmann,
Ulm University Medical Center, Germany

REVIEWED BY
Karupppasamy Subburaj,
Aarhus University, Denmark
Daniel Strack,
Aarhus University, Denmark

*CORRESPONDENCE
Yunhua Luo
Yunhua.Luo@umanitoba.ca

RECEIVED 02 December 2024
ACCEPTED 27 January 2025
PUBLISHED 04 March 2025

CITATION
Luo Y (2025) Biomechanical perspectives on image-based hip fracture risk assessment: advances and challenges.
Front. Endocrinol. 16:1538460.
doi: 10.3389/fendo.2025.1538460

Biomechanical perspectives on image-based hip fracture risk assessment: advances and challenges

Yunhua Luo[1,2]*

[1]Department of Mechanical Engineering, University of Manitoba, Winnipeg, MB, Canada, [2]Department of Biomedical Engineering (Graduate Program), University of Manitoba, Winnipeg, MB, Canada

Hip fractures pose a significant health challenge, particularly in aging populations, leading to substantial morbidity and economic burden. Most hip fractures result from a combination of osteoporosis and falls. Accurate assessment of hip fracture risk is essential for identifying high-risk individuals and implementing effective preventive strategies. Current clinical tools, such as the Fracture Risk Assessment Tool (FRAX), primarily rely on statistical models of clinical risk factors derived from large population studies. However, these tools often lack specificity in capturing the individual biomechanical factors that directly influence fracture susceptibility. Consequently, image-based biomechanical approaches, primarily leveraging dual-energy X-ray absorptiometry (DXA) and quantitative computed tomography (QCT), have garnered attention for their potential to provide a more precise evaluation of bone strength and the impact forces involved in falls, thereby enhancing risk prediction accuracy. Biomechanical approaches rely on two fundamental components: assessing bone strength and predicting fall-induced impact forces. While significant advancements have been made in image-based finite element (FE) modeling for bone strength analysis and dynamic simulations of fall-induced impact forces, substantial challenges remain. In this review, we examine recent progress in these areas and highlight the key challenges that must be addressed to advance the field and improve fracture risk prediction.

KEYWORDS

hip fracture, risk assessment, DXA, QCT, bone strength, fall-induced impact force

1 Introduction

Hip fractures are a significant health concern, particularly among older adults, who often have a high prevalence of osteoporosis, contributing to substantial morbidity, mortality, and healthcare costs worldwide (1–3). In 2019, there were 178 million new fractures globally, marking a 33.4% increase since 1990, partly driven by population aging (2, 3). Hip fractures constituted a significant proportion of these cases. Projections indicate that the number of hip fractures will nearly double by 2050, underscoring the urgency for

effective fracture risk assessment to identify high-risk individuals and implement preventive measures (4, 5). Accurate assessment of hip fracture risk is crucial, as it enables targeted interventions and support, thereby reducing the burden of these fractures (6).

The current clinical approach for diagnosing hip fracture risk and treating pre-fracture conditions relies primarily on risk factors such as bone mineral density (BMD) and population-based statistical models (7). Although low BMD is widely regarded as a key biomarker for bone fractures, this approach has significant limitations. Studies indicate that approximately 50% of fractures occur in individuals with BMD values above the established threshold (8, 9). BMD also serves as the primary target for many treatment options, particularly those aimed at osteoporosis (10, 11). FRAX is one of the most widely used tools globally to estimate the 10-year probability of hip fractures and other major osteoporotic fractures (12–15). It incorporates several key risk factors, including age, gender, BMD at the femoral neck, prior fractures, parental history of hip fractures, smoking status, alcohol consumption, glucocorticoid use, and rheumatoid arthritis. The predictive accuracy of FRAX has been reported as moderate (16, 17), with area under the receiver operating characteristic (ROC) curve (AUC) values ranging from 0.70 to 0.75 for hip fracture prediction. The tool tends to underestimate fracture risk in certain populations, such as those with frequent falls or advanced age, where fall risk is not fully incorporated (14, 18, 19). The primary limitation of the current tools lies in their reliance on statistical modeling of risk factors. These tools predict fracture risk by identifying broad population-level trends and applying them to individual cases (20).

To improve the accuracy of hip fracture risk assessments, there is a pressing need to develop biomechanical models (21). Image-based biomechanical approaches are theoretically more reliable and accurate than statistical models derived from clinical risk factors because they directly assess the mechanical properties of bone and the forces contributing to fractures (22, 23). Unlike statistical models, which rely on population-level data and indirect associations, biomechanical approaches evaluate individual-specific factors such as bone strength, geometry, and microstructure. These methods utilize advanced imaging techniques, such as high-resolution CT and finite element (FE) modeling, to simulate the mechanical response of bones to applied forces, providing a direct measurement of fracture risk. Furthermore, image-based dynamic simulations can model fall-induced impact forces by analyzing body kinematics, fall trajectories, and surface interactions (24, 25). These simulations allow for a detailed assessment of the magnitude, direction, and distribution of impact forces during a fall (25), which are critical in determining fracture risk. By integrating subject-specific bone properties with dynamic fall scenarios (26), biomechanical approaches can provide a comprehensive and personalized evaluation of fracture risk, addressing limitations in clinical tools that overlook the interplay between bone strength and fall mechanics. This capability highlights their potential to significantly enhance fracture risk assessment and prevention strategies.

Substantial progress has been made in developing image-based biomechanical models for predicting hip fracture risk. However, significant challenges remain, which must be addressed before these biomechanical models can be integrated into clinical practice. This review extensively examines recent advancements and discusses the key challenges that need resolution. The layout of the remainder of this paper is as follows: Section 2 outlines the framework of image-based biomechanical approaches; Section 3 reviews the progress and challenges in image-based finite element modeling of bone strength; Section 4 explores the advancements and remaining obstacles in image-based dynamic simulation of falls; and Section 5 concludes the review with proposals for future research directions.

2 Image-based biomechanical approach to assess hip fracture risk

Based on engineering material mechanics, hip fracture is determined by two key variables (Figure 1): femoral strength and the force applied to the hip, both of which are subject-specific. Femoral strength refers to the maximum force the femur can withstand before fracturing and is primarily determined by the bone's material composition—such as inorganic minerals, organic proteins, and water—along with its macroscopic geometry and microstructural integrity. Since the majority of hip fractures result from falls (27–30), the impact force generated during a fall from standing height is considered in assessing hip fracture risk. This force is influenced by variables such as body height, body mass, and fall orientation and can vary significantly depending on the dynamics of the fall and the compliance properties of the impacted surface. When the fall-induced force exceeds femoral strength, a hip fracture occurs. Accurately determining femoral strength, fall-induced impact force, and their interplay is essential

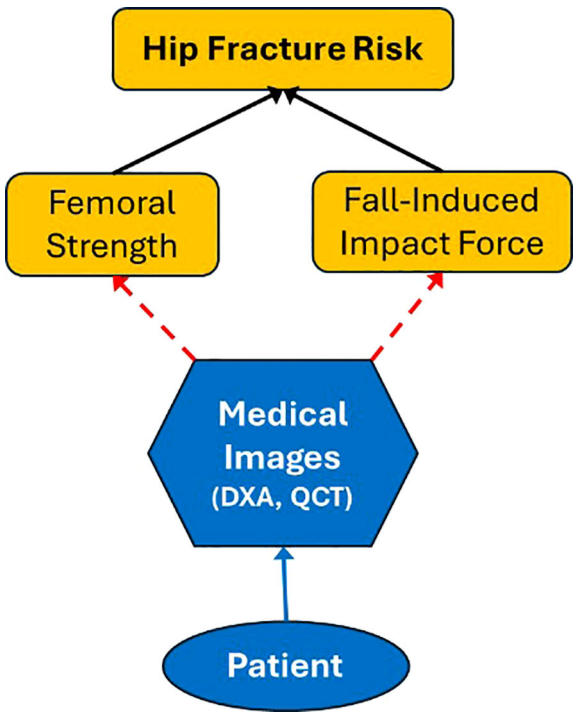

FIGURE 1
Image-based biomechanical approach to assess hip fracture risk.

for developing precise and predictive models of fracture risk, enabling more effective prevention and individualized treatment strategies.

Given the necessity for non-invasive approaches in assessing hip fracture risk, determining both femoral strength and fall-induced impact force must be conducted safely and without invasive procedures. Medical imaging offers an essential solution to this challenge, as illustrated in Figure 1. Advanced imaging technologies, such as dual-energy X-ray absorptiometry (DXA) and quantitative computed tomography (QCT), enable subject-specific assessment of bone structure, geometry, and tissue composition within the body. These imaging modalities provide critical data on bone mineral density, and material composition, which are essential for estimating femoral strength. Information about trabecular architecture can be partially inferred from QCT data, as it provides 3D volumetric imaging capable of analyzing parameters such as trabecular thickness, separation, and number. However, DXA, being a 2D imaging modality, lacks the resolution to capture detailed trabecular architecture. For more precise insights into individual trabecular microstructure, higher-resolution imaging modalities such as micro-CT or HR-pQCT are required, although these are typically limited to *in vitro* studies or extremities *in vivo*. Furthermore, imaging can capture patient-specific anatomical and kinetic properties, which can then be used in dynamic simulations to predict fall-induced impact forces. The integration of imaging data into biomechanical models ensures a personalized and accurate evaluation of fracture risk.

Significant advances have been made in the development of image-based finite element (FE) modeling for predicting femoral strength and dynamics simulations for analyzing fall-induced impact forces. While these advancements offer promising opportunities to assess subject-specific fracture risk more accurately, challenges and obstacles remain. The following sections provide a detailed review of these advancements, highlighting the progress achieved and the critical barriers that must be addressed to facilitate their integration into clinical practice.

3 Image-based finite element modeling of bone strength

To construct a finite element (FE) model of the femur for determining its strength, several key pieces of information are required. First, accurate geometry of the femur is essential, typically derived from high-resolution medical imaging modalities such as computed tomography (CT). These images provide detailed spatial data that allow for the reconstruction of the femur's shape and structural features, including cortical thickness, trabecular architecture, and overall bone dimensions. Second, the material properties of the bone must be specified, including the elastic modulus, yield strength, and density of both cortical and trabecular bone. These properties are often determined from CT-derived Hounsfield units, which can be mapped to bone density and subsequently used to estimate the material properties. Additionally, boundary conditions and loading scenarios must be defined to replicate physiological or fall-related forces acting on the femur, such as compressive loads during standing or oblique forces during a fall. Together, these inputs enable the FE model to simulate stress and strain distributions within the femur and predict its failure point under applied loads.

While DXA and QCT are the primary imaging modalities discussed in this paper due to their clinical relevance for biomechanical modeling, other advanced imaging technologies also hold promise. High-resolution peripheral QCT (HR-pQCT) offers detailed insights into bone microarchitecture but is limited to extremities due to its field of view. Dual-energy CT (DECT) enables improved material characterization by distinguishing between bone mineral density and other components, such as collagen and water. Magnetic resonance imaging (MRI) can provide complementary information on bone marrow composition and trabecular structure but lacks the spatial resolution necessary for finite element modeling of bone strength. Although these techniques have significant potential, their high cost, limited availability, and practical constraints currently limit their widespread application in hip fracture risk assessment.

Numerous finite element (FE) models have been developed for the femur, with most falling into two primary categories: those based on dual-energy X-ray absorptiometry (DXA) and those based on quantitative computed tomography (QCT).

3.1 DXA-based finite element models

DXA-based FE models are particularly attractive due to the merits of DXA over QCT, including lower cost, wider availability, and reduced radiation exposure. These models leverage two-dimensional (2D) DXA images to estimate femoral strength and fracture risk by incorporating simplified assumptions about bone geometry and material properties, as illustrated in Figure 2. First, a plane stress model (31) or engineering beam model (32) is adopted, representing the femur by projecting all the bone material along the DXA scanning direction, thereby reducing the complex 3D geometry of the femur to a simplified 2D model with uniform thickness. Second, the areal bone mineral density (aBMD) derived from DXA is correlated with key material properties (33), such as bone elasticity and yield stress, enabling the estimation of bone strength in the medial-lateral plane.

In DXA-based finite element analyses, material models primarily assume linear elastic behavior due to the simplicity and computational efficiency required for clinical applicability (36, 37). For instance, the Young's modulus is often estimated based on empirical relationships with areal bone mineral density (aBMD) (36, 37). Some studies incorporate piecewise linear models to account for yield points and post-yield behavior, though these are less common due to the limitations of 2D projections in capturing detailed material heterogeneity. Non-linear models, which consider failure criteria or plasticity, have been less frequently applied in DXA-based FE analyses due to the challenges in accurately representing complex bone material using 2D data (38). DXA-based finite element studies commonly employ simplified yet

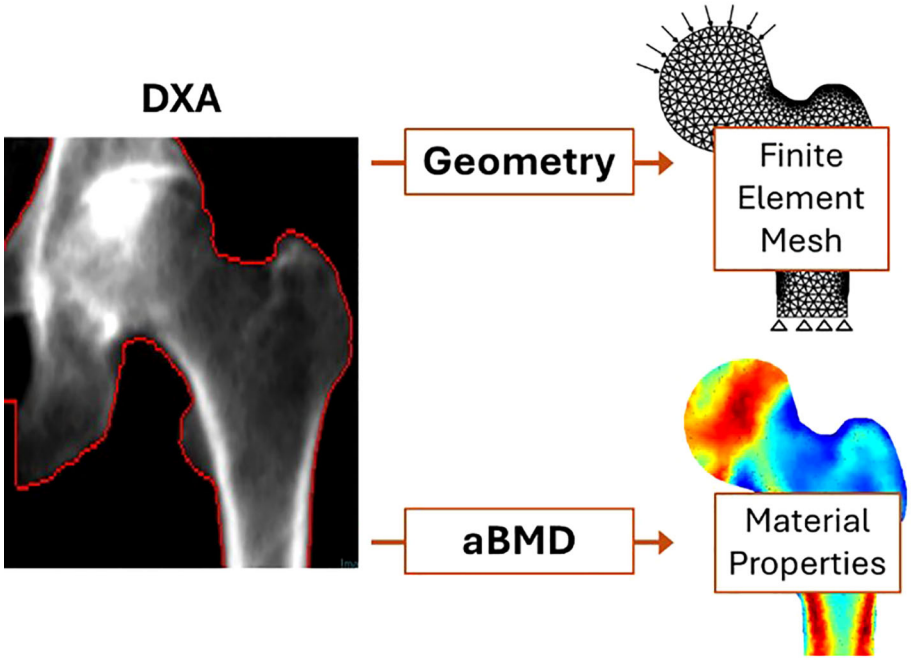

FIGURE 2
DXA-based finite element modeling of femoral strength [modified from (34, 35)].

clinically relevant loading and boundary conditions to simulate scenarios associated with hip fractures. The most frequently used loading scenario involves a sideways fall, which reflects the most common fall mechanism leading to hip fractures in older adults. In these simulations, the femoral head is typically subjected to oblique forces, representing the impact of the greater trochanter against the ground during a fall. These assumptions and correlations strike a practical balance between prediction accuracy and simplicity, positioning DXA-based FE models as a promising patient-specific tool for assessing hip fracture risk in clinical settings.

The development and improvement of DXA-based finite element models for hip fracture risk assessment have significantly advanced, driven by the need for more accurate and individualized predictions of bone strength and fracture risk. Early studies demonstrated the feasibility of integrating finite element analysis (FEA) with DXA imaging to estimate femoral strength (31, 34, 39). Luo et al. (35) investigated the precision of DXA-based finite element models, identifying body positioning during DXA scanning as a critical factor influencing model accuracy. Further advancements focused on automation and clinical applicability, as illustrated by Luo et al. (40) and Yang et al. (41), who developed fully automated DXA-based FEA tools that not only stratified fracture risk more effectively than femoral neck bone mineral density (BMD) but also streamlined workflows for routine clinical use. Validation efforts, such as those by Dall'Ara et al. (42), confirmed the accuracy of DXA-based FEA models against experimental data, reinforcing their reliability. Simplified 2D FEA models derived from DXA images were also validated against more complex 3D models by Terzini et al. (38), highlighting their practicality with reasonable predictive accuracy. These continuous improvements have established DXA-based FEA as a robust and clinically viable approach to addressing the limitations of traditional BMD-focused fracture risk assessments. DXA-based finite element models are increasingly being utilized for hip fracture risk assessment. Yang et al. (43) demonstrated the effectiveness of this approach in the Osteoporotic Fractures in Men (MrOS) study, where femoral strength estimates derived from FEA showed a strong association with incident fractures. Sarvi and Luo (44) investigated sex differences in hip fracture risk using biomechanical modeling and identified significant distinctions that traditional BMD measurements failed to capture. Additionally, Ferdous et al. (31) underscored the value of patient-specific FEA models in evaluating individualized fracture risk, further highlighting the adaptability and clinical potential of this technique. In addition to risk assessment, DXA-based FE models have been used to monitor the effectiveness of osteoporosis treatments. Mochizuki et al. (45) employed DXA-based hip structural analysis to evaluate changes in bone strength during teriparatide treatment, demonstrating significant improvements in femoral strength over 24 months.

Despite their advantages, DXA-based FE models have several limitations. DXA only provides 2D projections of the femur, which limits the model's ability to capture the 3D geometry and microstructural details essential for accurate stress and strain predictions. DXA-based FE models often rely on oversimplified assumptions about the relationship between aBMD and bone material properties. These assumptions may overlook variations in the spatial distribution of bone mass, including differences in cortical and cancellous component densities, which are critical for capturing the anisotropic nature of femoral strength. Additionally, the 2D nature of DXA imaging restricts its capacity to evaluate trabecular architecture and cortical porosity, both of which are

essential determinants of bone strength and fracture risk. Anatomical geometry reconstruction from DXA images models the entire femur as a single entity (46, 47), assigning subject-specific material properties based on areal bone mineral density (aBMD) values derived from DXA images. This method simplifies the geometry and computational requirements but inherently lacks the ability to distinguish between cortical and trabecular compartments, which are critical for accurately capturing the heterogeneity of bone properties. DXA-based FE models often use simplified loading scenarios to estimate femoral strength, which may not accurately represent the complex, multidirectional forces experienced during real-world falls. DXA-based FE models primarily reflect changes in BMD, making them less sensitive to other critical factors, such as improvements in bone collagen quality and the integrity of collagen crosslinks (48, 49), which play a significant role in bone strength and may result from osteoporosis treatments. Variations in DXA scanner calibration and software algorithms (50) can introduce inconsistencies in BMD measurements, affecting the reproducibility of FE model predictions.

3.2 QCT-based finite element models

QCT-based finite element models are constructed from three-dimensional data acquired through quantitative computed tomography (QCT). While the process of creating QCT-based finite element models shares similarities with that of DXA-based models, as illustrated in Figure 3, the key differences lie in the three-dimensional representation of femur geometry and the use of volumetric bone mineral density (vBMD) instead of areal BMD (51). The process begins with acquiring high-resolution QCT images of the femur. These datasets are segmented to differentiate bone tissue from surrounding structures, enabling the extraction of cortical and trabecular bone regions (52). The image data are then converted into 3D finite element meshes, typically composed of tetrahedral or hexahedral elements, to accurately approximate the femoral geometry (53). Tetrahedral elements are more versatile in conforming to complex geometries, making them suitable for irregular structures like the femur. In contrast, hexahedral elements offer higher accuracy and computational efficiency for simpler, structured geometries but are less adaptable to irregular shapes. The choice between the two depends on the trade-off between geometric fidelity and computational efficiency in the modeling process. Bone densities are obtained from QCT image intensities through calibration with phantoms, which provide reference values for converting Hounsfield units into equivalent bone density measures. Material properties are assigned based on the density values using empirical relationships that link density to Young's modulus and other mechanical parameters (51, 54). Boundary and loading conditions are applied to simulate physiological or traumatic scenarios, such as normal gait or sideways falls (52). Finally, these models are solved using numerical methods to estimate stress, strain, and overall femoral strength (53). Overall femoral strength is typically defined as the maximum load the femur can withstand before failure, as determined by the finite element simulation. This definition depends on the material model used; for linear elastic models, it is based on yield stress, while for non-linear models, it may incorporate ultimate stress or fracture criteria. The choice of strength definition varies depending on the specific study objectives and modeling assumptions.

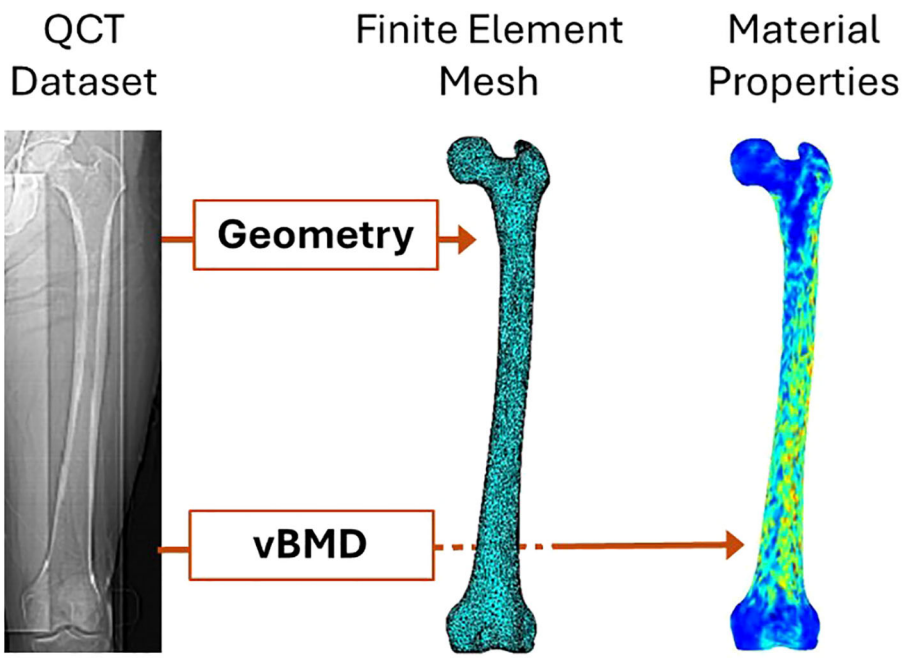

FIGURE 3
QCT-based finite element modeling of femoral strength [modified from (55)].

QCT-based finite element models have emerged as a robust tool for studying femoral strength and hip fracture risk. By integrating 3D imaging with advanced computational modeling, these models provide detailed insights into the mechanical behavior of the femur under different loading conditions. Below, we review key research applications of QCT-based FE models in this domain. QCT-based FE models have been widely used to evaluate the structural integrity of the femur under simulated loading conditions. Dragomir-Daescu et al. (56) developed robust models to predict femoral stiffness and fracture load during a sideways fall, demonstrating strong correlations with *in vitro* experimental data. Mirzaei et al. (57) applied QCT-based FE analysis to analyze strength and failure patterns in the human proximal femur, revealing critical mechanical insights that aid in fracture prediction. Dall'Ara et al. (58) validated nonlinear QCT-based FE models using *in vitro* human femur, showing their reliability across multiple experimental configurations. These studies highlight the utility of QCT-based FE models in quantifying femoral strength and identifying high-risk individuals.

QCT-based FE modeling has also been employed to study variations in femoral strength across different populations. Shen et al. (59) investigated the relationship between body mass index (BMI) and QCT-derived hip strength in older men, providing biomechanical explanations for the effects of BMI on fracture risk. Black et al. (60) conducted a large prospective study to assess the relationship between proximal femoral structure, as derived from QCT, and hip fracture risk in men, establishing the clinical relevance of QCT-based measurements. Faisal and Luo (55) examined differences in fracture risk between left and right femora using QCT-based FE models, identifying asymmetries that may inform individualized treatment strategies. Several studies have focused on evaluating hip fracture risk under specific mechanical or pathological conditions using QCT-based FE models. For example, Kheirollahi and Luo (61) used cross-sectional strain energy derived from QCT-based FE models to assess hip fracture risk, demonstrating the sensitivity of this method to variations in bone density and geometry. Carpenter et al. (62) emphasized the importance of fall orientation on femoral neck strength, showing that certain fall directions substantially increase fracture risk. Such studies underline the versatility of QCT-based FE models in replicating realistic fracture scenarios.

Traditional metrics for monitoring treatment effects typically include changes in areal bone mineral density (aBMD) as measured by DXA. Treatments such as bisphosphonates or anabolic agents like teriparatide are commonly assessed using these metrics. These methods focus on improving bone density and strength over time, offering a baseline for evaluating therapeutic outcomes. QCT-based FE models are employed to examine the contributions of cortical and trabecular compartments to overall femoral strength. Christiansen et al. (63) used these models to explore age-related changes in bone strength, showing how the cortical and trabecular components contribute differently to mechanical stability in men and women. These findings have enhanced the understanding of how age and sex influence fracture risk. QCT-based FE models have been applied to evaluate the impact of osteoporosis treatments and other clinical conditions on femoral strength. Engelke et al. (64) used these models to monitor regional changes in bone mineral density after ibandronate treatment, demonstrating how such treatments improve hip strength. Similarly, Black et al. (60) showed how QCT-based parameters could predict treatment outcomes more effectively than traditional metrics, emphasizing the potential of these models in clinical decision-making.

QCT-based finite element models provide a more detailed and robust approach than DXA-based models for assessing femoral strength and hip fracture risk. QCT offers greater detail compared to DXA by providing 3D volumetric imaging, allowing separate analysis of cortical and trabecular compartments. Additionally, QCT measures volumetric bone mineral density (vBMD), which is not influenced by bone size or projection errors, and enables assessment of bone geometry, microarchitecture, and material properties with higher spatial resolution. However, QCT-based models are not without limitations. A major challenge lies in the high radiation dose associated with QCT imaging, which restricts its routine clinical use, especially for longitudinal studies (65). Additionally, constructing and solving QCT-based finite element models require advanced computational resources and expertise, which can be a barrier to widespread adoption in clinical practice (56). Variability in imaging protocols and finite element modeling assumptions, such as mesh density and material property assignment, can introduce inconsistencies and limit reproducibility across studies (58, 63). Furthermore, the use of density-based material property assignment often oversimplifies bone's heterogeneous and anisotropic mechanical behavior, potentially reducing the accuracy of predictions (57). Finally, these models generally do not account for dynamic biological processes, such as bone remodeling or microdamage accumulation, which are critical for understanding changes in bone strength over time (61). Addressing these limitations through advancements in imaging, modeling, and computational techniques is essential to enhance the clinical utility of QCT-based finite element models.

3.3 Challenges in image-based finite element modeling of femoral strength

Finite element modeling of femoral strength based on medical imaging, such as QCT or DXA, has advanced significantly in recent years, offering valuable insights into bone mechanics and fracture risk. However, despite these advancements, and alongside the limitations discussed in the previous subsections, several critical challenges persist, hindering the accuracy, reliability, and clinical utility of these models. One major issue lies in the challenge of accurately characterizing bone material properties, such as Young's modulus, yield stress, and toughness, from medical images. Another significant challenge is capturing the anisotropic behavior of femoral strength, which varies with loading orientation and is influenced by the direction of impact forces during a fall. Bone anisotropy has been studied in vertebral bones (66), where transverse isotropy is modeled by scaling Young's modulus according to directional properties. Application of a similar approach to the femur requires experimentally derived scaling

factors. Addressing these complexities requires advancements in imaging technologies, image-based material characterization algorithms, and modeling techniques, as these elements are pivotal for enhancing the predictive accuracy and reliability of image-based finite element models.

3.3.1 Image-based characterization of bone material properties

Accurately characterizing bone material properties, such as Young's modulus, yield stress, and toughness, from DXA or QCT images remains a significant challenge due to the composite nature of bone. Bone is a hierarchical material composed of inorganic minerals (primarily hydroxyapatite), organic proteins (mostly collagen), and water. Each of these components contributes distinct mechanical properties to bone, and their interplay determines the overall strength and toughness of the tissue. However, medical imaging modalities like DXA and QCT are limited in their ability to quantify or assess the quality of these individual components, which hinders precise material characterization.

DXA and QCT provide information about bone density, which is a proxy for the amount of mineral content in bone. However, this metric alone does not capture variations in the organic matrix or water content, both of which critically influence mechanical properties. Studies have shown that the organic matrix, particularly collagen cross-linking, plays a pivotal role in bone toughness and resistance to fracture (67–69). Similarly, bound and free water in bone contribute to its viscoelastic and fatigue-resistant properties (70). Limited by their working principles, both DXA and QCT can measure only mineral density, while the characterization of organic proteins and water remains challenging with these imaging modalities. As a result, the contributions of organic proteins and water to bone strength, particularly toughness, are not accounted for in DXA- and QCT-based models (71, 72). Further complicating the issue is the heterogeneity of bone mineralization. The degree of mineralization varies across individuals and regions within the bone, affecting stiffness and brittleness. QCT-based finite element models often rely on empirical density-elasticity relationships derived from bone properties, which may not account for inter-individual variability in the inorganic-organic composition or regional differences within the same bone (54, 73). This limitation undermines the ability to predict mechanical properties accurately under diverse physiological or pathological conditions.

Another critical challenge lies in accurately determining the stress-strain curves for the individual components of bone, particularly minerals and proteins, which are dependent on the sub-compositions and sub-microstructure in the components. These curves are fundamental for understanding bone behavior under impact forces but are highly subject-dependent, adding complexity to their precise characterization. For instance, the mechanical behavior of hydroxyapatite, the primary mineral in bone, depends on its crystal size, orientation, and substitutional chemistry, all of which can vary significantly among individuals (74). Similarly, the organic matrix, predominantly composed of type I collagen, shows variability in structure and cross-linking patterns among individuals, directly influencing its mechanical response under load (75). Factors such as age, sex, ethnicity, and health status further modulate the quality and quantity of these bone components, resulting in significant differences in their mechanical properties (67). For example, aging reduces collagen quality while increasing mineral crystallinity, leading to stiffer but more brittle bones (76). Imaging modalities like QCT and DXA currently lack the capability to capture these subtle yet critical changes in bone composition and quality. Furthermore, the absence of standardized methods for characterizing these properties either *in vivo* or *ex vivo* complicates their integration into finite element models, underscoring a significant limitation in current biomechanical assessments.

Furthermore, the interaction between the inorganic and organic components introduces non-linearities that are not easily captured by existing imaging techniques. For example, the role of collagen in resisting crack propagation and maintaining post-yield behavior is critical for bone toughness, but current imaging modalities cannot quantify the functional quality of collagen or its integration with the mineral phase (49, 77). Advances in techniques like Raman spectroscopy and nanoindentation have provided insights into these interactions *in vitro*, but these are not yet translatable to clinical imaging settings. Raman spectroscopy, including methods like surface-enhanced Raman scattering (SERS) and tip-enhanced Raman scattering (TERS), offers detailed molecular information and high spatial resolution (78). Nanoindentation, on the other hand, allows for precise measurement of mechanical properties at the nanoscale (79). Despite their potential, these techniques face challenges in clinical translation due to issues like signal interference and the complexity of *in vivo* environments.

Addressing the challenges of characterizing bone material properties from medical images requires significant advancements in imaging technologies and computational modeling. Techniques that integrate imaging with compositional analysis, such as dual-energy CT (DECT) or high-resolution peripheral QCT (HR-pQCT), hold promise but remain in early stages of application (80). HR-pQCT is currently limited to extremities due to hardware and radiation constraints, making their use for larger regions like the proximal femur impractical. Empirical data from cadaveric studies could enhance finite element models, and future research could explore hybrid approaches combining high-resolution data with clinical imaging. Balancing radiation exposure with the need for detailed imaging is critical. Leveraging already-acquired clinical images for biomechanical modeling can reduce the need for additional scans. Standardizing imaging protocols in advance can further minimize radiation dose and costs while maintaining the necessary level of detail for accurate finite element analyses. Expanding our understanding of the material behavior of bone's components and improving the resolution and functionality of medical imaging will be critical for advancing finite element models and their clinical utility (81).

3.3.2 Anisotropy in bone mechanical properties and femoral strength

Anisotropy in bone mechanical properties refers to the variation in mechanical characteristics, such as Young's modulus and ultimate stress, depending on the orientation of the bone test

sample, even when taken from the same site. Similarly, anisotropy in femoral strength indicates that the maximum force the femur can sustain before fracturing varies with the direction of the applied force. This anisotropy arises from bone's hierarchical structure and composition, including the alignment of collagen fibers, the distribution of hydroxyapatite crystals, and the trabecular architecture within the femoral head and neck (75, 82, 83). Cortical bone in the femoral shaft, for instance, is stiffer and stronger along the longitudinal axis, making it particularly effective at resisting axial loads during activities like walking and running (84). In contrast, the trabecular bone in the femoral head and neck features a highly complex, orientation-specific architecture designed to distribute stresses arising from multi-directional loading scenarios (85).

The majority of QCT-based finite element models employ simplified isotropic material assumptions for bone mechanical properties; however, they can still demonstrate the anisotropic nature of femoral strength due to the influence of bone geometry and heterogeneous material distribution. These models reveal that bone is more resistant to compression and tension in certain orientations while being more susceptible to shear forces in others (52, 86). Studies have shown that the femur's ability to withstand impact forces is highly dependent on the direction and magnitude of the force applied during a fall (24, 87, 88). For example, sideways falls, which are the most common fall scenario in elderly individuals, generate impact forces that are poorly aligned with the femur's primary axis of strength, significantly increasing the risk of fracture (24). Conversely, frontal or posterior falls may exert forces along directions that the femur is better adapted to withstand, reducing fracture risk (87, 88).

However, the isotropic models of bone mechanical properties inherently overlook the directional dependence of these properties, limiting their accuracy in simulating real-world loading conditions. To address this limitation, finite element models must incorporate anisotropic mechanical properties that reflect the true directional behavior of bone material. Achieving this level of precision requires advanced imaging and material characterization techniques, such as those capable of capturing collagen fiber orientation and mineral distribution, which are not yet widely accessible. This presents a significant barrier to advancing modeling accuracy and clinical applicability.

Current imaging modalities, such as QCT and DXA, are limited in their ability to comprehensively characterize bone composition, including inorganic minerals, organic proteins, and water, let alone provide detailed orientation-specific data on bone strength (89, 90). Incorporating composition- and microstructure-dependent mechanical properties and anisotropy into finite element models requires a deeper understanding of the hierarchical structure of bone, particularly the trabecular and cortical microstructures. Advanced imaging techniques, such as dual-energy computed tomography (DECT), offer promising avenues for distinguishing and quantifying bone components with greater specificity (91, 92). However, these techniques are still under development and face challenges such as resolution limitations and the accurate extraction of anisotropic mechanical properties. Overcoming these barriers is essential to achieving more precise and clinically relevant models for fracture risk assessment.

4 Image-based dynamics modeling of falls to predict impact forces

Falls are the leading cause of hip fractures, with over 95% of hip fractures attributed to falls from standing height (93). The forces generated during a fall frequently exceed the strength of the femur, resulting in fractures even in young, healthy individuals—let alone older adults, who often have compromised bone strength due to age-related changes or conditions like osteoporosis (94). However, only 2% of falls result in fractures (95, 96), highlighting the complex interplay between individual biomechanics, fall dynamics, and environmental factors. This low percentage underscores the importance of understanding how variables such as bone strength, fall-induced forces, body orientation during impact, and surface compliance collectively influence fracture outcomes. Fall experiments, even controlled fall testing, are neither ethical nor safe for elderly individuals. Image-based dynamics modeling offers a promising alternative for simulating falls and predicting impact forces by integrating subject-specific anatomical and biomechanical data derived from advanced medical imaging techniques.

This section explores the necessity and potential of subject-specific dynamics modeling for fall simulations to predict impact forces. It discusses the importance of incorporating whole-body imaging data, such as DXA or QCT, to create accurate models, reviews the progress made in simulating falls from standing height, and examines the challenges that must be addressed to replicate real-world fall scenarios. By leveraging these advancements, the goal is to improve fracture risk prediction and develop more effective prevention strategies.

4.1 Subject-specific dynamics modeling of falls

Subject-specific factors, such as body height, weight, mass distribution, and flexibility, play a crucial role in determining the dynamics of a fall and the resulting impact forces (97). Generic models often fail to account for this variability, leading to inaccuracies in predicting impact forces and assessing fracture risks. For instance, a taller individual falling sideways may experience distinct dynamics and higher impact forces compared to a shorter individual under similar conditions. This variability underscores the need for personalized modeling. Subject-specific dynamics modeling of falls provides a more accurate approach by integrating individual characteristics, such as body dimensions, weight distribution, and flexibility, which significantly influence the trajectory and forces of a fall. Such precision is essential for reliably predicting impact forces and evaluating fracture risk.

Whole-body medical imaging techniques, such as DXA or QCT scans, offer valuable data on bone geometry, body composition, and soft tissue distribution, which are key parameters for developing

subject-specific dynamics models of falls. For example, DXA scans provide detailed estimates of regional fat and muscle distribution, as illustrated in Figure 4, which directly influence body mass properties and thus the dynamics of a fall. These parameters play a critical role in determining how the body interacts with the ground during impact and how forces are absorbed and transmitted through various tissues. By integrating this personalized information, subject-specific models can more accurately simulate fall mechanics, enhancing the prediction of impact forces and the evaluation of fracture risks. Substantial progress has been made in the development of subject-specific dynamics models for simulating falls. For instance, Luo et al. (25) developed and validated a method for constructing subject-specific dynamics models using whole-body DXA images. These models demonstrated improved accuracy in predicting impact forces during sideways falls, showing better agreement with experimental data compared to traditional empirical functions (98). Similarly, Fleps et al. (99) introduced a dynamic inertia-driven sideways fall protocol that tested full cadaveric femur-pelvis constructs under realistic fall conditions. This approach aimed to enhance the prediction of impact loads and fracture risk by replicating the dynamics of real-world falls, thereby bridging the gap between laboratory testing and clinical relevance. Studies using finite element models combined with dynamics simulations have demonstrated the potential to predict impact forces and their distribution during falls. For instance, researchers have utilized whole-body musculoskeletal models derived from DXA and QCT data to simulate falls and calculate site-specific impact forces (26, 44, 100). Some of these models have been validated using experimental data, such as motion capture systems and force plates, providing evidence of their predictive accuracy (25, 101). Furthermore, machine learning approaches have been integrated into fall dynamics modeling to enhance the efficiency and accuracy of simulations. Algorithms trained on large datasets can optimize model parameters, such as fall orientation and joint motion, based on subject-specific input (102). These approaches have improved the ability to predict real-world fall scenarios and their associated forces (103).

Dynamic fall models estimate forces that are subsequently used as boundary and loading conditions in finite element simulations. While these forces provide critical inputs, simplifications—such as assuming uniform force distribution or neglecting soft tissue effects—may introduce translational losses. These approximations can affect the accuracy of fracture risk predictions. Future research should focus on improving the fidelity of force translation and accounting for individual-specific factors to enhance prediction reliability.

4.2 Challenges in simulating real-world falls

Simulating real-world falls presents significant challenges due to the inherent complexity and variability of fall dynamics and subject-specific physiological factors (105, 106). Unlike controlled fall simulations, real-world falls are triggered by unpredictable and random events, such as tripping, slipping, or sudden loss of balance. These triggers introduce substantial variability in the initial conditions of the fall, including body posture, velocity, and the direction of movement at the onset of imbalance. Accurately replicating this randomness is crucial for realistic modeling but remains a significant hurdle.

Another critical factor is the reflexive response of muscles, which plays a pivotal role in influencing fall dynamics. When an individual loses balance, muscle reflexes are activated to counteract the fall, aiming to restore stability or reduce the severity of impact.

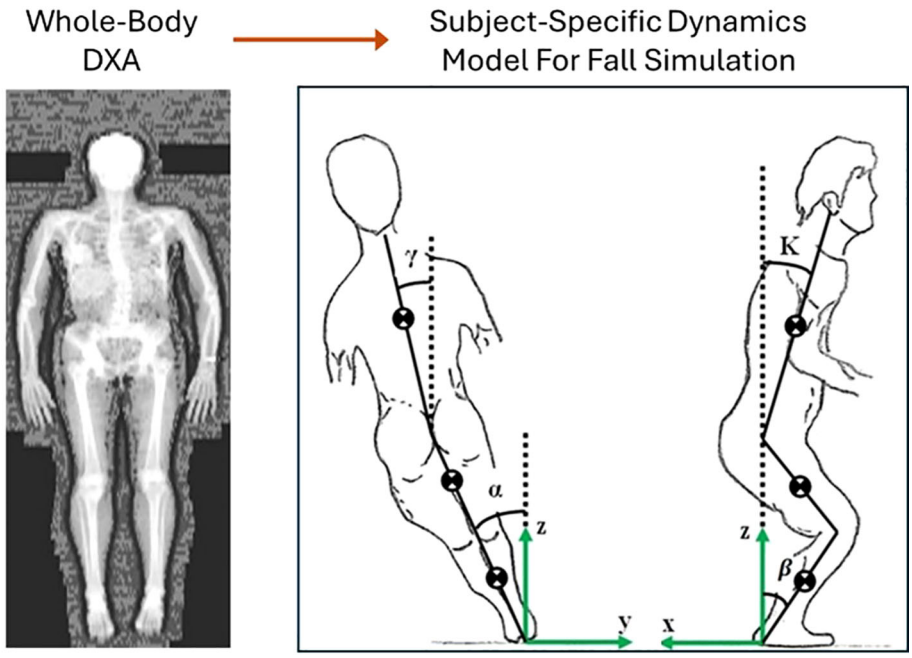

FIGURE 4
Construction of subject-specific dynamics model for simulating falls and predicting impact forces [modified from (26, 104)].

Muscle activation affects joint stiffness (107, 108), a key parameter in modulating the ability of the body to respond to destabilizing forces (109). Increased joint stiffness, resulting from heightened muscle activation, can stabilize the joints, preventing excessive movement that might exacerbate the fall. Conversely, insufficient muscle activation or weak muscle may lead to joint instability, increasing the likelihood of an uncontrolled descent. In addition to joint stiffness, muscle activation directly influences the actuator force generated by muscle fibers (110), which determines the strength and speed of corrective movements. For example, in a sideways fall, the hip abductor muscles play a crucial role in resisting lateral displacement of the torso (111), while the quadriceps and hamstrings stabilize the knees to reduce the impact force upon ground contact (112). These coordinated muscle activations help control body posture and orientation during the descent, potentially shifting the impact away from vulnerable areas like the hip.

The timing and intensity of muscle reflexes also vary between individuals, influenced by factors such as age, neuromuscular coordination, and physical fitness. Older adults, for instance, often exhibit delayed reflex responses and weaker muscle activation (113–115), which compromise their ability to mitigate the effects of a fall. In contrast, younger and physically active individuals tend to have faster and stronger reflexes, enhancing their capacity to absorb and dissipate impact energy. Additionally, muscle activation patterns influence the redistribution of body mass during a fall (97). For instance, active engagement of the arms and legs can alter the center of mass trajectory, reducing the likelihood of a high-impact collision at critical sites such as the hip. However, excessive or uncoordinated muscle activation can lead to counterproductive effects, such as increased rotational forces or misaligned body segments, potentially exacerbating the impact at the end of the fall (116).

Incorporating the randomness of fall triggers and the variability in muscle reflex responses into fall simulations requires sophisticated modeling approaches, along with subject-specific physiological and biomechanical parameters, which are extremely challenging to characterize. Current methodologies often rely on simplified assumptions regarding initial conditions and reflexive actions, limiting their ability to represent the full complexity of real-world falls. Advanced techniques, such as stochastic modeling to simulate random fall triggers and neuromuscular modeling to replicate reflexive muscle responses, are necessary to address these limitations. Overcoming these challenges is critical for improving the accuracy and applicability of fall dynamics models in assessing fracture risk and developing personalized prevention strategies.

5 Conclusion and future outlook

Recent advancements in image-based approaches for hip fracture risk assessment have significantly improved our understanding of the interplay between bone strength and fall-induced impact forces. Finite element (FE) models derived from imaging modalities such as DXA and QCT enable individualized assessments of femoral strength by capturing bone material properties, microstructure, and geometry. These models mark a notable improvement over traditional statistical tools by incorporating patient-specific risk factors. Similarly, subject-specific dynamics modeling of falls has advanced the prediction of forces applied to the hip during real-world falls, offering the potential for more reliable fracture risk assessments. However, challenges remain in refining these approaches for improved accuracy and reliability.

Advancing biomechanical models for hip fracture risk assessment requires addressing several challenges:

- DXA-based FE models are limited by the projection of three-dimensional bone structures into two dimensions, which may introduce inaccuracies in estimating femoral strength. A significant limitation of DXA-based FE models is their sensitivity to body positioning during scanning, which can introduce variability in the estimated femoral strength and fracture risk. Ensuring consistent and accurate positioning is critical to improving the reliability of these models. QCT-based models offer greater anatomical detail but face barriers such as higher costs, increased radiation exposure, and limited accessibility. Both approaches require further improvements in accurately integrating material properties, such as bone density distribution and anisotropic strength, to enhance predictive accuracy.
- Characterizing bone mechanical properties based on medical images presents a significant challenge due to the difficulty of accurately mapping image-derived parameters, such as bone density, to mechanical properties like strength, stiffness, and toughness. Current methods often rely on empirical relationships that may not fully account for bone heterogeneity, anisotropy, and microstructural variations. To address these challenges, there is a need for more robust methodologies that couple advanced imaging techniques with experimental validation and multiscale modeling approaches, enabling more accurate prediction of mechanical behavior.
- In fall dynamics simulation, the complexity of real-world falls presents additional obstacles. Randomness in fall triggers, variability in fall trajectories, and reflexive muscle responses are difficult to replicate accurately. Current models often rely on simplified assumptions, limiting their ability to capture the variability observed in real-life scenarios. Advanced techniques, such as stochastic modeling for fall triggers and neuromuscular modeling for reflex responses, are needed to address these challenges and improve the reliability of impact force predictions.
- The integration of these image-based biomechanical models into clinical workflows remains limited due to technical and logistical constraints. Despite their detailed insights into hip fracture mechanisms, these models require further optimization for practical use in routine healthcare settings. Collaboration between engineers, clinicians, and imaging specialists is essential to bridge the gap between research and clinical practice.

In summary, image-based hip fracture risk assessment has made significant progress in offering patient-specific insights into fracture susceptibility. However, addressing technical challenges, refining modeling techniques, and facilitating clinical integration are critical for unlocking their full potential in improving fracture prevention and patient outcomes.

Author contributions

YL: Conceptualization, Data curation, Formal Analysis, Funding acquisition, Investigation, Methodology, Project administration, Resources, Visualization, Writing – original draft, Writing – review & editing.

Funding

The author(s) declare that financial support was received for the research, authorship, and/or publication of this article. The author's research work has been supported by the Natural Sciences and Engineering Research Council (NSERC) and the University of Manitoba, Canada.

Conflict of interest

The author declares that the research was conducted in the absence of any commercial or financial relationships that could be construed as a potential conflict of interest.

Generative AI statement

The author(s) declare that Generative AI was used in the creation of this manuscript. To select English words, to improve grammar and to search relevant journal articles.

Publisher's note

References

1. Feng J, Zhang C, Li B, Zhan S, Wang S, Song C. Global burden of hip fracture: The Global Burden of Disease Study. *Osteoporos Int*. (2024) 35:41–52. doi: 10.1007/s00198-023-06907-3

2. Collaborators G 2019 F. Global, regional, and national burden of bone fractures in 204 countries and territories, 1990-2019: a systematic analysis from the Global Burden of Disease Study 2019. *Lancet Healthy Longev*. (2021) 2:e580–92. doi: 10.1016/S2666-7568(21)00172-0

3. Borgström F, Karlsson L, Ortsäter G, Norton N, Halbout P, Cooper C, et al. Fragility fractures in Europe: burden, management and opportunities. *Arch Osteoporos*. (2020) 15:59. doi: 10.1007/s11657-020-0706-y

4. Merlijn T, Swart KMA, van der Horst HE, Netelenbos JC, Elders PJM. Fracture prevention by screening for high fracture risk: a systematic review and meta-analysis. *Osteoporos Int*. (2020) 31:251–7. doi: 10.1007/s00198-019-05226-w

5. Engels A, Reber KC, Lindlbauer I, Rapp K, Büchele G, Klenk J, et al. Osteoporotic hip fracture prediction from risk factors available in administrative claims data – A machine learning approach. *PloS One*. (2020) 15:e0232969. doi: 10.1371/journal.pone.0232969

6. Sing C, Lin T, Bartholomew S, Bell JS, Bennett C, Beyene K, et al. Global epidemiology of hip fractures: secular trends in incidence rate, post-fracture treatment, and all-cause mortality. *J Bone Mineral Res*. (2023) 38:1064–75. doi: 10.1002/jbmr.4821

7. Cosman F, Lewiecki EM, Eastell R, Ebeling PR, Jan De Beur S, Langdahl B, et al. Goal-directed osteoporosis treatment: ASBMR/BHOF task force position statement 2024. *J Bone Mineral Res*. (2024) 39:1393–405. doi: 10.1093/jbmr/zjae119

8. Vilaca T, Schini M, Lui L-Y, Ewing SK, Thompson AR, Vittinghoff E, et al. The relationship between treatment-related changes in total hip BMD measured after 12, 18, and 24 mo and fracture risk reduction in osteoporosis clinical trials: the FNIH-ASBMR-SABRE project. *J Bone Mineral Res*. (2024) 39:1434–42. doi: 10.1093/jbmr/zjae126

9. Schwartz AV, Vittinghoff E, Bauer DC, Hillier TA, Strotmeyer ES, Ensrud KE, et al. Association of BMD and FRAX score with risk of fracture in older adults with type 2 diabetes. *JAMA*. (2011) 305:2184–92. doi: 10.1001/jama.2011.715

10. Johnell O, Kanis JA, Oden A, Johansson H, De Laet C, Delmas P, et al. Predictive value of BMD for hip and other fractures. *J Bone Mineral Res*. (2005) 20:1185–94. doi: 10.1359/JBMR.050304

11. Turcotte A-F, O'Connor S, Morin SN, Gibbs JC, Willie BM, Jean S, et al. Association between obesity and risk of fracture, bone mineral density and bone quality in adults: A systematic review and meta-analysis. *PloS One*. (2021) 16:e0252487. doi: 10.1371/journal.pone.0252487

12. Schini M, Johansson H, Harvey NC, Lorentzon M, Kanis JA, McCloskey EV. An overview of the use of the fracture risk assessment tool (FRAX) in osteoporosis. *J Endocrinol Invest*. (2023) 47:501–11. doi: 10.1007/s40618-023-02219-9

13. Richards C, Stevens R, Lix LM, McCloskey EV, Johansson H, Harvey NC, et al. Fracture prediction in rheumatoid arthritis: validation of FRAX with bone mineral density for incident major osteoporotic fractures. *Rheumatology*. (2025) 64:kead676. doi: 10.1093/rheumatology/kead676

14. Vandenput L, Johansson H, McCloskey EV, Liu E, Åkesson KE, Anderson FA, et al. Update of the fracture risk prediction tool FRAX: a systematic review of potential cohorts and analysis plan. *Osteoporos Int*. (2022) 33:2103–36. doi: 10.1007/s00198-022-06435-6

15. Mousa J, Peterson MN, Crowson CS, Achenbach SJ, Atkinson EJ, Amin S, et al. Validating the fracture risk assessment tool score in a US population-based study of patients with rheumatoid arthritis. *J Rheumatol*. (2023) 50:1279–86. doi: 10.3899/jrheum.2022-1293

16. Novel methods to evaluate fracture risk models | Journal of Bone and Mineral Research | Oxford Academic . Available online at: https://academic.oup.com/jbmr/article-abstract/26/8/1767/7597924?redirectedFrom=fulltext (Accessed October 23, 2024).

17. Marques A, Ferreira RJO, Santos E, Loza E, Carmona L, da Silva J. The accuracy of osteoporotic fracture risk prediction tools: a systematic review and meta-analysis. *Ann Rheum Dis*. (2015) 74:531. doi: 10.1136/annrheumdis-2015-eular.2984

18. Liu IT, Liang FW, Wang ST, Chang CM, Lu TH, Wu CH. The effects of falls on the prediction of osteoporotic fractures: epidemiological cohort study. *Arch Osteoporos*. (2021) 16:110. doi: 10.1007/s11657-021-00977-8

19. Harvey NC, Odén A, Orwoll E, Lapidus J, Kwok T, Karlsson MK, et al. Falls predict fractures independently of FRAX probability: A meta-analysis of the osteoporotic fractures in men (MrOS) study. *J Bone Mineral Res*. (2018) 33:510–6. doi: 10.1002/jbmr.3331

20. Beaudoin C, Moore L, Gagné M, Bessette L, Ste-Marie LG, Brown JP, et al. Performance of predictive tools to identify individuals at risk of non-traumatic fracture: a systematic review, meta-analysis, and meta-regression. *Osteoporos Int*. (2019) 30:721–40. doi: 10.1007/s00198-019-04919-6

21. Yosibash Z, Trabelsi N, Buchnik I, Myers KW, Salai M, Eshed I, et al. Hip fracture risk assessment in elderly and diabetic patients: combining autonomous finite element analysis and machine learning. *J Bone Mineral Res*. (2023) 38:876–86. doi: 10.1002/jbmr.4805

22. Galbusera F, Cina A, Panico M, Albano D, Messina C. Image-based biomechanical models of the musculoskeletal system. *Eur Radiol Exp*. (2020) 4:49. doi: 10.1186/s41747-020-00172-3

23. Boyd SK. Image-based finite element analysis. In: Hallgrimsson B, Sensen CW, editors. *Advanced Imaging in Biology and Medicine*. Berlin, Heidelberg, Germany: Springer (2009). p. 301–18.

24. Narsiri-Sarvi M, Luo Y. Sideways fall-induced impact force and its effect on hip fracture risk: a review. *Osteoporosis Int*. (2017) 28:2759–80. doi: 10.1007/s00198-017-4138-5

25. Luo Y, Sarvi MN, Sun P, Leslie W, Ouyang J. Prediction of impact force in sideways fall of the elderly by image-based subject-specific dynamics modeling. *Int Biomechanics*. (2014) 1:1–14. doi: 10.1080/23310472.2014.975745

26. Sarvi MN, Luo Y. A two-level subject-specific biomechanical model for improving prediction of hip fracture risk. *Clin Biomechanics*. (2015) 30:881–7. doi: 10.1016/j.clinbiomech.2015.05.013

27. Scott V, Wagar B, Sum A, Metcalfe S, Wagar L. A public health approach to fall prevention among older persons in Canada. *Clin Geriatr Med*. (2010) 26:705–18. doi: 10.1016/j.cger.2010.06.003

28. Yang Y, Komisar V, Shishov N, Lo B, Korall AM, Feldman F, et al. The effect of fall biomechanics on risk for hip fracture in older adults: A cohort study of video-captured falls in long-term care. *J Bone Miner Res*. (2020) 35:1914–22. doi: 10.1002/jbmr.4048

29. Parkkari J, Kannus P, Palvanen M, Natri A, Vainio J, Aho H, et al. Majority of hip fractures occur as a result of a fall and impact on the greater trochanter of the femur: a prospective controlled hip fracture study with 206 consecutive patients. *Calcif Tissue Int*. (2016) 65:183–7. doi: 10.1007/s002239900679

30. Lim S-K, Choi K, Heo NH, Kim Y, Lim J-Y. Characteristics of fragility hip fracture-related falls in the older adults: A systematic review. *J Nutrition Health Aging*. (2024) 28:100357. doi: 10.1016/j.jnha.2024.100357

31. Ferdous Z, Luo Y. Study of hip fracture risk by DXA-based patient-specific finite element model. *Bio-med Mater Eng*. (2015) 25:213–20. doi: 10.3233/BME-151271

32. Luo Y, Yang H. Assessment of hip fracture risk by cross-sectional strain-energy derived from DXA-based beam model. *Clin Biomechanics*. (2019) 63:48–53. doi: 10.1016/j.clinbiomech.2019.02.016

33. Luo Y. Empirical functions for conversion of femur areal and volumetric bone mineral density. *J Biomed Biol Eng*. (2019) 39:287–93. doi: 10.1007/s40846-018-0394-x

34. Luo Y, Ferdous Z, Leslie WD. A preliminary dual-energy X-ray absorptiometry-based finite element model for assessing osteoporotic hipfracture risk. *Proc Inst Mechanical Eng Part H: J Eng Med*. (2011) 225:1188–95. doi: 10.1177/0954411911424975

35. Luo Y, Ferdous Z, Leslie WD. Precision study of DXA-based patient-specific finite element modeling for assessing hip fracture risk. *Int J Numerical Methods Biomed Eng*. (2013) 29:615–29. doi: 10.1002/cnm.v29.5

36. Naylor KE, McCloskey EV, Eastell R, Yang L. Use of DXA-based finite element analysis of the proximal femur in a longitudinal study of hip fracture. *J Bone Miner Res*. (2013) 28:1014–21. doi: 10.1002/jbmr.1856

37. Yang L, Peel N, Clowes JA, McCloskey EV, Eastell R. Use of DXA-based structural engineering models of the proximal femur to discriminate hip fracture. *J Bone Miner Res*. (2009) 24:33–42. doi: 10.1359/jbmr.080906

38. Terzini M, Aldieri A, Rinaudo L, Osella G, Audenino AL, Bignardi C. Improving the hip fracture risk prediction through 2D finite element models from DXA images: validation against 3D models. *Front Bioeng Biotechnol*. (2019) 7:220. doi: 10.3389/fbioe.2019.00220

39. Danielson ME, Beck TJ, Karlamangla AS, Greendale GA, Atkinson EJ, Lian KY, et al. A comparison of DXA and CT based methods for estimating the strength of the femoral neck in post-menopausal women. *Osteoporos Int*. (2013) 24:1377–88. doi: 10.1007/s00198-012-2066-y

40. Luo Y, Ahmed S, Leslie WD. Automation of a DXA-based finite element tool for clinical assessment of hip fracture risk. *Comput Methods Programs Biomed*. (2018) 155:75–83. doi: 10.1016/j.cmpb.2017.11.020

41. Yang S, Leslie WD, Luo Y, Goertzen AL, Ahmed S, Ward LM, et al. Fully-automated DXA-based finite element analysis stratifies hip fracture better than femoral neck bone mineral density: a cross-sectional study. *Osteoporosis Int*. (2018) 29:191–200. doi: 10.1007/s00198-017-4232-8

42. Dall'Ara E, Eastell R, Viceconti M, Pahr D, Yang L. Experimental validation of DXA-based finite element models for prediction of femoral strength. *J Mechanical Behav Biomed Mater*. (2016) 63:17–25. doi: 10.1016/j.jmbbm.2016.06.004

43. Yang L, Parimi N, Orwoll ES, Black DM, Schousboe JT, Eastell R. Association of incident hip fracture with the estimated femoral strength by finite element analysis of DXA scans in the Osteoporotic Fractures in Men (MrOS) study. *Osteoporos Int*. (2018) 29:643–51. doi: 10.1007/s00198-017-4319-2

44. Sarvi MN, Luo Y. Study of sex differences in the association between hip fracture risk and body parameters by DXA-based biomechanical modeling. *Bone*. (2016) 90:90–8. doi: 10.1016/j.bone.2016.06.006

45. Mochizuki T, Yano K, Ikari K, Kawakami K, Hiroshima R, Koenuma N, et al. Hip structure analysis by DXA of teriparatide treatment: A 24-month follow-up clinical study. *J Orthop*. (2016) 13:414–8. doi: 10.1016/j.jor.2016.09.001

46. Dudle A, Gugler Y, Pretterklieber M, Ferrari S, Lippuner K, Zysset P. 2D-3D reconstruction of the proximal femur from DXA scans: Evaluation of the 3D-Shaper software. *Front Bioeng Biotechnol*. (2023) 11:1111020. doi: 10.3389/fbioe.2023.1111020

47. Grassi L, Väänänen SP, Jehpsson L, Ljunggren Ö, Rosengren BE, Karlsson MK, et al. 3D finite element models reconstructed from 2D dual-energy X-ray absorptiometry (DXA) images improve hip fracture prediction compared to areal BMD in osteoporotic fractures in men (MrOS) Sweden cohort. *J Bone Miner Res*. (2023) 38:1258–67. doi: 10.1002/jbmr.4878

48. Saito M, Marumo K. Collagen cross-links as a determinant of bone quality: a possible explanation for bone fragility in aging, osteoporosis, and diabetes mellitus. *Osteoporos Int*. (2010) 21:195–214. doi: 10.1007/s00198-009-1066-z

49. Viguet-Carrin S, Garnero P, Delmas PD. The role of collagen in bone strength. *Osteoporos Int*. (2006) 17:319–36. doi: 10.1007/s00198-005-2035-9

50. Banks KP, Farrell MB, Gunther RS, McWhorter NE, Byerly DW, Peacock JG. Improving DXA quality by avoiding common technical and diagnostic pitfalls: part 1. *J Nucl Med Technol*. (2023) 51:167–75. doi: 10.2967/jnmt.122.264885

51. Knowles NK, Reeves JM, Ferreira LM. Quantitative Computed Tomography (QCT) derived Bone Mineral Density (BMD) in finite element studies: a review of the literature. *J Exp Orthopaedics*. (2016) 3:1–16. doi: 10.1186/s40634-016-0072-2

52. Kheirollahi H, Luo Y. Understanding hip fracture by QCT-based finite element modeling. *J Med Biol Eng*. (2017) 37:686–94. doi: 10.1007/s40846-017-0266-9

53. Carpenter RD. Finite element analysis of the hip and spine based on quantitative computed tomography. *Curr Osteoporos Rep*. (2013) 11:156–62. doi: 10.1007/s11914-013-0141-8

54. Zysset P, Dall'Ara E, Varga P, Pahr DH. Finite element analysis for prediction of bone strength. *BoneKEy Rep*. (2013) 2:1–9. doi: 10.1038/bonekey.2013.120

55. Faisal TR, Luo Y. Study of fracture risk difference in left and right femur by QCT-based FEA. *Biomed Eng Online*. (2017) 16:116. doi: 10.1186/s12938-017-0407-y

56. Dragomir-Daescu D, Op Den Buijs J, McEligot S, Dai YF, Entwistle RC, Salas C, et al. Robust QCT/FEA models of proximal femur stiffness and fracture load during a sideways fall on the hip. *Ann Biomed Eng*. (2011) 39:742–55. doi: 10.1007/s10439-010-0196-y

57. Mirzaei M, Keshavarzian M, Naeini V. Analysis of strength and failure pattern of human proximal femur using quantitative computed tomography (QCT)-based finite element method. *Bone*. (2014) 64:108–14. doi: 10.1016/j.bone.2014.04.007

58. Dall'Ara E, Luisier B, Schmidt R, Kainberger F, Zysset P, Pahr D. A nonlinear QCT-based finite element model validation study for the human femur tested in two configurations *in vitro*. *Bone*. (2013) 52:27–38. doi: 10.1016/j.bone.2012.09.006

59. Shen J, Nielson CM, Marshall LM, Lee DC, Keaveny TM, Orwoll ES. The association between BMI and QCT-derived proximal hip structure and strength in older men: a cross-sectional study. *J Bone Miner Res*. (2015) 30:1301–8. doi: 10.1002/jbmr.2450

60. Black DM, Bouxsein ML, Marshall LM, Cummings SR, Lang TF, Cauley JA, et al. Proximal femoral structure and the prediction of hip fracture in men: a large prospective study using QCT. *J Bone Miner Res*. (2008) 23:1326–33. doi: 10.1359/jbmr.080316

61. Kheirollahi H, Luo Y. Assessment of hip fracture risk using cross-section strain energy determined from QCT-based finite element model. *BioMed Res Int*. (2015) 2015:Article ID 413839. doi: 10.1155/2015/413839

62. Carpenter RD, Beaupr? GS, Lang TF, Orwoll ES, Carter DR. New QCT analysis approach shows the importance of fall orientation on femoral neck strength. *J Bone Miner Res*. (2005) 20:1533–42. doi: 10.1359/JBMR.050510

63. Christiansen BA, Kopperdahl DL, Kiel DP, Keaveny TM, Bouxsein ML. Mechanical contributions of the cortical and trabecular compartments contribute to differences in age-related changes in vertebral body strength in men and women assessed by QCT-based finite element analysis. *J Bone Mineral Res*. (2011) 26:974–83. doi: 10.1002/jbmr.287

64. Engelke K, Fuerst T, Dasic G. al. et. Regional distribution of spine and hip QCT BMD responses after one year of once-monthly ibandronate in postmenopausal osteoporosis. *Bone*. (2010) 46:1626–32. doi: 10.1016/j.bone.2010.03.003

65. Engelke K, Lang T, Khosla S, Qin L, Zysset P, Leslie WD, et al. Clinical use of quantitative computed tomography (QCT) of the hip in the management of osteoporosis in adults: the 2015 ISCD official positions - part I. *J Clin Densitomet*. (2015) 18:338–58. doi: 10.1016/j.jocd.2015.06.012

66. Crawford RP, Cann CE, Keaveny TM. Finite element models predict *in vitro* vertebral body compressive strength better than quantitative computed tomography. *Bone*. (2003) 33:744–50. doi: 10.1016/S8756-3282(03)00210-2

67. Boskey AL. Bone composition: relationship to bone fragility and antiosteoporotic drug effects. *BoneKey Rep*. (2013) 447. doi: 10.1038/bonekey.2013.181

68. Boskey AL, Wright TM, Blank RD. Collagen and bone strength. *J Bone Mineral Res*. (1999) 14:330–5. doi: 10.1359/jbmr.1999.14.3.330

69. Nyman JS, Roy A, Acuna RL, Shen X, Tyler JH, Wang X. The influence of water removal on the strength and toughness of cortical bone. *J Biomech*. (2006) 39:931–8. doi: 10.1016/j.jbiomech.2005.01.012

70. Granke M, Does MD, Nymna JS. The role of water compartments in the material properties of cortical bone. *Calcif Tissue Int*. (2015) 97:292–307. doi: 10.1007/s00223-015-9977-5

71. Lang TF. Quantitative computed tomography. *Radiol Clin North Am*. (2010) 48:589–600. doi: 10.1016/j.rcl.2010.03.001

72. Adams JE. Advances in bone imaging for osteoporosis. *Nat Rev Endocrinol*. (2013) 9:28–42. doi: 10.1038/nrendo.2012.217

73. SChileo E, Taddei F, Malandrino A, Cristofolini L, Viceconti M. Subject-specific finite element models can accurately predict strain levels in long bones. *J Biomech*. (2007) 40:2982–9. doi: 10.1016/j.jbiomech.2007.02.010

74. Rodriguez-Palomo A, Østergaard M, Birkedal H. Bone hierarchical structure: heterogeneity and uniformity. *Adv Funct Mater*. (2024) 34:2307026. doi: 10.1002/adfm.202307026

75. Fratzl P, Weinkamer R. Nature's hierarchical materials. *Prog Mater Sci*. (2007) 52:1263–334. doi: 10.1016/j.pmatsci.2007.06.001

76. Boskey AL, Coleman R. Aging and bone. *J Dental Res*. (2010) 89:1333–48. doi: 10.1177/0022034510377791

77. Burr DB. The contribution of the organic matrix to bone's material properties. *Bone*. (2002) 31:8–11. doi: 10.1016/S8756-3282(02)00815-3

78. Buckley K, Kerns JG, Vinton J, Gikas PD, Smith C, Parker AW, et al. Towards the *in vivo* prediction of fragility fractures with Raman spectroscopy. *J Raman Spectrosc*. (2015) 46:610–8. doi: 10.1002/jrs.v46.7

79. Wang C-F, O'Callahan BT, Krayev A, El-Khoury PZ. Nanoindentation-enhanced tip-enhanced Raman spectroscopy. *J Chem Phys*. (2021) 154:241101. doi: 10.1063/5.0056541

80. de Bakker CMJ, Tseng W-J, Li Y, Zhao H, Liu XS. Clinical evaluation of bone strength and fracture risk. *Curr Osteoporos Rep*. (2017) 15:32–42. doi: 10.1007/s11914-017-0346-3

81. Williams S, Khan L, Licata AA. DXA and clinical challenges of fracture risk assessment in primary care. *CCJM*. (2021) 88:615–22. doi: 10.3949/ccjm.88a.20199

82. Reznikov N, Bilton M, Lari L, Stevens MM, Kröger R. Fractal-like hierarchical organization of bone begins at the nanoscale. *Science*. (2018) 360:eaao2189. doi: 10.1126/science.aao2189

83. Tzaphlidou M. Bone architecture: collagen structure and calcium/phosphorus maps. *J Biol Phys*. (2008) 34:39–49. doi: 10.1007/s10867-008-9115-y

84. Cuppone M, Seedhom BB, Berry E, Ostell AE. The longitudinal young's modulus of cortical bone in the midshaft of human femur and its correlation with CT scanning data. *Calcif Tissue Int*. (2004) 74:302–9. doi: 10.1007/s00223-002-2123-1

85. Cauley JA, Blackwell T, Zmuda JM, Fullman RL, Ensrud KE, Stone KL, et al. Correlates of trabecular and cortical volumetric bone mineral density (vBMD) at the femoral neck and lumbar spine: The osteoporotic fractures in men study (MrOS). *J Bone Miner Res*. (2010) 25:1958–71. doi: 10.1002/jbmr.86

86. Trabelsi N, Yosibash Z. Patient-specific finite-element analyses of the proximal femur with orthotropic material properties validated by experiments. *J Biomechanical Eng*. (2011) 133. doi: 10.1115/1.4004180

87. Ford CM, Keaveny TM, Hayes WC. The effect of impact direction on the structural capacity of the proximal femur during falls. *J Bone Mineral Res*. (1996) 11:377–83. doi: 10.1002/jbmr.5650110311

88. Pretty SP, Levine IC, Laing AC. Anatomically aligned loading during falls: influence of fall protocol, sex and trochanteric soft tissue thickness. *Ann BioMed Eng*. (2021) 49:3267–79. doi: 10.1007/s10439-021-02852-6

89. Choksi P, Jepsen KJ, Clines GA. The challenges of diagnosing osteoporosis and the limitations of currently available tools. *Clin Diabetes Endocrinol*. (2018) 4:12. doi: 10.1186/s40842-018-0062-7

90. Wang F, Zheng L, Theopold J, Schleifenbaum S, Heyde C-E, Osterhoff G. Methods for bone quality assessment in human bone tissue: a systematic review. *J Orthopaedic Surg Res*. (2022) 17:174. doi: 10.1186/s13018-022-03041-4

91. Engelke K, Libanati C, Fuerst T, Zysset P, Genant HK. Advanced CT based *in vivo* methods for the assessment of bone density, structure, and strength. *Curr Osteoporos Rep*. (2013) 11:246–55. doi: 10.1007/s11914-013-0147-2

92. Koch V, Hokamp NG, Albrecht MH, Gruenewald LD, Yel I, Borggrefe J, et al. Accuracy and precision of volumetric bone mineral density assessment using dual-source dual-energy versus quantitative CT: a phantom study. *Eur Radiol Exp*. (2021) 5:43. doi: 10.1186/s41747-021-00241-1

93. Barceló M, Casademont J, Mascaró J, Gich I, Torres OH. Indoor falls and number of previous falls are independent risk factors for long-term mortality after a hip fracture. *Aging Clin Exp Res*. (2023) 35:2483–90. doi: 10.1007/s40520-023-02551-3

94. Komisar V, Robinovitch SN. The role of fall biomechanics in the cause and prevention of bone fractures in older adults. *Curr Osteoporos Rep*. (2021) 19:381–90. doi: 10.1007/s11914-021-00685-9

95. Ardaneh M, Fararouei M, Hassanzadeh J. Factors contributing to falls leading to fracture among older adults. *Popul Ageing*. (2023) 16:121–35. doi: 10.1007/s12062-021-09326-6

96. Leavy B, Byberg L, Michaëlsson K, Melhus H, Åberg AC. The fall descriptions and health characteristics of older adults with hip fracture: a mixed methods study. *BMC Geriatrics*. (2015) 15:40. doi: 10.1186/s12877-015-0036-x

97. Pretty SP, Martel DR, Laing AC. The influence of body mass index, sex, & Muscle activation on pressure distribution during lateral falls on the hip. *Ann BioMed Eng*. (2017) 45:2775–83. doi: 10.1007/s10439-017-1928-z

98. Nasiri M, Luo Y, Sun P, Ouyang J. Experimental validation of subject-specific dynamics model for predicting impact force in sideways fall. *J Biomed Sci Eng*. (2014) 7:405–18. doi: 10.4236/jbise.2014.77043

99. Fleps I, Vuille M, Melnyk A, Ferguson SJ, Guy P, Helgason B, et al. A novel sideways fall simulator to study hip fractures ex vivo. *PloS One*. (2018) 13:e0201096. doi: 10.1371/journal.pone.0201096

100. Fleps I, Guy P, Ferguson SJ, Cripton PA, Helgason B. Explicit finite element models accurately predict subject-specific and velocity-dependent kinetics of sideways fall impact. *J Bone Mineral Res*. (2019) 34:1837–50. doi: 10.1002/jbmr.3804

101. Bliven EK, Fung A, Baker A, Fleps I, Ferguson SJ, Guy P, et al. How accurately do finite element models predict the fall impact response of ex vivo specimens augmented by prophylactic intramedullary nailing? *J Orthopaedic Res*. (2025) 43:396-406. doi: 10.1002/jor.25984

102. Tufisi C, Praisach Z-I, Gillich G-R, Bichescu AI, Heler T-L. Forward fall detection using inertial data and machine learning. *Appl Sci*. (2024) 14:10552. doi: 10.3390/app142210552

103. Lim ZK, Connie T, Goh MKO, Saedon N 'Izzati B. Fall risk prediction using temporal gait features and machine learning approaches. *Front Artif Intell*. (2024) 7:1425713. doi: 10.3389/frai.2024.1425713

104. Luo Y. *Image-based multilevel biomechanical modeling for fall-induced hip fracture*. New York, USA: Springer (2017).

105. Broadley RW, Klenk J, Thies SB, Kenney LPJ, Granat MH. Methods for the real-world evaluation of fall detection technology: A scoping review. *Sensors*. (2018) 18:2060. doi: 10.3390/s18072060

106. Tchalla AE, Dufour AB, Travison TG, Habtemariam D, Iloputaife I, Manor B, et al. Patterns, predictors, and outcomes of falls trajectories in older adults: the MOBILIZE boston study with 5 years of follow-up. *PloS One*. (2014) 9:e106363. doi: 10.1371/journal.pone.0106363

107. Jeong S, Nishikawa K. The force response of muscles to activation and length perturbations depends on length history. *J Exp Biol*. (2023) 226:jeb243991. doi: 10.1242/jeb.243991

108. Seth A, Hicks JL, Uchida TK, Habib A, Dembia CL, Dunne JJ, et al. OpenSim: Simulating musculoskeletal dynamics and neuromuscular control to study human and animal movement. *PloS Comput Biol*. (2018) 14:e1006223. doi: 10.1371/journal.pcbi.1006223

109. Krause A, Freyler K, Gollhofer A, Stocker T, Brüderlin U, Colin R, et al. Neuromuscular and kinematic adaptation in response to reactive balance training – a randomized controlled study regarding fall prevention. *Front Physiol*. (2018) 9:1075. doi: 10.3389/fphys.2018.01075

110. Wang Y, Liu C, Ren L, Ren L. Load-dependent variable gearing mechanism of muscle-like soft actuator. *J Bionic Eng*. (2022) 19:29–43. doi: 10.1007/s42235-021-00129-1

111. Lanza MB, Rock K, Marchese V, Addison O, Gray VL. Hip abductor and adductor rate of torque development and muscle activation, but not muscle size, are associated with functional performance. *Front Physiol*. (2021) 12:744153. doi: 10.3389/fphys.2021.744153

112. Walsh M, Boling MC, McGrath M, Blackburn JT, Padua DA. Lower extremity muscle activation and knee flexion during a jump-landing task. *J Athletic Training*. (2012) 47:406–13. doi: 10.4085/1062-6050-47.4.17

113. Clark BC. Neural mechanisms of age-related loss of muscle performance and physical function. *J Gerontol: Ser A*. (2023) 78:8–13. doi: 10.1093/gerona/glad029

114. Jeon W, Ramadan A, Whitall J, Alissa N, Westlake K. Age-related differences in lower limb muscle activation patterns and balance control strategies while walking over a compliant surface. *Sci Rep*. (2023) 13:16555. doi: 10.1038/s41598-023-43728-0

115. Cano Porras D, Jacobs JV, Inzelberg R, Bahat Y, Zeilig G, Plotnik M. Patterns of whole-body muscle activations following vertical perturbations during standing and walking. *J NeuroEng Rehabil*. (2021) 18:75. doi: 10.1186/s12984-021-00836-0

116. Adams M, Gordt-Oesterwind K, Bongartz M, Zimmermann S, Seide S, Braun V, et al. Effects of physical activity interventions on strength, balance and falls in middle-aged adults: A systematic review and meta-analysis. *Sports Med - Open*. (2023) 9:61. doi: 10.1186/s40798-023-00606-3

frontiers | Frontiers in Endocrinology

TYPE Original Research
PUBLISHED 18 March 2025
DOI 10.3389/fendo.2025.1558622

OPEN ACCESS

EDITED BY
Nico Sollmann,
Ulm University Medical Center, Germany

REVIEWED BY
David Paglia,
Rutgers University, Newark, United States
Qiang Jiao,
Second Hospital of Shanxi Medical University, China

*CORRESPONDENCE
Xinhua Ye
czyxh2000@163.com
Cuiping Zhao
Lnyxk2021@163.com

†These authors have contributed equally to this work and share first authorship

‡These authors have contributed equally to this work and share last authorship

RECEIVED 10 January 2025
ACCEPTED 28 February 2025
PUBLISHED 18 March 2025

CITATION
Zhao D, Bo Y, Bai H, Zhao C and Ye X (2025) Association between the minimal model of hip structure and risk of hip fracture in Chinese adults. *Front. Endocrinol.* 16:1558622. doi: 10.3389/fendo.2025.1558622

Association between the minimal model of hip structure and risk of hip fracture in Chinese adults

Dan Zhao[1†], Yawen Bo[1†], Huiling Bai[1], Cuiping Zhao[2*‡] and Xinhua Ye[1*‡]

[1]Department of Endocrinology, The Second People's Hospital of Changzhou, The Third Affiliated Hospital of Nanjing Medical University, Changzhou, Jiangsu, China, [2]Department of Geriatrics, The Second People's Hospital of Changzhou, The Third Affiliated Hospital of Nanjing Medical University, Changzhou, Jiangsu, China

Background: Multiple studies have indicated that the minimal model of hip structure can enhance hip fracture risk assessment. This study aimed to investigate the independent association between minimal model variables and hip fracture risk in Han Chinese individuals.

Methods: This cross-sectional study included 937 Han Chinese patients (248 with hip fractures). Minimal model variables were calculated from the hip structural analysis, including bone mineral density (BMD), femoral neck width (FNW), and Delta and Sigma values.

Results: This study included 937 patients (293 men; mean age = 68.3 years). In logistic regression analyses, BMD increase (per 0.1 g/cm^2) correlated with a 45% reduction in the hip fracture risk (odds ratio [OR] = 0.55; 95% confidence interval [CI]: 0.45–0.68) after adjusting for all covariates. However, FNW (per 0.1 cm) and Sigma (per 0.01 cm) and Delta values (per 0.01 cm) were associated with increased risks (OR = 1.28; 95% CI: 1.18–1.37; OR = 1.06; 95% CI: 1.03–1.09; OR = 1.06; 95% CI: 1.03–1.09, respectively). When the Delta was >0.17 cm, the risk of hip fracture rose considerably by 13% (OR = 1.13; 95% CI: 1.08–1.18) for every 0.01 cm that the Delta value increased. The area under the curve (AUC) for hip fracture prediction from BMD alone was significantl lower than those of minimal model (0.781 vs 0.838, p <0.05).

Conclusion: Large increases in FNW, Sigma and Delta values and notable declines in BMD were individually and significantly linked to a high hip fracture risk in Han Chinese adults. Our findings suggest that the minimal model of hip structure may improve hip fracture risk assessments.

KEYWORDS

hip structure, minimal model, delta, sigma, hip fracture

1 Introduction

Hip fracture is a significant public health concern worldwide. The projected total annual incidence of hip fractures in many countries will nearly double between 2018 and 2050 (1). In 2019, the incidence and prevalence of hip fractures in China were approximately 2.0 million and 2.6 million, respectively, each representing approximately 1/9 of the global total cases (2). As China's population continues to age in the forthcoming years, the country will encounter an increasing number of hip fracture-related issues.

Approximately 40 years after its inception, two-dimensional dual-energy X-ray absorptiometry (DXA), which measures the areal bone mineral density (aBMD) in the proximal femora, remains the most clinically used predictor of fracture risk (3, 4). However, academics are beginning to pay attention to the biomechanical implications of bone structural geometry on bone fragility (5–7). To capture the bone structure in cross sections at the femoral neck, Beck et al. created an eight-variable structural model known as hip structural analysis (HSA) using typical DXA imaging data (8). Rathbun et al. have reported that the proximal femur experiences a decline in bone structure and strength during hip fracture recovery that is significantly greater than that observed in older Caucasian men during normal aging (9). In native Chinese women, cortical thickness reduction or an increase in the buckling ratio may independently predict the risk of femoral neck fragility fractures, regardless of BMD (10).

However, the eight metrics typically documented using Beck's HSA approach at each anatomical location were not autonomous (11). Utilizing HSA variables, Khoo et al. investigated the beam theory to develop a novel formulation, termed the minimum model (MM), which encompasses information equivalent to the eight structural geometric measures typically supplied at the femoral neck using the HSA technique. The MM consists of four parameters as follows: BMD and femoral neck width (FNW), along with two novel summary measures of internal bone distribution: Sigma and Delta (11). Prince et al. concluded that the clinical prediction of hip fractures was significantly enhanced by adding Delta measurements to hip BMD and age in elderly women (12). However, studies regarding the independent correlation between MM variables and the risk of hip fractures in Chinese adults are scarce.

This study aimed to investigate whether MM variables are significantly related to hip fracture risk in Han Chinese individuals, while controlling for all confounders. Furthermore, we implemented a receiver operating characteristic (ROC) analysis to compare the discriminative ability of MM against the use of femoral neck BMD alone.

2 Materials and methods

2.1 Study population

This retrospective cross-sectional study was performed at the Department of Orthopedics of the Second People's Hospital of Changzhou, Changzhou, Jiangsu, China. The inclusion and exclusion criteria for the participants were previously delineated (13). Participants with malignant tumors, poliomyelitis, renal failure, hormone use, elevated serum liver enzyme activity, or increased serum creatinine levels (n = 54) were excluded. Hip fractures were confirmed through a physician's examination of the radiology reports, and the analysis included 937 participants, comprising 248 with hip fractures (Figure 1).

2.2 Measurements of clinical and laboratory parameters

Previous reports have documented the measurements of clinical and laboratory parameters (13). Weight (kg) and height (m) were assessed using a weighing scale, with the participants wearing light clothing and no shoes (RGZ-120-RT; Hengqi Inc., China). Body mass index (BMI; kg/m^2)was calculated by dividing weight (kg) by height squared (m^2). A glycosylated hemoglobin type-A1c (HbA1c) level > 6.5%, fasting glucose level > 7.0 mmol/L, and a self-reported history of a medical diagnosis of diabetes were considered indicators of diabetes.

Blood samples were collected from all participants within 24 h of admission following an overnight fast of at least 8 h. White blood cells (WBC), red blood cells (RBC), and platelets (PLT) were counted using a self-service hematology analyzer (XN-2800, Sysmex Inc.). Further biomarkers measured using a Siemens ADVIA-2400 included ALT, AST, alkaline phosphatase (ALP), albumin (ALB), blood urea nitrogen (BUN), creatinine (CCR),

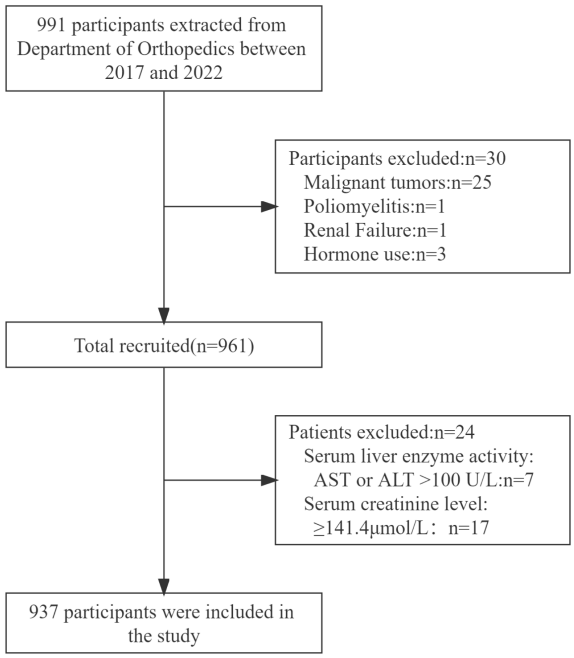

FIGURE 1
Flow diagram of the screening and enrollment processes of study participants. AST, aspartate aminotransferase; ALT, alanine aminotransferase.

triglycerides (TG), high-density lipoprotein cholesterol (HDL-C), low-density lipoprotein cholesterol (LDL-C), fasting plasma glucose (FPG), and C-reactive protein (CRP). HbA1c levels were evaluated using the TOSOH G8-90SL. An ALIFAX TEST1-2730 device was used to assess the erythrocyte sedimentation rate (ESR).

2.3 BMD measurements

DXA scans of the hips were acquired using the Hologic Discovery Wi (Hologic Inc., Bedford, MA, USA). All scanners were operated by certified personnel. The bone density analyzed was defined as the projected aBMD of the left femoral neck in participants without fractures. The contralateral femoral neck was measured in patients with hip fractures.

The HSA program used in this study was created at Johns Hopkins University and incorporated into Hologic's APEX product. As previously described (8), the HSA algorithm calculates structural parameters directly from the mass profiles: the total mineralized bone surface in the cross-section (CSA, cm^2), cross-sectional moment of inertia (CSMI, cm^4), section modulus (SM, cm^3), and FNW (cm), the femoral neck area divided by the width of the neck box (the width of the femoral neck region was standardized at 1.5 cm).

2.4 Minimal model of hip structure

After revisiting the beam theory, the MM was conceived by KB and developed by Khoo et al. (11). The standard deviation of this mineral mass projection profile was Sigma (σ, cm), which is a measure of the variability of the mineral mass distribution along the mineral mass projection profile. Delta (δ, cm) represents the distance between the center of mass and the center of geometry for the mineral mass projection profile, indicating the section's asymmetry. These two variables, in addition to BMD and FNW, constitute MM. Calculated from HSA measures, σ (Equation 1) and δ (Equation 2) can be defined as follows:

$$\sigma = \sqrt{\frac{CSMI}{CSA}} \tag{1}$$

$$\delta = \left(\frac{CSMI}{SM} - \frac{FNW}{2}\right) \tag{2}$$

2.5 Statistical analysis

Patients were categorized into two groups according to the incidence of hip fractures: normally distributed continuous variables are expressed as means ± standard deviations (SDs), whereas skewed continuous variables are reported as medians with interquartile ranges. Categorical variables are presented as percentages (%). The chi-squared test, independent samples t-test, and Kruskal–Wallis test were used for categorical, normally distributed variables, and skewed distributions, respectively. For continuous variables with missing values of <2%, missing values were substituted with means or median values.

The independent association between MM variables and risk of hip fracture was assessed using multivariate logistic regression analysis. Both non-adjusted and multivariate-adjusted models were used, with the results presented as odds ratios (ORs) and 95% confidence intervals (CIs). These confounders were selected based on expert judgment, previous scientific literature, and all significant covariates identified in univariate analysis. Two models were developed; model I was adjusted for age, BMI, and gender, and model II was adjusted for model I + diabetes, WBC, RBC, PLT, ALT, ALP, ALB, CCR, TG, LDL-C, FPG, CRP, and ESR.

Interaction and stratified analyses were performed based on gender, the presence of diabetes mellitus, age, and BMI. To measure the subgroup heterogeneity, we multiplied the two predictor variables and added a new term to the model. We assessed the potential effect of the modification of diabetes and Sigma on hip fracture risk by calculating the interactions on both multiplicative and additive scales. Sigma was categorized into two groups (dichotomized). A cross-product interaction term was incorporated into the logistic regression model to evaluate the multiplicative interactions. The additive interaction was evaluated using two indices: the relative excess risk due to the interaction (RERI) and the attributable proportion due to the interaction (AP) (14). Both the RERI and AP were 0 if there was no additive interaction.

Generalized additive models (GAM) were used to discern nonlinear relationships, considering that the MM variables were continuous, and potential confounders were adjusted for. Utilizing smoothed curves, a two-segment linear regression model was developed to ascertain the threshold effects. The threshold levels of Delta were established through a recursive methodology that included identifying turning points in conjunction with predefined intervals as well as selecting turning points that produced a maximum likelihood model. A log-likelihood ratio test was used to evaluate the two-segment linear regression model against a nonlinear linear model.

The evaluation of each model's predictive capability was conducted through receiver operating characteristic (ROC) curve analysis. The area under the ROC curve (AUC) served as a metric to assess the risk of hip fractures. The AUC of minimal model of hip structure was compared to the AUC of femoral neck BMD alone.

The R statistical software (version 4.2.2, http://www.R-project.org, The R Foundation) and Free Statistics Analysis Platform (version 1.9, Beijing, China, http://www.clinicalscientists.cn/freestatistics) were used to conduct all analyses (15). Free Statistics is a software program that provides user-friendly interfaces for common analysis and data visualization. The software uses R as the core statistical engine with a graphical user interface created in Python. Statistical significance was defined as a two-sided $p < 0.05$.

3 Results

3.1 Baseline characteristics of the study participants

This study included 937 Han Chinese individuals (293 men and 644 women). The baseline clinical and biochemical features of the patients stratified according to the incidence of hip fractures are presented in Table 1. The age of the participants ranged from 31 to 99 years, with a mean age of 68.3 years (SD = 10.5). Participants with fractures exhibited older age and greater height, FNW, and Sigma and Delta values than those without fractures. Additionally, they demonstrated significantly lower CSA, SM, BMI, and BMD values.

3.2 Logistic regression analyses

The risk of hip fracture increased with higher FNW (OR = 1.26; 95% CI: 1.20–1.32), Sigma values (OR = 1.06; 95% CI: 1.04–1.07), and Delta values (OR = 1.09; 95% CI:1.07–1.11) in the univariate logistic regression analyses. Additionally, a negative correlation was identified between the risk of hip fracture and BMD (OR = 0.47; 95% CI: 0.42–0.54). Age, BMI, WBC, RBC, PLT, ALT, ALP, ALB, CCR, TG, LDL-C, FPG, and CRP levels, and ESR were correlated with the risk of hip fracture, as adjusted in model II. Other factors such as AST, BUN, HDL-C, and HbA1c levels did not show significant associations (Supplementary Table 1).

The results of the multivariate logistic regression analysis are presented in Table 2. The association remained significant after controlling for age, BMI, and gender. In model II, BMD increase (per 0.1 g/cm^2) was associated with a 45% decrease in the risk of hip fracture (OR = 0.55; 95% CI: 0.45–0.68); however, FNW (per 0.1 cm), Sigma (per 0.01 cm), and Delta (per 0.01 cm) measurements were associated with an increased risk of hip fracture (OR = 1.28; 95% CI: 1.18–1.37; OR = 1.06; 95% CI: 1.03–1.09; OR = 1.06; 95% CI: 1.03–1.09).

3.3 Subgroup analyses

Subgroup analyses were conducted to further investigate the impact of age, gender, BMI, and diabetes on study outcomes. The results of these analyses are shown in Figure 2. The effect sizes of

TABLE 1 Baseline characteristics of participants.

Variables	Total (n = 937)	Without fracture (n = 689)	With fracture (n = 248)	*P*-value
gender, %				0.804
Male	293 (31.3)	217 (31.5)	76 (30.6)	
Female	644 (68.7)	472 (68.5)	172 (69.4)	
Age, years	68.3 ± 10.5	66.6 ± 9.5	73.0 ± 11.8	< 0.001
Diabetes, %				0.755
No	732 (78.1)	540 (78.4)	192 (77.4)	
Yes	205 (21.9)	149 (21.6)	56 (22.6)	
Weight, kg	62.9 ± 11.1	64.5 ± 11.0	58.5 ± 10.4	< 0.001
Height, m	1.58 ± 0.08	1.57 ± 0.08	1.60 ± 0.08	< 0.001
BMI, kg/m^2	25.1 ± 3.9	26.0 ± 3.7	22.7 ± 3.5	< 0.001
WBC, 10^9/L	6.2 (5.1, 7.8)	5.8 (4.9, 6.9)	8.0 (6.6, 9.8)	< 0.001
RBC, 10^9/L	4.3 ± 0.5	4.4 ± 0.5	4.1 ± 0.5	< 0.001
PLT, 10^9/L	211.9 ± 64.8	216.8 ± 59.1	198.3 ± 77.1	< 0.001
ALT, U/L	16.0 (12.0, 22.9)	17.0 (12.8, 23.7)	14.0 (11.0, 19.1)	< 0.001
AST, U/L	21.0 ± 8.6	20.9 ± 8.6	21.1 ± 8.7	0.684
ALP, U/L	80.6 ± 26.7	79.7 ± 26.3	83.3 ± 27.9	0.066
ALB, g/L	42.5 ± 4.2	43.5 ± 4.0	39.8 ± 3.8	< 0.001
BUN, mmol/L	5.8 (4.8, 6.9)	5.8 (4.8, 6.9)	5.7 (4.7, 7.0)	0.581
CCR, μmol/L	62.6 ± 16.8	62.0 ± 16.2	64.4 ± 18.4	0.05
TG, mmol/L	1.3 (0.9, 1.9)	1.4 (1.0, 2.0)	1.0 (0.8, 1.4)	< 0.001
HDL-C, mmol/L	1.4 ± 0.3	1.4 ± 0.3	1.4 ± 0.3	0.994

(Continued)

TABLE 1 Continued

Variables	Total (n = 937)	Without fracture (n = 689)	With fracture (n = 248)	*P*-value
LDL-C, mmol/L	2.6 ± 0.8	2.7 ± 0.7	2.4 ± 0.8	< 0.001
FPG, mmol/L	6.0 ± 1.8	5.9 ± 1.5	6.5 ± 2.5	< 0.001
CRP, mg/L	5.0 (3.5, 13.6)	5.0 (2.6, 6.1)	31.0 (9.7, 65.3)	< 0.001
HbA1c, %	6.2 ± 1.1	6.2 ± 1.0	6.2 ± 1.3	0.545
ESR, mm/h	21.0 (11.0, 34.0)	19.0 (9.0, 29.0)	28.0 (16.2, 46.0)	< 0.001
CSA, cm^2	2.572 ± 0.580	2.659 ± 0.548	2.331 ± 0.598	< 0.001
CSMI, cm^4	2.372 ± 0.895	2.380 ± 0.835	2.347 ± 1.047	0.616
SM, cm^3	1.201 ± 0.380	1.236 ± 0.356	1.105 ± 0.426	< 0.001
BMD, g/cm^2	0.785 ± 0.167	0.827 ± 0.153	0.668 ± 0.149	< 0.001
FNW, cm	3.458 ± 0.358	3.384 ± 0.317	3.664 ± 0.385	< 0.001
Sigma, cm	0.947 ± 0.096	0.934 ± 0.089	0.984 ± 0.103	< 0.001
Delta, cm	0.225 ± 0.081	0.211 ± 0.069	0.264 ± 0.098	< 0.001

Data presented are mean ± SD, median (Q1–Q3), or N (%).
BMI, body mass index; WBC, white blood cell; RBC, red blood cell; PLT, platelet; ALT, alanine aminotransferase; AST, aspartate aminotransferase; ALP, alkaline phosphatase; ALB, albumin; BUN, blood urea nitrogen; CCR, creatinine; TG, triglycerides; HDL-C, high-density lipoprotein cholesterol; LDL-C, low-density lipoprotein cholesterol; FPG, fasting plasma glucose; HbA1c, glycosylated hemoglobin type-A1c; CRP, C-reactive protein; ESR, erythrocyte sedimentation rate; BMD, bone mineral density; FNW, femoral neck width.

BMD, FNW, and Delta on the risk of hip fractures remained robust and reliable. Nevertheless, the association between Sigma and the risk of hip fracture was not statistically significant in the patients aged <65 years (OR = 1.04; 95% CI: 0.98–1.11) and diabetes (OR = 1.0; 95% CI: 0.94–1.07) groups. No interactions were detected, except for the impact of diabetes and Sigma on the risk of hip fracture (p for multiplicative interaction < 0.05). Subsequently, we analyzed additive interaction and observed no interactions between diabetes and Sigma regarding the risk of hip fractures (all p > 0.05; Supplementary Table 2).

3.4 GAM

A multivariate logistic regression model based on restricted cubic splines was used to fit the data with confounders adjusted in accordance with model II. The estimated dose–response curve revealed a substantial linear association between BMD, FNW, Sigma, and the risk of hip fracture (Supplementary Figure 1; p for nonlinearity > 0.05). A curved rather than a linear relationship was observed between the Delta measurement and risk of hip fracture after adjusting for all covariates. Using a two-segment linear regression model, the Delta value was 0.17 cm (Figure 3).

3.5 Threshold effect analysis

Above the threshold, the risk of hip fracture was significantly increased by 13% (OR = 1.13; 95% CI: 1.08–1.18) for every 0.01 cm Delta increase. When Delta was <0.17 cm, a decrease in Delta was linked to a higher risk of hip fracture; however, this association was not statistically significant (p > 0.05) (Table 3).

3.6 ROC analysis

Figure 4 presents the C-statistic for sensitivity and specificity regarding hip fracture risks. The area under the curve for predicting

TABLE 2 Association between simplified hip structure analysis method and the risk of hip fracture.

Variable	Nonadjusted	*P*-value	Adjust I	*P*-value	Adjust II	*P*-value
BMD, per 0.1 g/cm^2	0.47 (0.42~0.54)	<0.001	0.52 (0.44~0.60)	<0.001	0.55 (0.45~0.68)	<0.001
FNW, per 0.1 cm	1.26 (1.20~1.32)	<0.001	1.32 (1.24~1.40)	<0.001	1.28 (1.18~1.37)	<0.001
Sigma, per 0.01 cm	1.06 (1.04~1.07)	<0.001	1.07 (1.05~1.09)	<0.001	1.06 (1.03~1.09)	<0.001
Delta, per 0.01 cm	1.09 (1.07~1.11)	<0.001	1.08 (1.05~1.10)	<0.001	1.06 (1.03~1.09)	<0.001

Data are presented as ORs and 95% CIs.
Adjusted model I was adjusted for age, body mass index, and gender; adjusted model II was adjusted for model I + diabetes, white blood cells, red blood cells, platelets, alanine aminotransferase, alkaline phosphatase, albumin, creatinine, triglycerides, low-density lipoprotein cholesterol, fasting plasma glucose, C-reactive protein, and erythrocyte sedimentation rate.
BMD, bone mineral density; FNW, femoral neck width.

10.3389/fendo.2025.1558622

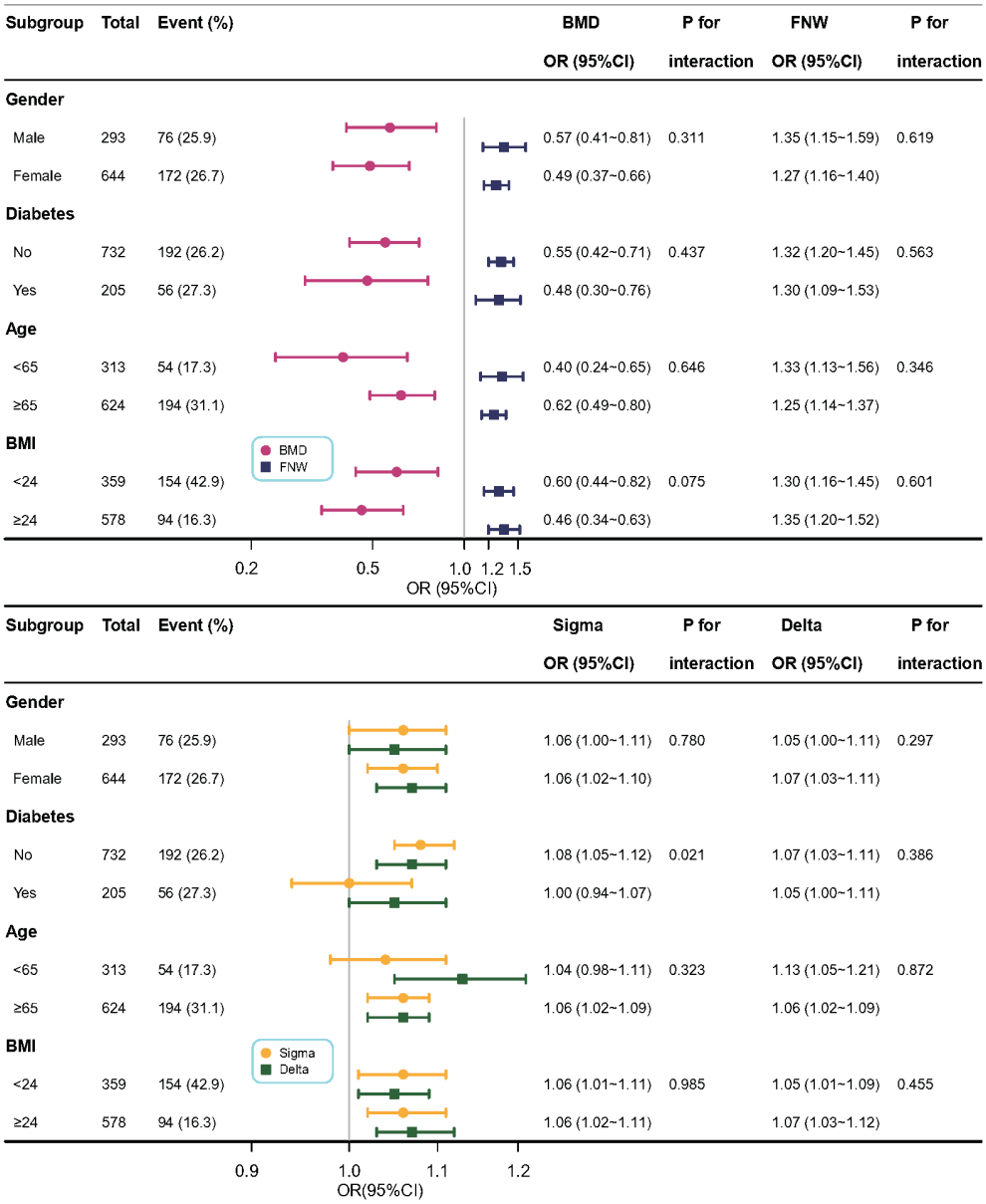

FIGURE 2
Association between BMD, FNW, Sigma, Delta, and the risk of hip fracture in Subgroup analyses based on gender, diabetes, age, and BMI. Each stratification adjusted for all factors (age, BMI, gender, diabetes, white blood cells, red blood cells, platelets, alanine aminotransferase, alkaline phosphatase, albumin, creatinine, triglycerides, low-density lipoprotein cholesterol, fasting plasma glucose, C-reactive protein, erythrocyte sedimentation rate) except the stratification factor itself. BMI, body mass index; BMD, bone mineral density; FNW, femoral neck width.

hip fractures based on BMD was 0.781 (0.747, 0.816). The AUC2 for minimal model of hip structure was significantly greater than that of BMD (0.838 vs 0.781, $p < 0.05$).

4 Discussion

This retrospective cross-sectional study included 937 Han Chinese adults, of whom 248 had hip fractures. Large increases in FNW and Sigma and Delta values and notable declines in BMD were separately and significantly linked to a higher risk of hip fracture after adjusting for age, BMI, gender, and clinical risk factors. The subgroup and additive interaction analyses confirmed the robustness of these associations. Apart from Delta measurement, we observed a linear association between BMD, FNW, Sigma, and the risk of hip fracture in the GAM analysis.

An increased Delta value indicates a downward shift in the center of mass, suggesting a decrease in bone mass in the upper region of the femoral neck cross-section (16). This deficiency in the superior segment is commonly acknowledged to contribute to hip fractures by facilitating buckling, a type of compressive failure (17). Prince has reported that each SD increment of Delta corresponded to a hazard ratio (HR) of 1.51 for the risk of femoral neck fracture (95% CI: 1.17–1.94) (12), aligning with findings reported by Khoo

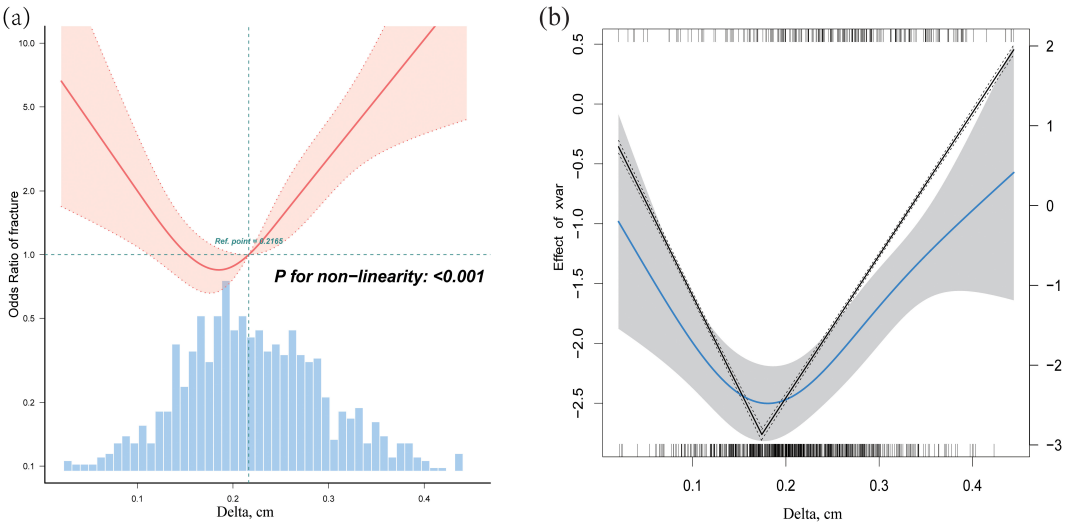

FIGURE 3
(a) A curved relationship between Delta and the risk of hip fracture. Adjustment factors included age, body mass index, gender, diabetes, white blood cells, red blood cells, platelets, alanine aminotransferase, alkaline phosphatase, albumin, creatinine, triglycerides, low-density lipoprotein cholesterol, fasting plasma glucose, C-reactive protein, and erythrocyte sedimentation rate. **(b)** Threshold levels of Delta were determined using a recursive approach that involved selecting turning points along with predefined intervals and selecting turning points that yielded a maximum likelihood model.

et al. (18, 19). In our study, an increase in Delta (per 0.01 cm) was linked to a 6% higher risk of hip fracture (OR = 1.06; 95% CI: 1.03–1.09).

Interestingly, the Delta value and risk of hip fracture showed a curved link. A decrease in Delta value was associated with a lower hip fracture risk (OR = 0.89; 95% CI: 0.76–1.04) when the Delta value decreased to <0.17 cm. Above the threshold, the risk of hip fracture increased considerably by 13% (OR = 1.13; 95% CI: 1.08–1.18) for every 0.01 cm increase in the Delta value. To the best of our knowledge, this study is the first to comprehensively elucidate the dose–response relationship, providing new insights into the prediction and treatment of femoral neck fractures.

However, the relationship between Sigma and fracture risk remains unclear. In a study involving elderly women from Beijing, Khoo et al. indicated a low Sigma (per SD) as a risk factor (OR = 0.70; 95% CI: 0.54–0.92) (19). However, Prince did not identify a significant association in the Perth Longitudinal Study of Aging in Women Sigma [(per SD); HR = 0.72; 95% CI: 0.46–1.10] (12). In Khoo's study, each SD increment of Sigma corresponded to a 116% increase in the risk of hip fracture among Chinese men (OR = 2.16; 95% CI: 1.24–3.78) (18). Our data indicate a significant association between Sigma and the risk of hip fractures [Sigma (per 0.01 cm); OR = 1.06; 95% CI: 1.03–1.09], applicable to both genders.

TABLE 3 Threshold effect analysis of the association between Delta values and the risk of hip fracture.

Outcome:	OR (95% CI)	*P*-value
One-line linear regression model	1.06 (1.03~1.09)	<0.001
Two-piecewise linear regression model		
< 0.17cm	0.89 (0.76~1.04)	0.151
≥ 0.17cm	1.13 (1.08~1.18)	<0.001
Log-likelihood ratio test		<0.001

Delta per change 0.01 cm. ORs were adjusted for age, body mass index, gender, diabetes, white blood cells, red blood cells, platelets, alanine aminotransferase, alkaline phosphatase, albumin, creatinine, triglycerides, low-density lipoprotein cholesterol, fasting plasma glucose, C-reactive protein, and erythrocyte sedimentation rate.

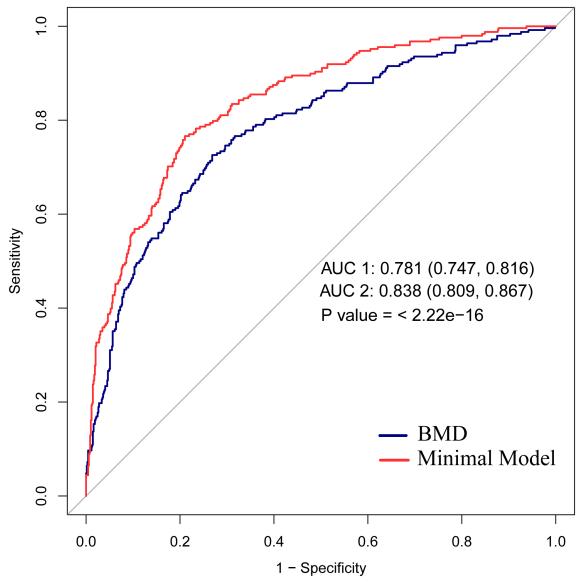

FIGURE 4
ROC analysis and AUC for hip fracture prediction. AUC1: BMD; AUC2: Minimal Model. BMD, FNW, Delta, and Sigma values comprised the minimal model variables. C statistics for the difference between AUC1 (0.781) and AUC2 (0.838), P < 0.001. BMD, bone mineral density; FNW, femoral neck width.

Greater Sigma values reflect a reduction in trabecular bone mass near the center of mass of the femoral neck cross-section because they indicate a larger mineral mass distribution (17).

In this study, we observed a lower BMD, greater FNW, wider mineral mass distribution around the center of mass, and an inferomedial shift in the center of mass, which were significantly associated with a higher risk of hip fractures, which is consistent with previous research findings (20–22). Structural inadequacy of the femoral neck may be correlated with the prevalent remodeling imbalance associated with aging (7, 23, 24). The limited mechanical requirements of middle and old age may be accommodated by the retention of the inferomedial femoral neck cortex and preferential loss of the superolateral cortex (25). This alteration may confer a protective effect during physiological stance loading as demonstrated by Fox et al. Conversely, it should reduce strength during bending during falls (26).

Multiple studies indicate that low BMD is the most sensitive predictor of hip fractures among clinical risk factors (27, 28). However, the present study demonstrated that minimal model of hip structure had a much greater prediction ability for hip fractures compared to BMD alone (AUC: 0.838 vs 0.781, $p < 0.05$). Our findings indicate that minimal model of hip structure may improve hip fracture risk assessments.

Our study has several limitations. First, this study was conducted on Han Chinese individuals; therefore, the findings may not apply to other ethnic groups. Second, the cross-sectional retrospective design prevented us from confirming a causal relationship between hip MM variables and risk of hip fractures. Third, we cannot rule out the possibility that unmeasured confusing elements could be responsible for the observed correlations, even after adjusting for confounding factors to the fullest extent possible. Finally, the two groups revealed some differences in baseline characteristics, and the participants with hip fractures were older than those without hip fractures. Nevertheless, we managed the most pertinent variables in the logistic regression models. Consequently, multicenter randomized controlled trials with robust designs are essential to validate our findings.

5 Conclusions

Large increases in FNW, Sigma and Delta values, and notable declines in BMD were separately and significantly linked to a high risk of hip fractures in Han Chinese adults. The Delta value and risk of hip fracture showed a curved link. Thus, our findings suggest that the minimal model of hip structure may improve hip fracture risk assessments.

Data availability statement

The datasets presented in this article are not readily available because the data contains sensitive patient information that is subject to strict confidentiality and ethical guidelines. The data includes personal health records and identifiable information, which cannot be shared publicly to protect patient privacy and comply with data protection regulations. Requests to access the datasets should be directed to Dan Zhao, gleam2024@163.com.

Ethics statement

The studies involving humans were approved by Ethics Review Board of Changzhou Second People's Hospital (approval number: KY017-01; April 24, 2023). The studies were conducted in accordance with the local legislation and institutional requirements. Written informed consent for participation was not required from the participants or the participants' legal guardians/next of kin in accordance with the national legislation and institutional requirements.

Author contributions

DZ: Conceptualization, Formal Analysis, Methodology, Software, Writing – original draft, Writing – review & editing. YB: Investigation, Supervision, Writing – original draft. HB: Data curation, Investigation, Writing – original draft. CZ: Investigation, Methodology, Writing – original draft. XY: Conceptualization, Project administration, Supervision, Writing – review & editing.

Funding

The author(s) declare that no financial support was received for the research and/or publication of this article.

Acknowledgments

We thank the Free Statistics team for providing technical assistance and valuable tools for data analysis and visualization. In addition, DZ wishes to thank all the members of the team of Clinical Scientists who have provided her with powerful spiritual support and encouragement.

Conflict of interest

The authors declare that the research was conducted in the absence of any commercial or financial relationships that could be construed as a potential conflict of interest.

Generative AI statement

The author(s) declare that no Generative AI was used in the creation of this manuscript.

Publisher's note

All claims expressed in this article are solely those of the authors and do not necessarily represent those of their affiliated organizations, or those of the publisher, the editors and the reviewers. Any product that may be evaluated in this article, or claim that may be made by its manufacturer, is not guaranteed or endorsed by the publisher.

Supplementary material

The Supplementary Material for this article can be found online at: https://www.frontiersin.org/articles/10.3389/fendo.2025.1558622/full#supplementary-material

References

1. Sing C-W, Lin T-C, Bartholomew S, Bell JS, Bennett C, Beyene K, et al. Global epidemiology of hip fractures: Secular trends in incidence rate, post-fracture treatment, and all-cause mortality. *J Bone Miner Res*. (2023) 38:1064–75. doi: 10.1002/jbmr.4821

2. Yang W, Li G, Liu J. The incidence, prevalence, and health burden of hip fractures in China: Data from the global burden of disease study 2019. *Prev Med Rep*. (2024) 38:102622. doi: 10.1016/j.pmedr.2024.102622

3. Marshall D, Johnell O, Wedel H. Meta-analysis of how well measures of bone mineral density predict occurrence of osteoporotic fractures. *BMJ*. (1996) 312:1254–9. doi: 10.1136/bmj.312.7041.1254

4. Nordin BEC, Prince RL, Tucker GRR. Bone density and fracture risk. *Med J Aust*. (2008) 189:7–8. doi: 10.5694/j.1326-5377.2008.tb01885.x

5. Nurzenski MK, Briffa NK, Price RI, Khoo BCC, Devine A, Beck TJ, et al. Geometric indices of bone strength are associated with physical activity and dietary calcium intake in healthy older women. *J Bone Miner Res*. (2007) 22:416–24. doi: 10.1359/jbmr.061115

6. Kaptoge S, Beck TJ, Reeve J, Stone KL, Hillier TA, Cauley JA, et al. Prediction of incident hip fracture risk by femur geometry variables measured by hip structural analysis in the study of osteoporotic fractures. *J Bone Miner Res*. (2008) 23:1892–904. doi: 10.1359/jbmr.080802

7. Poole KES, Mayhew PM, Rose CM, Brown JK, Bearcroft PJ, Loveridge N, et al. Changing structure of the femoral neck across the adult female lifespan. *J Bone Miner Res*. (2010) 25:482–91. doi: 10.1359/jbmr.090734

8. Beck TJ. Extending DXA beyond bone mineral density: Understanding hip structure analysis. *Curr Osteoporos Rep*. (2007) 5:49–55. doi: 10.1007/s11914-007-0002-4

9. Rathbun AM, Magaziner J, Shardell MD, Beck TJ, Yerges-Armstrong LM, Orwig D, et al. Differences in geometric strength at the contralateral hip between men with hip fracture and non-fractured comparators. *Bone*. (2020) 132:115187. doi: 10.1016/j.bone.2019.115187

10. Li L, Shen Y, Tan L-H, Zhang H, Dai R-C, Yuan L-Q, et al. Association of osteoporotic fractures of femoral neck and femoral neck geometric parameters in native Chinese women. *BMC Musculoskelet Disord*. (2024) 25:349. doi: 10.1186/s12891-024-07483-1

11. Khoo BCC, Brown K, Zhu K, Price RI, Prince RL. Effects of the assessment of 4 determinants of structural geometry on QCT- and DXA-derived hip structural analysis measurements in elderly women. *J Clin Densitom*. (2014) 17:38–46. doi: 10.1016/j.jocd.2013.03.009

12. Prince R, Khoo B, Brown K, Lewis J. Differences in femoral neck and trochanteric structure in elderly women prior to hip fracture: role in hip fracture prediction. *J Bone Miner Res*. (2023) 38:869–75. doi: 10.1002/jbmr.4789

13. Zhao D, Bai H, Bo Y. Association between composite indices of femoral neck strength and odds of hip fracture. *Arch Osteoporos*. (2024) 19:76. doi: 10.1007/s11657-024-01436-w

14. Assmann SF, Hosmer DW, Lemeshow S, Mundt KA. Confidence intervals for measures of interaction. *Epidemiology*. (1996) 7:286–90. doi: 10.1097/00001648-199605000-00012

15. Yang Q, Zheng J, Chen W, Chen X, Wen D, Chen W, et al. Association between preadmission metformin use and outcomes in intensive care unit patients with sepsis and type 2 diabetes: A cohort study. *Front Med (Lausanne)*. (2021) 8:640785. doi: 10.3389/fmed.2021.640785

16. Khoo BCC, Lewis JR, Brown K, Prince RL. Evaluation of a simplified hip structure analysis method for the prediction of incident hip fracture events. *Osteoporosis Int*. (2016) 27:241–8. doi: 10.1007/s00198-015-3282-z

17. Thomas CDL, Mayhew PM, Power J, Poole KE, Loveridge N, Clement JG, et al. Femoral neck trabecular bone: Loss with aging and role in preventing fracture. *J Bone Miner Res*. (2009) 24:1808–18. doi: 10.1359/jbmr.090504

18. Khoo BCC, Wang L, Lewis JR, Brown K, Cheng X, Prince RL. Structural factors associated with femoral neck fractures and its prediction in Chinese males. *J Clin Densitometry*. (2021) 24:597–602. doi: 10.1016/j.jocd.2021.01.002

19. Khoo BCC, Wang L, Lewis JR, Brown K, Cheng X, Prince RL. Anatomical factors associated with femoral neck fractures of elderly beijing women. *Arch Osteoporos*. (2020) 15:112. doi: 10.1007/s11657-020-00780-x

20. Rivadeneira F, Zillikens MC, De Laet CE, Hofman A, Uitterlinden AG, Beck TJ, et al. Femoral neck BMD is a strong predictor of hip fracture susceptibility in elderly men and women because it detects cortical bone instability: the Rotterdam study. *J Bone Miner Res*. (2007) 22:1781–90. doi: 10.1359/jbmr.070712

21. Ensrud KE, Schousboe JT, Crandall CJ, Leslie WD, Fink HA, Cawthon PM, et al. Hip fracture risk assessment tools for adults aged 80 years and older. *JAMA Netw Open*. (2024) 7:e2418612. doi: 10.1001/jamanetworkopen.2024.18612

22. Tobias JH, Nethander M, Faber BG, Heppenstall SV, Ebsim R, Cootes T, et al. Femoral neck width genetic risk score is a novel independent risk factor for hip fractures. *J Bone Mineral Res*. (2024) 39:241–51. doi: 10.1093/jbmr/zjae002

23. Johannesdottir F, Poole KES, Reeve J, Siggeirsdottir K, Aspelund T, Mogensen B, et al. Distribution of cortical bone in the femoral neck and hip fracture: A prospective case-control analysis of 143 incident hip fractures; the AGES-REYKJAVIK study. *Bone*. (2011) 48:1268–76. doi: 10.1016/j.bone.2011.03.776

24. K B, B K, L JR, P E, P Rl. Ageing effects on 3-dimensional femoral neck cross-sectional asymmetry: Implications for age-related bone fragility in falling. *J Clin densitometry*. (2019) 22(2):153-61. doi: 10.1016/j.jocd.2018.08.001

25. Mayhew PM, Thomas CD, Clement JG, Loveridge N, Beck TJ, Bonfield W, et al. Relation between age, femoral neck cortical stability, and hip fracture risk. *Lancet*. (2005) 366:129–35. doi: 10.1016/S0140-6736(05)66870-5

26. Jc F, Tm K. Trabecular eccentricity and bone adaptation. *J Theor Biol*. (2001) 212 (2):211-21. doi: 10.1006/jtbi.2001.2371

27. Johnell O, Kanis JA, Oden A, Johansson H, De Laet C, Delmas P, et al. Predictive value of BMD for hip and other fractures. *J Bone Miner Res*. (2005) 20:1185–94. doi: 10.1359/JBMR.050304

28. Svejme O, Ahlborg HG, Nilsson J-Å, Karlsson MK. Low BMD is an independent predictor of fracture and early menopause of mortality in post-menopausal women–a 34-year prospective study. *Maturitas*. (2013) 74:341–5. doi: 10.1016/j.maturitas.2013.01.002

frontiers | Frontiers in Endocrinology

TYPE Original Research
PUBLISHED 20 March 2025
DOI 10.3389/fendo.2025.1552780

OPEN ACCESS

EDITED BY
Nico Sollmann,
Ulm University Medical Center, Germany

REVIEWED BY
Vladimir Palicka,
University Hospital Hradec Kralove, Czechia
Plauto Christopher A. Watanabe,
University of São Paulo, Brazil

*CORRESPONDENCE
Lei Ma
malei@hebmu.edu.cn
Huangda An
anhuangda@hebmu.edu.cn

†These authors have contributed equally to this work and share first authorship

RECEIVED 29 December 2024
ACCEPTED 28 February 2025
PUBLISHED 20 March 2025

CITATION
Chen J, Zheng H, Li H, Yu Q, Li Y, An H and Ma L (2025) Evaluating bone mineral density in osteoporotic vertebral compression fractures: the clinical utility of anterior column Hounsfield units.
Front. Endocrinol. 16:1552780.
doi: 10.3389/fendo.2025.1552780

Evaluating bone mineral density in osteoporotic vertebral compression fractures: the clinical utility of anterior column Hounsfield units

Jiabao Chen[1†], Han Zheng[1†], Haotian Li[1†], Qingsong Yu[1], Yanhong Li[2], Huangda An[1*] and Lei Ma[1*]

[1]Department of Spinal Surgery, The Third Hospital of Hebei Medical University, Shijiazhuang, China, [2]Department of cardiology, Hebei General Hospital, Shijiazhuang, China

Study Design: Retrospective radiological analysis.

Objective: This study aimed to evaluate the clinical utility of anterior column Hounsfield units (HU) in assessing bone mineral density (BMD) in patients with osteoporotic vertebral compression fractures (OVCFs) and to investigate its potential advantages over traditional measurement methods.

Method: In this retrospective study, we analyzed data from 106 patients with acute OVCFs treated between January 2020 and June 2024. Inclusion criteria encompassed single-segment fractures from T10 to L2, with clear imaging results. HU values were measured from computed tomography (CT) scans, specifically targeting the anterior column of the vertebral body. Interobserver reliability was assessed via intraclass correlation coefficients (ICCs). Correlations between HU values, dual-energy X-ray absorptiometry (DEXA) results, and vertebral compression degrees were analyzed using Pearson correlation and receiver operating characteristic (ROC) curve analysis.

Results: The average HU values were significantly lower in the anterior column (50.39 ± 21.62 HU) compared to the middle column (63.12 ± 25.14 HU). The anterior column HU values showed a strong positive correlation with DEXA T-scores (r = 0.643) and BMD (r = 0.656). The degree of vertebral compression also correlated positively with both HU values and DEXA results, with the anterior column HU demonstrating the highest correlation (r = 0.727). ROC analysis indicated that the anterior column HU value had the largest area under the curve (AUC = 0.913) for predicting severe OVCFs, with an optimal cutoff of 59.07 HU.

Conclusion: The anterior column HU value serves as a superior predictor of BMD in patients with OVCFs compared to traditional methods. This study highlights the potential of using anterior column HU measurements to guide clinical decision-making regarding treatment options for OVCF patients, suggesting a

shift towards more nuanced assessment strategies in osteoporosis management. Further research with larger sample sizes is warranted to validate these findings and explore the comprehensive application of HU values in osteoporosis evaluation.

KEYWORDS

Hounsfield unit, osteoporosis, bone mineral density, osteoporotic vertebral compression fractures (OVCFs), spinal surgery

Introduction

Osteoporosis is characterized by a decrease in bone density for various reasons, along with the destruction of bone microstructure, which leads to increased bone fragility. Dual - energy X - ray absorptiometry (DXA) is currently the gold standard for quantifying bone mineral density and diagnosing osteoporosis. However, it still has certain limitations in evaluating spinal bone (1). In recent years, the measurement of Hounsfield unit (HU) by computed tomography (CT) has become an accepted technique for assessing bone quality. Previous studies have demonstrated that the HU value is closely associated with bone mineral density and the compressive strength of bone (2–7) HU values have been widely utilized in osteoporosis assessment, with the advantage of providing bone mineral density (BMD) data within the vertebrae. The CT HU value of the middle - axial image of the vertebral body is widely applied in clinical practice. It has high clinical value in predicting cage settlement and evaluating the pedicle screw holding force and may even be superior to the DEXA T - score (8–10).

For patients with vertebral compression fractures, it is very necessary to evaluate bone quality in order to guide the next step of treatment. Zou et al. (8) discovered that the L1 - HU value can serve as an excellent predictor of vertebral compression fractures. In their study, the average L1 - HU value in patients with acute vertebral fragility fractures was 66.0 HU. Nevertheless, this measurement fails to consider the uneven distribution of BMD within the vertebral body. Given the complexity of the spinal structure and the uniqueness of the load, the distribution of BMD in the vertebral bone is non – uniform (11).

In the majority of patients with osteoporotic vertebral compression fractures (OVCFs), the fracture typically occurs in the anterior column of the vertebral body (12, 13). Consequently, this study enhanced the measurement method for the CT HU value of the vertebral body. The HU value of the anterior column of the vertebral body was collected to explore its potential greater value for BMD assessment in OVCF patients.

The objectives of this study were twofold: first, to demonstrate the feasibility of the anterior - column CT HU value in evaluating the BMD of the thoracolumbar spines; second, to investigate the clinical application and advantages of the anterior - column CT HU value.

Methods

Patient cohort

This study received approval from the Institutional Review Board of our hospital. All patient data were retrospectively retrieved from the hospital's medical record system. We examined the files of patients who had been treated for OVCFs in our department between January 2020 and June 2024.

Inclusion criteria

1.Acute vertebral compression fracture resulting from low - energy trauma, involving a single segment within T10 - L2. 2.Clear MRI, X - ray, CT, and DEXA examinations were obtainable. 3.The morphology of the vertebral body adjacent to the fractured vertebra was normal.

Exclusion criteria

1.Multilevel vertebral compression fracture. 2.Vertebral compression fractures induced by high - energy trauma. 3.Pathological fracture. 4.History of spinal surgery. 5.Kummel disease or diffuse idiopathic skeletal hyperostosis (DISH) morphology. 6.Long - term use of glucocorticoids.

Date collection and assessment

The demographic data of the patients, such as gender, age, body mass index (BMI), and DEXA results, were recorded. Vertebral compression fractures were classified according to the method proposed by Genant (14). The imaging data were measured by two spine surgeons who had over three years of experience in imaging measurements. The HU measurement was obtained using a protocol similar to that described by Schreiber in CT examination.

All subjects were scanned with a 64 slice multi-detector CT scanner (Siemens Sensation 64, Erlangen, Germany) according to the following parameters: slice thickness 1.5 mm, distance 1.5 mm, tube voltage 120 kV. HU measurements were obtained from PACS (Picture Archiving and Communication Systems) Imaging System for lumbar vertebra.

For the vertebrae with compression fractures, two adjacent vertebrae were selected for the measurement of HU values. Three different axial sections in each vertebral body were chosen, namely immediately below the superior end plate, at the mid - vertebral body, and above the inferior end plate. At the mid - axial image, HU values were obtained following the methods described in previous studies (15). For the two axial slices close to the upper and lower end plates, two different locations in each axial slice were selected as regions of interest (ROI) for HU measurements: the anterior two - thirds of the vertebrae and the posterior one - third of the vertebrae. The ROI was designed to encompass as much trabecular bone as possible while avoiding cortical bone and heterogeneous areas such as the posterior venous plexus and bone islands. The average of the HU values in the anterior two - thirds of the vertebral body represents the HU value of the anterior column of the vertebral body, and the average HU value in the posterior one - third of the vertebral body represents the HU value of the middle column of the vertebral body (Figure 1).

For osteoporotic vertebral compression fractures, the compression ratio is defined as the ratio of the height of the most compressed part of the vertebral body to that of the posterior edge of the vertebral body. In cases where whole - body compression has occurred, the compression ratio for osteoporotic vertebral compression fractures is the ratio of the height of the most compressed part of the vertebral body to the average height of the posterior edges of the upper and lower vertebral bodies.

Statistical analysis

Data were analyzed using Statistical Product and Service Solutions software (version 26; SPSS, Chicago, IL). Continuous variables were documented as mean ± standard deviation. The interclass correlation coefficients (ICCs) were computed to appraise interobserver reliability. The Pearson correlation test was employed to analyze the correlation between the outcomes of different HU measurements and DEXA results. Receiver operating characteristic curve (ROC) analysis and the area under the curve (AUC) were utilized to assess the performance of using HU value and T - score in differentiating severe compression fractures.

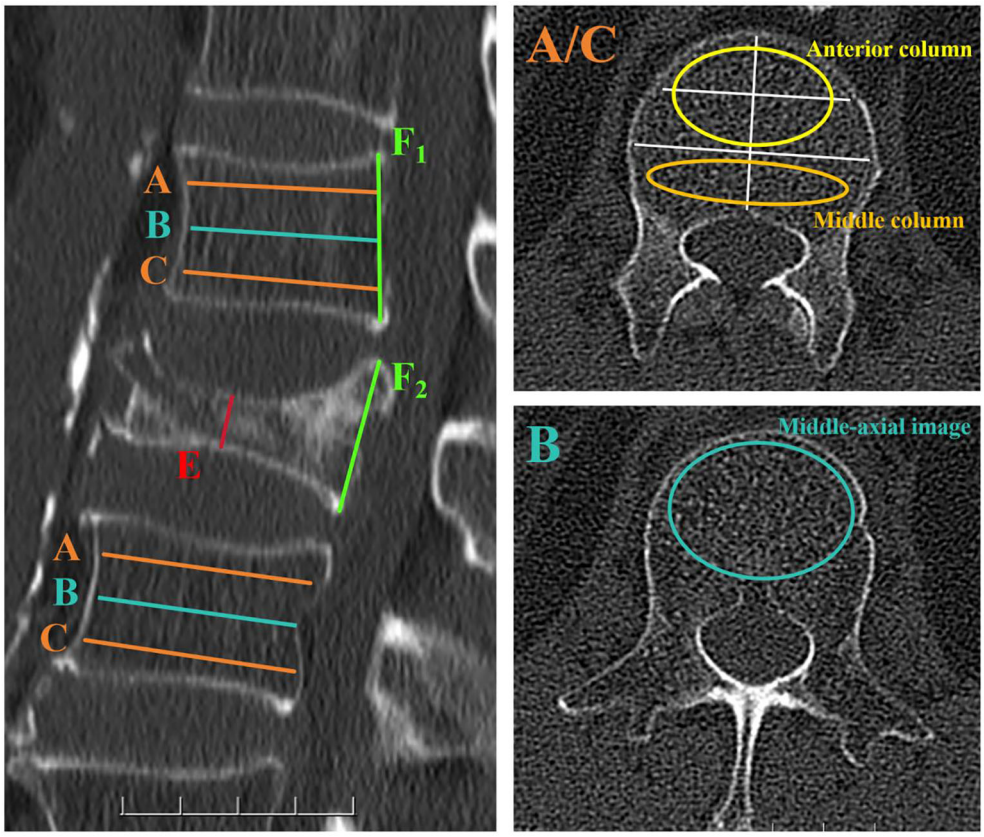

FIGURE 1
Computed tomography (CT) scan demonstrating the method for determining the HU value using an elliptical ROI. In the left - hand image, the axial slices of interest are shown on a sagittal slice of a CT scan of the lumbar vertebra. Slice A was obtained inferior to the superior end plate, while slice C was taken superior to the inferior end plate. Slice B represented the middle - axial image of the vertebral body. For slices A and C, two distinct locations on each axial slice were selected as ROIs for HU measurements: the anterior two - thirds of the vertebrae and the posterior one - third of the vertebrae. For slice B, a large elliptical area was used as an ROI to measure HU values. Elliptical ROIs were drawn as large as possible, excluding cortical edges to prevent volume averaging. The compression ratio of osteoporotic vertebral compression fractures was determined by E/F1. If no compression occurred at the posterior edge of the fractured vertebra, E/F2 was used to determine the compression ratio.

Results

Patient characteristics

A total of 106 patients were enrolled in the study, including 22 males and 84 females. The mean age of the patients was 70.92 ± 7.878 years. There were 7 cases of T10 fracture, 22 cases of T11 fracture, 33 cases of T12 fracture, 30 cases of L1 fracture and 14 cases of L2 fracture. The degree of fracture compression was graded according to Genant classification, including 4 patients with grade 0, 7 patients with grade 1, 37 patients with grade 2 and 58 patients with grade 3. The mean BMD and T value of DEXA were 0.53 ± 0.10g/cm2 and -2.88 ± 0.81, respectively. The average HU value of the axial position was 67.35 ± 28.31HU, the average HU value of the anterior column was 50.39 ± 21.62HU, and the average HU value of the middle column was 63.12 ± 25.14HU. The average vertebral compression ratio was 0.48 ± 0.14 (Tables 1, 2).

TABLE 1 Analysis of general data of 106 patients with OVCFs.

Variable	ALL (n=106)
Age	70.92 ± 7.878
Sex	
Male	22
Female	84
BMI	24.50 ± 2.76
Fractured vertebral body	
T10	7
T11	22
T12	33
L1	30
L2	14
Genant classification	
Grade 0	4
Grade 1	7
Grade 2	37
Grade 3	58
Femoral neck BMD	0.53 ± 0.10
Femoral neck T-score	-2.88 ± 0.81
HU value	
Anterior column	50.39 ± 21.62
Middle column	63.12 ± 25.14
Middle-axial image	67.35 ± 28.31
Vertebral compression ratio	0.48 ± 0.14

Consistency test

The inter-rater reliability of measurements obtained by two spinal surgeons was assessed using the Interclass Correlation Coefficient (ICC), which exceeded 0.96 at each location (Five ROI in each vertebral body), indicating high agreement between the data measured. For the vertebral compression ratio, the ICC across the 106 cases for both observers was 0.975, which indicated high agreement between the data measured.

Correlation between T - value/BMD value of DEXA and HU value of anterior and middle vertebral column

Both anterior and middle column CT HU values were positively correlated with the femoral neck T - score/BMD in DEXA results. (Table 3, Figure 2) The correlation coefficient between the HU value of anterior column and T-score (r = 0.643)/BMD (r = 0.656) was the highest, which was greater than that between the middle-axial image HU value and T - score (r = 0.555)/BMD (r = 0.564).

Correlation between vertebral compression degree and DEXA results as well as HU values

In patients with osteoporotic vertebral compression fractures, the degree of vertebral compression exhibited a positive correlation with both HU values and DEXA results. Notably, the HU value of the anterior column and the degree of vertebral compression demonstrated a relatively high Pearson correlation coefficient (r = 0.727) (Table 4).

Identifying optimal predictors for severe osteoporotic fractures using ROC curves

ROC curves were generated and the area under the curve (AUC) was measured to identify the optimal predictors for severe osteoporotic compression fractures (Grade 3). The results demonstrated that the ROC curve of the anterior column HU value had the largest AUC of 0.913. The Youden index was utilized to determine the optimal cutoff value of 59.07 HU, with a sensitivity of 0.75 and a specificity of 0.914. The AUC of the ROC curve of the HU value in the middle - axial image was 0.836, and the Youden index determined the optimum critical value to be 64.55 HU, with a sensitivity of 0.833 and a specificity of 0.724. The AUC of the ROC curve of the T - score was 0.820, and the Youden index determined the optimum critical value to be - 2.85, with a sensitivity of 0.813 and a specificity of 0.759 (Figure 3).

TABLE 2 Evaluation of BMD for different degrees of vertebral compression fractures.

		Grade0-2 (n=48)	Grade 3 (n=58)	ALL (n=106)
Femoral neck BMD		0.59 ± 0.09	0.49 ± 0.08	0.53 ± 0.10
Femoral neck T-score		-2.42 ± 0.71	-3.26 ± 0.68	-2.88 ± 0.81
HU Value	Anterior column	66.76 ± 14.20	36.85 ± 16.80	50.39 ± 21.62
	Middle column	81.01 ± 17.90	48.31 ± 20.18	63.12 ± 25.14
	Middle-axial image	85.22 ± 23.97	52.56 ± 22.61	67.35 ± 28.31

Discussion

Osteoporosis frequently occurs in the elderly and postmenopausal women, thereby augmenting their fracture risk and imposing a burden on society. In accordance with national and international guidelines, bone quality should be evaluated by DEXA or quantitative computed tomography (qCT). DEXA, a non - invasive spectral imaging method, is regarded as the gold standard for diagnosing osteoporosis. Nevertheless, spinal degeneration might result in inaccurate BMD measurements when using this technique (16). Quantitative computed tomography can surmount these limitations. In qCT, HU are converted to BMD values via software using a standard CT scanner and additional reference standards. However, this technique is not the preferred recommendation of the World Health Organization (WHO) for BMD measurement and is not as extensively utilized as DEXA.

At present, the average HU value of the lumbar spine has been widely utilized in clinical practice. The common approach for HU measurement is to select the region of interest in the mid - axial image of the vertebral body. However, as per previous studies, the uneven distribution of bone mineral density within the vertebral body has been rarely taken into account. According to the Delpech - Wolff law, bone formation is influenced by mechanical stimuli. The distribution of pressure and tension molds the microstructure of the bone and promotes bone formation, thereby increasing bone density, and vice versa. The structure of the human spine is complex. The spine endures multi - dimensional stress and shear forces, and the load within the spine is highly complex; thus, the distribution of bone mineral density is also uneven.

In clinical practice, the uneven distribution of BMD in vertebrae is frequently overlooked. Consequently, the application and measurement of HU values require improvement. In 1984, Ferguson refined Denis's three - column theory of the spine. Ferguson defined the anterior column as the anterior longitudinal ligament and the anterior two - thirds of the vertebral body and disc, and the middle column as the posterior longitudinal ligament and the posterior one - third of the vertebral body and disc. In this study, we enhanced the measurement method of HU values and selected the ROI at the anterior column of the vertebral body.

TABLE 3 Pearson correlation coefficients between CT HU values of different ROI of the vertebral body and femoral neck T-score or BMD in DEXA.

		Correlation coefficients	
		T-score	BMD
HU Value	Anterior column	0.643**	0.656**
	Middle column	0.609**	0.627**
	Middle-axial image	0.555**	0.564**

**P value<0.001.

Feasibility of anterior column HU value in evaluating vertebral BMD

In this study, the ROI for HU value measurement was selected differently from previous studies. Slices adjacent to the upper and lower endplates were chosen as the ROI to measure the HU value of the anterior column. Meanwhile, according to previous studies, the middle - axial image of the vertebral body was selected as the ROI for reference. The results demonstrated that both the HU values of the anterior column and those of the middle - axial image were significantly correlated with the DEXA results. This suggests that the anterior column HU value can serve as a reliable indicator for bone mineral density evaluation in OVCF patients.

Moreover, the HU values of the anterior column were more strongly correlated with the DEXA results than those of the middle - axial images. In light of this result, we supposed that there could be more blood vessels in the middle - axial image of the vertebral body, although the ROI did not include the vertebral basal vein foramen.

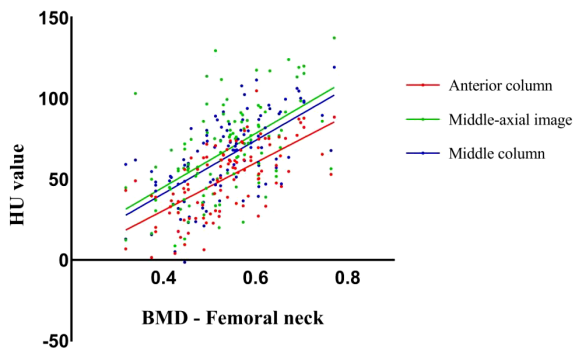

FIGURE 2
Scatter plots showed the correlation between CT HU values in different ROI of the vertebral body and bone mineral density scores obtained from DEXA of the femoral neck.

TABLE 4 Pearson correlation coefficients between vertebral compression ratio and CT HU value/DEXA results.

		HU Value			T-score	BMD
		Anterior column	Middle column	Middle-axial image		
Vertebral compression ratio	Correlation coefficients	0.727	0.657	0.600	0.502	0.517
	p	0.000	0.000	0.000	0.000	0.000

In elderly patients with osteoporosis, uncalcified or calcified blood vessels in the vertebra may interfere with the measurement of HU values. Thus, HU values measured away from the middle - axial images are more strongly correlated with DEXA results.

The utility of anterior column hu value in assessing vertebral bone mineral density

In the spinal structure, the intervertebral disc and facet joints exhibit a certain degree of motion during spinal flexion and extension. This causes the middle column of the spine to function analogously to the fulcrum of a seesaw. Consequently, relative to the anterior column of the vertebral body, the middle column bears more stress, leading to a higher bone mineral density. However, when a vertebral compression fracture occurs, it is typically a result of a relatively stronger load on the anterior column of the spine.

In this study, according to the three - column theory of the spine, not only were the HU values of the middle - axial image measured, but also the CT HU values of the anterior and middle columns of the vertebral body were measured. The results demonstrated that there was a significant difference between the average HU value of the anterior column and that of the middle - axial image, with the HU value of the anterior column being lower. In the T10 - L2 vertebral body, compared with other osteoporosis evaluation indicators, the HU value of the anterior column and the degree of vertebral compression exhibited a more obvious correlation. Moreover, the HU value of the anterior column has a higher predictive value for severe OVCF (grade 3), which may offer important information for the selection of treatment options for OVCF patients.

In previous clinical experiences, the majority of patients with OVCF are recommended to stay in absolute bed rest (ABR) for one to two months prior to getting out of bed. Nevertheless, long - term bed rest can result in a series of complications, including pneumonia, bedsore, urinary tract infection, deep vein thrombosis, and cerebral infarction. Even just one week of ABR can cause severe muscle atrophy and insulin resistance throughout the body (17). Moreover, bone formation ceases during ABR, leading to further bone loss. Previous studies have proposed that patients with OVCF might benefit from a short - term 3 - day ABR followed by bracing (18). However, this treatment has not been accepted by most clinicians yet.

In this study, we observed that the HU value in the middle column of the vertebra was substantially higher than that in the anterior column, signifying a greater BMD in the middle column. This surely offers a foundation for the short - term ARB treatment concept in OVCF patients. With the brace's protection, the anterior column of the OVCF vertebral body can evade excessive stress, while the middle column can endure relatively more stress. Nevertheless, we also noted that patients with severe OVCF (Grade 3) had an average anterior - column HU of merely 36.85, implying that patients with short - term ARB might be at a higher risk of further vertebral compression.

ROC curves were employed to analyze the predictive value of these osteoporosis measures for severe OVCFs. The results

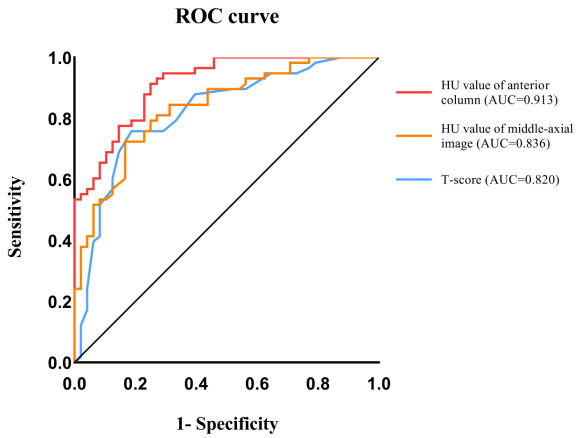

FIGURE 3
Receiver-operating characteristic curve (ROC) analysis was used to evaluate the performance of HU value and T-score in distinguishing severe compression fractures.

demonstrate that the anterior column HU value has the highest AUC, indicating a higher predictive value for severe OVCFs. The AUC of the ROC curve for the anterior - column HU value was 0.913, and the optimal cut - off value, determined by the Youden index, was 59.07 HU, with a specificity of 0.9140. The results suggest that when the HU value of the anterior column of the vertebral body is greater than 59.07, severe vertebral compression fracture is less likely to occur upon the vertebral body being subjected to low - energy trauma.

To the best of our knowledge, no studies have yet identified a suitable BMD evaluation index for assessing whether OVCF patients are suitable for short - term ABR. This study offers insights for subsequent clinical diagnosis and treatment, and the anterior - column HU value can serve as a favorable BMD evaluation index to guide patients towards further treatment. We look forward to future studies further validating these results and exploring the broader application of HU values in osteoporosis assessment.

Limitations

Although the results of this study provide new insights for clinical practice, there are still some limitations: 1.In this study, strict inclusion criteria were adopted for restriction, so the sample size of patients was small, and studies with a larger sample size are still required for verification. 2.Previous studies have shown that vertebral compression fractures are related to other factors such as lumbar muscle strength, but similar parameters were not included in this study. 3.This study only conducted research on patients with OVCFs, lacking the comparison of the anterior column HU values in non - OVCFs patients. 4.This study did not explore the comprehensive application of HU values and other osteoporosis - related indicators, and multi - index combined evaluation can be considered in the future.

Data availability statement

The raw data supporting the conclusions of this article will be made available by the authors, without undue reservation.

Ethics statement

The studies involving humans were approved by Medical Ethics Committee of the Third Hospital of Hebei Medical University. The studies were conducted in accordance with the local legislation and institutional requirements. Written informed consent for participation was not required from the participants or the participants' legal guardians/next of kin in accordance with the national legislation and institutional requirements.

Author contributions

JC: Writing – original draft, Writing – review & editing. HZ: Writing – original draft. HL: Writing – original draft. QY: Writing – original draft. YL: Writing – original draft. HA: Writing – review & editing. LM: Writing – review & editing.

Funding

The author(s) declare that financial support was received for the research and/or publication of this article. The work was supported by Hebei Province medical technology tracking project (GZ2024051) and Hebei Natural Science Foundation (H2020206379).

Conflict of interest

The authors declare that the research was conducted in the absence of any commercial or financial relationships that could be construed as a potential conflict of interest.

Generative AI statement

The author(s) declare that no Generative AI was used in the creation of this manuscript.

Publisher's note

All claims expressed in this article are solely those of the authors and do not necessarily represent those of their affiliated organizations, or those of the publisher, the editors and the reviewers. Any product that may be evaluated in this article, or claim that may be made by its manufacturer, is not guaranteed or endorsed by the publisher.

References

1. Li C, Lai XM, Liu N, Lin Y, Hu W. Correlation analysis of the vertebral compression degree and CT HU value in elderly patients with osteoporotic thoracolumbar fractures. *J Orthop Surg Res.* (2023) 18:457. doi: 10.1186/s13018-023-03941-z

2. Schreiber JJ, Anderson PA, Rosas HG, Buchholz AL, Au AG. Hounsfield units for assessing bone mineral density and strength: a tool for osteoporosis management. *J Bone Joint Surg Am.* (2011) 93:1057–63. doi: 10.2106/JBJS.J.00160

3. Lee S, Chung CK, Oh SH, Park SB. Correlation between bone mineral density measured by dual-energy X-ray absorptiometry and hounsfield units measured by diagnostic CT in lumbar spine. *J Korean Neurosurg Soc.* (2013) 54:384–9. doi: 10.3340/jkns.2013.54.5.384

4. Silva IM, Freitas DQ, Ambrosano GM, Bóscolo FN, Almeida SM. Bone density: comparative evaluation of Hounsfield units in multislice and cone-beam computed tomography. *Braz Oral Res.* (2012) 26:550–6. doi: 10.1590/S1806-83242012000600011

5. Mi J, Li K, Zhao X, Zhao CQ, Li H, Zhao J. Vertebral body compressive strength evaluated by dual-energy X-ray absorptiometry and hounsfield units *in vitro*. *J Clin Densitom*. (2018) 21(1):148–53. doi: 10.1016/j.jocd.2016.08.011

6. Zou D, Jiang S, Zhou S, Sun Z, Zhong W, Du G, et al. Prevalence of osteoporosis in patients undergoing lumbar fusion for lumbar degenerative diseases: A combination of DXA and hounsfield units. *Spine (Phila Pa 1976)*. (2020) 45(7):E406–10. doi: 10.1097/BRS.0000000000003284

7. Choi MK, Kim SM, Lim JK. Diagnostic efficacy of Hounsfield units in spine CT for the assessment of real bone mineral density of degenerative spine: correlation study between T-scores determined by DEXA scan and Hounsfield units from CT. *Acta Neurochir (Wien)*. (2016) 158:1421–7. doi: 10.1007/s00701-016-2821-5

8. Zou D, Ye K, Tian Y, Li W, Zhou F, Zhang Z, et al. Characteristics of vertebral CT Hounsfield units in elderly patients with acute vertebral fragility fractures. *Eur Spine J*. (2020) 29(5):1092–7. doi: 10.1007/s00586-020-06363-1

9. Pisano AJ, Fredericks DR, Steelman T, Riccio C, Helgeson MD, Wagner SC. Lumbar disc height and vertebral Hounsfield units: association with interbody cage subsidence. *Neurosurg Focus*. (2020) 49(2):E9. doi: 10.3171/2020.4.FOCUS20286

10. Li W, Zhu H, Hua Z, Miao D, Wang F, Tong T, et al. Vertebral bone quality score as a predictor of pedicle screw loosening following surgery for degenerative lumbar disease. *Spine (Phila Pa 1976)*. (2023) 48(23):1635–41. doi: 10.1097/BRS.0000000000004577

11. Chen J, Li Y, Zheng H, Li H, Wang H, Ma L. Hounsfield unit for assessing bone mineral density distribution within lumbar vertebrae and its clinical values. *Front Endocrinol (Lausanne)*. (2024) 15:1398367. doi: 10.3389/fendo.2024.1398367 Erratum in: *Front Endocrinol (Lausanne)*. (2025) 16:1568596. doi: 10.3389/fendo.2025.1568596

12. Denis F. The three column spine and its significance in the classification of acute thoracolumbar spinal injuries. *Spine (Phila Pa 1976)*. (1983) 8:817–31. doi: 10.1097/00007632-198311000-00003

13. Denis F. Spinal instability as defined by the three-column spine concept in acute spinal trauma. *Clin Orthop Relat Res*. (1984) 189):65–76. doi: 10.1097/00003086-198410000-00008

14. Genant HK, Wu CY, van Kuijk C, Nevitt MC. Vertebral fracture assessment using a semiquantitative technique. *J Bone Miner Res*. (1993) 8:1137–48. doi: 10.1002/jbmr.5650080915

15. Zou D, Li W, Deng C, Du G, Xu N. The use of CT Hounsfield unit values to identify the undiagnosed spinal osteoporosis in patients with lumbar degenerative diseases. *Eur Spine J*. (2019) 28:1758–66. doi: 10.1007/s00586-018-5776-9

16. Muraki S, Yamamoto S, Ishibashi H, Horiuchi T, Hosoi T, Orimo H, et al. Impact of degenerative spinal diseases on bone mineral density of the lumbar spine in elderly women. *Osteoporos Int*. (2004) 15(9):724–8. doi: 10.1007/s00198-004-1600-y

17. Dirks ML, Wall BT, van de Valk B, Holloway TM, Holloway GP, Chabowski A, et al. One week of bed rest leads to substantial muscle atrophy and induces whole-body insulin resistance in the absence of skeletal muscle lipid accumulation. *Diabetes*. (2016) 65(10):2862–75. doi: 10.2337/db15-1661

18. Cho ST, Kim SJ, Nam BJ, Kim KW, Lee GH, Kim JH. Absolute bed rest duration of 3 days for osteoporotic vertebral fractures: A retrospective study. *Asian Spine J*. (2022) 16(6):898–905. doi: 10.31616/asj.2021.0396

frontiers | Frontiers in Endocrinology

TYPE Original Research
PUBLISHED 26 March 2025
DOI 10.3389/fendo.2025.1566424

OPEN ACCESS

EDITED BY
Egon Burian,
Zurich University Hospital, Switzerland

REVIEWED BY
Ram Naresh Yadav,
Henry Ford Hospital, United States
Florian Gassert,
Technical University of Munich, Germany

*CORRESPONDENCE
Klaus Engelke
klaus.engelke@fau.de

RECEIVED 24 January 2025
ACCEPTED 05 March 2025
PUBLISHED 26 March 2025

CITATION
Hummel J, Engelke K, Freitag-Wolf S, Yilmas E, Bartenschlager S, Sigurdsson S, Gudnason V, Glüer CC and Chaudry O (2025) Trabecular texture and paraspinal muscle characteristics for prediction of first vertebral fracture: a QCT analysis from the AGES cohort. *Front. Endocrinol.* 16:1566424. doi: 10.3389/fendo.2025.1566424

Trabecular texture and paraspinal muscle characteristics for prediction of first vertebral fracture: a QCT analysis from the AGES cohort

Jana Hummel[1], Klaus Engelke[1]*, Sandra Freitag-Wolf[2], Eren Yilmas[3], Stefan Bartenschlager[1], Sigurdur Sigurdsson[4], Vilmundur Gudnason[4], Claus-C. Glüer[3] and Oliver Chaudry[1,5]

[1]Department of Medicine 3, Friedrich-Alexander-University Erlangen-Nürnberg and Universitätsklinikum Erlangen, Erlangen, Germany, [2]Institute of Medical Informatics and Statistics, Kiel University, Kiel, Germany, [3]Section Biomedical Imaging, Department of Radiology and Neuroradiology, Kiel University, Kiel, Germany, [4]Icelandic Heart Association Research Institute, Kopavogur, Iceland, [5]Institute of Radiology, Friedrich-Alexander-University Erlangen-Nürnberg and Universitätsklinikum Erlangen, Erlangen, Germany

Introduction: Vertebral fractures (VFs) significantly increase risk of subsequent fractures. Areal bone mineral density (BMD) assessed by DXA and volumetric BMD by QCT, are strong predictors of VF. Nevertheless, risk prediction should be further improved. This study used data from the Age, Gene/Environment Susceptibility Reykjavik (AGES-Reykjavik) cohort to evaluate whether trabecular texture and paraspinal muscle assessments improve the prediction of the first incident VF.

Methods: CT scans of the L1 and L2 vertebrae of 843 elderly subjects; including 167 subjects with incident, VFs occurring within a 5-year period and 676 controls without fractures. Image analysis included measurement of BMD, cortical thickness and of parameters characterizing trabecular architecture and the autochthonous muscles. Fifty variables were used as predictors, including a BMD, a trabecular texture and a muscle subset. Each included age, BMI and corresponding parameters of the QCT analysis. The number of variables in each subset was reduced using stepwise logistic regression to create multivariable fracture prediction models. Model accuracy was assessed using the likelihood ratio test (LRT) and the area under the curve (AUC) criteria. Bootstrap analyses were performed to assess the stability of the model selection process.

Results: 96 women and 78 men with prior VF were excluded. Of 50 initial predictors, 17 were significant for women and 11 for men. Bone and texture models showed significantly better fracture prediction in women ($p<0.001$) and men ($p<0.01$) than the combination of age and BMI. The muscle model showed better fracture prediction in men only ($p<0.03$). Compared to the BMD model alone, LRT showed a significantly improved VF prediction of the combinations of BMD with texture (women and men) ($p<0.05$) or with muscle models (men only) ($p=0.03$) but no significant increases in AUC values (AUC women: Age&BMI: 0.57, BMD: 0.69, combined model: 0.69; AUC men: Age&BMI: 0.63, BMD: 0.71, combined models 0.73-0.77)

Discussion: Trabecular texture and muscle parameters significantly improved prediction of first VF over age and BMI, but improvements were small compared to BMD, which remained the primary predictor for both sexes. Although muscle measures showed some predictive power, particularly in men, their clinical significance was marginal. Integral BMD should remain the focus for fracture risk assessment in clinical practice.

KEYWORDS

fracture prediction, vertebral fracture, computed tomography, BMD, muscle, trabecular texture

1 Introduction

Vertebral fractures (VF) are the most common type of osteoporotic fracture (1–3) and significantly increase the risk of subsequent vertebral and other osteoporotic fractures (4, 5). Therefore, risk prediction and prevention of VF is an important goal in osteoporosis (3, 6). Areal bone mineral density (BMD) assessed by Dual X-ray Energy Absorptiometry (DXA) and volumetric BMD assessed by Quantitative Computed Tomography (QCT) are strong predictors of VF. Standardized risk ratios of approximately 2-3 have been determined (7–9), but risk prediction still should be improved and several QCT-based strategies have been developed toward this aim. One successful approach is the determination of vertebral strength by finite element analysis (FEA) (10, 11). Another is the measurement of additional parameters from the QCT scans, such as cortical thickness, trabecular texture and paraspinal muscle characteristics (12).

This study addresses two key questions: (1) Can fracture risk prediction be improved beyond standard BMD measurement? (2) Are additional parameters that would improve fracture risk prediction are easy to measure and applicable across different CT scanners and can they be measured with precision errors of 1-2% (13). From a clinical perspective the first question is most important but from a pathophysiological perspective it may be more interesting to determine whether muscle density, muscle volume and parameters characterizing the muscle fat infiltration predict fractures independently of BMD. Of further interest are the separate contributions of trabecular and cortical bone and of the trabecular architecture to the prediction of the first incident VF.

As shown by a recent meta-analysis there is an increasing number of studies evaluating the ability of QCT to discriminate prevalent VF (14). However, prospective studies using QCT to predict incident VF are rare. A number of different analyses using FEA and lumbar and thoracic BMD parameters have been reported for the AGES-Reykjavik study (7, 15). Thoracic trabecular BMD also predicted incident VF in a large multiethnic MESA study of 6800 subjects with atherosclerosis (16). However, a multivariable approach has not been reported so far.

The relevance of paraspinal, thigh and pelvic muscles and also of soft tissue characteristics for hip (17–21), vertebral (22–24) or multiple (25) fractures has been addressed in several recent CT studies. However, most of these studies focused on the hip and most of them were cross-sectional in design with limited sample size, making the interpretation of multivariable results difficult. As summarized in a recent review (26), other studies have used magnetic resonance imaging to investigate the associations between paraspinal muscle characteristics and osteoporotic fracture, but these studies did not obtain BMD data and MR studies are too time consuming and expensive for wide spread use.

In this study we used a subset of the prospective Age, Gene/Environment Susceptibility Reykjavik (AGES-Reykjavik) study, a large epidemiologic study from Iceland (27) to compare the prognostic power of various CT assessments, including BMD, trabecular texture and paraspinal muscle characteristics in univariate and multivariable models, hypothesizing that prediction of the first incident VF occurrence based on vertebral BMD by QCT may be improved by these additional assessments. The same subset of the AGES-Reykjavik study has been analyzed previously (8), allowing to put our results in perspective with vertebral strength measurement by FEA.

2 Materials and methods

2.1 Subjects

This study utilizes a retrospective analysis of CT scans of the lumbar vertebrae L1 and L2 from a subset of subjects of the study AGES-Reykjavik (27) of over 5,000 elderly subjects from Iceland. In summary, in a previous study (8) a case-control design was employed to select a subset of 843 subjects (497 women and 346 men). 167 subjects had sustained an incident spine fracture within a 5-year period. Spine fractures were confirmed on CT scout scans covering T6-L4, which were obtained at 5 years after baseline, using the Genant SQ scoring system (28). CT scout scans from the baseline CT scans were used to identify prior vertebral fractures,

i.e., those that were already present at the time of the baseline scan. By excluding those, incident vertebral fractures were identified. The 676 subjects of the control group were randomly selected from the AGES cohort without fractures.

2.2 CT scanning and analysis

All CT scans were performed using the same CT scanner (Sensation 4, Siemens, Erlangen, Germany) with the same CT acquisition and reconstruction protocol (120 kV, tube current modulation with 150 effective mAs, 50 cm FOV, 1 mm slice thickness, 1 mm reconstruction increment, B30s reconstruction kernel). An Image Analysis type 4 phantom (Image Analysis, Inc., Columbia, KY) was utilized for the purpose of simultaneous calibration of CT to BMD values. In the majority of subjects, the CT scan encompassed L1 and L2 vertebrae. However, in cases of fracture or other conditions that resulted in the exclusion of one of these vertebrae from the analysis, T12 and L1 or L2 and L3 vertebrae were scanned instead. The QCT analysis was performed using MIAF-Spine version 6.0.7 (Figure 1, Supplementary Figure S1). All QCT parameters that were analyzed were averaged over the two vertebrae that were covered by the CT scan. It should be noted that DXA scans were not obtained.

A comprehensive investigation was conducted, encompassing the measurement of three distinct QCT subsets (S1–S3). The first subset, designated as S1 - BMD set, involved a conventional analysis of integral, cortical, and trabecular BMD, BMC, and volume, complemented by an assessment of cortical thickness (13). The second set (S2 - texture set) involved parameters that characterized the trabecular architecture of the vertebral body. The third set (S3 - muscle set) involved parameters that characterized the autochthonous muscles at the vertebral levels present in the CT scan (Figure 1). A detailed description of the parameters used in this study is given in the Supplement. These muscles were not further subdivided. The psoas was not assessed because in comparison to the autochthonous muscles the percentage of intermuscular adipose tissue of the psoas is much lower and the distribution of the muscle tissue is more homogeneous. To enhance the reproducibility of the autochthonous muscle parameters, the outer edges of the muscles were excluded from the segmentation process (29). The distribution of muscle fat infiltration was subsequently measured once more via texture parameters. Further details can be found in the Supplement (Figure S2).

2.3 Statistics

The initial data set comprised age, BMI, and 50 variables that were analyzed by MIAF-Spine. These variables served as predictors for the assessment of the first incident VF. Specifically, S1 comprised 18 predictors, S2 contained 7 predictors and S3 comprised 25 predictors. Detailed descriptions can be found in the Supplement. The z-transformation was employed to standardize all predictors. Subsequent analyses were conducted in two distinct groups: men and women. Sex-specific standard deviations of the control group were utilized for standardization purposes. Standardized age- and BMI-adjusted univariate odds ratios (OR) were calculated for each parameter.

For each subset S1-S3, stepwise logistic regression was used to obtain multivariable fracture prediction models. The initial number of predictors was reduced by minimizing the Akaike information criterion (30). The bidirectional stepwise selection was initiated with a model comprising only age and BMI, and it iteratively evaluated the inclusion or exclusion of predictors. Irrespective of their statistical significance, age and BMI were retained in all models. Other non-significant predictors ($p > 0.05$) were excluded. The variance inflation factor (VIF) was employed to assess multicollinearity. Predictors with VIF values greater than 5 were systematically eliminated, beginning with the predictor that

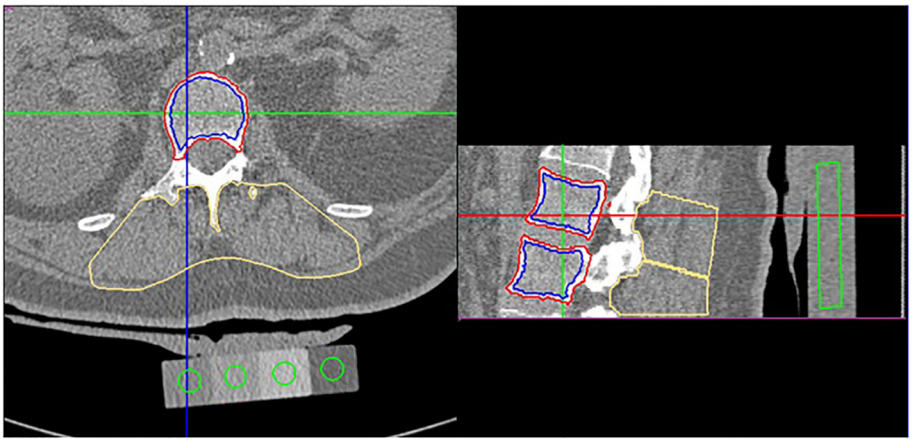

FIGURE 1
CT of the lumbar spine covering L1 and L2. The images show cropped axial and sagittal views. The green cylinders show the volumes of interest (VOIs) used to analyze the 4 different density compartments of the Image Analysis type 4 phantom. The red and blue contours delineate the integral and trabecular VOIs resulting from the 3D segmentation of L1 and L2. The yellow contours delineate the autochthonous muscle VOIs for L1 and L2.

exhibited the highest VIF. Subsequent to each elimination, a re-evaluation of the model ensued, resulting in the exclusion of further nonsignificant predictors. This iterative process was repeated until all VIF values were below 5, thereby ensuring minimal collinearity among the final predictors of each subset's model.

The BMD model S1 was selected as the reference model. Significant predictors from another subset model, e.g. the muscle model, were added to S1 to create combined models. The fracture prediction of the combined models was compared with that of S1 using nested logistic regression following the approach suggested by Harrell (30). To ascertain whether the combined model significantly improved fracture prediction compared to S1, the likelihood ratio test (LRT) was used. The LRT adheres to a chi-squared (χ^2) distribution and provides p-values for the comparison of nested models. Receiver operator characteristic (ROC) curves and their area under the curve (AUC) values, also used as performance metric, were compared using bootstrap confidence intervals (CI) and tests (31).

The same procedure was applied to compare fracture prediction of individual subsets S1-S3 with that of age and BMI. To assess the stability of the stepwise model selection process, a bootstrap analysis was performed with 1,000 resampled data sets. For each bootstrap sample, the stepwise procedure was repeated, and the frequency of predictor inclusion in the resulting models was recorded. Furthermore, the AUC values were calculated for each bootstrap iteration to assess the variability of model performance.

Finally, the combined models were also calculated in women with fracture SQ grades of 2 and 3, thereby excluding the mild SQ 1 fractures. All statistics were performed using R (R Core Team, version 4.3.2, functions 'stepAIC' [package: MASS] and 'roc.test' [package: pROC]).

3 Results

A total of 826 CT data sets (486 women and 340 men) of the original subsample of 843 subjects were analyzed. The analysis of CT scans from 17 subjects was not possible, for the majority of cases due to the presence of excessive osteophyte formation and substantial bone sclerosis in the vicinity of the endplates. At baseline, 96 of the 486 women and 78 of the 340 men had prior VF (Figure 2). These subjects were excluded from the analysis of the current study with the objective of determining the risk prediction of the first incident VF.

Patient characteristics and significant univariate predictors for fracture occurrence in women are shown in Table 1 and in men in Table 2. All univariate ORs were adjusted for age and BMI, which are also included in the aforementioned tables. In women, 17 of the initial 50 predictors were found to be significant predictors of future fractures, while in men, 11 of the initial 50 predictors were found to be significant. The non-significant predictors ($p < 0.05$) are not displayed in the tables.

In both sexes, a trabecular texture predictor demonstrated the numerically highest OR for the first incident VF. However, the confidence intervals of ORs for all significant predictors largely overlapped. It is noteworthy that among women, no muscle parameters exhibited statistically significant ORs for the first incident VF, while among men, only one muscle parameter demonstrated a statistically significant OR for the first incident VF. However, the means of this predictor did not differ significantly between male control and fracture cases ($p = 0.42$).

Table 3; Supplementary Tables S2, S3 present the results of the subset-specific stepwise logistic regressions. The AUC results are presented in Table 3. The predictors that remained in the S1, S2 and S3 models are listed in Supplementary Tables S2, S3. In addition to age and BMI, in the final models only one or two predictors remained of each subset, indicating a high correlation among the parameters analyzed of a given subset. For the sake of comparison, Table 3 also shows results of the model of age and BMI. From LRT results, the models based on S1 and S2 exhibited significantly ($p \leq 0.01$) higher fracture prediction than the combination of age and BMI alone (Table 4). This was also the case for S3 in men ($p = 0.03$) but not in women. Combinations of S2 and S3 models with S1 showed a significant improvement in VF prediction compared to S1 alone ($p < 0.05$), except for S3 in women.

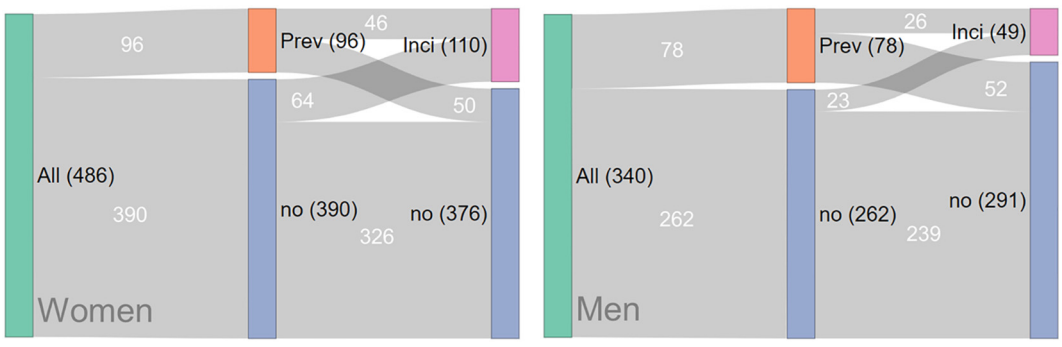

FIGURE 2
Sankey plots illustrating the populations of female and male subjects with prevalent, incident, and no vertebral fractures (VF). QCT images corresponding to the central blue and orange bars were available, while fracture status information for the right blue and pink bars was also included. Black numbers indicate the number of patients in each bar, while white numbers denote the contributions from other bars. It is important to note that subjects with prevalent fractures (orange) were excluded from the analysis in this study; thus, only patients represented in the central blue bar (controls and those with first incident VF) were included for analysis.

10.3389/fendo.2025.1566424

TABLE 1 Significant univariate predictors of the first incident vertebral fracture in women.

		Controls	Incident VF					
	n	326	64					
		Mean ± SD		AUC	CI	OR/SD	CI	p
	Age [y]	73.9 ± 5.1	75.2 ± 5.6	0.57	(0.49; 0.64)	0.79	(0.6; 1.0)	0.07
	BMI [kg/m^2]	27.6 ± 4.5	27.5 ± 5.2	0.51	(0.43; 0.60)	1.03	(0.8; 1.3)	0.83
Subset	Predictor	Mean ± SD		AUC	CI	OR/SD	CI	p
S2-Texture	Trab_gInhomo	73.9 ± 5.1	75.2 ± 5.6	0.66	(0.59; 0.73)	2.07	(1.4; 3.1)	< 0.001
S1-BMD	BMD_Int_tVB [mg/cm^3]	175.7 ± 37.5	156 ± 33.9	0.67	(0.60; 0.74)	1.86	(1.3; 2.6)	< 0.001
S1-BMD	BMD_Trab_mCy [mg/cm^3]	83.7 ± 33.3	67.6 ± 27.6	0.66	(0.59; 0.73)	1.84	(1.2; 2.7)	< 0.01
S1-BMD	BMC_Int_tVB [g]	5.6 ± 1.25	4.95 ± 1.08	0.67	(0.59; 0.74)	1.84	(1.3; 2.6)	< 0.001
S2-Texture	Trab_Vario_slope	6.1 ± 1	5.8 ± 0.8	0.62	(0.55; 0.70)	1.83	(1.2; 2.8)	< 0.01
S1-BMD	BMD_Trab_tVB [mg/cm^3]	90.8 ± 30.5	75.8 ± 28.6	0.66	(0.59; 0.73)	1.79	(1.2; 2.5)	< 0.01
S1-BMD	BMD_Trab_cCy [mg/cm^3]	77.9 ± 29.5	64.2 ± 25.5	0.65	(0.58; 0.72)	1.78	(1.2; 2.6)	< 0.01
S1-BMD	BMC_Trab_tVB [g]	1.72 ± 0.56	1.45 ± 0.5	0.65	(0.58; 0.72)	1.74	(1.2; 2.4)	< 0.01
S1-BMD	Thick_Cort_LE [mm]	1.06 ± 0.13	1.02 ± 0.07	0.62	(0.55; 0.69)	1.70	(1.1; 2.5)	< 0.01
S1-BMD	BMC_Cort_tVB [g]	2.79 ± 0.7	2.48 ± 0.61	0.65	(0.58; 0.72)	1.70	(1.2; 2.4)	< 0.01
S1-BMD	BMD_Cort_tVB [mg/cm^3]	367.1 ± 52.9	342.4 ± 51.2	0.65	(0.57; 0.73)	1.64	(1.2; 2.2)	< 0.01
S1-BMD	BMC_Cort_mVB [g]	0.62 ± 0.2	0.54 ± 0.17	0.64	(0.56; 0.71)	1.62	(1.1; 2.3)	< 0.01
S1-BMD	Thick_Cort_tVB [mm]	1.31 ± 0.18	1.25 ± 0.14	0.62	(0.55; 0.70)	1.58	(1.1; 2.2)	< 0.01
S1-BMD	BMD_Cort_mVB [mg/cm^3]	403.1 ± 63	377 ± 60.6	0.64	(0.56; 0.72)	1.53	(1.1; 2.1)	0.010
S1-BMD	Thick_Cort_mVB [mm]	1 ± 0.28	0.89 ± 0.24	0.63	(0.55; 0.71)	1.50	(1.1; 2.1)	0.013
S1-BMD	Vol_Cort_mVB [cm^3]	1.5 ± 0.29	1.39 ± 0.26	0.62	(0.55; 0.70)	1.48	(1.1; 2.1)	0.012
S1-BMD	Vol_Cort_tVB [cm^3]	7.53 ± 1.2	7.16 ± 1.02	0.61	(0.53; 0.68)	1.43	(1.1; 1.9)	0.025

Mean ± SD of univariate predictors with area under curve (AUC) values and their confidence intervals (CI), all values are sorted by Odds ratios (OR). OR are calculated per one standard deviation decrease. AUC and OR values are adjusted for age and BMI, n.s. predictors are not listed here. CI gives the confidence interval of OR and p the significance level. A detailed description of the parameters is given in the Supplement.

ROC curve plots are summarized in Figure 3. For women, AUC values of S1 (0.69) and of the S1-S2 combination (0.69) were significantly ($p < 0.05$) higher than for the combination of age and BMI (0.57) but AUC values of the S1-S2 combination were not significantly higher than for the S1 model. For men, only the S1-S3 combination (0.77) was significantly ($p < 0.05$) higher than the combination of age and BMI (0.63), no other significant differences were detected.

Integral BMD of the vertebral body remained a significant predictor for both men and women in S1, the reference model utilized in this study. In women, the cortical thickness of the lower endplate also persisted as a significant predictor in S1. The bootstrap procedure demonstrated that, including age and BMI, on average 5.4 (CI 3-9) predictors remained significant in women, with a mean AUC of 0.72 (CI 0.65 – 0.79). In men, an average of 5.7 (CI 3-11) predictors remained significant, with a mean AUC of 0.8 (CI 0.71 – 0.92). The frequency of predictors that remained significant in each of the 1,000 resampled datasets is documented in Supplementary Table S4.

For the sake of comparison, the AUC values were also calculated for a manually selected model based on clinical expertise. This model, in addition to age and BMI, consisted of integral BMD of the total vertebral body (BMD_Int_tVB) and cortical thickness measured at the midsection of the vertebral body (Thick_Cort_mVB). However, the latter variable did not emerge as a significant predictor in the previous analysis for both men and women. The AUC results were found to be 0.67 (CI 0.60 – 0.74) for women and 0.72 (CI 0.61 – 0.83) for men.

In women, 34 first incident VFs were diagnosed with SQ 1, while an additional 30 were diagnosed with SQ 2 or SQ 3. Excluding SQ 1 fractures, the AUC values increased to 0.72 for S1, 0.7 for S2, and 0.73 for S3 compared to the values in Table 3. The LRT of S3 exhibited a borderline significant increase ($p = 0.05$) in comparison to that of age and BMI. The performance of the combined models is shown in Supplementary Table S5. In contrast to the subset encompassing SQ1 to SQ3 fractures, the combination of S2 and S1 no longer was statistically superior in comparison to S1. However, the incorporation of a muscle predictor enhanced the

10.3389/fendo.2025.1566424

TABLE 2 Significant univariate predictors of the first incident vertebral fracture in men.

		Controls	Incident VF					
	n	239	23					
		Mean ± SD		AUC	CI	OR/SD	CI	p
	Age [y]	74.4 ± 5.1	76.3 ± 4.8	0.62	(0.51; 0.73)	0.71	(0.5; 1.1)	0.10
	BMI [kg/m^2]	26.8 ± 3.6	26.0 ± 3.4	0.58	(0.45; 0.71)	1.27	(0.8; 2.0)	0.31
Subset	Predictor	Mean ± SD		AUC	CI	OR/SD	CI	p
S1-BMD	BMD_Int_tVB [mg/cm^3]	195.5 ± 38.9	169.1 ± 34.7	0.71	(0.61; 0.82)	2.05	(1.2; 3.5)	< 0.01
S1-BMD	BMD_Trab_tVB [mg/cm^3]	104.8 ± 29.7	84.6 ± 27.2	0.70	(0.59; 0.82)	2.02	(1.2; 3.4)	< 0.01
S1-BMD	BMC_Trab_tVB [g]	2.79 ± 0.83	2.24 ± 0.74	0.71	(0.59; 0.82)	2.01	(1.1; 3.5)	0.012
S1-BMD	BMD_Cort_tVB [mg/cm^3]	411.7 ± 59.4	372.7 ± 48.6	0.71	(0.61; 0.82)	1.98	(1.2; 3.3)	< 0.01
S1-BMD	BMC_Int_tVB [g]	8.45 ± 2	7.27 ± 1.56	0.69	(0.58; 0.80)	1.96	(1.1; 3.5)	0.017
S1-BMD	BMD_Cort_mVB [mg/cm^3]	457.5 ± 69.9	413.9 ± 57.4	0.70	(0.60; 0.80)	1.92	(1.1; 3.2)	0.011
S1-BMD	BMD_Trab_cCy [mg/cm^3]	87.5 ± 28.8	69.2 ± 26.6	0.70	(0.58; 0.81)	1.83	(1.1; 3.1)	0.020
S1-BMD	BMD_Trab_mCy [mg/cm^3]	93 ± 34.1	73.8 ± 30.6	0.69	(0.58; 0.80)	1.72	(1.0; 2.9)	0.042
S3-Muscle	M_gAniso_Bin6	57.3 ± 0.2	57.4 ± 0.2	0.69	(0.60; 0.78)	0.61	(0.4; 1.0)	0.031
S2-Texture	Diff_Box_C	2.65 ± 0.04	2.66 ± 0.04	0.68	(0.58; 0.79)	0.48	(0.3; 0.9)	0.022
S2-Texture	Trab_lAniso	69.3 ± 1.9	69.7 ± 1.8	0.69	(0.59; 0.80)	0.46	(0.2; 0.8)	0.013

Mean ± SD of univariate predictors with area under curve (AUC) values and their confidence intervals (CI), all values are sorted by Odds ratios (OR). OR are calculated per one standard deviation decrease. AUC and OR values are adjusted for age and BMI, n.s. predictors are not listed here. CI gives the confidence interval of OR and p the significance level. A detailed description of the parameters is given in the Supplement.

prediction of VF, surpassing the performance of S1. The AUC values remained significantly different for the comparison against age and BMI. For men there were too few cases to perform such an analysis.

4 Discussion

In this study, the performance of 50 parameters obtained from QCT scans of the spine was assessed to predict the first incident VF univariately or in combination. Volumetric BMD based models significantly predicted the first incident VF with AUCs at about the same level as those reported for FEA in previously published studies on a sample very similar to ours (8). The analysis revealed that independent of BMD, parameters of trabecular texture and with limitations also of autochthonous muscle significantly improved the prediction of vertebral fractures (VF), compared to age and BMI alone. However, when compared to BMD, the enhancement was minimal and likely to be of negligible clinical significance. Thus age and BMI adjusted volumetric BMD, that can easily be measured with QCT and with excellent precision is the parameter of choice for prediction of incident fractures in clinical routine.

TABLE 3 AUC values for a combination of age and BMI and for the subset specific models (that are also adjusted for age and BMI).

	Women		Men	
	AUC	CI	AUC	CI
Age & BMI	0.57	(0.49; 0.65)	0.63	(0.51; 0.74)
S1 BMD	0.69	(0.62; 0.76)	0.71	(0.60; 0.82)
S2 Texture	0.67	(0.59; 0.75)	0.72	(0.62; 0.83)
S3 Muscle	*		0.69	(0.60; 0.79)

*No predictors of S3-Muscle remained in the final model.

QCT of the spine is typically used to measure average trabecular and integral BMD of L1 and L2 (32). Therefore, the reference model (S1) extracted from 18 different BMD and cortical thickness measures was used as 'QCT gold standard' for prediction of the first incident VF. After the reduction of variables in the stepwise logistic regression, only integral BMD of the vertebral body remained for both sexes and in addition, cortical thickness of the lower endplate for women. As age and BMI alone are important predictors of incident VF and in order to be consistent with most publications on fracture prediction that typically report age and BMI adjusted risk ratios or AUC values, age and BMI were retained in all models, even if these two parameters were not significant in the regression step.

The term 'gold standard' implies that there is an optimum set of variables that should be used for fracture prediction. However, the bootstrap analysis demonstrated that S1 models with different predictor combinations exhibited average AUCs that were analogous to the reference S1 model utilized in this study. It is noteworthy that parameters of cortical thickness were more frequently incorporated into the models resulting from the bootstrap process than BMD. However, with the exception of

TABLE 4 Performance of combinations of nested models tested by LRT: Model 1, which is the base model, and Model 2, which represents the combined model.

Comparison of Nested Models		Women			Men		
Model 1	Model 2	DoF	$\chi 2$	p	DoF	$\chi 2$	p
Age & BMI	S1 BMD	385	18.5	<0.001	259	6.4	0.01
Age & BMI	S2 Texture	386	15.0	<0.001	258	6.9	0.01
Age & BMI	S3 Muscle	*			258	4.8	0.03
S1 BMD	S2 Texture	385	5.9	0.02	258	4.5	0.05
S1 BMD	S3 Muscle	*			258	4.8	0.03

*No predictors of S3-Muscle remained in the final model.

cortical thickness of the lower endplate, none of the 18 input predictors occurred in more than 30% of the 1,000 models. While it is unlikely that the S1 reference model of this study overestimated fracture risks due to overfitting, a common problem in multivariable analyses, there is no unique best set of S1 QCT variables to be used for fracture prediction. Conducting a separate analysis of a distinct subset of the AGES population, or even a different study, is likely to yield a different S1 reference model. This phenomenon is also evident in the univariate results, where the adjusted ORs for many variables were found to be highly comparable, despite adjustments for age and BMI.

From a clinical perspective, this is favorable news because a combination of rather esoteric predictor combinations will most likely not predict the first incident VF risk better than a standard set of predictors. Integral BMD, a variable that can easily be measured with high precision (13), is an adequate predictor of incident VF. Cortical thickness of the lower endplate may more reflect sclerotization of the trabecular bone due to vertebral disk impairments than actual cortical thickness of the endplate. Segmentation in this case is challenging and disk impairments were frequent in the AGES population. Nevertheless, the observation that degenerative features of the vertebrae may also be predictive of the first incident VF should be further pursued.

Therefore for the handpicked S1 model cortical thickness of the mid vertebral body was selected, which is less affected by degenerative changes (33–35). AUC values of the handpicked model were well in the range of the bootstrapping results. The addition of mid cortical thickness did only marginally improve VF prediction compared to integral BMD alone.

A notable finding is the observation that the S2 texture model predicted VF independently of the S1 BMD model. In scenarios where a BMD assessment is not feasible, for example in MRI scans, VF prediction is still possible using parameters of trabecular texture, at least in principle. Recent studies have shown that an MRI based texture analysis can be used to discriminate subjects with and without prevalent vertebral fractures (36, 37). However, it is important to remember that texture assessments depend on noise and spatial resolution (38). Thus, MRI texture results will vary

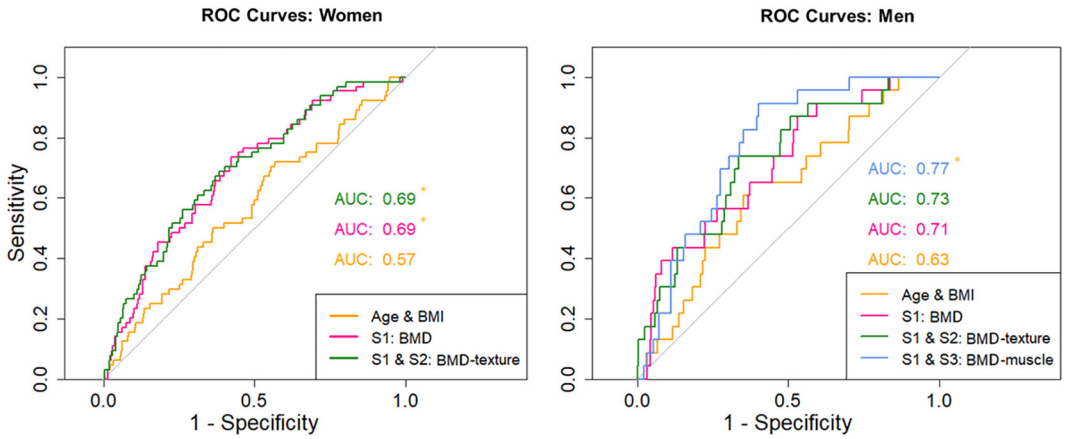

FIGURE 3
Receiver operator curves for women - for age/BMI, S1 and combinations of S1 with S2. Receiver operator curves for men - for age/BMI, S1 and combinations of S1 with S2 and S1 with S3. Asterisk marks significant difference ($p < 0.05$) in the AUC values against the model only including age and BMI.

significantly among MRI sequences. It should also be noted that all scans analyzed in this study were obtained from the same CT scanner using the same CT protocol. Texture measurements from different scanners may not be directly comparable.

Several other studies have demonstrated the ability of histomorphometry or texture parameters to improve the discrimination of vertebral fractures when compared with BMD (39–43), but none have investigated the ability to predict incident osteoporotic vertebral fractures. Therefore, it is an important finding of this study that texture parameters can be used to predict incident vertebral fractures. Of course, there are many different texture parameters and a radiomics approach may more systematically exploit the potential of texture parameters than the heuristic approach chosen in this study.

A substantial body of research has demonstrated a correlation between muscle metrics and spinal fractures (26, 44, 45). However, the majority of these studies were cross-sectional in design, investigating the associations of muscle metrics with prevalent conditions rather than the prediction of incident VF. In this study the predictive value of paraspinal muscle characteristics was weak, questioning their utility in clinical practice. Muscle parameters significantly predicted VF in women only after excluding the SQ 1 mild fractures and even then, the improvement of fracture prediction compared to age and BMI was only borderline significant. This finding is particularly noteworthy given the comprehensive array of parameters that were examined, encompassing muscle density, fat fraction, and a multitude of texture parameters that characterized the distribution of muscle tissue and intermuscular adipose tissue. In men, a modest effect was observed for muscle tissue anisotropy. However, the clinical interpretation of this finding is challenging, as the anisotropy did not differ significantly between men with and those without incident VF.

In the event of confirmation, the implications are substantial. The role of paraspinal muscle exercise in preventing vertebral fractures remains uncertain. Actually, a recent 12-month study in men demonstrated that exercise had no effect on paraspinal muscles, despite significant training effects on spinal BMD and thigh muscle parameters (46). Further research is needed to determine whether muscle deterioration is a cause or a consequence of fractures.

The multivariable analysis is a big advantage of this study. Instead of just presenting univariate odds or hazard ratios after adjustment for age and BMI (7, 8) the advanced statistical approach of comparing nested combinations of predictors provided the possibility to compare the performance of fracture prediction of different models. The use of the log-likelihood ratio as performance criterion guarantees statistical rigor in identifying the set of predictors that best fit the pattern of incident fractures (30, 47) but beyond the result whether fracture prediction differs, the clinical interpretation of the magnitude of improvement of fracture prediction is difficult. Therefore, we also calculated AUC values as established performance characteristic, which, however, offers less statistical power to test which model is better than others.

As shown in Table 4 and Supplementary Table S5 compared to S1 the inclusion of S2 predictors, which characterize trabecular architecture significantly improved prediction of VF in men and women. However, in women this was no longer the case once mild fractures were excluded. Compared to S1 the inclusion of S3 predictors, which characterize muscle significantly improved prediction of VF in men and after exclusion of SQ 1 fractures also in women. However, the ROC graphs show that AUC values of the combined models did not significantly increase AUC values. Thus, the clinical benefit is rather limited and may not be worth the effort of an advanced QCT analysis. It is a limitation of the study that the number of incident vertebral fractures with grade 2 or 3 was too small in men to perform a separate analysis.

It is another limitation of this study that FEA was not performed and therefore it was not possible to test whether a strength determination would have increased fracture prediction beyond that of BMD. Such an analysis was also not performed in the earlier study that analyzed the same cohort (8). While in that study strength showed the highest OR for fracture prediction, integral BMD was not measured and CI of the OR largely overlapped. OR calculation may be strongly affected by the distribution of the data but no test of normal distribution has been reported in the earlier study. Judging the performance based on ROC analysis showed our QCT results at the same level as the FEA data reported earlier Whether from clinical perspective the advanced method of FEA is worth the additional effort compared to a standard QCT analysis still has to be determined.

While our results do not provide a definitive solution for predicting the first incident VF, they offer valuable insights that may guide future advancements in addressing this inherently complex and unresolved challenge. Surprisingly even with our comprehensive analysis of texture, muscle and bone parameters, none of the parameters or a combination of parameters gave an outstanding improvement over established predictors, namely age and BMI adjusted volumetric BMD. Even muscle parameters that are known to perform well in cross-sectional studies did not perform extraordinary for the prediction of incident VF. The analyzed dataset is exceptionally rare and one of the few that enable such an in-depth analysis. Unfortunately, less than a handful of datasets exist for the prospective analysis of VF using QCT. Nevertheless, it would be highly valuable to validate these findings in future studies.

Data availability statement

The datasets presented in this article are not readily available because they were used under license. Restrictions also apply to the availability of data generated or analyzed during this study to preserve patient confidentiality. Data from the AGES-Reykjavik study are available through collaboration under a data usage agreement with the Icelandic Heart Association. Requests to access the datasets should be directed to AGES_data_request@hjarta.is.

Ethics statement

The studies involving humans were approved by National Institute on Aging, National Bioethics Committee (VSN: 00-063) and the Data Protection Authority. The studies were conducted in accordance with the local legislation and institutional requirements. The participants provided their written informed consent to participate in this study.

Author contributions

JH: Formal analysis, Investigation, Writing – original draft, Writing – review & editing. KE: Conceptualization, Funding acquisition, Investigation, Project administration, Supervision, Writing – original draft, Writing – review & editing. SF-W: Formal analysis, Methodology, Writing – review & editing. EY: Methodology, Validation, Writing – review & editing. SB: Formal analysis, Investigation, Software, Writing – review & editing. SS: Data curation, Resources, Writing – review & editing. VG: Data curation, Resources, Writing – review & editing. CG: Funding acquisition, Project administration, Supervision, Writing – review & editing. OC: Conceptualization, Formal analysis, Methodology, Software, Supervision, Visualization, Writing – original draft, Writing – review & editing.

Funding

The author(s) declare that financial support was received for the research and/or publication of this article. This study was in part supported by the Bundesministerium für Bildung und Forschung (BMBF) Project ARTEMIS - Artificial intelligence musculoskeletal disorders study (reference 01EC190B).

Acknowledgments

The present work was performed in partial fulfilment of the requirements to obtain the degree Dr. med./Dr. med. dent. at Friedrich-Alexander-Universität Erlangen-Nürnberg.

Conflict of interest

The authors declare that the research was conducted in the absence of any commercial or financial relationships that could be construed as a potential conflict of interest.

Generative AI statement

The author(s) declare that no Generative AI was used in the creation of this manuscript.

Publisher's note

Supplementary material

The Supplementary Material for this article can be found online at: https://www.frontiersin.org/articles/10.3389/fendo.2025.1566424/full#supplementary-material

References

1. Ballane G, Cauley JA, Luckey MM, El-Hajj-Fuleihan G. Worldwide prevalence and incidence of osteoporotic vertebral fractures. *Osteoporos Int.* (2017) 28:1531–42. doi: 10.1007/s00198-017-3909-3

2. Clark P, Cons-Molina F, Deleze M, Ragi S, Haddock L, Zanchetta JR, et al. The prevalence of radiographic vertebral fractures in Latin American countries: the Latin American Vertebral Osteoporosis Study (LAVOS). *Osteoporos Int.* (2009) 20:275–82. doi: 10.1007/s00198-008-0657-4

3. Kendler DL, Bauer DC, Davison KS, Dian L, Hanley DA, Harris ST, et al. Vertebral fractures: clinical importance and management. *Am J Med.* (2016) 129:221 e1–10. doi: 10.1016/j.amjmed.2015.09.020

4. Lorentzon M, Litsne H, Axelsson KF. The significance of recent fracture location for imminent risk of hip and vertebral fractures-a nationwide cohort study on older adults in Sweden. *Osteoporos Int.* (2024) 35:1077–87. doi: 10.1007/s00198-024-07072-x

5. Kanis JA, Johansson H, McCloskey EV, Liu E, Akesson KE, Anderson FA, et al. Previous fracture and subsequent fracture risk: a meta-analysis to update FRAX. *Osteoporos Int.* (2023) 34:2027–45. doi: 10.1007/s00198-023-06870-z

6. Allam AK, Anand A, Flores AR, Ropper AE. Computer vision in osteoporotic vertebral fracture risk prediction: A systematic review. *Neurospine.* (2023) 20:1112–23. doi: 10.14245/ns.2347022.511

7. Johannesdottir F, Allaire B, Kopperdahl DL, Keaveny TM, Sigurdsson S, Bredella MA, et al. Bone density and strength from thoracic and lumbar CT scans both predict incident vertebral fractures independently of fracture location. *Osteoporos Int.* (2021) 32:261–9. doi: 10.1007/s00198-020-05528-4

8. Kopperdahl DL, Aspelund T, Hoffmann PF, Sigurdsson S, Siggeirsdottir K, Harris TB, et al. Assessment of incident spine and hip fractures in women and men using finite element analysis of CT scans. *J Bone Miner Res.* (2014) 29:570–80. doi: 10.1002/jbmr.2069

9. Johansson L, Johansson H, Axelsson KF, Litsne H, Harvey NC, Liu E, et al. Improved fracture risk prediction by adding VFA-identified vertebral fracture data to BMD by DXA and clinical risk factors used in FRAX. *Osteoporos Int.* (2022) 33:1725–38. doi: 10.1007/s00198-022-06387-x

10. Wang X, Sanyal A, Cawthon PM, Palermo L, Jekir M, Christensen J, et al. Prediction of new clinical vertebral fractures in elderly men using finite element analysis of CT scans. *J Bone Miner Res.* (2012) 27:808–16. doi: 10.1002/jbmr.1539

11. Zysset P, Qin L, Lang T, Khosla S, Leslie WD, Shepherd JA, et al. Clinical use of quantitative computed tomography-based finite element analysis of the hip and spine in the management of osteoporosis in adults: the 2015 ISCD official positions-part II. *J Clin Densitom.* (2015) 18:359–92. doi: 10.1016/j.jocd.2015.06.011

12. Engelke K, Museyko O, Wang L, Laredo JD. Quantitative analysis of skeletal muscle by computed tomography imaging-State of the art. *J Orthop Translat.* (2018) 15:91–103. doi: 10.1016/j.jot.2018.10.004

13. Engelke K, Mastmeyer A, Bousson V, Fuerst T, Laredo JD, Kalender WA. Reanalysis precision of 3D quantitative computed tomography (QCT) of the spine. *Bone*. (2009) 44:566–72. doi: 10.1016/j.bone.2008.11.008

14. Ma HY, Zhang RJ, Zhou LP, Wang YX, Wang JQ, Shen CL, et al. Comparative effectiveness of four techniques for identifying vertebral fragility fractures among elderly patients. *Eur Radiol*. (2024). doi: 10.1007/s00330-024-11292-4

15. Johannesdottir F, Allaire B, Bouxsein ML. Fracture prediction by computed tomography and finite element analysis: current and future perspectives. *Curr Osteoporos Rep*. (2018) 16:411–22. doi: 10.1007/s11914-018-0450-z

16. Li D, Mao SS, Budoff MJ. Trabecular bone mineral density as measured by thoracic vertebrae predicts incident hip and vertebral fractures: the multi-ethnic study of atherosclerosis. *Osteoporos Int*. (2024) 35:1061–8. doi: 10.1007/s00198-024-07040-5

17. Lang T, Cauley JA, Tylavsky F, Bauer D, Cummings S, Harris TB, et al. Computed tomographic measurements of thigh muscle cross-sectional area and attenuation coefficient predict hip fracture: the health, aging, and body composition study. *J Bone Miner Res*. (2010) 25:513–9. doi: 10.1359/jbmr.090807

18. Lang T, Koyama A, Li C, Li J, Lu Y, Saeed I, et al. Pelvic body composition measurements by quantitative computed tomography: association with recent hip fracture. *Bone*. (2008) 42:798–805. doi: 10.1016/j.bone.2007.12.002

19. Muhlberg A, Museyko O, Bousson V, Pottecher P, Laredo JD, Engelke K. Three-dimensional distribution of muscle and adipose tissue of the thigh at CT: association with acute hip fracture. *Radiology*. (2019) 290:426–34. doi: 10.1148/radiol.2018181112

20. Wang L, Yin L, Yang M, Ge Y, Liu Y, Su Y, et al. Muscle density is an independent risk factor of second hip fracture: a prospective cohort study. *J Cachexia Sarcopenia Muscle*. (2022) 13:1927–37. doi: 10.1002/jcsm.12996

21. Wang L, Yin L, Zhao Y, Su Y, Sun W, Liu Y, et al. Muscle density discriminates hip fracture better than computed tomography X-ray absorptiometry hip areal bone mineral density. *J Cachexia Sarcopenia Muscle*. (2020) 11:1799–812. doi: 10.1002/jcsm.12616

22. Sollmann N, Franz D, Burian E, Loffler MT, Probst M, Gersing A, et al. Assessment of paraspinal muscle characteristics, lumbar BMD, and their associations in routine multi-detector CT of patients with and without osteoporotic vertebral fractures. *Eur J Radiol*. (2020) 125:108867. doi: 10.1016/j.ejrad.2020.108867

23. Zhang Y, Dilixiati Y, Jiang W, Cao X, Chen Y, Guo H. Correlation of psoas muscle index with fragility vertebral fracture: A retrospective cross-sectional study of middle-aged and elderly women. *Int J endocrinol*. (2022) 2022:4149468. doi: 10.1155/2022/4149468

24. Zhang J, Xia L, Zhang X, Liu J, Tang J, Xia J, et al. Development and validation of a predictive model for vertebral fracture risk in osteoporosis patients. *Eur Spine J*. (2024) 33:3242–60. doi: 10.1007/s00586-024-08235-4

25. Wong AK, Cawthon PM, Peters KW, Cummings SR, Gordon CL, Sheu Y, et al. Bone-muscle indices as risk factors for fractures in men: the Osteoporotic Fractures in Men (MrOS) Study. *J Musculoskelet Neuron Interact*. (2014) 14:246–54.

26. Chen Z, Shi T, Li W, Sun J, Yao Z, Liu W. Role of paraspinal muscle degeneration in the occurrence and recurrence of osteoporotic vertebral fracture: A meta-analysis. *Front endocrinol*. (2022) 13:1073013. doi: 10.3389/fendo.2022.1073013

27. Harris TB, Launer LJ, Eiriksdottir G, Kjartansson O, Jonsson PV, Sigurdsson G, et al. Age, Gene/Environment Susceptibility-Reykjavik Study: multidisciplinary applied phenomics. *Am J Epidemiol*. (2007) 165:1076–87. doi: 10.1093/aje/kwk115

28. Genant HK, Wu CY, van Kuijk C, Nevitt M. Vertebral fracture assessment using a semi-quantitative technique. *J Bone Miner Res*. (1993) 8:1137–48. doi: 10.1002/jbmr.5650080915

29. Engelke K, Museyko O, Günzel D, Meier A, Laredo J eds. *A new CT based approach to quantify adipose tissue in paraspinal muscle*. Montreal, Canada: JBMR (2018).

30. Harrell FE. *Regression Modeling Strategies*. Springer International Publishing (2015).

31. Davison AC, Hinkley D. *Bootstrap Methods and Their Application*. New York, NY, USA: Cambridge University Press (1997).

32. Engelke K, Adams JE, Armbrecht G, Augat P, Bogado CE, Bouxsein ML, et al. Clinical use of quantitative computed tomography and peripheral quantitative computed tomography in the management of osteoporosis in adults: the 2007 ISCD official positions. *J Clin Densitom*. (2008) 11:123–62. doi: 10.1016/j.jocd.2007.12.010

33. Grams AE, Rehwald R, Bartsch A, Honold S, Freyschlag CF, Knoflach M, et al. Correlation between degenerative spine disease and bone marrow density: a retrospective investigation. *BMC Med Imag*. (2016) 16:17. doi: 10.1186/s12880-016-0123-2

34. Guglielmi G, Floriani I, Torri V, Li J, van Kuijk C, Genant HK, et al. Effect of spinal degenerative changes on volumetric bone mineral density of the central skeleton as measured by quantitative computed tomography. *Acta Radiol*. (2005) 46:269–75. doi: 10.1080/02841850510012661

35. Wang Y, Battie MC, Boyd SK, Videman T. The osseous endplates in lumbar vertebrae: thickness, bone mineral density and their associations with age and disk degeneration. *Bone*. (2011) 48:804–9. doi: 10.1016/j.bone.2010.12.005

36. Dash AS, Breighner R, Gonzalez FQ, Blumberg O, Koff MF, Billings E, et al. Individuals with heterogenous trabecular bone texture by clinical MRI have lower bone strength and stiffness by QCT based finite element analysis. *J Bone Miner Res*. (2024) 40 (3):339–47. doi: 10.1093/jbmr/zjae207

37. Zaworski C, Cheah J, Koff MF, Breighner R, Lin B, Harrison J, et al. MRI-based texture analysis of trabecular bone for opportunistic screening of skeletal fragility. *J Clin Endocrinol Metab*. (2021) 106:2233–41. doi: 10.1210/clinem/dgab342

38. Lowitz T, Museyko O, Bousson V, Kalender WA, Laredo JD, Engelke K. Characterization of knee osteoarthritis-related changes in trabecular bone using texture parameters at various levels of spatial resolution-a simulation study. *BoneKEy Rep*. (2014) 3:615. doi: 10.1038/bonekey.2014.110

39. Ito M. Assessment of bone quality using micro-computed tomography (micro-CT) and synchrotron micro-CT. *J Bone Miner Metab*. (2005) 23 Suppl:115–21. doi: 10.1007/BF03026335

40. Saravi B, Zink A, Tabukashvili E, Guzel HE, Ulkumen S, Couillard-Despres S, et al. Integrating radiomics with clinical data for enhanced prediction of vertebral fracture risk. *Front Bioeng Biotechnol*. (2024) 12:1485364. doi: 10.3389/fbioe.2024.1485364

41. Yadav RN, Oravec DJ, Drost J, Flynn MJ, Divine GW, Rao SD, et al. Textural and geometric measures derived from digital tomosynthesis discriminate women with and without vertebral fracture. *Eur J Radiol*. (2025) 183:111925. doi: 10.1016/j.ejrad.2025.111925

42. Poullain F, Champsaur P, Pauly V, Knoepflin P, Le Corroller T, Creze M, et al. Vertebral trabecular bone texture analysis in opportunistic MRI and CT scan can distinguish patients with and without osteoporotic vertebral fracture: A preliminary study. *Eur J Radiol*. (2023) 158:110642. doi: 10.1016/j.ejrad.2022.110642

43. Nagarajan MB, Checefsky WA, Abidin AZ, Tsai H, Wang X, Hobbs SK, et al. Characterizing trabecular bone structure for assessing vertebral fracture risk on volumetric quantitative computed tomography. *Proc SPIE Int Soc Opt Eng*. (2015) 9417. doi: 10.1117/12.2082059

44. Huang W, Cai XH, Li YR, Xu F, Jiang XH, Wang D, et al. The association between paraspinal muscle degeneration and osteoporotic vertebral compression fracture severity in postmenopausal women. *J Back Musculoskelet Rehabil*. (2023) 36:323–9. doi: 10.3233/BMR-220059

45. Kim HJ, Yang JH, Chang DG, Suk SI, Suh SW, Song KS, et al. Significance of paraspinal muscle quality in risk between single and multiple osteoporotic vertebral fractures. *Eur Spine J*. (2023) 32:1763–70. doi: 10.1007/s00586-023-07670-z

46. Ghasemikaram M, Chaudry O, Nagel AM, Uder M, Jakob F, Kemmler W, et al. Effects of 16 months of high intensity resistance training on thigh muscle fat infiltration in elderly men with osteosarcopenia. *Geroscience*. (2021) 43:607–17. doi: 10.1007/s11357-020-00316-8

47. Kleinbaum DG, Klein M. *Survival Analysis. 3 ed*. New York, NY, USA: Springer Science+Business Media (2012). doi: 10.1007/978-1-4419-6646-9

frontiers | Frontiers in Endocrinology

TYPE Systematic Review
PUBLISHED 22 April 2025
DOI 10.3389/fendo.2025.1532355

OPEN ACCESS

EDITED BY
Nico Sollmann,
Ulm University Medical Center, Germany

REVIEWED BY
Mario Ganau,
Oxford University Hospitals NHS Trust, United Kingdom
Andrei Tica,
University of Craiova, Romania
Andrea Angelini,
University of Padua, Italy
Thomas Caffard,
Universitäts- und Rehabilitationskliniken Ulm, Germany

*CORRESPONDENCE
Zhang Zhiqiang
zz18051060806@gmail.com;
18051060806@163.com

RECEIVED 21 November 2024
ACCEPTED 17 February 2025
PUBLISHED 22 April 2025

CITATION
Ahmed Mohamed A, Xuyang X, Zhiqiang Z and Chen J (2025) Association between thoracolumbar fascia injury and residual back pain following percutaneous vertebral augmentation: a systematic review and meta-analysis.
Front. Endocrinol. 16:1532355.
doi: 10.3389/fendo.2025.1532355

Association between thoracolumbar fascia injury and residual back pain following percutaneous vertebral augmentation: a systematic review and meta-analysis

Abdiaziz Ahmed Mohamed[1,2], Xu Xuyang[1,2], Zhang Zhiqiang[1]* and Jianghu Chen[1,3]

[1]Department of Orthopedics, Northern Jiangsu People's Hospital Affiliated Hospital to Yangzhou University, Yangzhou, Jiangsu, China, [2]Medical College of Yangzhou University, Yangzhou, Jiangsu, China, [3]Yangzhou Clinical Medical College of Xuzhou Medical University, Xuzhou, Jiangsu, China

Objective: To evaluate the association between a thoracolumbar fascia injury (TLFI) and the development of residual back pain (RBP) following percutaneous vertebral augmentation (PVA).

Background: Osteoporotic vertebral compression fractures (OVCF) commonly affect elderly individuals and those with osteoporosis, leading to pain and limited mobility. Percutaneous vertebral augmentation provides immediate pain relief and stabilization of the fractures. However, some patients experience residual pain after the treatment. Although recent studies have suggested a potential association, the role of TLFI in RBP remains inconclusive. The aim of this meta-analysis was to evaluate this association.

Methods: A thorough search was performed across the PubMed, Medline, Embase, Web of Science, and Cochrane Library databases from inception to 31 December 2024 to identify studies examining the link between TLFI and RBP following PVA. A random-effects model was used to combine the outcome data to account for the potential heterogeneity among the included studies.

Results: This meta-analysis included 13 studies with a total of 4,542 participants and a TLFI incidence rate of 28%. Univariate analysis indicated that patients with a TLFI were significantly more likely to develop RBP compared to those without a TLFI, with an odds ratio (OR) of 4.19 (95% CI: 2.49 to 7.05, I^2 = 76.9%). The sensitivity analysis identified two studies as significant influential outliers that contributed to the majority of the observed heterogeneity. Excluding these studies resulted in an OR of 4.62 (95% CI: 3.61 to 5.92, I^2 = 0%). The multivariate analysis confirmed a strong association between TLFI and RBP after adjusting for confounders and other risk factors, with an OR of 4.57 (95% CI: 3.28 to 6.37, I^2 = 81.5%). The sensitivity analysis identified three studies as significant influential outliers, and excluding them resulted in an OR of 4.79 (95% CI: 3.76 to 6.11, I^2 = 0%) with no heterogeneity. This finding further confirms the association with a more homogenous overall effect estimate.

Conclusion: The pooled effect size of both univariate and multivariate analyses consistently demonstrated that a TLFI significantly increased the risk of developing RBP after PVA regardless of other related risk factors. Recognizing fascia injury as a potential source of postoperative pain in clinical practice could enhance the care of these patients and mitigate postoperative pain.

KEYWORDS

fascia injury, osteoporosis, compression fracture, meta-analysis, fragility fracture, residual back pain

1 Introduction

Osteoporotic vertebral compression fractures (OVCF) are extremely common, particularly in elderly individuals and in those with osteoporosis (1, 2). Compression of the vertebrae causes these fractures, resulting in severe pain, limited mobility, and decreased quality of life (3, 4). OVCF is typically caused by low-energy trauma, although many patients do not report any traumatic incidents (5). However, the prevalence of osteoporosis and the occurrence of OVFs vary significantly across racial groups and geographic regions. These variations can be attributed to epigenetic and genetic factors. These factors not only influence bone mineral density but also uniquely influence and predispose different populations to fragility fractures (6). Percutaneous vertebral augmentation (PVA) is a minimally invasive treatment procedure for OVCFs that includes percutaneous vertebroplasty (PVP) and percutaneous kyphoplasty (PKP). These procedures have emerged as effective interventions that can alleviate back pain and stabilize vertebral fractures (7, 8). Percutaneous vertebroplasty involves the injection of bone cement into the fractured vertebra, stabilizing it and providing immediate pain relief (9). Percutaneous Kyphoplasty, on the other hand, involves the use of an inflated balloon to create a cavity within the vertebral body, with the objective of correcting deformity and restoring vertebral height prior to cement injection (10, 11). Despite the fact that PVA procedures provide immediate pain alleviation and improve the functionality of patients, moderate to severe postoperative pain may persist in certain individual patients (12, 13). According to the literature, a subset of OVCF patients, ranging from 5% to 32%, experienced residual back pain (RBP) following PVA procedures (14). Our findings also revealed similar results, the incidence of RBP was between 4.6% to 24.2% with an average of 13.9% across included studies in the analysis. It is essential to fully understand the root causes of residual back pain in these patients following vertebral augmentation procedures to maximize and revise treatment procedures, reduce the frequency of postoperative pain, and enhance long-term results for OVCF patients. Insufficient height restoration, cement leakage, inadequate cement distribution, advanced osteoporosis, sarcopenia, and intervertebral vacuum cleft are among the various risk factors identified in the literature as causes of residual back pain experienced by these patients following percutaneous vertebral augmentation procedures (15). The role of preoperative thoracolumbar fascia injury (TLFI) on residual back pain is still unknown and remains controversial and uncertain (16). Some studies have reported that a preoperative TLFI serves as a risk factor for back pain in the short term and is not a rare condition in OVCF patients but rather an overlooked condition, which becomes apparent after the pain associated with the fracture is alleviated (17, 18). The thoracolumbar fascia is a complex, multilayered connective tissue located in the lower back. It extends from the thoracic spine to the sacrum and plays an important role in the biomechanical stability and movements of the spine, such as forward flexion (19). Additionally, it provides attachment points to various paraspinal muscles, thereby facilitating the transmission of forces across the trunk and contributing to core stability (20). In patients with OVCFs, the presence of a TLFI is diagnosed by analyzing the signal produced by magnetic resonance imaging (MRI), which may manifest as posterior fascia edema or swelling. This meta-analysis aimed to evaluate the association between TLFI and residual back pain following PVA.

Abbreviations: TLFI, thoracolumbar fascia injury; RBP, residual back pain; OVCFs, osteoporotic vertebral compression fractures; PVA, percutaneous vertebral augmentation; PVP, percutaneous vertebroplasty; PKP, percutaneous kyphoplasty.

2 Methods

The present systematic review and meta-analysis were carried out following the principles outlined by the Preferred Reporting Items for Systematic Reviews and Meta-Analyses (PRISMA) (21) and the Cochrane Handbook for Systematic Reviews and Meta-analyses (22); however, this review was not registered in PROSPERO.

2.1 Literature search

We searched the PubMed, Medline, Embase, Web of Science, and Cochrane Library databases and conducted two separate

searches: the first up to 31 January 2024 and a follow-up update search up to 31 December 2024 almost a year after the first search with the same search query used without change to ensure consistency. The following free search terms were used: osteoporotic vertebral compression fractures OR OVCF OR osteoporotic thoracolumbar compression fractures OR osteoporotic spinal compression fracture OR percutaneous vertebroplasty OR percutaneous kyphoplasty OR percutaneous cementoplasty OR percutaneous vertebral augmentation OR vertebral body augmentation OR percutaneous spinal augmentation OR vertebral augmentation OR Risk factor OR Predictor OR residual back pain OR residual low back pain OR persistent back pain OR chronic back pain OR recurrent pain OR thoracolumbar fascia injury. We used the Boolean operator AND to combine the title, abstract, and keyword phrases with medical subject headings (MeSH terms) to generate a broad search and identify the most relevant articles. The included studies were only published in English. Search terms were adjusted based on the database of interest. In addition, we performed a manual review of the references for eligible studies (see Supplementary Data Sheet 1).

2.2 Selection criteria

The study inclusion criteria followed the PICO guidelines and focused on patients diagnosed with osteoporotic vertebral compression fractures. The intervention or treatment option for this condition is percutaneous vertebral augmentation, involving either PVP or PKP. The control group was comprised of individuals who did not experience postoperative back pain. The outcome was the identification of TLFI as an independent risk factor for RBP along with its odds ratio in a multivariate analysis, which included observational studies or randomized controlled trials (RCTs) published in English as complete articles in peer-reviewed journals. Articles were excluded if they met the following criteria: (1) studies not including patients with OVCFs; (2) not reported TLFI as an independent risk factor in a multivariate analysis; (3) had missing or inadequate outcome data, such as multivariate analysis; (4) case reports, expert opinions, reviews, or commentaries/editorial letters; (5) abstracts only; (6) animal-related studies; and (7) non-English.

2.3 Search and selection

In total, 4,316 items were identified following a broad database search. After removing duplicates using EndNote v21 (28), 2,828 articles remained for screening. Two independent authors reviewed the titles. If the titles lacked sufficient information, we further examined the abstracts for inclusion, and 2,790 articles were excluded based on the inclusion and exclusion criteria. 38 articles were retrieved and assessed for analysis; subsequently, 25 were excluded due to explanations listed in Figure 1. The remaining 13 publications satisfied the study criteria for quantitative analysis in the meta-analysis. The primary outcome of our search was to assess whether TLFI was associated with RBP as an independent risk factor for OVCF following percutaneous vertebral augmentation.

2.4 Data extraction

Two authors completed the literature search and performed data extraction in accordance with the defined inclusion and exclusion criteria. They extracted and cross-verified the data using standardized data extraction forms. The author discussed and resolved instances of disagreement, seeking guidance from a third author as needed. General information of the studies collected was: (1) authors, year of publication, and study design; (2) patient characteristics, diagnosis, sample size, age, sex, and BMI; (3) intervention and control information; (4) incidence of TLFI (5); adjusted or matched variables (Table 1).

2.5 Quality assessment

Since all the studies included in the analysis were observational studies, quality assessment was carried out using the Newcastle–Ottawa scale (36) (Table 2). Each study received a total of nine points based on quality, which was assessed across three broad classifications. There were four points for selection, two points for compatibility, and three points for outcome. A study quality score of six points or more was deemed to be good, whereas a score of five points or lower was regarded as low quality.

2.6 Statistical analysis

All data analyses were conducted using R software version 4.3.2 https://www.R-project.org/ (37). The analyses used the "meta", "dmetar", and "esc" packages (38–41) to determine the overall effect size for the outcome. The pooled effect sizes of the odds ratios (ORs) and 95% confidence intervals (CIs) were calculated. The extent of heterogeneity was assessed using Cochran's Q test along with the I^2 statistic for the included publications. I^2 values ≥50% indicate heterogeneity and correspond to $p < 0.05$, as determined by Cochran's Q test. If the observed I^2 value was ≥50, we investigated the possible reasons for heterogeneity and the studies contributing to it. Considering the prospect of variation across studies, a random-effects model was applied to combine the effect sizes. We used the DerSimonian–Laird estimator (42) to calculate the variance in study heterogeneity. We also applied Knapp–Hartung adjustments (43) to calculate the 95% CI of the overall pooled effect. To investigate the possible reasons and the studies contributing to heterogeneity, we adopted the leave-one-out analysis method (44). Statistical significance was set at $P < 0.05$.

2.6.1 Sensitivity analysis

Influential and outlier study analyses were conducted to ensure the robustness of the overall pooled effect estimates and to investigate each study's contribution to both observed heterogeneity and overall effect

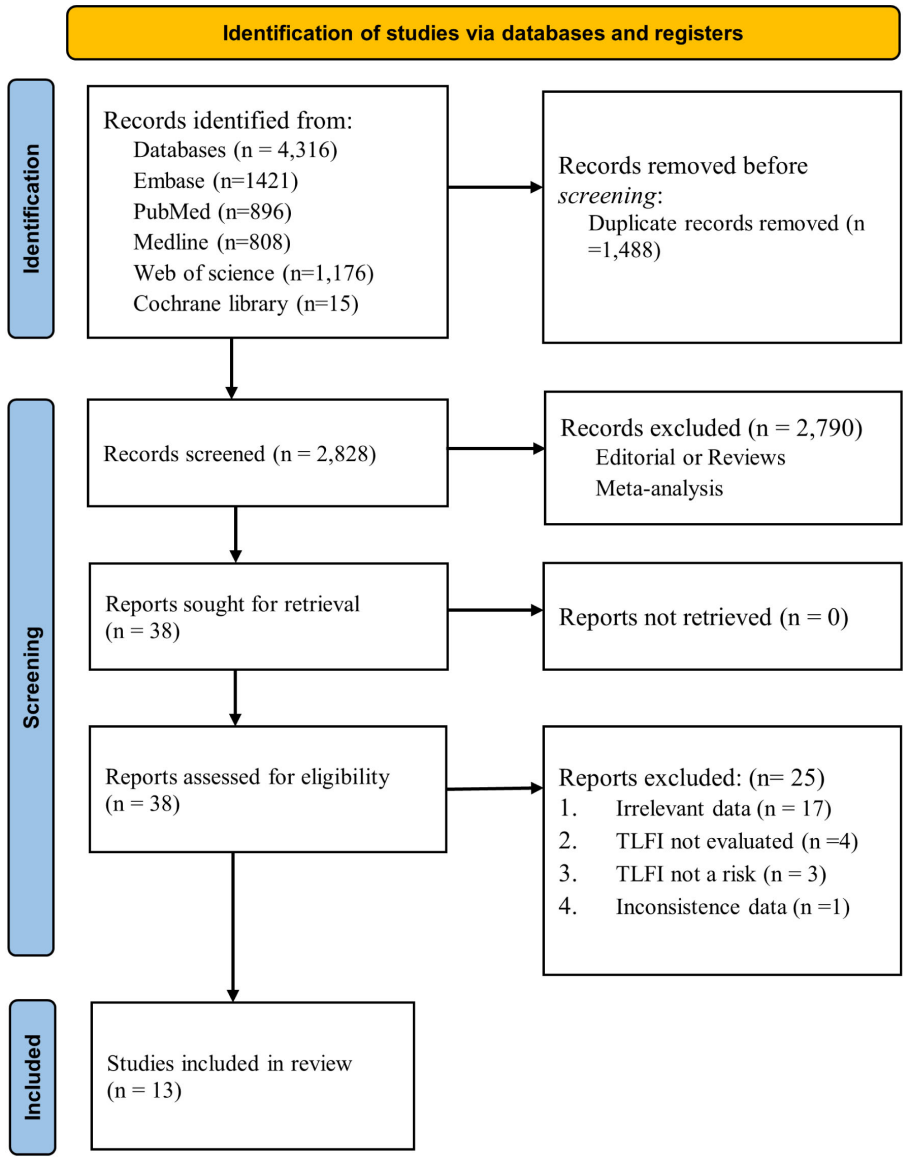

FIGURE 1
PRISMA flowchart for the literature search and selection process.

size. Outliers were identified using the "find.outliers" function in the "dmetar" package in the univariate analysis with two studies (31), and (34), identified as outliers. Similarly, in the multivariate analysis, one study (30) was also recognized as an outlier. Furthermore, we carried out an influence diagnostic analysis to identify influential studies that may distort the pooled effect estimate in one direction or another using the "influenceAanalysis" function in the same package. The influence diagnostic analysis included multiple diagnostic tests, namely, the Baujat plot (45), influence diagnostic analysis according to Viechtbauer and Cheung (44), leave-one-out analysis, and graphical display of heterogeneity (GOSH) plot (46) diagnostics.

2.6.2 Baujat diagnostic plot

The Baujat plot detects how each study contributes to heterogeneity based on Cochran's Q and how they influence the overall effect using the leave-one-out method (45). Studies concentrated on the right side of the plot heavily contributed to the heterogeneity of the meta-analysis. Studies on the upper right side are considered particularly influential and contribute to both heterogeneity and overall effect size. In both the univariate and multivariate analyses, two studies were found to be influential outliers, namely (31) and (34) and (27) and (30), respectively, and these excessively contributed to both heterogeneity and the overall effect estimate (Figure 2).

2.6.3 Influence diagnostics

Influence diagnostics display and detect each study's influence on the overall effect size of the meta-analysis (44). This influence diagnostic displays different plots that measure different influence diagnostic metrics. Studies with extreme values that may distort

TABLE 1 Basic characteristics of the included studies.

References	Year	Country	Study design	Diagnosis	PVA procedure	Sample size (cases/ Control)	Mean age (years)	Sex (Female %)	RBP (incidence rate%)	TLFI (incidence rate %)	Fellow-up period	Matched or adjusted variables
Yang et al. (23)	2019	China	Retrospective	OVCF	PVP	60/60	69.3	66.7	4.6%	50%	12 months	Age, sex, BMI
Li et al. (24)	2020	China	Retrospective	OVCF	PKP	52/163	75.4	66.5	24.19%	7.4%	1 month	Age, sex, BMI
Li et al. (25)	2021	China	Retrospective	OVCF	PVP	37/231	75	80	13.80%	6.7%	1 month	Age, sex, BMI, surgical level.
Ge et al. (26)	2022	China	Prospective	OVCF	PKP	81/731	70	77.4	11.08%	6.7%	1 month	Age, sex, surgical level
Gao et al. (27)	2023	China	Retrospective	OVCF	PVA	86/790	76.6	64.7	9.82%	44.7%	12 months	Age, sex, BMI, surgical level
Lin et al. (28)	2023	China	Retrospective	OVCF	PKP	47/234	74.5	82.6	16.95%	16.4%	6 months	Age, sex, BMI, surgical level
Wang et al. (29)	2023	China	Retrospective	OVCF	PVP	46/629	77	58.2	6.81%	28%	12 months	Age, sex, BMI, surgical levels
Wang et al. (30)	2023	China	Retrospective	OVCF	PKP	28/155	79	50%	15.30%	53%	12 months	Age, sex, surgical levels
Tu et al. (31)	2024	China	Retrospective	OVCF	PKP	46/221	71.5	82%	17.22%	19.1%	3 months	Age, sex, BMI, surgical level
Chen et al. (32)	2024	China	Retrospective	OVCF	PVP	17/143	75.3	81%	10.62%	23.75%	6 months	Age, sex, BMI
Zhang et al. (33)	2024	China	Retrospective	OVCF	PVP	34/114	75	77%	22.97%	66.89%	N/R	Sex, surgical level,
Shen et al. (34)	2024	China	Retrospective	OVCF	PKP	50/339	74.8	58%	12.85%	22.62%	2 days	Age, sex, BMI, surgical level
Chen et al. (35)	2024	China	Retrospective	OVCF	PVP	48/100	74.7	80%	8.0%	14.19%	1 month	Age, sex, BMI, surgical level

OVCF, Osteoporotic vertebral compression fractures; PVA, percutaneous vertebral augmentation; PVP, percutaneous vertebroplasty; PKP, percutaneous kyphoplasty; RBP, Residual back pain; TLFI, Thoracolumbar fascia injury; BMI, Body mass index.

10.3389/fendo.2025.1532355

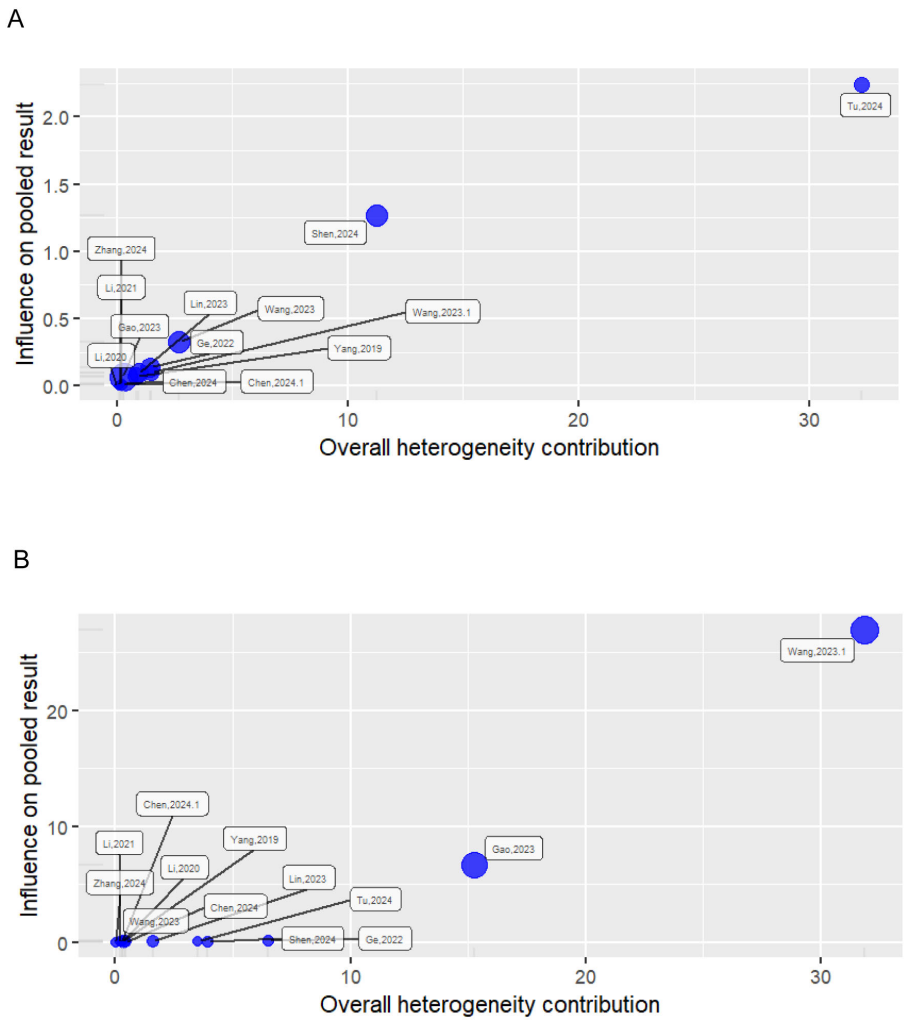

FIGURE 2
Baujat plot showing the influence of studies on heterogeneity and pooled effect. **(A)** Univariate analysis; **(B)** multivariate analysis.

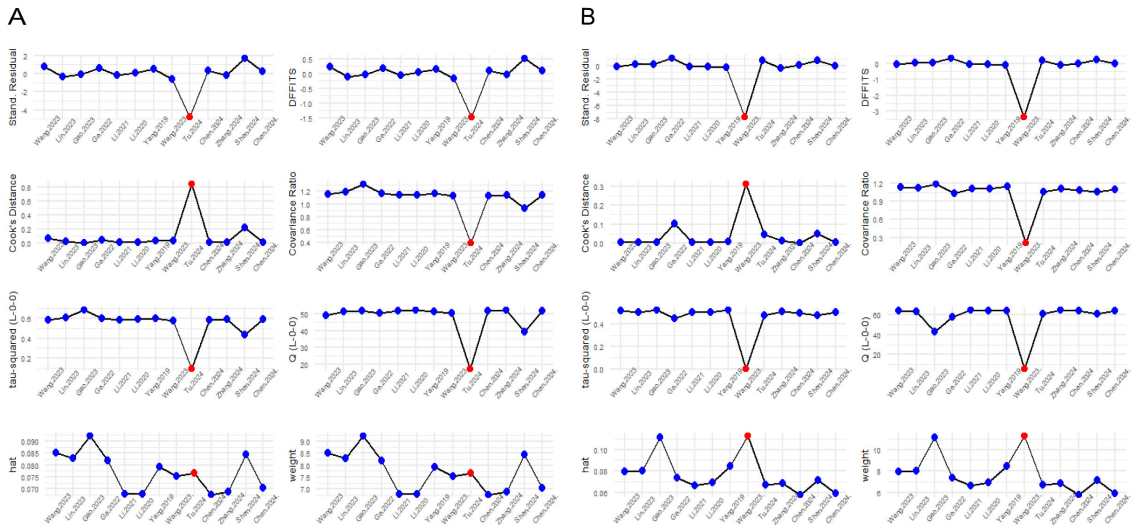

FIGURE 3
Influence diagnostic plot showing different influence diagnostic metrics. **(A)** Univariate analysis; **(B)** Multivariate analysis.

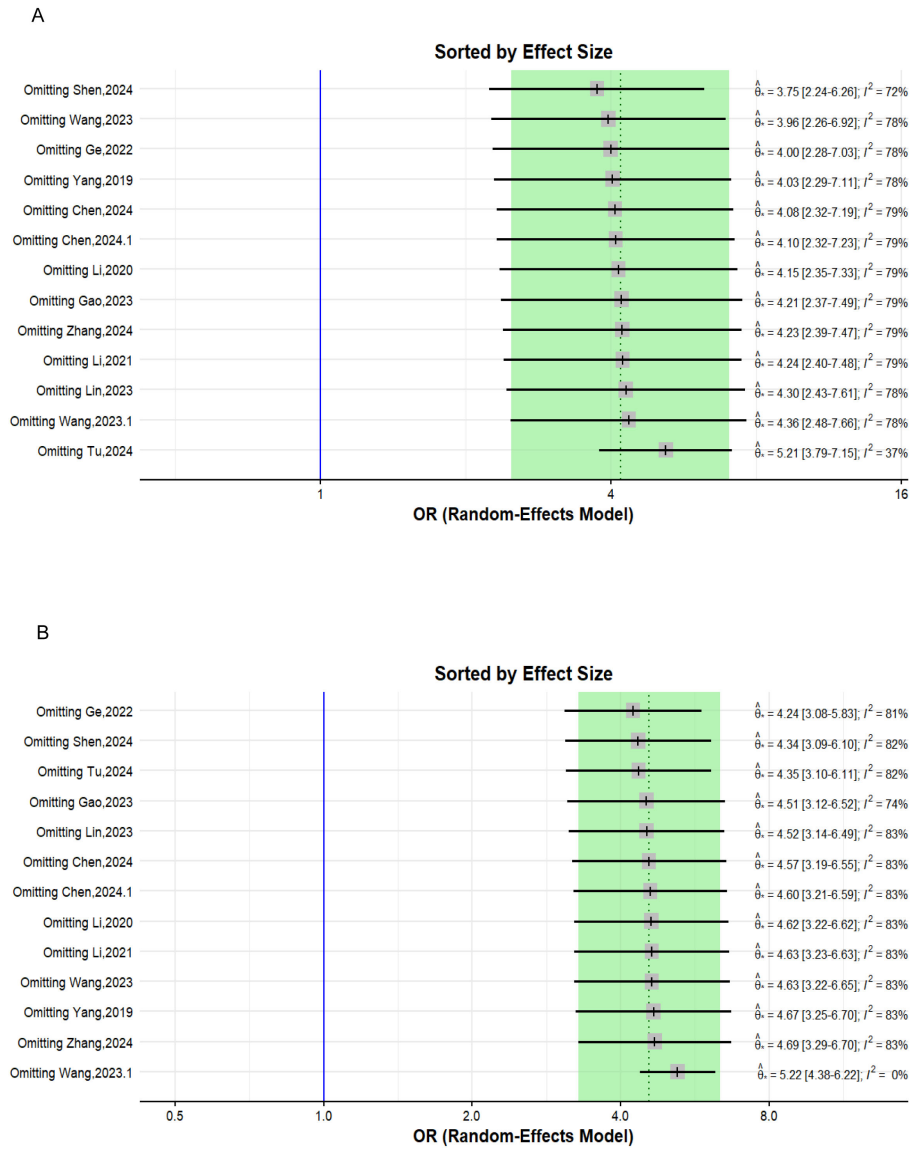

FIGURE 4
Forest plot depicting the leave-one-out sensitivity analysis. **(A)** Univariate analysis; **(B)** multivariate analysis.

the overall effect estimate are shown in red in the different plots. This diagnostic test flagged the same studies as the previous sensitivity analysis in both the univariate and multivariate analyses, namely (31) and (34) and (27) and (30), respectively, as shown in Figure 3.

2.6.4 Leave-one-out-analysis method

The leave-one-out method sensitivity analysis omits one study at a time and recalculates the overall pooled effect size each time. Determining how both heterogeneity and the overall effect estimate change as different studies are excluded each time. In our analysis, the lowest heterogeneity and most robust overall effect estimate were reached after excluding the studies previously flagged by the other sensitivity analyses in both the univariate and multivariate analyses (Figure 4).

2.6.5 GOSH plot diagnostics

GOSH plots (46) are another method that explores the pattern of heterogeneity in a meta-analysis by fitting all possible subsets of the studies into clusters to detect which study combinations contribute to heterogeneity. This can be achieved using the "Gosh.Diagnostics" function in the "dmetar' package that uses three clustering or unsupervised algorithm K-means clustering (47), density reachability and connectivity clustering (DBSCAN) (48), and Gaussian mixture models (49) to display the heterogeneity pattern and study combinations that most likely contribute to it. In our meta-analysis, in both the univariate and multivariate analyses, the GOSH plot demonstrated an apparently high heterogeneity-effect estimate combination pattern (Supplementary Figure 2). This indicates that more than one study contributed to the observed heterogeneity of the effect size. The results of both the univariate

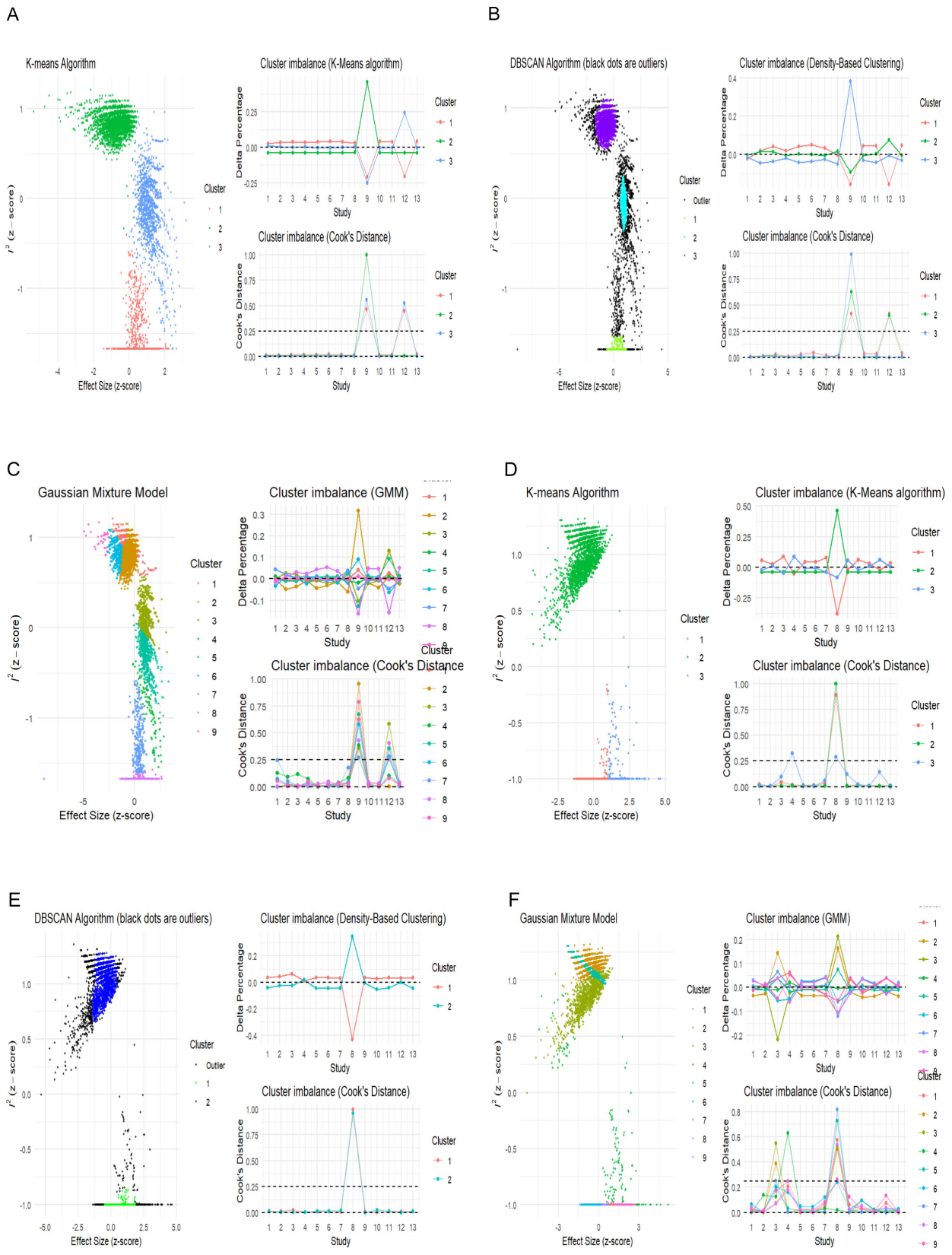

FIGURE 5
Unsupervised machine learning algorithms detecting influential studies. **(A–C)** Univariate analysis; **(D–F)** multivariate analysis.

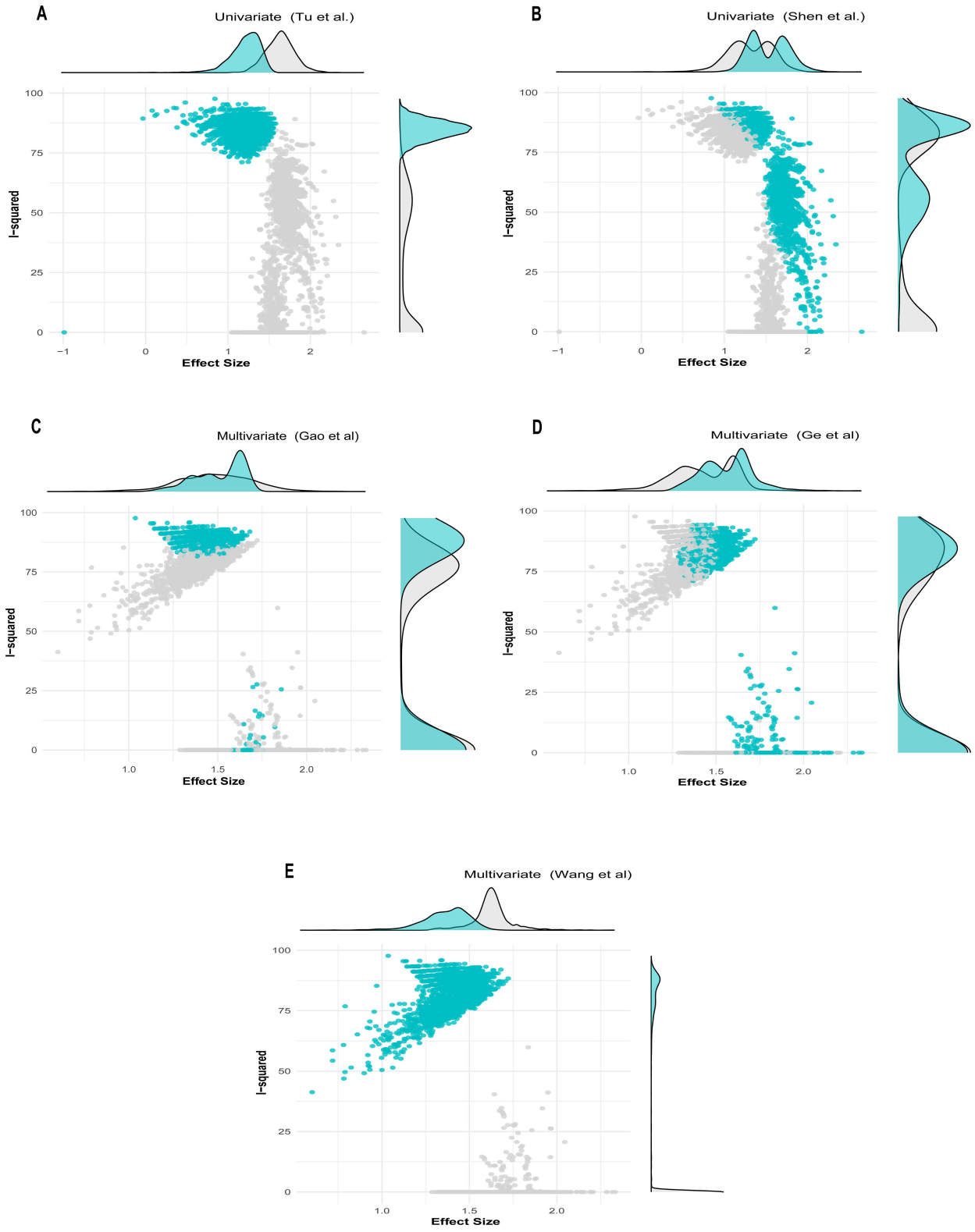

FIGURE 6
GOSH plot showing influential studies with shaded points depicting when the influential study is included in the analysis. **(A, B)** Univariate analysis; **(C–E)** multivariate analysis.

TABLE 2 Newcastle–Ottawa score for quality assessment.

Author	Selection				Comparability		Outcome			Overall score
	1	2	3	4	5	6	7	8	9	
Yang, 2019 (23)	*	*	*	*	*	/	*	*	*	8
Li, 2020 (24)	*	*	*	*	*	*	*	*	/	8
Li, 2021 (25)	*	*	*	*	*	*	*	*	/	8
Ge, 2022 (26)	*	*	*	*	*	/	*	*	/	7
Gao, 2023 (27)	*	*	*	*	*	*	*	*	*	9
Lin, 2023 (28)	*	*	*	*	*	/	*	*	/	7
Wang, 2023 (29)	*	*	*	*	*	/	*	/	*	7
Wang, 2023 (30)	*	*	*	*	*	*	*	*	*	9
Tu, 2024 (31)	*	*	*	*	*	*	*	/	/	7
Chen, 2024 (32)	*	*	*	*	*	/	*	*	*	8
Zhang, 2024 (33)	*	*	*	*	*	/	*	/	/	6
Shen, 2024 (34)	*	*	*	*	*	*	*	/	/	7
Chen, 2024 (35)	*	*	*	*	*	*	*	/	/	7

and multivariate analyses of the different clustering algorithms are shown in Figure 5.

The univariate GOSH plot clustering algorithm results in identifying potential outliers contributing to heterogeneity are as follows (Figure 6):

- K-means: Study 9 (31) and Study 12 (34).
- DBSCAN: Study 9 (31) and Study 12 (34).
- Gaussian mixture model: Study 9 (31) and Study 12 (34)

In the univariate analysis, all cluster combinations incorporating the study by Tu et al. (31), exhibited high heterogeneity with low effect size, indicating the influential nature of this study (Figure 6A). Similarly, all the results in which the study by Shen et al. (34) was included demonstrated reduced heterogeneity contribution but high effect size, rendering this study influential due to its substantial effect on underestimating the overall effect size (Figure 6B).

The multivariate GOSH plot clustering algorithm results in identifying potential outliers contributing to heterogeneity are as follows (Figure 6):

- K-means: Study 8 (30) and Study 4 (26).
- DBSCAN: Study 8 (30).
- Gaussian mixture model: Study 4, Study 8, and Study 3 (26, 27, 30)

In the multivariate analysis, the results from the combinations of studies in which (26) and (27) were included exhibited a small degree of heterogeneity contribution. However, the study by Gao et al. (27), due to its narrow confidence interval, received a high weight and was recognized as an influential study despite its average effect size (Figure 6C). Conversely, the results incorporating the study by Ge et al. (26) demonstrated comparable heterogeneity contribution to that of (27). However, due to its substantial effect contribution relative to the overall effect size, it was considered influential. (Figure 6D). Similarly, the clusters that included the study by Wang et al. (30) demonstrated that this study contributed the highest level of heterogeneity. Despite having the smallest effect size among the studies included in the analysis, this study was previously identified as an influential outlier. (Figure 6E).

3 Results

3.1 Basic characteristics of the included studies

The evaluation included 13 observational studies, consisting of 12 retrospective cohort studies and one prospective research study. These studies collectively involved a study population of 4,542 individuals. Other important parameters from the included studies are listed in the baseline characteristics in Table 1. All studies assessed the association between TLFI as a risk factor and RBP, among other risk factors, following percutaneous vertebral augmentation.

3.2 Findings of the included studies

Yang et al. (23) conducted retrospective case-control research to identify the risk factors for persistent back pain after PVP. From 1,316 patients who underwent PVP for OVCF, 120 were selected. In total, 60 patients reported residual back pain (VAS score >4) 1 month postoperatively and were compared with 60 patients who

did not report residual back pain. Univariate regression analysis revealed that the prevalence of TLFI was 71.7% in the case group and 28.3% in the control group, suggesting that TLFI is a potential risk factor for RBP. Multiple logistic regression analysis adjusted for confounders confirmed TLFI as an independent risk factor associated with RBP post-PVP (OR = 3.805; P = 0.002). Li et al. (24) performed a retrospective study to identify risk factors for residual back pain after PKP in 809 patients with osteoporotic vertebral compression fractures. The final analysis included 215 patients: 52 with moderate-to-severe residual pain (VAS ≥4) 1 month postoperatively and 163 with no or mild pain as controls. Univariate analysis showed that TLFI incidence was 17.3% in the case group and 4.3% in the control group. Multivariate logistic regression adjusted for other risk factors indicated that TLFI was independently associated with residual back pain post-PKP (OR = 4.11; P = 0.014). Li et al. (25) conducted a retrospective analysis to identify risk factors for persistent back pain after PVP. The study included 268 patients with OVCFs divided into residual pain (VAS score ≥4 after 1 month, n=37) and non-residual pain groups (n=231). They observed a TLFI incidence of 16.2% in the residual pain group and 5.2% in the non-residual pain group. Multiple logistic regression analysis showed that TLFI was an independent risk factor for residual pain post-PVP (OR, 3.965; P = 0.022). Similarly, Ge et al. (26) reported that in a population of 731 patients who underwent percutaneous kyphoplasty, 81 developed residual back pain after analyzing the risk factors in a prediction model. In a univariate analysis, they found that TLFI was associated with residual back after PKP surgery (OR, 6.933; P=<0.001) and the multivariate analysis indicated it was an independent risk factor for postoperative pain (OR, 11.377; p <0.001). Gao et al. (27) retrospectively reviewed the data of individuals treated with PVA, both percutaneous vertebroplasty and percutaneous kyphoplasty, to assess the causes of residual pain following the operation. In total, 86 patients were classified in the residual back pain group based on a VAS score ≥4, and 790 patients were in the control group. In a univariate analysis, they found that posterior fascia injury was associated with postoperative back pain with an incidence of 73% in the RBP group compared to 41.6% in the control group. In a multivariate analysis, they found that fascia injury was an independent risk factor associated with residual back pain (OR,5.23; P=<0.001). Lin et al. (28) analyzed retrospective data to identify the risk factors for residual back pain and developed a predictive nomogram after percutaneous kyphoplasty. They categorized subjects into a residual back pain group with a VAS score ≥4 1 month postoperatively and a non-residual back pain group, with 47 patients in the RBP group and 234 in the control group. Univariate analysis revealed that TLFI was associated with persistent pain in 31.9% of cases versus 13.2% of controls. Multivariate logistic regression, after accounting for confounders, indicated that TLFI was independently associated with residual back pain (OR, 5.36; P < 0.001). Wang et al. (29) investigated the risk factors associated with RBP following percutaneous vertebroplasty. In a study of 675 patients with OVCFs, 46 developed RBP (VAS score ≥4) 1 month postoperatively. The univariate logistic regression analysis showed that TLFI was present in 71.7% of the RBP cases compared to 24.8% of the control group. The multivariate analysis adjusted for other risk factors confirmed TLFI as a significant independent risk factor for RBP (OR, 4.083; P= 0.032). Wang et al. (30) conducted a risk factor analysis in a retrospective study on the causes of postoperative pain following PKP in patients with OVCFs. They divided 183 patients who received PKP into RBP and control groups based on a VAS score ≥4 postoperatively, although a pain measurement cutoff was not reported. A TLFI was diagnosed using preoperative MRI fat-suppression sequences. In univariate analysis, TLFI was present in 71.4% of the cases and 49.7% of the control group. After adjusting for confounders in the multivariate logistic regression, TLFI was identified as an independent risk factor for back pain (OR, 1.528; P<0.001). Tu et al. (31) evaluated risk factors for residual pain following PKP and developed a risk prediction model using data from 267 patients with OVCFs. RBP was defined as a VAS score ≥4 1 day postoperatively, dividing patients into RBP and non-RBP groups. A TLFI was identified based on preoperative MRI signal changes, low signal on T1-weighted images (T1WI), and high signal on both T2-weighted images (T2WI) and Short-TI Inversion Recovery (STIR). Multivariate logistic regression analysis, controlling for other factors, revealed that TLFI was independently associated with RBP (OR, 9.1; P < 0.01). Chen et al. (32) investigated the impact of enhanced central sensitization on RPB and its connection to RBP after a PVP procedure and related risk factors. RBP was defined as a VAS score of ≥4 at 1 d, 2 weeks, and 1 month after PVA. In the multivariate logistic regression analysis, TLFI was recognized as an independent risk factor for RBP and was defined according to preoperative MRI signal changes, low signal on T1W1, and high signal intensity on T2W1 and STIR sequences. Zhang et al. (33) concluded in a multivariate logistic regression analysis that preoperative TLFI is an independent risk factor for RPB post-PVA interventions. However, this study did not report a specific VAS score cut-off point or TLFI diagnostic method but referenced TLFI findings from previous studies (29). Shen et al. (34) examined the short-term risk factors associated with RBP after PKP. A VAS score of ≥4 at 2 days postoperatively was defined as RBP. A TLFI was defined as the presence of preoperative fascia injury and was diagnosed using MRI signal intensity changes, low signal on T1W1, and high signal on both T2W1 and fat-suppressed sequences. The multivariate risk analysis showed that preoperative TLFI was an independent risk factor for RBP after PKP surgery. Chen et al. (35) likewise examined the risk factors associated with RBP in patients who underwent PVP. The presence or absence of RBP was defined as a VAS score ≥4 immediately and 1 month postoperatively. The TLFI diagnostic method was not explicitly reported but referenced

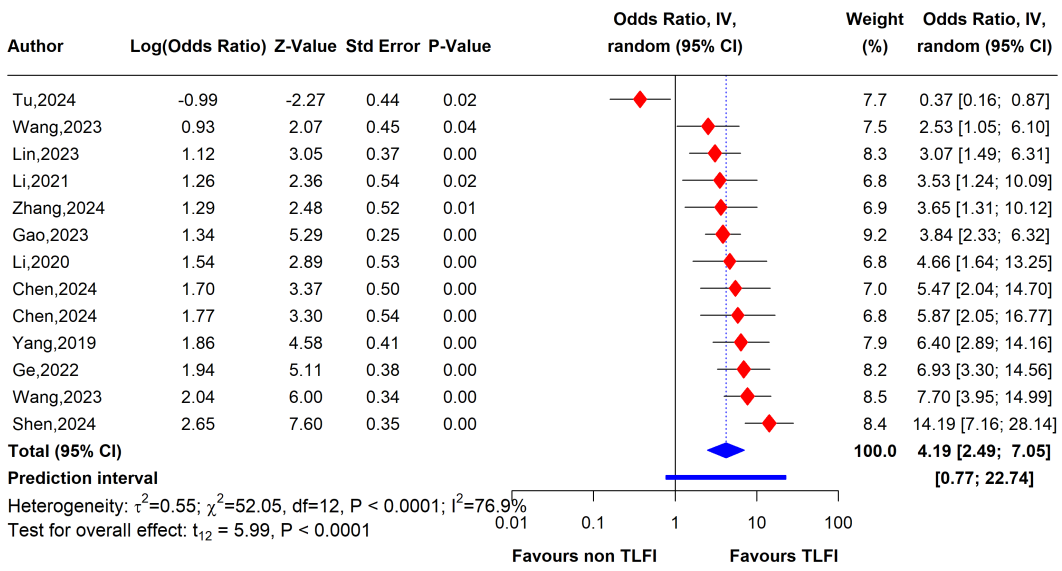

FIGURE 7
Forest plot depicting an association between TLFI and RBP following PVA with influential studies and outliers included (univariate analysis).

(28, 31). After adjusting for related risk factors in the multivariate logistic regression analysis, the presence of a preoperative TLFI was a risk factor that could lead to postoperative pain.

3.3 Results of current meta-analysis

The univariate analysis revealed that patients with a TLFI were significantly more likely to develop RBP than those without a TLFI. The pooled results of 13 studies indicate that the odds ratio (OR) for developing RBP in TLFI patients is 4.19 (95% CI: 2.49 to 7.05, I^2 = 76.9%), with the presence high level of heterogeneity. This suggests a more than three-fold increase in risk following PVA, as shown in Figure 7. The multivariate analysis of the pooled effect also demonstrated a substantial correlation between TLFI and the risk of RBP development post-PVA after accounting for confounders and other risk factors related to RBP, with an OR of 4.57 (95% CI: 3.28 to 6.37, I^2 = 81.5%) (Figure 8). However, high heterogeneity was observed in the multivariate analysis, indicating a considerable difference between the studies.

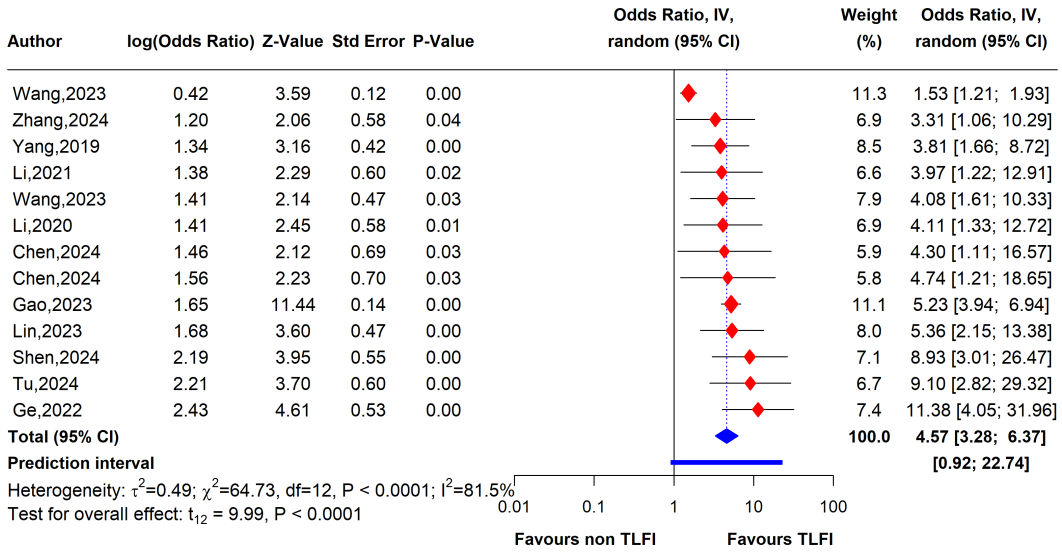

FIGURE 8
Forest plot depicting an association between TLFI and RBP following PVA with influential studies and outliers included (multivariate analysis).

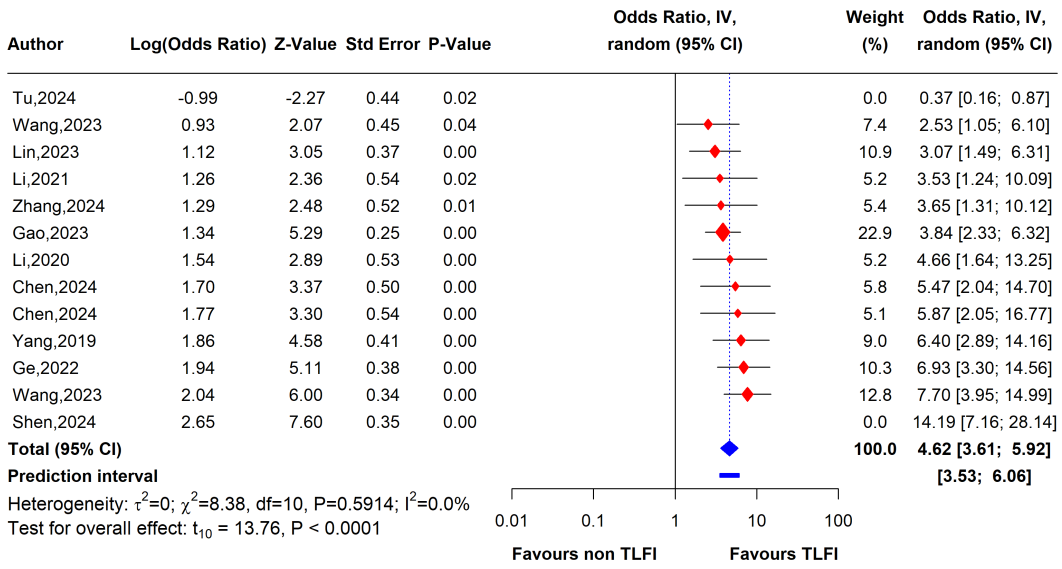

FIGURE 9
Forest plot depicting an association between TLFI and RBP following PVA with influential studies and outliers excluded (univariate analysis).

3.3.1 Univariate sensitivity analysis

To evaluate the heterogeneity of these results and assess the influential studies contributing to it, a sensitivity analysis was performed and all different sensitivity analysis metrics identified two studies, i.e., (31) and (34) as influential outliers contributing to the majority of the observed heterogeneity and underestimating the overall effect size. After excluding these two studies, the overall effect size increased to an OR of 4.62 (95% CI: 3.61 to 5.92, I^2 = 0%) with no heterogeneity, indicating a more homogenous and stable estimate and reinforcing the significant association between TLFI and RBP (Figure 9).

3.3.2 Multivariate sensitivity analysis

To assess the heterogeneity of these results and investigate the influential studies contributing to it, a sensitivity analysis using the leave-one-out method was performed. The sensitivity analysis identified three studies, i.e., (26, 27, 30), to be influential and outliers contributed significantly to the high heterogeneity observed and overall effect size. After excluding these studies, the overall effect size was recalculated, showing a somewhat stronger and more homogenous estimate than the initial one with an OR of 4.79 (95% CI: 3.76 to 6.11, I^2 = 0%), with no heterogeneity. This indicates that the initial results were affected by the presence of influential and outlier studies that underestimated the overall effect size. However, the recalculated effect size confirmed a significant association between TLFI and increased risk of RBP following PVA (Figure 10)

3.4 Publication bias

We used a funnel plot to evaluate the presence of small study bias by visually inspecting the symmetry of the plot, imputing any missing effect estimate using the Duval and Tweedie trim-and-fill method and generating a contour-enhanced funnel plot (50, 51). After omitting influential studies, due to the limitations of the trim-and-fill method with the existence of high heterogeneity among studies (52), neither the visual inspection nor the trim-and-fill method showed any funnel plot asymmetry or missing effects, indicating no small study bias (Figure 11).

Additionally, Egger's regression test did not suggest the presence of asymmetry in the funnel plot (53) (Table 3).

4 Discussion

The thoracolumbar fascia, also known as the lumbodorsal fascia, is an intricate multilayered connective tissue structure located in the posterior region of the trunk. Extending from the thoracic vertebrae to the sacrum, this fascia plays a vital role in maintaining the biomechanical stability of the spine and facilitating movements such as forward spinal flexion. Furthermore, it serves as an anchor point for various muscles along the vertebral column, enabling the distribution of forces across the trunk and enhancing core stability (20).

The precise mechanisms by which thoracolumbar fascia injury causes back pain remain unclear. However, based on the existing research, three mechanisms have been suggested for how TLFI contributes to back pain, and these proposed mechanisms may exist in isolation or in combination (16). First, by disrupting the structural integrity of the fascia, TLFI can cause micro-injuries or inflammation that may directly stimulate nociceptive nerve endings, which are specialized sensory nerve endings found in abundance within the fascial tissue. This direct stimulation can elicit back pain. A study conducted by Barry et al. (54) demonstrated that the thoracolumbar fascia contained approximately three times the concentration and distribution of

sensory nerve fibers with calcitonin gene-related peptide (CGRP)-positive fibers compared with the back muscles. Similarly, Tesarz et al. (55) found that the fascia possesses a dense network of nociceptive nerves and the majority of CGRP-and substance P (SP)-containing sensory fibers are located in the outer layer of the fascia and subcutaneous tissue. Second, following TLF micro-injury and inflammation, restructuring, remodeling, or tissue stiffness is possible, leading to compromised functional integrity and proprioceptive signaling that alters the sensory input of fascial nociceptors (56). Finally, injury to the fascia can activate nociceptive nerve terminals, resulting in enhanced sensitivity and pain radiating from adjacent tissues with spinal connections similar to those of the thoracolumbar fascia (TLF) (16). Other studies have also indicated that these nerve endings proliferate following inflammatory or chemical stimulation in both experimental rats and humans, suggesting that fascial damage may contribute to back pain (57, 58). A study conducted by Schilder et al. (59) revealed the crucial role of the human thoracolumbar fascia in lower back pain. Their findings demonstrated that this tissue exhibits greater sensitivity to chemical stimuli than the muscle or subcutaneous tissues. This study involved artificially inducing inflammation by administering hypertonic saline into the thoracolumbar fascia, which elicited severe pain, extended pain duration, and a more extensive pain distribution pattern reminiscent of acute lower back pain symptoms. Moreover, the findings suggest that disruption or disorganization of fascial structures could be a contributing factor to chronic low back pain. These findings elucidate the role of the TLF as a significant etiological factor for back pain.

This systematic review and meta-analysis was conducted to assess the relationship between TLFI as an independent risk factor for the development of residual back pain following PVA treatment in patients with OVCFs. Our meta-analysis revealed that TLFI significantly increased the risk of RBP after PVA. The univariate analysis showed that patients with a TLFI were more than four times (OR: 4.62) more likely to develop postoperative pain than those without a TLFI, without adjusting for other related risk factors that may contribute to RBP. This result is consistent with previous findings (30). The sensitivity analysis indicated reduced heterogeneity to no heterogeneity after excluding two studies that contributed the majority of the observed heterogeneity, as shown in Figures 7, 9. Similarly, after accounting for confounders and other related risk factors, the multivariate analysis confirmed an independent relationship between TLFI and the development of postoperative pain (OR: 4.79). This indicates that patients with a TLFI are more than four times more likely to develop residual back pain than those without a TLFI, demonstrating a strong association. Our findings are consistent with those of previous studies (33, 36). A sensitivity analysis was performed to ensure the robustness of the pooled effect estimate of the outcome and investigate the studies contributing to the heterogeneity observed in the analysis. After excluding three influential studies identified to be contributing to heterogeneity and affecting the overall effect estimate, there was no heterogeneity in the overall effect size, demonstrating the robustness of the overall effect estimate (Figures 8, 10). Both the univariate and multivariate analyses robustly indicated that TLFI significantly increased the risk of RBP development after PVA. The sensitivity analysis confirmed that the observed associations were consistent and not unduly influenced by any individual study. The observed heterogeneity likely occurred due to statistical heterogeneity rather than methodological differences between the studies.

Recent studies have reported that osteoporotic vertebral compression fractures often involve thoracolumbar fascia injury, which is associated with residual back pain following percutaneous vertebral augmentation. A prospective cohort study by Yan et al. (60) investigated the causes of persistent back pain following vertebroplasty and found that fascia injury was present in 42.1% of the cases. Yang

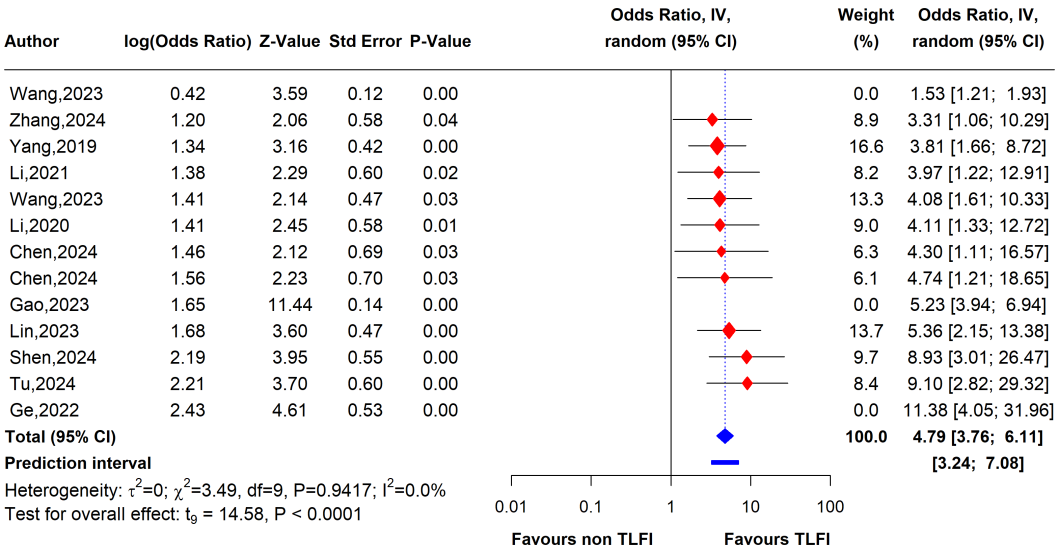

FIGURE 10
Forest plot depicting an association between TLFI and RBP following PVA with influential studies and outliers excluded (multivariate analysis).

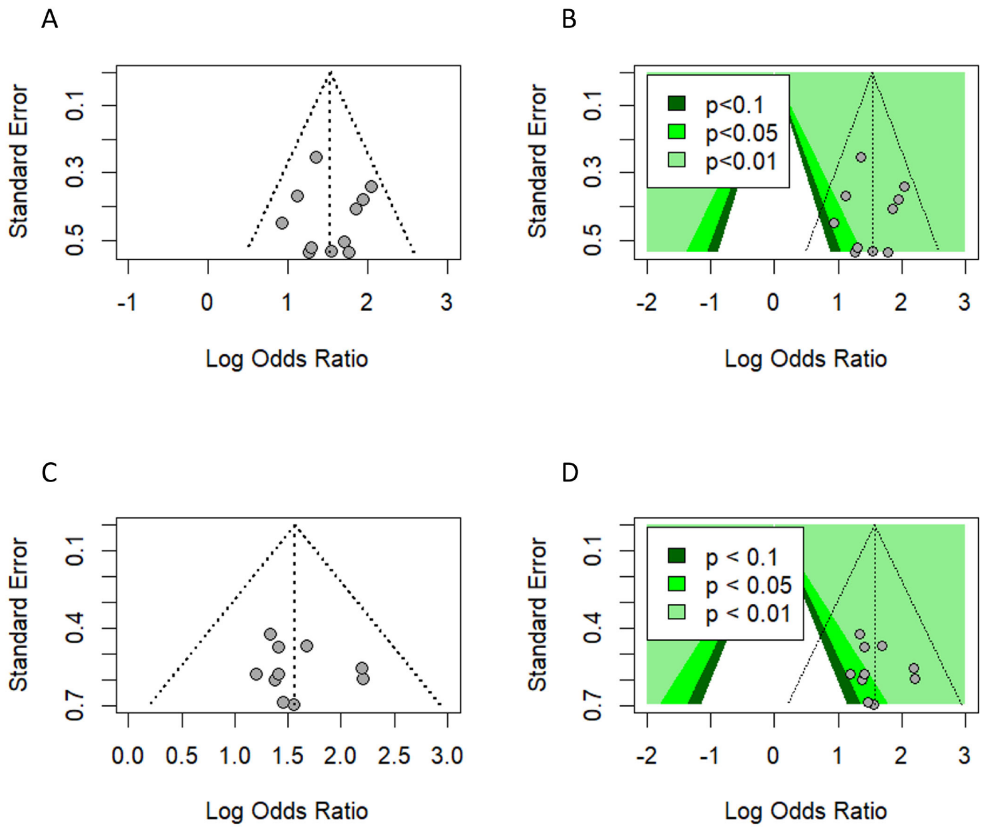

FIGURE 11
Publication bias. **(A, B)** Funnel plot and contour-enhanced funnel plot (univariate analysis). **(C, D)** Funnel plot and contour-enhanced funnel plot (multivariate analysis) with influential and outlier studies excluded.

et al. (61) retrospectively analyzed the data of 132 patients with OVCFs and determined that TLFI has a substantial impact on the absence of immediate pain alleviation with a 39.4% incidence rate compared to those without a TLFI and it prolongs the ambulation time following PVP. Similarly, they reported that TLFI and associated pain could persist for over 3 months in certain patients, with follow-up MRI revealing worsened fascia injury compared to the preoperative condition, potentially contributing to prolonged postoperative pain. In this meta-analysis, the TLFI incidence rate was 28%, which indicates that fascia injury is a frequently overlooked complication that often coexists with osteoporotic vertebral fractures, underscoring the need for greater clinical attention. Osteoporotic vertebral compression fractures predominantly result from low-energy trauma and routine daily activities, such as lifting and twisting, or even occur without any noticeable trauma, rather than from high-impact trauma. This is due to the loss of bone quality and integrity (62, 63). However, this may not be the case for patients with OVCFs with a thoracolumbar fascia injury who are likely to have sustained high-impact trauma. A recent study by Deng et al. (17) evaluated the occurrence of TLFIs with an incidence of 27.8% in patients with OVCFs treated with PKP and found that the severity of fascia injury increased with the severity of trauma sustained by the patient. Moreover, they observed that a TLFI showed multilevel involvement, which was positively associated with the degree of trauma and impacted the efficacy of PKP, leading to acute residual pain. However, other medical situations in patients with OVCFs may contribute to fascia injury, which leads to postoperative pain following the augmentation procedure. In a retrospective study conducted by Luo et al. (18), TLFI contributed to RBP in patients with OVCFs after PVP. Simultaneously, they evaluated the risk factors that may lead to a TLFI and determined that a low body mass index (BMI), elevated blood pressure, and sarcopenia were significant risk factors for a TLFI. Sarcopenia was significantly more prevalent in the TLFI group than in the non-TLFI group, affecting 51.1% of individuals, compared to 14.7% in the non-TLFI cohort. Identifying these risk factors preoperatively can facilitate better risk stratification and counseling for patients undergoing PVA.

TABLE 3 Quantification of funnel plot asymmetry.

Study analysis	Test	Bias estimate	Confidence interval	t	P
Univariate	Egger's regression test	0.022	-2.3-2.34	0.018	0.9858
Multivariate	Egger's regression test	0.653	-1.91-3.21	0.500	0.6305

A TLFI is currently diagnosed by careful examination of the posterior fascia for any anomalous signals that may suggest the presence of edema on a preoperative MRI image. These signals may appear as low-intensity signals on T1WIs and as high-intensity signals on T2WIs and T2W1 fat-suppression sequences. Early detection and diagnosis of TLFI using advanced imaging modalities, such as MRI, can facilitate tailored interventions to alleviate residual pack pain. Thoracolumbar fascia injuries on MRI often present as elongated or flake-like patterns across multiple segments. These injuries are difficult to detect with only T1WIs and T2WIs but are clearly visible on T2WI fat-suppression imaging (17, 61). The development of standardized imaging protocols can ensure consistent detection and optimize preoperative planning. Although PVA procedures are effective treatment options for alleviating pain originating from OVCFs, they have no effect on improving the pain associated with fascia injury, which becomes obvious early in the postoperative period or the subsequent inflammation, and treating the fracture alone can result in suboptimal pain alleviation, patient dissatisfaction, and postoperative pain (61). Furthermore, reversing fascia injury may require a long recovery time. Langevin et al. (64) found that 4 weeks of passive stretching exercise did not restore fascia mobility following injury and removal of a movement restriction device, suggesting that a fascia injury could become a long-term issue and may not resolve automatically. Similarly, recent studies also suggest that TLFI and associated pain could persist longer in some individual patients and could even become exacerbated, leading to prolonged residual pain (61). These findings underscore the importance of identifying the origin of TLFI in patients with OVCFs to ensure successful PVA interventions. Additionally, considering patients with OVCFs are often elderly and have multiple comorbidities. The incidence of TLFI could be multifactorial and linked to natural age-related deterioration of the fascia due to overuse and poor posture. Furthermore, it could indicate severe traumatic injury or possibly suggest an undiagnosed comorbidity, such as sarcopenia, which is relatively common among elderly individuals with OVCFs (15, 17, 18, 31).

By recognizing TLFI as a risk factor for residual pain, it may be possible to devise more effective preoperative and postoperative patient care strategies and reduce the development of RBP. Preoperative treatment options may include focused pain management protocols such as localized anti-inflammatory injections to relieve TLFI-associated pain. Liu et al. (65) administered a cocktail of ropivacaine and betamethasone to a group of OVCF patients with TLFI prior to the PVP augmentation procedure. They compared the results to those of the control group and concluded that combined treatment can help alleviate pain, reduce the chance of RBP, and shorten the need for postoperative pain medication. However, this may prolong the duration of the surgery. Moreover, adding specific individually tailored physical therapy and functional exercises postoperatively aimed at helping recover thoracolumbar fascia integrity could help reduce fascia inflammation, mitigate chronic postoperative pain, and support fascia recovery (66, 67). Combining these preoperative medical interventions and postoperative physiotherapies based on individual patient needs may reduce postoperative pain associated with TLFI and its complications (61). Furthermore, although some degree of fascia damage is inevitable during vertebral augmentation procedures, reducing it as much as possible by more effectively utilizing navigation equipment such as C-arm fluoroscopy to better locate pedicles, reduce operation time, and reduce unnecessary needle punctures, particularly for OVCF patients with existing TLFI, could be an important step in mitigating persistent postoperative pain.

4.1 Implications of TLFI

The findings of this meta-analysis indicate that failing to address TLFI or its potential causes before and after surgery may prevent PVA treatment from fully achieving the intended outcomes of immediate pain alleviation and fracture stabilization. A thorough medical history and general health assessments of patients with OVCFs can aid physicians in differential diagnoses, and understanding the cause of the fracture traumatic or non-traumatic could be a vital step in ascertaining the origin of TLFI, as it eliminates trauma-related fascia injury. Currently, the presence of TLFI is reported in radiology reports as incidental soft tissue edema without any emphasis and many orthopedic doctors regard it as a minor issue, often attributing it to trauma, which is not applicable to all patients with OVCFs. Consequently, it is frequently overlooked compared to more pressing osteoporotic vertebral fractures. However, as demonstrated in this study, there is growing evidence indicating that a preoperative TLFI may have a negative clinical impact on the treatment outcome and pain relief in patients with OVCFs. A preoperative TLFI should be considered an indicator of early postoperative back pain (17). Additionally, considering that TLFI as a postoperative pain indicator goes beyond PVA, it could inform other musculoskeletal or spine-related conditions such as chronic back pain.

4.2 Strengths

This systematic review and meta-analysis has several strengths and limitations. To ensure the inclusion of all eligible studies, we conducted an exhaustive database search using a rigorous search strategy and criteria. We established a robust relationship between TLFI and postoperative residual pain through univariate and multivariate analyses, modifying the other risk factors in the multivariate analysis following PVA. In addition, we conducted a sensitivity analysis to investigate heterogeneity among the studies. After removing the two outliers that contributed to heterogeneity, we further confirmed the link between TLFI and RBP. Furthermore, this is the first meta-analysis to demonstrate an independent relationship between TLFI and RBP development after post-PVA treatment.

4.3 Limitations

In total, 12 of the 13 studies included in the analysis were retrospective cohort studies with a limited number of patients. These studies inherently contain bias and may introduce bias into

the results of the review. Furthermore, some degree of variability may exist in the definition of fascia injury due to a lack of specific guidelines and definitions to follow, which may limit our conclusion. In addition, the data analyzed in this meta-analysis pertained to the short-term relationship between TLFI and RBP. There is a lack of information on the medium and long-term outcomes.

4.4 Future research

In order to validate the connection between TLFI and RBP after PVA, prospective studies are necessary. Researchers should also investigate the precise manner in which TLFI contributes to RBP, which could potentially mitigate this risk. Future studies should also evaluate the risk factors that may cause fascia injury in addition to the trauma associated with an OVCF, which may not always exist in patients, such as sarcopenia, which has been implicated in fascia injury. Current diagnostic procedures for what constitutes a TLFI and what degree of fascia injury should be considered a TLFI are lacking. To minimize this difference and the heterogeneity that inevitably arises from the lack of guidelines to follow, quantitative diagnostic methods are needed in future research.

5 Conclusion

This study demonstrated that preoperative TLFI is associated with postoperative residual pain after PVA, and the pooled effect consistently showed that, with or without the presence of other risk factors, patients with TLFIs have an increased risk of developing RBP. Recognizing fascia injury as a potential source of postoperative pain in clinical practice could enhance the care of these patients and mitigate postoperative pain. Additional research is needed to fully understand TLFIs and to develop effective treatments to reduce the risk of postoperative residual pain.

Data availability statement

The original contributions presented in the study are included in the article/Supplementary Material. Further inquiries can be directed to the corresponding author.

Author contributions

AA: Conceptualization, Writing – review & editing, Data curation, Formal analysis, Investigation, Methodology, Software, Writing – original draft. XX: Investigation, Methodology, Writing – review & editing. ZZ: Conceptualization, Funding acquisition, Methodology, Project administration, Supervision, Visualization, Writing – review & editing. JC: Investigation, Methodology, Writing – review & editing.

Funding

The author(s) declare that financial support was received for the research and/or publication of this article. This study was supported by the Traditional Chinese Medicine Science and Technology Development Program of Jiangsu Province (MS2021079).

Conflict of interest

The authors declare that the research was conducted in the absence of any commercial or financial relationships that could be construed as a potential conflict of interest.

Generative AI statement

The author(s) declare that no Generative AI was used in the creation of this manuscript.

Publisher's note

Supplementary material

The Supplementary Material for this article can be found online at: https://www.frontiersin.org/articles/10.3389/fendo.2025.1532355/full#supplementary-material

References

1. Johnell O, Kanis JA. An estimate of the worldwide prevalence and disability associated with osteoporotic fractures. *Osteoporos Int*. (2006) 17:1726–33. doi: 10.1007/s00198-006-0172-4

2. Sözen T, Özışık L, Başaran NÇ. An overview and management of osteoporosis. *Eur J Rheumatol*. (2017) 4:46–56. doi: 10.5152/eurjrheum.2016.048

3. Ong KL, Beall DP, Frohbergh M, Lau E, Hirsch JA. Were VCF patients at higher risk of mortality following the 2009 publication of the vertebroplasty "sham" trials? *Osteoporos Int*. (2018) 29:375–83. doi: 10.1007/s00198-017-4281-z

4. Lau E, Ong K, Kurtz S, Schmier J, Edidin A. Mortality following the diagnosis of a vertebral compression fracture in the Medicare population. *J Bone Joint Surg Am*. (2008) 90:1479–86. doi: 10.2106/JBJS.G.00675

5. Li F, Eckstrom E, Harmer P, Fitzgerald K, Voit J, Cameron KA. Exercise and fall prevention: narrowing the research-to-practice gap and enhancing integration of clinical and community practice. *J Am Geriatrics Soc*. (2016) 64:425–31. doi: 10.1111/jgs.13925

6. Himič V, Syrmos N, Ligarotti GKI, Kato S, Fehlings MG, Ganau M. The role of genetic and epigenetic factors in determining the risk of spinal fragility fractures: new

insights in the management of spinal osteoporosis. *Quantitative Imaging Med Surg*. (2023) 13:7632645–7637645. doi: 10.21037/qims-23-513

7. Klazen CA, Lohle PN, de Vries J, Jansen FH, Tielbeek AV, Blonk MC, et al. Vertebroplasty versus conservative treatment in acute osteoporotic vertebral compression fractures (Vertos II): an open-label randomised trial. *Lancet*. (2010) 376:1085–92. doi: 10.1016/S0140-6736(10)60954-3

8. Yang H, Chen L, Zheng Z, Yin G, Lu WW, Wang G, et al. Therapeutic effects analysis of percutaneous kyphoplasty for osteoporotic vertebral compression fractures: A multicentre study. *J Orthopaedic Translation*. (2017) 11:73–7. doi: 10.1016/j.jot.2017.04.003

9. Galibert P, Deramond H, Rosat P, Le Gars D. Preliminary note on the treatment of vertebral angioma by percutaneous acrylic vertebroplasty. *Neuro-chirurgie*. (1987) 33:166–8.

10. Yimin Y, Zhiwei R, Wei M, Jha R. Current status of percutaneous vertebroplasty and percutaneous kyphoplasty – a review. *Med Sci Monit*. (2013) 19:826–36. doi: 10.12659/MSM.889479

11. Dohm M, Black CM, Dacre A, Tillman JB, Fueredi G. A randomized trial comparing balloon kyphoplasty and vertebroplasty for vertebral compression fractures due to osteoporosis. *Am J Neuroradiology*. (2014) 35:2227–36. doi: 10.3174/ajnr.A4127

12. Boonstra AM, Schiphorst Preuper HR, Balk GA, Stewart RE. Cut-off points for mild, moderate, and severe pain on the visual analogue scale for pain in patients with chronic musculoskeletal pain. *Pain*. (2014) 155:2545–50. doi: 10.1016/j.pain.2014.09.014

13. Gerbershagen HJ, Rothaug J, Kalkman CJ, Meissner W. Determination of moderate-to-severe postoperative pain on the numeric rating scale: a cut-off point analysis applying four different methods. *BJA: Br J Anaesthesia*. (2011) 107:619–26. doi: 10.1093/bja/aer195

14. Yang X-G, Dong Y-Q, Liu X, Liu X-L, Luo H-T, Bao Y, et al. Incidence and prognostic factors of residual back pain in patients treated for osteoporotic vertebral compression fractures: a systematic review and meta-analysis. *Eur Spine J*. (2024) 33:4521–37. doi: 10.1007/s00586-024-08426-z

15. Peng Y, Wu X, Ma X, Xu D, Wang Y, Xia D. Comparison between the clinical effect of percutaneous kyphoplasty for osteoporosis vertebral compression fracture patient with or without sarcopenia: A retrospective cohort study. *IJGM*. (2023) 16:3095–103. doi: 10.2147/IJGM.S423016

16. Wilke J, Schleip R, Klingler W, Stecco C. The lumbodorsal fascia as a potential source of low back pain: A narrative review. *BioMed Res Int*. (2017) 2017:e5349620. doi: 10.1155/2017/5349620

17. Deng Z, Feng T, Wu X, Xie H, Song D, Wang J, et al. Thoracolumbar fascia injury in osteoporotic vertebral fracture: the important concomitant damage. *BMC Musculoskeletal Disord*. (2023) 24:166. doi: 10.1186/s12891-023-06280-6

18. Luo Y, Jiang T, Guo H, Lv F, Hu Y, Zhang L. Osteoporotic vertebral compression fracture accompanied with thoracolumbar fascial injury: risk factors and the association with residual pain after percutaneous vertebroplasty. *BMC Musculoskelet Disord*. (2022) 23:343. doi: 10.1186/s12891-022-05308-7

19. Stecco C, Macchi V, Porzionato A, Duparc F, De Caro R. The fascia: the forgotten structure. *IJAE: Ital J Anat Embryology*. (2011) 116:127–38. doi: 10.1400/207563

20. Willard FH, Vleeming A, Schuenke MD, Danneels L, Schleip R. The thoracolumbar fascia: anatomy, function and clinical considerations. *J Anat*. (2012) 221:507–36. doi: 10.1111/j.1469-7580.2012.01511.x

21. Page MJ, McKenzie JE, Bossuyt PM, Boutron I, Hoffmann TC, Mulrow CD, et al. The PRISMA 2020 statement: an updated guideline for reporting systematic reviews. *BMJ*. (2021) 372:n71. doi: 10.1136/bmj.n71

22. Higgins JP, Green S. Cochrane handbook for systematic reviews of interventions. *Wiley*. (2008). doi: 10.1002/9780470712184

23. Yang J-S, Liu J-J, Chu L, Li J, Chen C, Chen H, et al. Causes of residual back pain at early stage after percutaneous vertebroplasty: A retrospective analysis of 1,316 cases. *Pain Physician*. (2019) 22:E495–503. doi: 10.36076/ppj/2019.22.e495

24. Li Y, Yue J, Huang M, Lin J, Huang C, Chen J, et al. Risk factors for postoperative residual back pain after percutaneous kyphoplasty for osteoporotic vertebral compression fractures. *Eur Spine J*. (2020) 29:2568–75. doi: 10.1007/s00586-020-06493-6

25. Li Q, Shi L, Wang Y, Guan T, Jiang X, Guo D, et al. A nomogram for predicting the residual back pain after percutaneous vertebroplasty for osteoporotic vertebral compression fractures. *Pain Res Manage*. (2021) 2021:1–12. doi: 10.1155/2021/3624614

26. Ge C, Chen Z, Lin Y, Zheng Y, Cao P, Chen X. Preoperative prediction of residual back pain after vertebral augmentation for osteoporotic vertebral compression fractures: Initial application of a radiomics score based nomogram. *Front Endocrinol*. (2022) 13:1093508. doi: 10.3389/fendo.2022.1093508

27. Gao X, Du J, Hao D, He B, Yan L. Risk factors for residual back pain following percutaneous vertebral augmentation: the importance of paraspinal muscle fatty degeneration. *Int Orthopaedics (SICOT)*. (2023) 47:1797–804. doi: 10.1007/s00264-023-05809-7

28. Lin M, Wen X, Huang Z, Huang W, Zhang H, Huang X, et al. A nomogram for predicting residual low back pain after percutaneous kyphoplasty in osteoporotic vertebral compression fractures. *Osteoporos Int*. (2023) 34:749–62. doi: 10.1007/s00198-023-06681-2

29. Wang Z-W, Wang G-Y, Liu D-K, Zhang D-Z, Zhao C. Risk factors for residual back pain after PVP treatment for osteoporotic thoracolumbar compression fractures: A retrospective cohort study. *World Neurosurg*. (2023) 180:e484–93. doi: 10.1016/j.wneu.2023.09.094

30. Wang R, Xu Y, Ma X. Risk factors and strategies for recovery quality, postoperative pain, and recurrent fractures between percutaneous kyphoplasty and percutaneous vertebroplasty in elderly patients with thoracolumbar compression fractures: a retrospective comparative cohort study. *Ann Trans Med*. (2023) 11:122–2. doi: 10.21037/atm-22-6475

31. Tu W, Niu Y, Su P, Liu D, Lin F, Sun Y. Establishment of a risk prediction model for residual low back pain in thoracolumbar osteoporotic vertebral compression fractures after percutaneous kyphoplasty. *J Orthop Surg Res*. (2024) 19:41. doi: 10.1186/s13018-024-04528-y

32. Chen K, Gao T, Zhu Y, Lyu F, Jiang J, Zheng C. Augmented Central Pain Processing Occurs after Osteoporotic Vertebral Compression Fractures and Is Associated with Residual Back Pain after Percutaneous Vertebroplasty. *Asian Spine J*. (2024) 18:380–9. doi: 10.31616/asj.2023.0429

33. Zhang Z. Risk factors for low back pain following percutaneous vertebroplasty in patients with osteoporotic vertebral compression fracture. *Am J Transl Res*. (2024) 16:3778–86. doi: 10.62347/SKKU1066

34. Shen L, Yang H, Zhou F, Jiang T, Jiang Z. Risk factors of short-term residual low back pain after PKP for the first thoracolumbar osteoporotic vertebral compression fracture. *J Orthopaedic Surg Res*. (2024) 19:792. doi: 10.1186/s13018-024-05295-6

35. Chen C, Wu B, Yu H, Dai Z, Yan L, Cai D, et al. Association between vertebral bone quality score and residual back pain following percutaneous vertebroplasty for osteoporotic vertebral compression fractures. *Eur Spine J*. (2024) 34:537–45. doi: 10.1007/s00586-024-08619-6

36. Wells GA, Shea B, O'Connell D, Peterson J, Welch V, Losos M, et al. The Newcastle-Ottawa Scale (NOS) for assessing the quality of nonrandomised studies in meta-analyses. (2000).

37. R Core Team. R: A Language and Environment for Statistical Computing (2023). Available online at: https://www.R-project.org/ (Accessed July 13, 2024).

38. Balduzzi S, Rücker G, Schwarzer G. How to perform a meta-analysis with R: a practical tutorial. *Evid Based Ment Health*. (2019) 22:153–60. doi: 10.1136/ebmental-2019-300117

39. Harrer M, Cuijpers P, Furukawa T, Ebert DD. dmetar: companion R package for the guide "Doing meta-analysis in R. (2019). doi: 10.5281/zenodo.2551802

40. Harrer M, Cuijpers P, Furukawa TA, Ebert DD. *Doing Meta-Analysis with R: A Hands-On Guide. 1st ed*. Boca Raton, FL and London: Chapman & Hall/CRC Press (2021).

41. Lüdecke D. esc: effect size computation for meta analysis (Version 0.5.1). (2019). doi: 10.5281/zenodo.1249218

42. DerSimonian R, Laird N. Meta-analysis in clinical trials. *Controlled Clin Trials*. (1986) 7:177–88. doi: 10.1016/0197-2456(86)90046-2

43. Knapp G, Hartung J. Improved tests for a random effects meta-regression with a single covariate. *Stat Med*. (2003) 22:2693–710. doi: 10.1002/sim.1482

44. Viechtbauer W, Cheung MW-L. Outlier and influence diagnostics for meta-analysis. *Res Synthesis Methods*. (2010) 1:112–25. doi: 10.1002/jrsm.11

45. Baujat B, Mahé C, Pignon J-P, Hill C. A graphical method for exploring heterogeneity in meta-analyses: application to a meta-analysis of 65 trials. *Stat Med*. (2002) 21:2641–52. doi: 10.1002/sim.1221

46. Olkin I, Dahabreh IJ, Trikalinos TA. GOSH - a graphical display of study heterogeneity. *Res synthesis Methods*. (2012) 3:214–23. doi: 10.1002/jrsm.1053

47. Hartigan JA, Wong MA. Algorithm AS 136: A K-means clustering algorithm. *J R Stat Soc Ser C (Applied Statistics)*. (1979) 28:100–8. doi: 10.2307/2346830

48. Schubert E, Sander J, Ester M, Kriegel HP, Xu X. DBSCAN revisited, revisited: why and how you should (Still) use DBSCAN. *ACM Trans Database Syst*. (2017) 42:1–21. doi: 10.1145/3068335

49. Fraley C, Raftery AE. Model-based clustering, discriminant analysis, and density estimation. *J Am Stat Assoc*. (2002) 97:611–31. doi: 10.1198/016214502760047131

50. Duval S, Tweedie R. Trim and fill: A simple funnel-plot–based method of testing and adjusting for publication bias in meta-analysis. *Biometrics*. (2000) 56:455–63. doi: 10.1111/j.0006-341X.2000.00455.x

51. Peters JL, Sutton AJ, Jones DR, Abrams KR, Rushton L. Contour-enhanced meta-analysis funnel plots help distinguish publication bias from other causes of asymmetry. *J Clin Epidemiol*. (2008) 61:991–6. doi: 10.1016/j.jclinepi.2007.11.010

52. Peters JL, Sutton AJ, Jones DR, Abrams KR, Rushton L. Performance of the trim and fill method in the presence of publication bias and between-study heterogeneity. *Stat Med*. (2007) 26:4544–62. doi: 10.1002/sim.2889

53. Egger M, Smith GD, Schneider M, Minder C. Bias in meta-analysis detected by a simple, graphical test. *BMJ*. (1997) 315:629–34. doi: 10.1136/bmj.315.7109.629

54. Barry CM, Kestell G, Gillan M, Haberberger RV, Gibbins IL. Sensory nerve fibers containing calcitonin gene-related peptide in gastrocnemius, latissimus dorsi and erector spinae muscles and thoracolumbar fascia in mice. *Neuroscience*. (2015) 291:106–17. doi: 10.1016/j.neuroscience.2015.01.062

55. Tesarz J, Hoheisel U, Wiedenhöfer B, Mense S. Sensory innervation of the thoracolumbar fascia in rats and humans. *Neuroscience*. (2011) 194:302–8. doi: 10.1016/j.neuroscience.2011.07.066

56. Langevin HM, Sherman KJ. Pathophysiological model for chronic low back pain integrating connective tissue and nervous system mechanisms. *Med Hypotheses*. (2007) 68:74–80. doi: 10.1016/j.mehy.2006.06.033

57. Hoheisel U, Rosner J, Mense S. Innervation changes induced by inflammation of the rat thoracolumbar fascia. *Neuroscience*. (2015) 300:351–9. doi: 10.1016/j.neuroscience.2015.05.034

58. Mense S. Innervation of the thoracolumbar fascia. *Eur J Transl Myol*. (2019) 29:8297. doi: 10.4081/ejtm.2019.8297

59. Schilder A, Hoheisel U, Magerl W, Benrath J, Klein T, Treede R-D. Sensory findings after stimulation of the thoracolumbar fascia with hypertonic saline suggest its contribution to low back pain. *Pain®*. (2014) 155:222–31. doi: 10.1016/j.pain.2013.09.025

60. Yan Y, Xu R, Zou T. Is thoracolumbar fascia injury the cause of residual back pain after percutaneous vertebroplasty? A prospective cohort study. *Osteoporosis Int*. (2015) 26:1119–24. doi: 10.1007/s00198-014-2972-2

61. Yang S, Tang J, Yang Z, Jin H, Wang Q, Wang H. Effect of thoracolumbar fascia injury on reported outcomes after percutaneous vertebroplasty. *Front Surg*. (2024) 11:1379769. doi: 10.3389/fsurg.2024.1379769

62. Yoo J-H, Moon S-H, Ha Y-C, Lee DY, Gong HS, Park SY, et al. Osteoporotic fracture: 2015 position statement of the Korean society for bone and mineral research. *J Bone Metab*. (2015) 22:175–81. doi: 10.11005/jbm.2015.22.4.175

63. Gerdhem P. Osteoporosis and fragility fractures: Vertebral fractures. *Best Pract Res Clin Rheumatol*. (2013) 27:743–55. doi: 10.1016/j.berh.2014.01.002

64. Langevin HM, Bishop J, Maple R, Badger GJ, Fox JR. Effect of stretching on thoracolumbar fascia injury and movement restriction in a porcine model. *Am J Phys Med Rehabil*. (2018) 97:187. doi: 10.1097/PHM.0000000000000824

65. Liu X, Zhou Q, Sun Z, Tian J, Wang H. Clinical effects of cocktail injection on the thoracolumbar fascia injury during percutaneous vertebroplasty for osteoporotic vertebral compression fractures: a single-center, retrospective case-control study. *BMC Musculoskelet Disord*. (2024) 25:18. doi: 10.1186/s12891-023-07130-1

66. Berrueta L, Muskaj I, Olenich S, Butler T, Badger GJ, Colas RA, et al. Stretching impacts inflammation resolution in connective tissue. *J Cell Physiol*. (2016) 231:1621–7. doi: 10.1002/jcp.25263

67. Corey SM, Vizzard MA, Bouffard NA, Badger GJ, Langevin HM. Stretching of the back improves gait, mechanical sensitivity and connective tissue inflammation in a rodent model. *PloS One*. (2012) 7:e29831. doi: 10.1371/journal.pone.0029831

frontiers | Frontiers in Medicine

TYPE Original Research
PUBLISHED 09 May 2025
DOI 10.3389/fmed.2025.1549653

OPEN ACCESS

EDITED BY
Nico Sollmann,
Ulm University Medical Center, Germany

REVIEWED BY
Jian Mei,
University of Regensburg, Germany
Jordana Fradico,
Oswaldo Cruz Foundation, Brazil

*CORRESPONDENCE
Wei Ji
✉ weiweiji1103@163.com

RECEIVED 21 December 2024
ACCEPTED 23 April 2025
PUBLISHED 09 May 2025

CITATION
Yang X, Cheng Q, Li Y, Tang H, Chen X, Ma L, Gao J and Ji W (2025) Development and validation of a nomogram for predicting low bone mineral density in male patients with ankylosing spondylitis.
Front. Med. 12:1549653.
doi: 10.3389/fmed.2025.1549653

Development and validation of a nomogram for predicting low bone mineral density in male patients with ankylosing spondylitis

Xiaotong Yang[1], Qin Cheng[2], Yifan Li[1], Hao Tang[1,3], Xin Chen[1], Lijun Ma[1], Jing Gao[1] and Wei Ji[4]*

[1]Nanjing University of Chinese Medicine, Nanjing, China, [2]Nanjing Jiangning Hospital of Chinese Medicine, Nanjing, China, [3]Department of Rheumatology, Liyang Hospital of Chinese Medicine, Liyang, China, [4]Department of Rheumatology, Jiangsu Province Hospital of Chinese Medicine, Nanjing, China

Objective: This retrospective cohort study aimed to develop and validate clinical nomogram models for predicting site-specific low bone mineral density (BMD) risk in male patients with ankylosing spondylitis (AS).

Methods: This study enrolled male AS patients treated at the Rheumatology Department of Jiangsu Provincial Hospital of Traditional Chinese Medicine between January 2017 and September 2024. A total of 322 eligible patients were randomly allocated to training and validation cohorts at a 7:3 ratio. Potential predictors of low BMD at the lumbar spine (LS) and left hip (LH) were initially screened through univariate logistic regression ($p < 0.05$), followed by stepwise bidirectional multivariate logistic regression (entry criteria $p < 0.05$) to identify independent predictors for each anatomical site. Based on the regression coefficients, we developed visualized nomogram prediction models for LS and LH low BMD, accompanied by an interactive online prediction tool. The models were comprehensively evaluated for discrimination, calibration, and clinical utility. After identifying the primary predictive factors, exploratory subgroup analyses were conducted to assess effect heterogeneity of key variables (BMI and serum uric acid).

Results: This study included 322 male AS patients randomly allocated to training ($n = 225$) and validation ($n = 97$) cohorts with balanced baseline characteristics (all $p > 0.05$). Multivariate logistic regression identified age at onset (LS OR = 0.96, 95%CI:0.93–0.99; LH OR = 0.97, 95%CI: 0.95–0.99), BMI (LS OR = 0.90, 95%CI: 0.81–0.99; LH OR = 0.81, 95%CI: 0.72–0.91), serum uric acid (LS/LH OR = 0.99, 95%CI: 0.99–0.99), and hip involvement (LS OR = 3.22, 95%CI: 1.71–6.05; LH OR = 8.03, 95%CI: 4.01–16.09) as common independent predictors for low BMD at both sites, while serum calcium (OR = 12.19, 95%CI: 1.44–103.25) was specific to LS. The developed nomograms, including web-based versions, demonstrated good discrimination (LS AUC: 0.77 training/0.73 validation; LH AUC: 0.82/0.85) and calibration. Decision curve analysis revealed significant net clinical benefit across probability thresholds (LS: 0.17–0.86 training/0.20–0.82 validation; LH: 0.15–0.92/0.27–0.91). The protective effect of BMI exhibited site-specific patterns: LS (low-TC: OR = 0.86; high-TC: OR = 0.77), LH (low-TC: OR = 0.77; mid-TC: OR = 0.74), with the most pronounced effect observed in the LS low-TG subgroup (OR = 0.79). SUA demonstrated consistent protective

effects (LS/LH: OR = 0.95–0.99, all $p < 0.05$), potentially independent of disease stage. Interaction analyses revealed that neither lipid levels nor disease stage significantly modified the effects of BMI and SUA (all interaction $p > 0.4$).

Conclusion: This study developed clinical prediction models with excellent discriminative ability and substantial clinical utility for male patients with AS. These models offer rheumatologists an efficient tool to rapidly assess individual risks of low BMD, facilitating early diagnostic decision-making and enabling personalized interventions tailored to anatomical site-specific osteoporosis risks.

KEYWORDS

ankylosing spondylitis, dynamic nomogram, early prevention, low bone mineral density, prediction model

1 Introduction

Ankylosing spondylitis (AS) represents a chronic autoimmune inflammatory disease that primarily impacts the axial skeleton and sacroiliac joints, resulting in symptoms such as inflammatory back pain, stiffness, and limited mobility (1). The pathological features of AS exhibit notable gender disparities, with a higher prevalence in males, where the male-to-female proportions fluctuate from 2:1 to 9:1 (2). Furthermore, studies have revealed that male individuals with AS exhibit higher rates of low bone mineral density (BMD) at early disease onset relative to their female counterparts (3). Low BMD is a common complication associated with AS (4), and its prevalence in male patients has been reported to range from 41.9 to 68% (5, 6). The existence of low BMD increases the likelihood of fractures, vertebral deformities, and spinal cord injuries in these patients, which can severely affect their posture and overall physical function, thus leading to a marked decline in both physical health and quality of life (7). However, the early detection of bone loss proves challenging due to its subtle progression and individual variability. Additionally, the high cost and invasiveness of dual-energy X-ray absorptiometry (DXA) have hindered its widespread use, particularly in developing regions (8). Therefore, developing a simple, effective tool for early screening of low BMD in male AS patients remains a pressing priority.

The nomogram prediction model is a statistical tool that visually represents mathematical models, which are designed to analyze multiple predictive variables for forecasting specific clinical outcomes. Displaying prediction probabilities in a graphical format offers an intuitive means of quantifying and illustrating disease risks, thereby supporting clinicians' early diagnosis and treatment (9). Currently, nomogram models are employed to predict the diagnosis and prognosis of a variety of conditions, including colorectal cancer, heart failure, and immunoglobulin A (IgA) nephropathy. Nonetheless, there remains a gap in nomogram prediction models tailored specifically for male AS patients with low BMD.

This study specifically focuses on male AS patients to develop and validate a nomogram for predicting concomitant low BMD in this population. Furthermore, an online dynamic nomogram tool has been created to allow rheumatologists to perform efficient and convenient screening of male AS patients, thereby offering scientific and reliable evidence for early diagnosis, disease evaluation, and subsequent treatment planning for these individuals.

2 Materials and methods

2.1 Subject selection

Male individuals with AS who received treatment at Jiangsu Province Hospital of Chinese Medicine between January 2017 and September 2024 were chosen as the study participants. The inclusion criteria were as follows: 1. Meeting the modified New York criteria for AS (10); 2. Age ≥ 18 years; 3. Clear consciousness and reading ability, with the capacity to communicate independently with researchers or through relatives without barriers; 4. Voluntary participation after being informed of the study's purpose. The exclusion criteria were: (1) Cases with >20% missing clinical data; (2) Concurrent diagnosis of other rheumatic autoimmune diseases or metabolic bone disorders (e.g., primary hyperparathyroidism); (3) Presence of severe systemic comorbidities (including but not limited to hepatic insufficiency or chronic kidney disease stage ≥3); (4) Recent exposure (within 3 months preceding enrollment) to medications with known skeletal effects (including systemic glucocorticoids at any dose, chronic heparin therapy, or enzyme-inducing antiepileptic drugs); (5) Documented history of excessive alcohol consumption (daily alcohol intake >40 g); (6) Prior total hip arthroplasty.

2.2 Clinical indicator information

The clinical indicators considered in this investigation were as follows: (1) basic clinicodemographic information: chronological age, body mass index (BMI), age at onset, course of disease, smoking history (cumulative cigarette consumption >100 cigarettes), alcohol history (daily ethanol intake >20 g), and history of long-term glucocorticoid use (prednisone-equivalent dose ≥5 mg/day for ≥3 consecutive months); (2) blood indicators: hemoglobin (Hb), serum uric acid (SUA), serum calcium (Ca), serum phosphorus (P), total cholesterol (TC), triglycerides (TG), comprehensive immunology panel (including immunoglobulin and complement levels), C-reactive protein (CRP), erythrocyte sedimentation rate (ESR), 25-hydroxyvitamin D [25 (OH) D], and HLA-B27 status; (3) radiological indicators: sacroiliitis grading, hip involvement, and BMD of the lumbar spine (LS) and left hip (LH).

Chronological age groups were primarily based on WHO standards but modified by data availability: young adults (18–44 years), middle-aged adults (45–64 years), and older adults (≥65 years).

Lipid parameters were categorized based on tertile distributions, with TC classified as low (<3.70 mmol/L), intermediate (3.70–4.52 mmol/L), or high (>4.52 mmol/L), and TG classified as low (<0.89 mmol/L), intermediate (0.89–1.40 mmol/L), or high (>1.40 mmol/L).

In accordance with the ASAS-2023 consensus criteria for early axial spondyloarthritis (11), early-stage AS cases in this study were strictly defined by meeting all of the following criteria: (1) fulfillment of the modified New York diagnostic criteria for AS; (2) duration of axial symptoms (including inflammatory back pain, buttock pain, or morning stiffness) ≤ 2 years; and confirmation by a board-certified rheumatologist that the symptoms were attributable to AS.

The grading of sacroiliitis was determined by radiologists using sacroiliac joint CT scans in accordance with the modified New York criteria (1984). This grading system comprises five levels, ranging from grade 0 (normal) to grade 4 (most severe) (10).

The definition of "hip involvement" was derived from previously published studies: (1) "Clinical hip involvement" was assessed by rheumatologists based on clinical symptoms, including hip pain, limited mobility, or medical records indicating either "current or previous hip arthritis"; (2) "Radiological hip involvement" was evaluated by rheumatologists using the BASRI-hip scoring system, with reference to recent (1 year) hip magnetic resonance imaging (12).

This study underwent review and was sanctioned by the Research Ethics Committee of Jiangsu Province Hospital of Chinese Medicine (Ethics number: 2023NL-135-02) and was executed per the Declaration of Helsinki.

2.3 Grouping method

The BMD (g/cm^2) of the LS (L1-L4) and LH (encompassing the femoral neck, trochanter, and internal region) were assessed using DXA (Discovery W, Hologic). Utilizing the BMD measurements, patients were split into two cohorts: normal BMD and low BMD. According to the World Health Organization diagnostic criteria, patients exhibiting a T-score of less than −1 at any site were categorized as having low BMD (13).

2.4 Statistical analysis

Statistical analyses for this investigation were performed using Zstats software[1] and R version 4.4.0. The normality of the data was evaluated through the Kolmogorov–Smirnov test. Normally distributed continuous variables were denoted as mean ± standard deviation, while non-normally distributed continuous variables were reported as median (interquartile range, 25th-75th percentiles). Categorical variables were summarized using frequencies and percentages. Between-group differences were evaluated utilizing *t*-tests, Mann–Whitney tests, or chi-square tests, as appropriate. Missing data were addressed using the multiple imputation method in SPSS (version 25.0).

Independent predictors of low BMD in male AS patients were identified through univariate and multivariate logistic regression analyses. Variables demonstrating statistical significance ($p < 0.05$) in the univariate logistic regression analysis were included in the multivariate model, with further adjustments made for clinically relevant confounders such as chronological age, smoking status, and alcohol history. Effect sizes were reported as odds ratios (OR) with 95% confidence intervals (CI), and variable selection was guided by both clinical relevance and statistical criteria. To assess the robustness of core predictors, we compared effect estimates between the primary and confounder-adjusted models. Stability was quantified using relative OR change rates:

$$\text{Relative Change}(\%) = \left| \frac{ORadjusted - ORprimary}{ORprimary} \right| \times 100$$

Predictors with change rates <20% were considered stable, while directional consistency was required for those exceeding this threshold. Multicollinearity was assessed using generalized variance inflation factors (GVIF), with GVIF^[1/(2 × Df)] values <2 considered acceptable. Furthermore, subgroup analyses were performed to investigate potential effect modification by disease stage and metabolic factors on key predictor variables. Based on the final set of independent predictors, a multi-site (LS and LH) nomogram prediction model was developed using R software. A dynamic visualization tool was subsequently created with the "shinyPredict" package and deployed on the shinyapps online platform for enhanced accessibility. Model validation encompassed discrimination assessment through receiver operating characteristic (ROC) curve analysis with area under the curve (AUC) calculation, calibration assessment via the Hosmer-Lemeshow test and calibration curves, and clinical utility evaluation using decision curve analysis (DCA) and clinical impact curves (CIC) to determine net benefit. This investigation implemented a statistical significance level of $p < 0.05$.

3 Results

3.1 Patient characteristics

We enrolled 322 male AS patients, randomly allocated into a training cohort ($n = 225$) and a validation cohort ($n = 97$) at a 7:3 ratio. Tables 1, 2 present the comparative analysis of baseline characteristics and disease-related parameters between the two cohorts, demonstrating well-balanced distributions in demographic features, basic clinical characteristics, and disease profiles (all $p > 0.05$). No significant differences were observed in chronological age distribution ($p = 0.308$), with comparable median ages at onset (30 vs. 29 years, $p = 0.471$) and median course of disease (both 9 years). BMI (25.03 ± 3.53 kg/m^2 vs. 24.65 ± 3.11 kg/m^2, $p = 0.332$), smoking history (44.44% vs. 43.30%, $p = 0.849$), and alcohol history (28.00% vs. 27.84%, $p = 0.976$) also showed no statistically significant differences. Regarding low BMD prevalence, the overall rates in the LS and LH were 55.9 and 56.83%, respectively. Intergroup comparisons revealed similar proportions between the training and validation cohorts for both LS (55.56% vs. 56.70%, $p = 0.849$) and LH (54.22% vs. 62.89%, $p = 0.15$). Furthermore, no significant disparities were

1 www.zstats.net

TABLE 1 Comparison of demographic and clinical characteristics between training and validation cohorts.

Variables	Total (*n* = 322)	Train (*n* = 225)	Test (*n* = 97)	*p*-value
Chronological age groups, years, *n* (%)				0.308
18–44	197 (61.18)	142 (63.11)	55 (56.70)	
45–64	99 (30.75)	68 (30.22)	31 (31.96)	
≥65	26 (8.07)	15 (6.67)	11 (11.34)	
Age at onset, years (median, IQR)	30.00 (23.00, 38.00)	30.00 (23.00, 37.00)	29.00 (23.00, 39.00)	0.471
Course of disease, years (median, IQR)	9.00 (3.62, 14.00)	9.00 (3.50, 13.00)	9.00 (4.00, 18.00)	0.473
BMI, kg/m^2 (mean ± SD)	24.77 ± 3.24	25.03 ± 3.53	24.65 ± 3.11	0.332
Smoking history, *n* (%)				0.849
Never	180 (55.90)	125 (55.56)	55 (56.70)	
Ever	142 (44.10)	100 (44.44)	42 (43.30)	
Alcohol history, *n* (%)				0.976
Never	232 (72.05)	162 (72.00)	70 (72.16)	
Ever	90 (27.95)	63 (28.00)	27 (27.84)	
Lumbar spine, *n* (%)				0.849
Normal BMD	142 (44.10)	100 (44.44)	42 (43.30)	
Low BMD	180 (55.90)	125 (55.56)	55 (56.70)	
Left hip, *n* (%)				0.15
Normal BMD	139 (43.17)	103 (45.78)	36 (37.11)	
Low BMD	183 (56.83)	122 (54.22)	61 (62.89)	

Data are presented as the mean ± standard deviation (SD), median (interquartile range), or number (percentage). BMI, Body mass index.

detected in laboratory parameters—including ESR, CRP, SUA, and 25 (OH) D levels—or radiographic features such as sacroiliitis grading and hip involvement (all $p > 0.05$). This comprehensive baseline equilibrium provides robust data support for the subsequent development and validation of the predictive model.

3.2 Results of univariate and multivariate analysis

The univariate logistic regression analysis demonstrated that chronological age, age at onset, BMI, serum calcium, SUA, and hip involvement were significantly associated with low BMD at the LS ($p < 0.05$). These associations persisted in the multivariate logistic regression analysis, with age at onset (OR = 0.96, 95%CI:0.93–0.99), BMI (OR = 0.97, 95%CI:0.95–0.99), serum calcium (OR = 12.19, 95%CI: 1.44–103.25), SUA (OR = 0.99, 95%CI:0.99–0.99), and hip involvement (OR = 3.22, 95%CI: 1.71–6.05) remaining independently predictive of LS low BMD (Table 3).

For low BMD at the LH, univariate analysis identified course of disease, age at onset, BMI, SUA, hip involvement, and sacroiliitis grade (specifically grade 3 versus 4) as significant predictors ($p < 0.05$). Subsequent multivariate analysis confirmed age at onset (OR = 0.97, 95%CI: 0.95–0.99), BMI (OR = 0.81, 95%CI: 0.72–0.91), SUA (OR = 0.99, 95%CI: 0.99–0.99), and hip involvement (OR = 8.03, 95%CI: 4.01–16.09) as independent predictors for LH low BMD (Table 4).

Prior to conducting the multivariate logistic regression, we performed collinearity diagnostics on all variables that showed significance in the univariate analysis. The results indicated no substantial multicollinearity concerns, with all variables demonstrating GVIF^[1/(2 × Df)] values below 1.5 in both the LS and LH models (Supplementary Tables S1, S2).

3.3 Confounder adjustment and model robustness

To enhance the clinical applicability of our findings, we adjusted for known confounding factors including smoking history, alcohol history, glucocorticoid use, and lipid profiles in our multivariate analysis. For the LS, hip involvement (OR = 4.01, 95%CI: 2.01–8.03), BMI (OR = 0.87, 95%CI: 0.78–0.97), SUA (OR = 0.99, 95%CI: 0.99–0.99), and serum calcium (OR = 10.84, 95%CI: 1.05–112.32) emerged as significant predictors. Similar patterns were observed for the LH, where hip involvement (OR = 7.72, 95%CI: 3.51–16.98), BMI (OR = 0.80, 95%CI: 0.71–0.90), and SUA (OR = 0.99, 95%CI: 0.99–0.99) maintained their predictive value. Of particular clinical interest was our finding that elevated triglyceride levels (1.40 mmol/L) were associated with a significantly increased risk of LS BMD (OR = 3.34, 95%CI: 1.26–8.84). While age at onset exhibited site-specific effects (lumbar OR = 0.96 vs. hip OR = 0.97), traditional risk factors including smoking history, alcohol history, and glucocorticoid use showed no significant associations in either model (all $p > 0.05$). Complete details of these analyses are provided in Supplementary Tables S3, S4.

TABLE 2 Comparison of disease-related variables between training and validation cohorts.

Variables	Total (*n* = 322)	Train (*n* = 225)	Test (*n* = 97)	*p*-value
Hb, g/L (median, IQR)	140.00 (128.00, 150.00)	141.00 (129.00, 151.00)	138.00 (125.00, 150.00)	0.307
Ca, mmol/L (median, IQR)	2.37 (2.26, 2.46)	2.38 (2.27, 2.47)	2.36 (2.24, 2.44)	0.211
P, mmol/L (median, IQR)	1.06 (0.93, 1.19)	1.06 (0.92, 1.20)	1.05 (0.94, 1.18)	0.561
SUA, μmol/L (median, IQR)	357.50 (314.00, 413.70)	357.00 (316.00, 403.00)	365.00 (297.00, 424.00)	0.507
IgG, g/L (median, IQR)	12.20 (10.50, 14.70)	12.00 (10.50, 14.80)	12.50 (10.60, 14.20)	0.874
IgA, g/L (median, IQR)	2.90 (2.13, 3.98)	2.83 (2.14, 3.98)	2.91 (2.07, 3.97)	0.721
IgM, g/L (median, IQR)	0.91 (0.69, 1.27)	0.90 (0.69, 1.25)	0.91 (0.68, 1.31)	0.986
C3, g/L (median, IQR)	1.01 (0.88, 1.18)	1.01 (0.88, 1.19)	1.00 (0.89, 1.16)	0.607
C4, g/L (median, IQR)	0.24 (0.21, 0.29)	0.24 (0.20, 0.28)	0.25 (0.21, 0.29)	0.91
CRP, mg/L (median, IQR)	9.97 (4.14, 24.62)	9.55 (4.23, 22.20)	11.00 (3.31, 30.50)	0.469
ESR, mm/h	23.00 (9.00, 44.00)	22.00 (9.00, 43.00)	25.00 (10.00, 45.00)	0.557
25 (OH) D, ng/mL (median, IQR)	20.96 (16.00, 26.00)	21.00 (16.00, 26.00)	20.00 (17.00, 25.00)	0.742
TC groups, mmol/L, *n* (%)				0.408
<3.70	107 (33.23)	78 (34.67)	29 (29.90)	
3.70–4.52	109 (33.85)	71 (31.56)	38 (39.18)	
>4.52	106 (32.92)	76 (33.78)	30 (30.93)	
TC groups, mmol/L, *n* (%)				0.217
<0.89	107 (33.23)	69 (30.67)	38 (39.18)	
0.89–1.40	109 (33.85)	76 (33.78)	33 (34.02)	
>1.40	106 (32.92)	80 (35.56)	26 (26.80)	
HLA-B27, *n* (%)				0.137
Negative	34 (10.56)	20 (8.89)	14 (14.43)	
Positive	288 (89.44)	205 (91.11)	83 (85.57)	
Sacroiliitis average, *n* (%)				0.747
2	143 (44.41)	102 (45.33)	41 (42.27)	
2.5	6 (1.86)	4 (1.78)	2 (2.06)	
3	76 (23.60)	49 (21.78)	27 (27.84)	
3.5	15 (4.66)	12 (5.33)	3 (3.09)	
4	82 (25.47)	58 (25.78)	24 (24.74)	
Hip involvement, *n* (%)				0.245
No	185 (57.45)	134 (59.56)	51 (52.58)	
Yes	137 (42.55)	91 (40.44)	46 (47.42)	
Patients on GC, *n* (%)				1
No	311 (96.58)	217 (96.44)	94 (96.91)	
Yes	11 (3.42)	8 (3.56)	3 (3.09)	

Data are presented as the mean ± standard deviation (SD), median (interquartile range), or number (percentage). Hb, Hemoglobin; SUA, Serum uric acid; Ca, Serum calcium; P, Serum phosphorus; TC, Total cholesterol; TG, Triglycerides; IgG, Immunoglobulin G; IgA, Immunoglobulin A; IgM, Immunoglobulin M; C3, Complement component 3; C4, Complement component 4; CRP, C-reactive protein; ESR, Erythrocyte sedimentation rate; 25 (OH) D, 25-hydroxyvitamin D.

To validate the robustness of core predictors, we compared effect sizes between the primary model and the confounder-adjusted model (Supplementary Table S5). Age at onset (0% OR change), BMI (lumbar spine −3.3%, left hip −1.2%), and serum uric acid (0% change) demonstrated high stability across both models. The OR for hip involvement in the lumbar spine increased by 24.5% (3.22 → 4.01) after confounder adjustment, suggesting potential underestimation in the unadjusted model. Although serum calcium showed an 11.1% OR reduction, its wide confidence interval (1.05–112.32) indicates the need for validation in larger samples. The consistent effect directions across all variables support the clinical credibility of our models.

3.4 Subgroup and interaction analyses

BMI showed site-specific and metabolic state-dependent protective effects against low BMD in subgroup analyses. In total cholesterol (TC) stratification, BMI showed significant protective effects against LS low

TABLE 3 Univariate and multivariate logistic regression analysis of LS training cohort.

Variables	Univariate regression		Multivariate regression	
	OR (95%CI)	*p*-value	OR (95%CI)	*p*-value
Chronological age groups				
18–44	1.00 (Reference)			
45–64	0.47 (0.26, 0.85)	**0.012**		
≥65	0.40 (0.13, 1.18)	0.096		
Age at onset	0.95 (0.93, 0.98)	**<0.001**	0.96 (0.93, 0.99)	0.003
Course of disease	1.03 (0.99, 1.06)	0.152		
BMI	0.86 (0.79, 0.95)	**0.002**	0.90 (0.81, 0.99)	0.035
Hb	1.01 (0.99, 1.02)	0.248		
Ca	9.05 (1.56, 52.60)	**0.014**	12.19 (1.44, 103.25)	0.022
P	0.83 (0.24, 2.93)	0.774		
SUA	0.99 (0.99, 0.99)	**0.006**	0.99 (0.99, 0.99)	0.011
IgG	0.97 (0.90, 1.04)	0.422		
IgA	0.96 (0.80, 1.16)	0.699		
IgM	1.23 (0.80, 1.91)	0.349		
C3	2.62 (0.76, 9.07)	0.129		
C4	2.06 (0.13, 31.57)	0.605		
CRP	1.00 (0.99, 1.01)	0.414		
ESR	1.00 (0.99, 1.01)	0.727		
25 (OH) D	1.01 (0.98, 1.04)	0.687		
TC groups				
<3.70	1.00 (Reference)			
3.70–4.52	1.12 (0.58, 2.16)	0.732		
>4.52	0.95 (0.50, 1.81)	0.872		
TG groups				
<0.89	1.00 (Reference)			
0.89–1.40	1.05 (0.55, 2.01)	0.882		
>1.40	1.01 (0.53, 1.90)	0.987		
HLA-B27				
Negative	1.00 (Reference)			
Positive	1.59 (0.63, 4.01)	0.323		
Sacroiliitis average				
2	1.00 (Reference)			
2.5	2.88 (0.29, 28.66)	0.366		
3	1.98 (0.97, 4.04)	0.06		
3.5	1.92 (0.54, 6.79)	0.31		
4	0.96 (0.50, 1.83)	0.905		
Hip involvement				
No	1.00 (Reference)		1.00 (Reference)	
Yes	3.66 (2.05, 6.52)	**<0.001**	3.22 (1.71, 6.05)	<0.001
Smoking history				
Never	1.00 (Reference)			
Ever	0.77 (0.45, 1.31)	0.337		

(Continued)

TABLE 3 (Continued)

Variables	Univariate regression		Multivariate regression	
	OR (95%CI)	*p*-value	OR (95%CI)	*p*-value
Alcohol history				
Never	1.00 (Reference)			
Ever	0.84 (0.47, 1.50)	0.55		
Patients on GC				
No	1.00 (Reference)			
Yes	0.47 (0.11, 2.00)	0.306		

OR, Odds ratio; CI, Confidence interval. Hb, Hemoglobin; SUA, Serum uric acid; Ca, Serum calcium; P, Serum phosphorus; TC, Total cholesterol; TG, Triglycerides; IgG, Immunoglobulin G; IgA, Immunoglobulin A; IgM, Immunoglobulin M; C3, Complement component 3; C4, Complement component 4; CRP, C-reactive protein; ESR, Erythrocyte sedimentation rate; 25 (OH) D, 25-hydroxyvitamin D. Bold values indicate statistical significance ($p < 0.05$) in the univariate logistic regression results.

BMD in both low-TC (OR = 0.86, 95%CI: 0.74–1.00, $p = 0.047$) and high-TC subgroups (OR = 0.77, 95%CI: 0.62–0.96, $p = 0.019$), but not in the moderate-TC subgroup ($p = 0.108$). In contrast, its protective effect on LH low BMD was primarily observed in low- and moderate-TC subgroups (OR = 0.77 and 0.74, both $p < 0.01$). Triglyceride (TG) stratification further demonstrated that BMI's protective effect was most pronounced for the LS in the low-TG subgroup (OR = 0.79, 95%CI: 0.66–0.95, $p = 0.014$), while maintaining significant protection for the LH across all TG subgroups (OR = 0.70–0.83, all $p < 0.05$) (Figure 1).

SUA subgroup analysis indicated its protective effect against low BMD was independent of disease stage. In early-stage AS patients, SUA showed significant associations with both LS (OR = 0.99, $p = 0.022$) and LH low BMD (OR = 0.95, $p = 0.023$). A similar trend was observed in advanced AS patients (LS: OR = 0.99, $p = 0.007$; LH: OR = 0.99, $p = 0.004$), albeit with smaller effect sizes, suggesting its clinical significance requires comprehensive evaluation with other indicators (Figure 2).

Interaction analyses demonstrated that neither lipid levels (TC interaction $p = 0.714/0.581$, TG interaction $p = 0.428/0.439$) nor disease stage (interaction $p > 0.4$) significantly modified the effects of BMI and SUA, indicating their protective roles may be independent of metabolic status and disease progression. However, it should be noted that these negative findings might be limited by sample size and statistical power, warranting future studies with larger cohorts to validate potential heterogeneity trends.

3.5 Development of nomogram model

Based on the outcomes of the multifactorial logistic regression analysis, clinical nomogram prediction models for the LS and LH were developed, as presented in Figure 3. Subsequently, an online dynamic nomogram prediction tool (Figure 4) was created, accessible via any device with Internet connectivity through the following links: LS: https://asresearch.shinyapps.io/shiny1/; LH: https://asresearch.shinyapps.io/shiny/.

3.6 Evaluation of the nomogram model

The discriminative ability of the model was evaluated through ROC curve analysis (Figure 5). The LS low BMD prediction model demonstrated good discriminative performance in the training cohort [AUC = 0.77 (95%CI: 0.70–0.83)], with comparable results in the validation cohort [AUC = 0.73 (95%CI: 0.63–0.83)], indicating stable predictive performance of the model. The LH low BMD model exhibited even better discriminative ability, with AUC values of 0.82 (95%CI: 0.77–0.88) and 0.85 (95%CI: 0.76–0.93) in the training and validation cohorts respectively, suggesting superior predictive capability of this model.

The calibration analysis demonstrated that our prediction models exhibited good overall predictive accuracy. As shown in the calibration plots (Figure 6), the predicted probabilities in the training cohort showed excellent agreement with observed probabilities, with the calibration curve closely following the ideal reference line (dashed diagonal). Although the validation cohort displayed a similar trend, its alignment with the ideal line was slightly less precise than that of the training cohort. Hosmer-Lemeshow test results confirmed satisfactory calibration performance for both models: the LS model showed no significant deviation between predicted and observed probabilities in either the training ($p = 0.894$) or validation cohorts ($p = 0.729$); similarly, the LH model demonstrated good calibration in both the training ($p = 0.710$) and validation cohorts ($p = 1.000$). Notably, while the bias-corrected line (black solid line) and the apparent line (LS model: blue solid line; LH model: red solid line) showed high concordance in the training cohort, minor deviations were observed in the validation cohort. These findings suggest a slight decrease in predictive performance during external validation, though the overall calibration remained within acceptable limits for clinical application.

The decision curve analysis demonstrated the clinical utility of our prediction models. For the LS model, both the training cohort (threshold probability range: 0–0.85) and validation cohort (range: 0–0.82) showed positive net clinical benefit. Similarly, the LH model exhibited excellent clinical applicability, providing net benefit across threshold probability ranges of 0.15–0.92 (training cohort) and 0.27–0.91 (validation cohort) (Figure 7). These findings indicate that both models offer valuable clinical decision-making guidance across wide threshold probability ranges.

The clinical impact curve analysis provided a visual assessment of the model's practical clinical utility, demonstrating high concordance between the number of high-risk individuals identified by the model and the actual occurrence of low BMD at risk thresholds >60%

TABLE 4 Univariate and multivariate logistic regression analysis of LH training cohort.

Variables	Univariate regression		Multivariate regression	
	OR (95%CI)	*p*-value	OR (95%CI)	*p*-value
Chronological age groups				
18–44	1.00 (Reference)			
45–64	0.63 (0.35, 1.13)	0.121		
≥65	1.51 (0.49, 4.63)	0.475		
Age at onset	0.97 (0.95, 0.99)	**0.014**	0.97 (0.95, 0.99)	0.035
Course of disease	1.07 (1.03, 1.11)	**<0.001**		
BMI	0.80 (0.72, 0.88)	**<0.001**	0.81 (0.72, 0.91)	<0.001
Hb	1.00 (0.98, 1.01)	0.55		
Ca	5.49 (0.98, 30.87)	0.053		
P	0.43 (0.12, 1.53)	0.191		
SUA	0.99 (0.99, 0.99)	**<0.001**	0.99 (0.99, 0.99)	0.023
IgG	1.00 (0.93, 1.07)	0.922		
IgA	1.12 (0.93, 1.35)	0.245		
IgM	1.12 (0.78, 1.61)	0.534		
C3	1.08 (0.32, 3.65)	0.897		
C4	0.30 (0.02, 4.73)	0.39		
CRP	1.00 (0.99, 1.01)	0.929		
ESR	1.00 (0.99, 1.01)	0.867		
25 (OH) D	0.98 (0.95, 1.01)	0.277		
TC groups				
<3.70	1.00 (Reference)			
3.70–4.52	0.84 (0.44, 1.63)	0.613		
>4.52	0.65 (0.34, 1.24)	0.194		
TC groups				
<0.89	1.00 (Reference)			
0.89–1.40	1.23 (0.64, 2.34)	0.537		
>1.40	1.17 (0.62, 2.21)	0.621		
HLA-B27				
Negative	1.00 (Reference)			
Positive	1.50 (0.60, 3.78)	0.388		
Sacroiliitis average				
2	1.00 (Reference)			
2.5	1.43 (0.19, 10.55)	0.727		
3	2.26 (1.12, 4.53)	**0.022**		
3.5	2.86 (0.81, 10.11)	0.103		
4	3.17 (1.61, 6.28)	**<0.001**		
Hip involvement				
No	1.00 (Reference)		1.00 (Reference)	
Yes	8.68 (4.55, 16.55)	**<0.001**	8.03 (4.01, 16.09)	<0.001
Smoking history				
Never	1.00 (Reference)			
Ever	1.06 (0.62, 1.79)	0.834		

(Continued)

TABLE 4 (Continued)

Variables	Univariate regression		Multivariate regression	
	OR (95%CI)	*p*-value	OR (95%CI)	*p*-value
Alcohol history				
Never	1.00 (Reference)			
Ever	1.08 (0.60, 1.93)	0.802		
Patients on GC				
No	1.00 (Reference)			
Yes	0.84 (0.20, 3.44)	0.807		

OR, Odds ratio; CI, Confidence interval. Hb, Hemoglobin; SUA, Serum uric acid; Ca, Serum calcium; P, Serum phosphorus; TC, Total cholesterol; TG, Triglycerides; IgG, Immunoglobulin G; IgA, Immunoglobulin A; IgM, Immunoglobulin M; C3, Complement component 3; C4, Complement component 4; CRP, C-reactive protein; ESR, Erythrocyte sedimentation rate; 25 (OH) D, 25-hydroxyvitamin D. Bold values indicate statistical significance ($p < 0.05$) in the univariate logistic regression results.

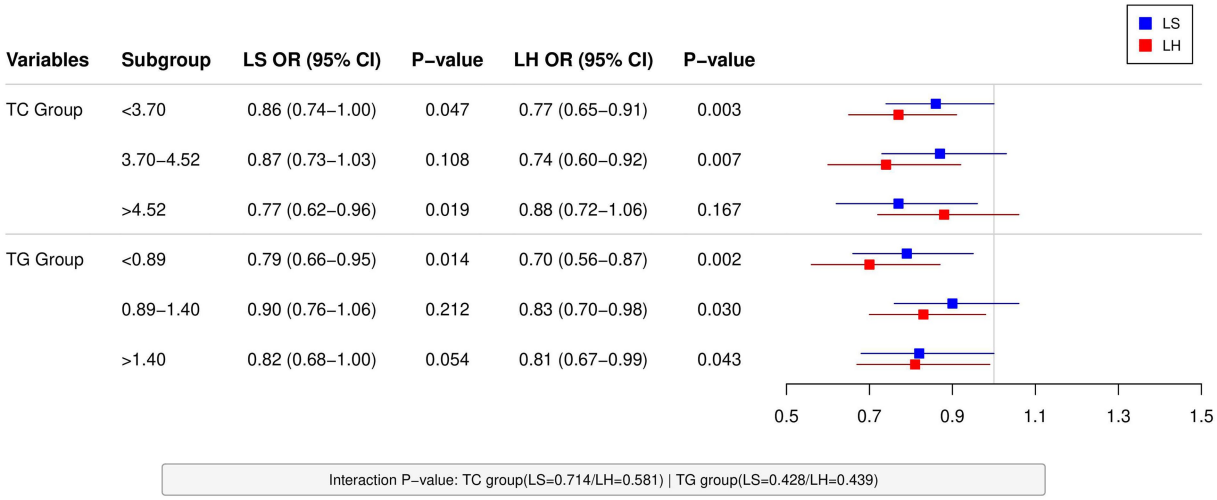

FIGURE 1
Subgroup analysis of BMI's protective effects against low BMD in male AS patients: Integrated forest plot displays LS and LH data stratified by lipid profiles (TC/TG tertiles). Protective trends were observed in most subgroups (LS: significant in low/high-TC [OR = 0.86/0.77] and low-TG [OR = 0.79]; LH: significant in low/mid-TC [OR = 0.77/0.74] and all TG subgroups [OR = 0.70–0.83]), though nonsignificant in mid-TC for LS ($p = 0.108$). Nonsignificant interaction terms (all $p > 0.4$) suggest lipid-level-independent protective mechanisms of BMI.

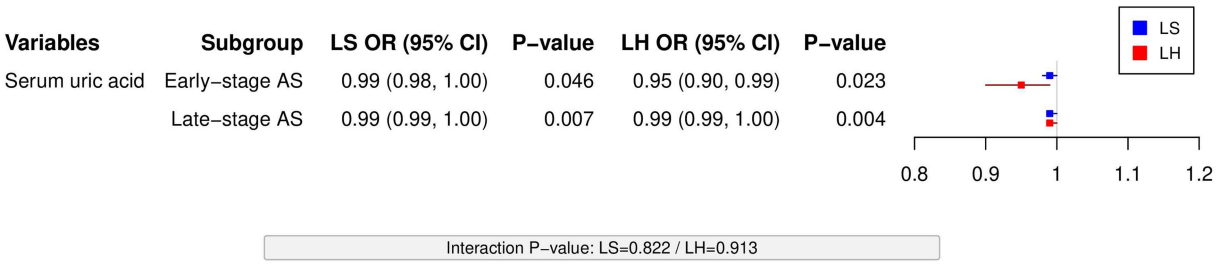

FIGURE 2
Subgroup analysis of SUA effects on low BMD: Unified forest plot presents LS and LH data across AS disease stages (early-stage: LS OR = 0.99/LH OR = 0.95; advanced-stage: LS/LH OR = 0.99). Interaction *p*-values (0.8) suggest stage-independent protection.

(Figure 8). Curve morphology analysis revealed that the predicted curve (LS model: blue; LH model: red) and the actual observed curve (black) maintained essentially parallel trajectories in the >60% threshold range, indicating stable predictive accuracy of the model, while the minimal vertical separation between the two curves reflected the model's relatively small margin of error. This consistent performance across higher risk thresholds suggests robust clinical applicability for identifying patients who would most benefit from targeted interventions.

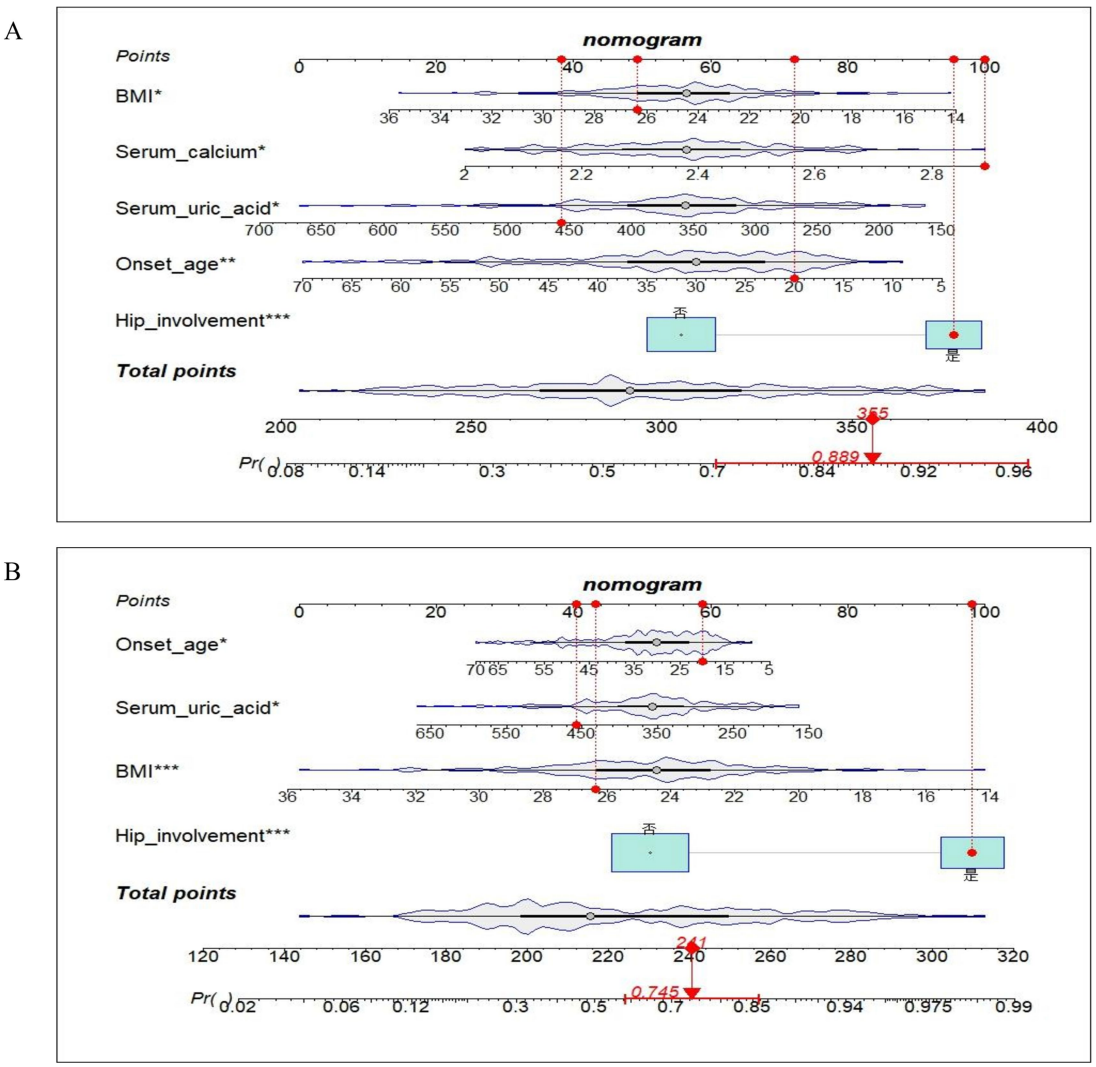

FIGURE 3
Low BMD nomograms for **(A)** LS and **(B)** LH in male AS patients, with interactive red dots for variable input (e.g., age at onset, BMI) and real-time display of total points/predicted probability (%). Example: 20-year-old male with BMI 26.35 kg/m^2, serum calcium 2.89 mmol/L, SUA 457 μmol/L, and hip involvement (LS: 355 points → 88.9% risk; LH: 241 points → 74.5% risk).

4 Discussion

By utilizing readily available clinical data, the present study developed a nomogram prediction model to accurately assess the likelihood of low BMD at various sites (LS and LH) in male individuals with AS. Following a thorough and methodical evaluation, both prediction models were found to exhibit strong discriminative ability, high accuracy, and substantial clinical benefit. These models have the potential to support clinicians in more effectively and efficiently screening for low BMD in male AS patients.

The research findings identified age at onset, BMI, SUA levels, and hip involvement as common predictors for low BMD in both the LS and the LH. These factors have been consistently reported in previous literature as being strongly linked to low BMD in AS patients. The results indicated that a younger age at onset was linked to an elevated risk of low BMD in individuals with AS. In juvenile-onset AS (JoAS), chronic inflammation disrupts normal bone metabolism before the completion of skeletal development. This persistent inflammatory state stimulates osteoclast activity while suppressing osteoblast function, ultimately impairing bone mass accumulation and heightening the risk of low BMD (14). Furthermore, an earlier disease onset signifies a prolonged duration of skeletal involvement. As the disease advances, issues related to low BMD may become more pronounced, potentially elevating the risk of osteoporosis (OP) and fractures in the later stages. Several studies have affirmed that low BMD can manifest even in the early stages of AS (3, 15), underscoring the importance of timely BMD monitoring and consideration of appropriate interventions for JoAS patients to mitigate progressive bone loss.

The study identified BMI as an independent protective factor against low BMD in male AS patients, which aligns with previous reports of a positive BMI-BMD association (16–18). The osteoprotective mechanisms of BMI may involve mechanical stress stimulation, hormonal regulation, and nutritional status. In accordance with Wolff's law, increased body weight enhances mechanical loading on bones, thereby promoting osteogenesis

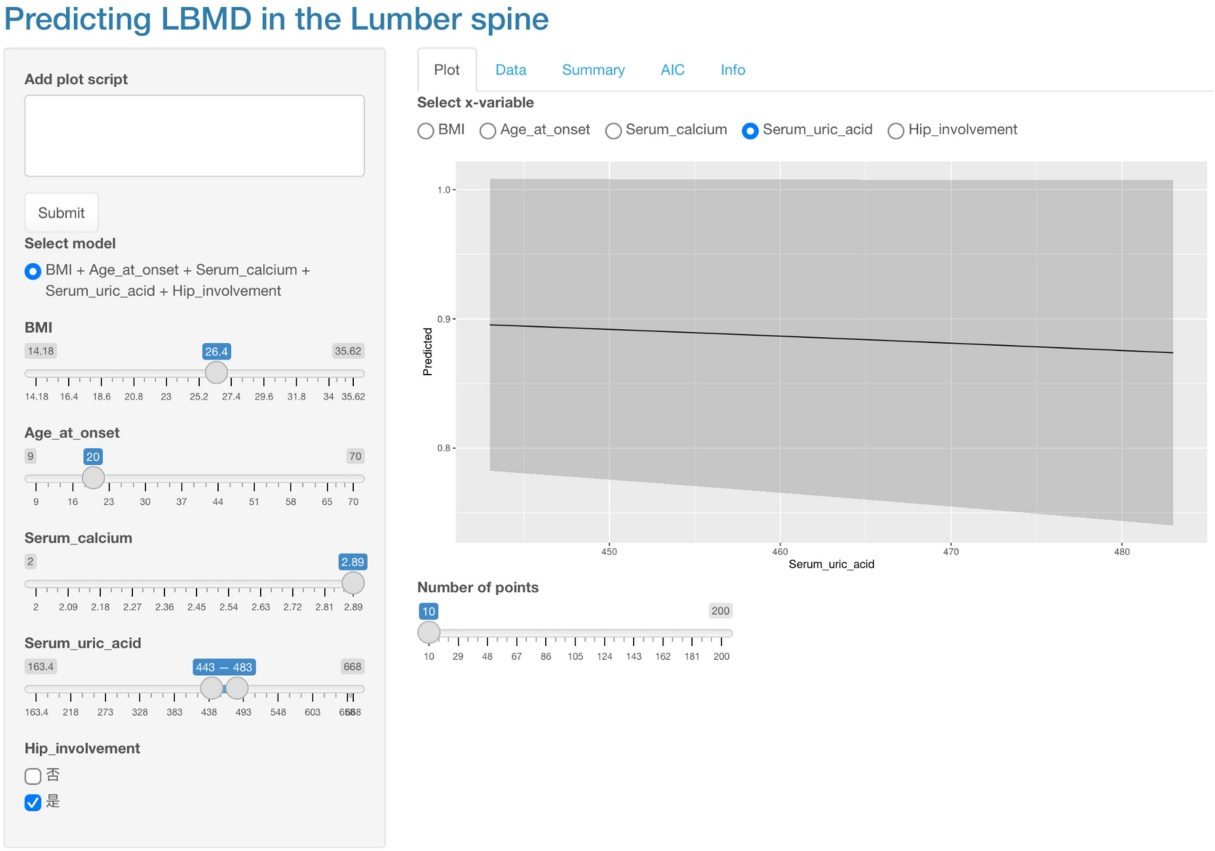

FIGURE 4
Web-based nomogram for LS low BMD prediction in male AS patients, demonstrating real-time risk probability calculation through interactive input of clinical parameters (left panel) with automated graphical output display. Operational example: Users adjust sliders for variables including age at onset, BMI, and serum biomarkers to generate instant probability estimates visualized along the scoring continuum.

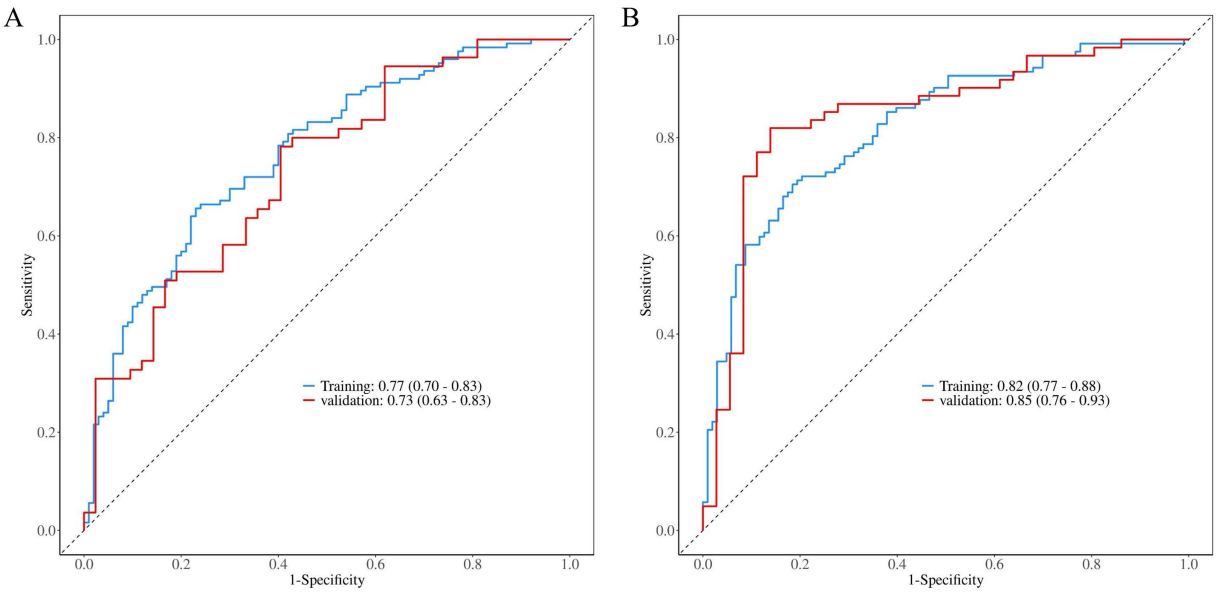

FIGURE 5
ROC analysis of low BMD prediction models for **(A)** LS and **(B)** LH, with training (blue) and validation (red) cohort performance relative to reference (dashed line, AUC = 0.5), displaying sensitivity-specificity relationships and AUC (95% CI) values.

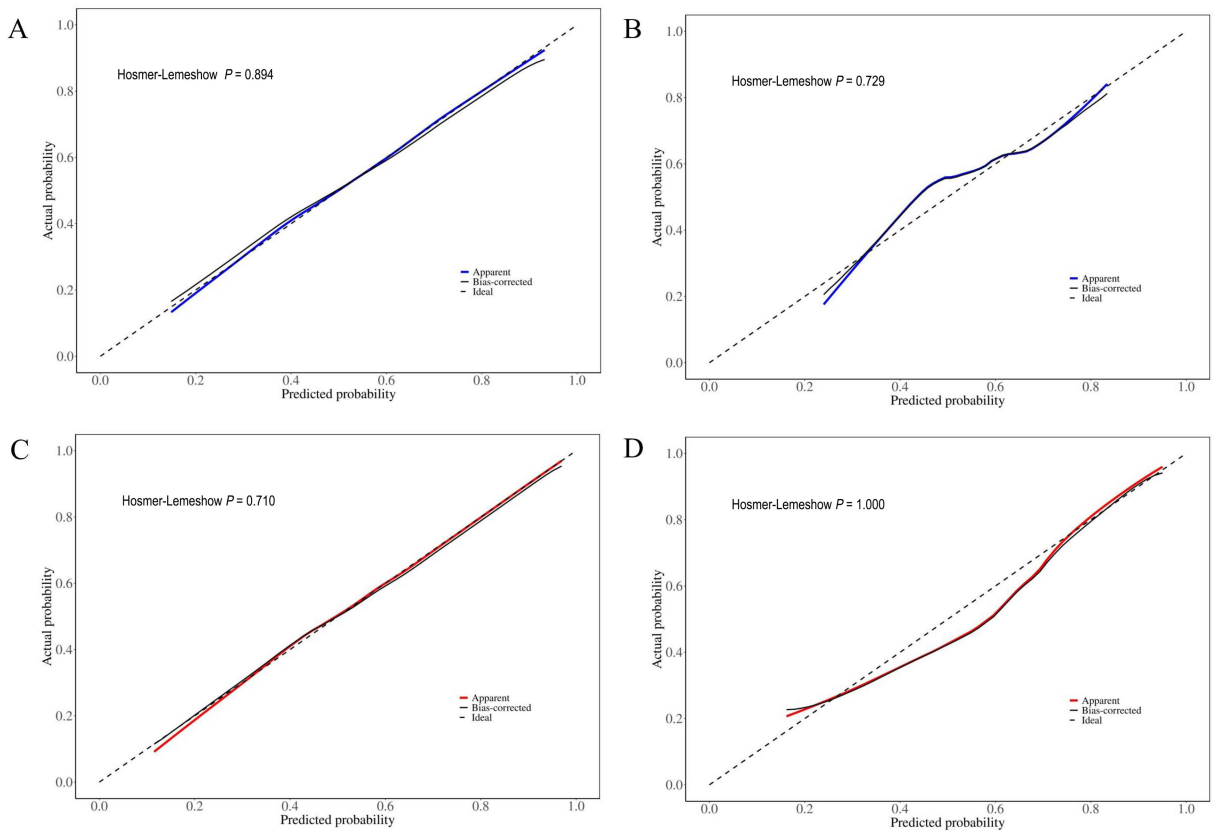

FIGURE 6
Calibration curves for **(A)** LS training cohort, **(B)** LS validation cohort, **(C)** LH training cohort, and **(D)** LH validation cohort. The dashed diagonal line (ideal) represents perfect prediction, the solid black line (bias-corrected) shows the adjusted calibration, and the apparent predictions are depicted by the blue solid line (LS model) and red solid line (LH model). The convergence of these curves demonstrates calibration performance: proximity between apparent (blue/red) and ideal lines reflects prediction accuracy, whereas agreement between apparent and bias-corrected (black) lines indicates model stability.

(19). Additionally, adipose tissue-derived factors such as estrogen and adiponectin participate in bone metabolism regulation (20). Moreover, higher BMI reflects better nutritional status, with adequate intake of protein, calcium, and vitamin D playing crucial roles in maintaining bone density. To further investigate potential heterogeneity in BMI's effects, our lipid-stratified analyses revealed significant protective associations in both low-TC (OR = 0.86, $p = 0.047$) and high-TC subgroups (OR = 0.77, $p = 0.019$), with consistent LH protection observed in low/moderate-TC subgroups (OR = 0.77/0.74, both $p < 0.01$). These findings suggest that BMI's protective effects may operate independently of lipid metabolism status (interaction $p > 0.4$). However, it must be emphasized that BMI, as a composite measure of weight and height, has inherent limitations – it cannot differentiate the heterogeneous contributions of lean mass versus fat mass (21), nor does it account for variations in fat distribution (e.g., visceral fat accumulation) (22) or regulatory effects of related hormones (e.g., testosterone, PTH) (23). Therefore, while our study supports the overall protective role of BMI, future research should incorporate DXA-based body composition analysis, waist-to-height ratio measurements, and metabolic marker assessments to more precisely evaluate the BMI-BMD relationship and inform individualized clinical decision-making.

Our study identified SUA as a protective factor against low BMD in AS patients, which is consistent with previous research. A cross-sectional study demonstrated a positive correlation between SUA levels and LS BMD in young male AS patients (24), while a Chinese multicenter study further confirmed SUA's protective effects against osteopenia and osteoporosis (25). The bone-protective mechanisms of SUA may involve its anti-inflammatory and antioxidant properties. Current evidence suggests oxidative stress as a potential mechanism underlying osteoporosis (26). As a potent endogenous antioxidant, SUA may inhibit osteoclast differentiation and promote osteoblast activity by scavenging oxygen free radicals (27). This was validated in an *in vitro* study showing that SUA dose-dependently reduced osteoclast formation and decreased ROS production in osteoclast precursors (28). Additionally, Lai et al. found that physiological concentrations of SUA exerted anti-inflammatory effects by suppressing pro-inflammatory cytokine expression and cartilage-degrading enzyme production, thereby preventing cartilage damage and bone erosion (29). However, some studies have reported that intracellular urate in hyperuricemia may stimulate superoxide and free radical formation, leading to oxidative damage and inflammatory stress that disrupts bone remodeling (30, 31). This "double-edged sword" effect suggests a potential U-shaped relationship between SUA and

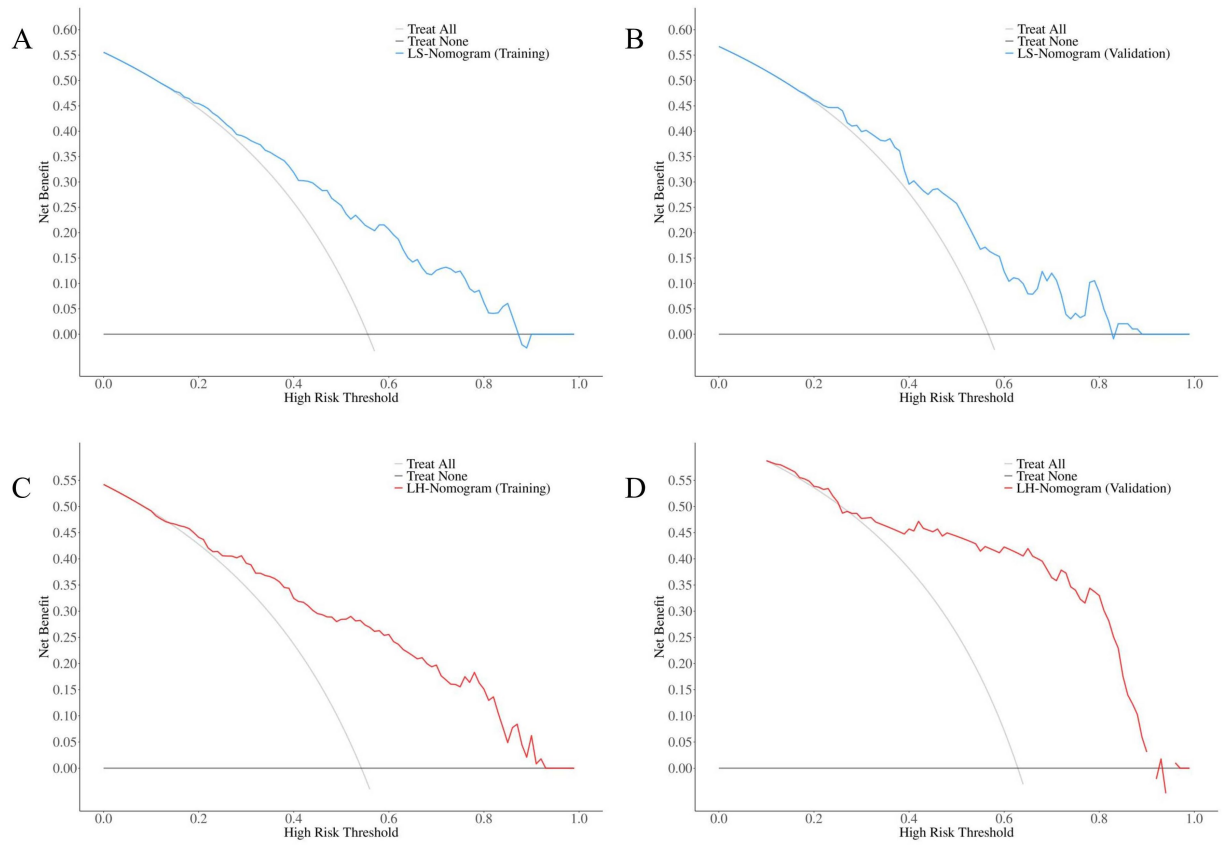

FIGURE 7
Decision curve analysis for **(A)** LS training, **(B)** LS validation, **(C)** LH training, and **(D)** LH validation cohorts, showing the nomogram models' net benefit (blue/red solid lines) versus reference strategies: "Treat All" (diagonal solid line, indicating treat-all approach with inherent over-treatment) and "Treat None" (horizontal solid line, representing no-intervention strategy). The models' curves exceed both reference lines across most threshold probability ranges, demonstrating significant net benefit advantages in clinically relevant probability intervals.

BMD. As our study population had SUA levels primarily within the physiological range, we were unable to fully explore this U-shaped association. This limitation highlights the need for future large-scale prospective studies focusing specifically on different SUA level intervals (particularly the >420 μmol/L subgroup) to comprehensively elucidate the dose–response relationship between SUA and bone metabolism.

To clarify whether the protective effect of SUA is influenced by disease progression, we conducted further subgroup analyses. The results demonstrated that SUA's protective effects remained stable in both early-stage AS (LS: OR = 0.99, $p = 0.022$; LH: OR = 0.95, $p = 0.023$) and advanced-stage AS (LS: OR = 0.99, $p = 0.007$; LH: OR = 0.99, $p = 0.004$). Although the effect sizes were modest, interaction analysis revealed no significant modification by disease stage ($p > 0.8$). These findings suggest that SUA's effect may not be stage-dependent, showing relatively consistent impacts on BMD across different phases of the disease.

The results suggested that hip involvement served as an IRF for low BMD in AS patients, which aligns with prior findings (32). A number of studies have demonstrated that hip involvement correlates with more extensive spinal radiographic damage, elevated disease activity, prolonged course of disease, and diminished physical function (33–35). Spinal radiographic damage is closely linked to disease progression, particularly in later stages when the formation of bone bridges and spinal fusion occurs. These processes reduce mechanical stress stimulation on the bones, thereby exacerbating bone loss (36). Disease activity in AS patients is strongly associated with systemic inflammation. In states of heightened inflammation, immune cells secrete a range of cytokines, encompassing TNF, IL-6, IL-1, and IL-17, which activate the OPG/RANKL/RANK signaling pathway, influencing osteoclasts. This activation leads to increased bone resorption and a concomitant decrease in bone formation (37, 38). AS, as a chronic inflammatory condition, implies that prolonged course of disease not only reflects long-term inflammatory disruption of bone metabolism but also entails additional factors, such as aging and declining physical function, which negatively affect BMD.

In addition to the four common predictors previously discussed, serum calcium was identified as an IRF for low BMD in the LS in this study. Serum calcium exists in the blood in both free and bound forms, serving a function in bone mineral deposition and serving as a marker of bone metabolism. During bone metabolism, alterations in blood calcium levels regulate the secretion of parathyroid hormone (PTH) and calcitonin through feedback mechanisms, indirectly influencing osteoblast and osteoclast activity. This process facilitates a dynamic equilibrium exchange between bone calcium and blood calcium, thus contributing to bone mineral deposition. An animal experiment demonstrated that

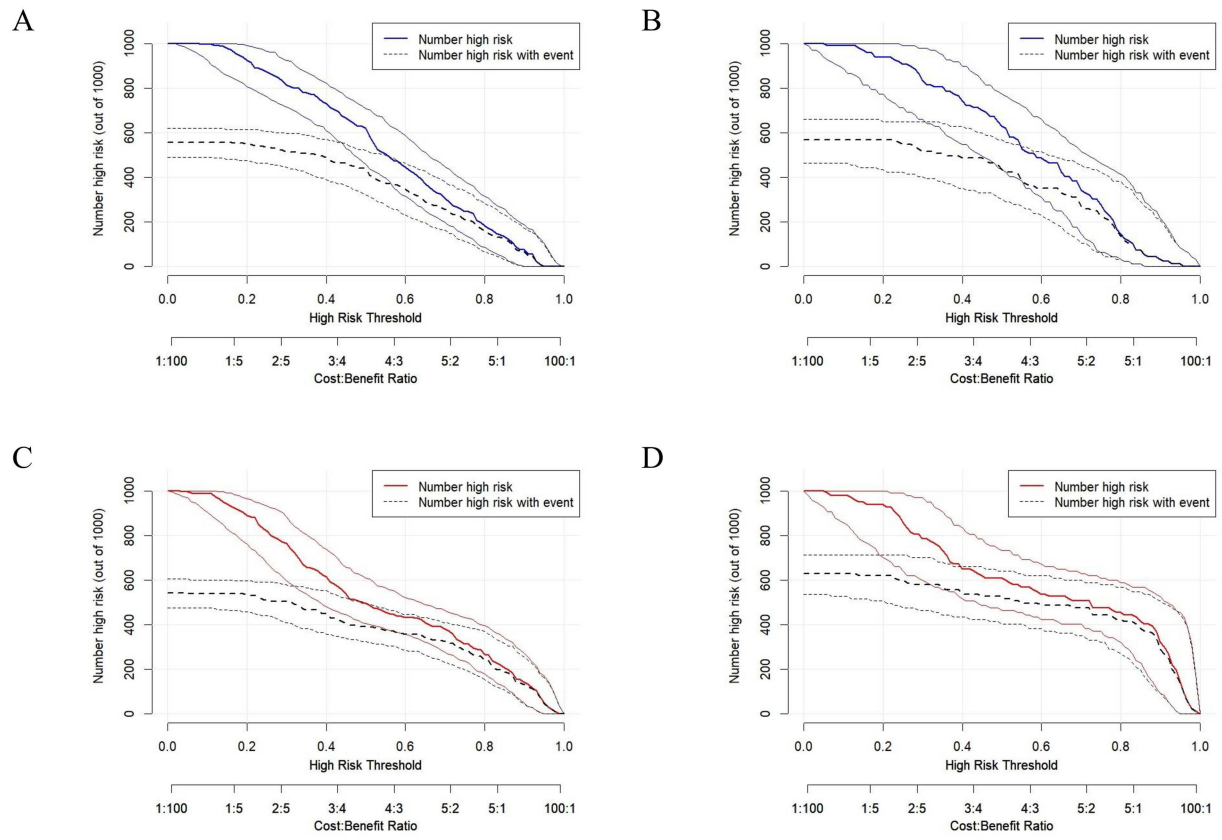

FIGURE 8
Clinical impact curves for **(A)** lumbar spine training cohort, **(B)** lumbar spine validation cohort, **(C)** left hip training cohort, and **(D)** left hip validation cohort. Axes: x = High Risk Threshold; y = *Number high risk (out of 1,000)* (estimated individuals classified as high-risk per 1,000 patients). Curves: predicted events by lumbar spine (blue) and left hip (red) nomograms; observed events (black).

compared to the negative control cohort, the AS, OP, and AS + OP cohorts exhibited markedly higher levels of serum calcium and tartrate-resistant acid phosphatase ($p < 0.05$) (39). It is hypothesized that the observed elevation in serum calcium levels results from bone metabolic imbalance in AS, where osteoclast-mediated bone resorption surpasses bone formation. However, the precise mechanism underlying this process warrants further investigation and validation.

In conclusion, nomograms were developed to predict low BMD at different sites (LS and LH) in male AS patients. When compared to prior nomogram models (32), the current models are more specific and practical. These models are designed with a focus on the male AS population, effectively eliminating the confounding influences of gender and menopause during model construction. Furthermore, following their development and evaluation, the models have been made publicly accessible online. In clinical settings, healthcare professionals can easily utilize these models via the internet to assess the risk of low BMD, thereby enabling early prevention and personalized treatment for male AS patients with low BMD.

However, this study has several limitations. First, the single-center retrospective design and modest sample size ($n = 322$) may restrict the statistical power of interaction analyses and potentially introduce selection bias—for example, underestimating the prevalence of hyperuricemia. Although chronological age stratification was included, potential recall bias in self-reported symptom onset and substantial missing data (40%) for the exact diagnostic age could compromise the precision of course of disease-related analyses. Second, crucial clinical variables such as malnutrition, fracture history, testosterone, parathyroid hormone (PTH), and the Ankylosing Spondylitis Disease Activity Score (ASDAS) were not incorporated, which may undermine the model's comprehensiveness—especially for patients with metabolic abnormalities or advanced disease stages. Additionally, while an internal validation cohort was used to assess model performance, the absence of external cohort validation warrants prudence when generalizing these results to broader populations. Finally, interpreting the protective role of BMI is hindered by the lack of DXA-based body composition data (e.g., lean vs. fat mass distribution) and obesity-related metabolic markers (e.g., insulin resistance), which might exert differential effects on bone metabolism. Future multicenter prospective studies integrating advanced imaging techniques, metabolic profiling, and standardized diagnostic datasets are essential to address these research gaps.

5 Conclusion

Drawing from the BMD results and clinical data of male AS patients, this study identified several factors as predictive of low BMD

at the LS, including age at onset, BMI, serum calcium, SUA, and hip involvement ($p < 0.05$). Similarly, predictive factors for low BMD in the LH were found to include age at onset, BMI, SUA, and hip involvement ($p < 0.05$). Based on these observations, nomogram prediction models were developed for both the LS[2] and LH.[3] These models aim to aid rheumatologists in conducting rapid screening screening of male patients with AS by utilizing simple and commonly available clinical indicators, thereby facilitating early prevention and personalized treatment strategies for low BMD and contributing to clinical translation.

Data availability statement

The raw data supporting the conclusions of this article will be made available by the authors, without undue reservation.

Ethics statement

The studies involving humans were approved by the Research Ethics Committee of Jiangsu Province Hospital of Chinese Medicine. The studies were conducted in accordance with the local legislation and institutional requirements. The ethics committee/institutional review board waived the requirement of written informed consent for participation from the participants or the participants' legal guardians/next of kin because this data is secondary data and does not contain any data which can identify individual.

Author contributions

XY: Data curation, Formal analysis, Investigation, Validation, Writing – original draft. QC: Data curation, Investigation, Writing – review & editing. YL: Data curation, Investigation, Writing – review & editing. HT: Data curation, Investigation, Writing – review & editing. XC: Data curation, Writing – review & editing. LM: Data curation, Writing – review & editing. JG: Data curation, Writing – review & editing. WJ: Funding acquisition, Supervision, Writing – review & editing.

2 Accessible at: https://asresearch.shinyapps.io/shiny1/.

3 Accessible at: https://asresearch.shinyapps.io/shiny/.

Funding

The author(s) declare that financial support was received for the research and/or publication of this article. This investigation was supported by the Jiangsu Province Traditional Chinese Medicine Science and Technology Development Plan, grant number ZD202218; and Jiangsu Province Graduate Practice and Innovation Program Project, grant number SJCX24_0988 and Science and Technology Program of Liyang Hospital of Traditional Chinese Medicine, grant number YN202301.

Acknowledgments

The support from Jiangsu Province Hospital of Chinese Medicine is gratefully acknowledged.

Conflict of interest

The authors declare that the research was conducted in the absence of any commercial or financial relationships that could be construed as a potential conflict of interest.

Generative AI statement

The authors declare that no Gen AI was used in the creation of this manuscript.

Publisher's note

Supplementary material

The Supplementary material for this article can be found online at: https://www.frontiersin.org/articles/10.3389/fmed.2025.1549653/full#supplementary-material

References

1. Deodhar A. The classification and diagnostic criteria of ankylosing spondylitis. *J Autoimmun*. (2014) 48-49:128–33. doi: 10.1016/j.jaut.2014.01.015

2. Smith EUR. Seronegative spondyloarthritis. Best Practice & Research. *Clin Rheumatol*. (2010) 24:747–56. doi: 10.1016/j.berh.2011.02.002

3. Van Der Weijden MAC, Van Denderen JC, Lems WF, Heymans MW, Dijkmans BAC, Van Der Horst-Bruinsma IE. Low bone mineral density is related to male gender and decreased functional capacity in early spondylarthropathies. *Clin Rheumatol*. (2011) 30:497–503. doi: 10.1007/s10067-010-1538-8

4. Danda D. Osteoporosis in ankylosing spondylitis. *Int J Rheum Dis*. (2008) 11:374–80. doi: 10.1111/j.1756-185X.2008.00394.x

5. Muntean L, Rojas-Vargas M, Font P, Simon S-P, Rednic S, Schiotis R, et al. Relative value of the lumbar spine and hip bone mineral density and bone turnover markers in men with ankylosing spondylitis. *Clin Rheumatol*. (2011) 30:691–5. doi: 10.1007/s10067-010-1648-3

6. Korczowska I, Przepiera-Bedzak H, Brzosko M, Lacki J, Trefler J, Hrycaj P. Bone tissue metabolism in men with ankylosing spondylitis. *Adv Med Sci*. (2011) 56:264–9. doi: 10.2478/v10039-011-0049-4

7. Roux C. Inflammation, bone loss and fracture risk in spondyloarthritis. *RMD Open*. (2015) 1:e000052. doi: 10.1136/rmdopen-2015-000052

8. Wang J, Kong C, Pan F, Lu S. Construction and validation of a nomogram clinical prediction model for predicting osteoporosis in an asymptomatic elderly population in Beijing. *JCM*. (2023) 12:1292. doi: 10.3390/jcm12041292

9. Li L. Establishment and validation of a prediction model for apnea on bronchiolitis. *Front Pediatr*. (2024) 12:1397750. doi: 10.3389/fped.2024.1397750

10. Van der Linden S, Valkenburg HA, Cats A. Evaluation of diagnostic criteria for ankylosing spondylitis. A proposal for modification of the New York criteria. *Arthritis Rheum*. (1984) 27:361–8. doi: 10.1002/art.1780270401

11. Navarro-Compán V, Benavent D, Capelusnik D, van der Heijde D, Landewé RB, Poddubnyy D, et al. ASAS consensus definition of early axial spondyloarthritis. *Ann Rheum Dis*. (2024) 83:1093–9. doi: 10.1136/ard-2023-224232

12. Vander Cruyssen B, Muñoz-Gomariz E, Font P, Mulero J, De Vlam K, Boonen A, et al. Hip involvement in ankylosing spondylitis: epidemiology and risk factors associated with hip replacement surgery. *Rheumatology*. (2010) 49:73–81. doi: 10.1093/rheumatology/kep174

13. LeBoff MS, Greenspan SL, Insogna KL, Lewiecki EM, Saag KG, Singer AJ, et al. The clinician's guide to prevention and treatment of osteoporosis. *Osteoporos Int*. (2022) 33:2049–102. doi: 10.1007/s00198-021-05900-y

14. Adami G. Regulation of bone mass in inflammatory diseases. *Best Pract Res Clin Endocrinol Metab*. (2022) 36:101611. doi: 10.1016/j.beem.2021.101611

15. Hinze AM, Louie GH. Osteoporosis Management in Ankylosing Spondylitis. *Curr Treat Options Rheum*. (2016) 2:271–82. doi: 10.1007/s40674-016-0055-6

16. Ma W, Zhou X, Huang X, Xiong Y. Causal relationship between body mass index, type 2 diabetes and bone mineral density: Mendelian randomization. *PLoS One*. (2023) 18:e0290530. doi: 10.1371/journal.pone.0290530

17. Ouyang Y, Quan Y, Guo C, Xie S, Liu C, Huang X, et al. Saturation effect of body mass index on bone mineral density in adolescents of different ages: a population-based study. *Front Endocrinol*. (2022) 13:922903. doi: 10.3389/fendo.2022.922903

18. Morin S, Tsang JF, Leslie WD. Weight and body mass index predict bone mineral density and fractures in women aged 40 to 59 years. *Osteoporos Int*. (2009) 20:363–70. doi: 10.1007/s00198-008-0688-x

19. Teichtahl AJ, Wluka AE, Wijethilake P, Wang Y, Ghasem-Zadeh A, Cicuttini FM. Wolff's law in action: a mechanism for early knee osteoarthritis. *Arthritis Res Ther*. (2015) 17:207. doi: 10.1186/s13075-015-0738-7

20. Rinonapoli G, Pace V, Ruggiero C, Ceccarini P, Bisaccia M, Meccariello L, et al. Obesity and bone: a complex relationship. *IJMS*. (2021) 22:13662. doi: 10.3390/ijms222413662

21. Shin D, Kim S, Kim KH, Park SM. Importance of fat mass and lean mass on bone health in men: the fourth Korean national health and nutrition examination survey (KNHANES IV). *Osteoporos Int*. (2014) 25:467–74. doi: 10.1007/s00198-013-2412-8

22. Chen B, Liu G, Wang Y, Xu Y. The influence of body fat content and distribution on bone mass in healthy Chinese adults. *Front Med*. (2024) 11:1403971. doi: 10.3389/fmed.2024.1403971

23. Puntus T, Schneider B, Meran J, Peterlik M, Kudlacek S. Influence of age and gender on associations of body mass index with bone mineral density, bone turnover markers and circulating calcium-regulating and bone-active sex hormones. *Bone*. (2011) 49:824–9. doi: 10.1016/j.bone.2011.06.003

24. Kang KY, Hong YS, Park S-H, Ju JH. Low levels of serum uric acid increase the risk of low bone mineral density in young male patients with ankylosing spondylitis. *J Rheumatol*. (2015) 42:968–74. doi: 10.3899/jrheum.140850

25. Lin X, Zhao C, Qin A, Hong D, Liu W, Huang K, et al. Association between serum uric acid and bone health in general population: a large and multicentre study. *Oncotarget*. (2015) 6:35395–403. doi: 10.18632/oncotarget.6173

26. Xu R, Lian D, Xie Y, Mu L, Wu Y, Chen Z, et al. Relationship between serum uric acid levels and osteoporosis. *Endocr Connect*. (2023) 12:e230040. doi: 10.1530/EC-23-0040

27. Wang R, Gao Y, Wang P, He C, Lu H. Association between serum uric acid and bone mineral density in males from NHANES 2011–2020. *Sci Rep*. (2024) 14:4292. doi: 10.1038/s41598-024-52147-8

28. Ahn SH, Lee SH, Kim B-J, Lim K-H, Bae SJ, Kim EH, et al. Higher serum uric acid is associated with higher bone mass, lower bone turnover, and lower prevalence of vertebral fracture in healthy postmenopausal women. *Osteoporos Int*. (2013) 24:2961–70. doi: 10.1007/s00198-013-2377-7

29. Lai J-H, Luo S-F, Hung L-F, Huang C-Y, Lien S-B, Lin L-C, et al. Physiological concentrations of soluble uric acid are chondroprotective and anti-inflammatory. *Sci Rep*. (2017) 7:2359. doi: 10.1038/s41598-017-02640-0

30. Preyer O, Concin H, Nagel G, Zitt E, Ulmer H, Brozek W. Serum uric acid is associated with incident hip fractures in women and men – results from a large Austrian population-based cohort study. *Maturitas*. (2021) 148:46–53. doi: 10.1016/j.maturitas.2021.03.005

31. Lin K-M, Lu C-L, Hung K-C, Wu P-C, Pan C-F, Wu C-J, et al. The paradoxical role of uric acid in osteoporosis. *Nutrients*. (2019) 11:2111. doi: 10.3390/nu11092111

32. Sun W, Mu W, Jefferies C, Learch T, Ishimori M, Wu J, et al. Interaction effects of significant risk factors on low bone mineral density in ankylosing spondylitis. *PeerJ*. (2023) 11:e16448. doi: 10.7717/peerj.16448

33. Zhao J, Zheng W, Zhang C, Li J, Liu D, Xu W. Radiographic hip involvement in ankylosing spondylitis: factors associated with severe hip diseases. *J Rheumatol*. (2015) 42:106–10. doi: 10.3899/jrheum.140428

34. Guo S, Zhang L, Man S, Bian T, Ma S, Wu X, et al. Association of radiological severity of hip involvement with clinical characteristics and sagittal spinopelvic balance in patients with ankylosing spondylitis. *Clin Rheumatol*. (2024) 43:233–40. doi: 10.1007/s10067-023-06789-0

35. Ferreira Azevedo S, Mazeda C, Barcelos A. Hip involvement in axial spondylarthritis patients: comparison between ankylosing spondylitis and non-radiographic axial spondylarthritis – a retrospective study. *Joint Bone Spine*. (2024) 91:105694. doi: 10.1016/j.jbspin.2024.105694

36. Lee SY, Song R, Yang HI, Chung SW, Lee Y-A, Hong S-J, et al. The bone bridge significantly affects the decrease in bone mineral density measured with quantitative computed tomography in ankylosing spondylitis. *PLoS One*. (2021) 16:e0249578. doi: 10.1371/journal.pone.0249578

37. Chisălău B, Cringuș L-I, Vreju F, Pârvănescu C, Firulescu S, Ștefan D, et al. New insights into IL-17/IL-23 signaling in ankylosing spondylitis (review). *Exp Ther Med*. (2020) 20:3493–7. doi: 10.3892/etm.2020.8981

38. Ashany D, Stein EM, Goto R, Goodman SM. The effect of TNF inhibition on bone density and fracture risk and of IL17 inhibition on radiographic progression and bone density in patients with axial spondyloarthritis: a systematic literature review. *Curr Rheumatol Rep*. (2019) 21:20. doi: 10.1007/s11926-019-0818-9

39. Hu Z-B, Wei B, Wu S-K, Sun J-C, Xiang M, Zhang Z-M. Changes in bone mineral density and bone metabolic indexes in ankylosing spondylitis mouse model complicated with osteoporosis. *Exp Ther Med*. (2018) 16:811–5. doi: 10.3892/etm.2018.6220

frontiers | Frontiers in Aging Neuroscience

TYPE Original Research
PUBLISHED 21 May 2025
DOI 10.3389/fnagi.2025.1552381

OPEN ACCESS

EDITED BY
Nico Sollmann,
Ulm University Medical Center, Germany

REVIEWED BY
Jan Kassubek,
University of Ulm, Germany
YI Zhan,
Yiwu Central Hospital, China

*CORRESPONDENCE
Ickpyo Hong
✉ ihong@yonsei.ac.kr
Min Seok Baek
✉ minbaek@yonsei.ac.kr

†These authors have contributed equally to this work and share first authorship

RECEIVED 27 December 2024
ACCEPTED 28 April 2025
PUBLISHED 21 May 2025

CITATION
Jin Y, Choi BK, Lee JW, Hong JY, Hong I and Baek MS (2025) Association between osteoporosis and mortality in Parkinson's disease with mediating effect of hip fractures: a Korean nationwide population-based study. *Front. Aging Neurosci.* 17:1552381. doi: 10.3389/fnagi.2025.1552381

Association between osteoporosis and mortality in Parkinson's disease with mediating effect of hip fractures: a Korean nationwide population-based study

Yeonju Jin[1†], Bo Kyu Choi[2†], Jong Woo Lee[3], Jin Yong Hong[3], Ickpyo Hong[4*] and Min Seok Baek[3,5*]

[1]Department of Occupational Therapy, Graduate School, Yonsei University, Wonju, Republic of Korea, [2]Department of Neurology, Yonsei University College of Medicine, Gangnam Severance Hospital, Seoul, Republic of Korea, [3]Department of Neurology, Yonsei University Wonju College of Medicine, Wonju Severance Christian Hospital, Wonju, Republic of Korea, [4]Department of Occupational Therapy, College of Software and Digital Healthcare Convergence, Yonsei University, Wonju, Republic of Korea, [5]Research Institute of Metabolism and Inflammation, Yonsei University Wonju College of Medicine, Wonju, Republic of Korea

Introduction: This study investigated the association between osteoporosis and mortality in patients with Parkinson's disease (PD) and the mediating role of hip fractures.

Methods: A retrospective cohort study. Data were obtained from the 2009–2019 Korean National Health Insurance Service–National Sample Cohort databases. We extracted both the International Classification of Diseases, 10th Edition code (G20) and PD registration code (V124) to identify patients with PD. A Cox proportional hazards model was used to analyze the association between osteoporosis and mortality. Mediation analyses were performed to estimate the mediating effect of hip fracture between osteoporosis and mortality in patients with PD.

Results: Of the 2,084 patients with PD, 474 (18.5%) were diagnosed with osteoporosis, and 112 (4.4%) experienced hip fractures after PD diagnosis. In unadjusted mediation analysis, the direct effect of osteoporosis on mortality was not significant ($\beta = 0.0309$, 95%: confidence interval [CI] −0.0180–0.0798, $p = 0.2149$), whereas the indirect effect of hip fracture was ($\beta = 0.0130$, 95% CI 0.0048–0.0212, $p = 0.0019$). Similarly, in the adjusted model controlling for sex, age at diagnosis, and Charlson Comorbidity Index, the direct effect was not significant ($\beta = 0.0011$, 95% CI−0.0508–0.0529, $p = 0.9675$), whereas the indirect effect was ($\beta = 0.0061$, 95% CI 0.0009–0.0114, $p = 0.0223$).

Discussion: This study elucidated the association between osteoporosis and mortality in patients with PD by highlighting the mediating role of hip fractures. These findings thus underscore the importance of managing osteoporosis in patients with PD.

KEYWORDS

Parkinson's disease, hip fracture, osteoporosis, mortality, mediating effect

1 Introduction

Parkinson's disease (PD) is a neurodegenerative disease typically characterized by abnormal motor symptoms, including tremors, rigidity, and bradykinesia. PD also affects gait, balance, and postural stability, consequently elevating the susceptibility to fractures (Samii et al., 2004). The prevalence of PD is associated with an increased risk of fractures, with disease severity being linearly associated with fracture risk (Nam et al., 2021; Koo et al., 2023). Fracture risk has been observed across all body parts in patients with PD, with hip fractures presenting the greatest risk (Mühlenfeld et al., 2021). Furthermore, the risk of mortality in PD with hip fractures is twice as high as those without fractures (Schini et al., 2020).

Osteoporosis, a condition characterized by decreased bone mineral density (BMD), bone mass, and alterations in bone structure and strength, presents a potential risk for fractures. PD progression can lead to malnutrition and sarcopenia, which increase the risk of osteoporosis (Torsney et al., 2014). Decreased BMD further exacerbates the susceptibility to hip fractures in patients with PD. The risk of osteoporotic fractures in patients with PD and osteoporosis is nearly double, while the risk of hip fractures is triple those of patients with PD without osteoporosis (Pouwels et al., 2013).

However, a study previously reported that osteoporosis did not significantly affect the risk of hip fractures in patients with PD (Kim et al., 2022). Instead, patients with PD had a higher risk of fractures than those without PD, regardless of their osteoporosis status. Although PD and osteoporosis independently influence facture risk, their relationship at the time of fracture occurrence remains unclear. Furthermore, although clinicians recognize that hip fractures and osteoporosis contribute to mortality among patients with PD, the specific mediating effect of hip fractures on the association between osteoporosis and mortality in patients with PD remains insufficiently explored.

Therefore, this study investigated the association between osteoporosis and mortality in patients with PD and explored the mediating role of hip fractures in the progression from osteoporosis to mortality.

2 Materials and methods

2.1 Study population

In this retrospective cohort study, we analyzed data obtained from the South Korea National Health Insurance Service–National Sample Cohort (NHIS-NSC) databases. The NHIS operates as a mandatory single-payer healthcare system (http://nhiss.nhis.or.kr). The NHIS-NSC database is a large cohort representing 2% of the entire national population and sampled based on sex, age, income level, and region. The database collects demographic characteristics, diagnoses according to the International Classification of Diseases, 10th Edition (ICD-10), and mortality (Lee et al., 2018; Kim et al., 2020). Furthermore, for rare and intractable diseases, the claims database includes a special code (V-code) designated by the national registration program (Park et al., 2015).

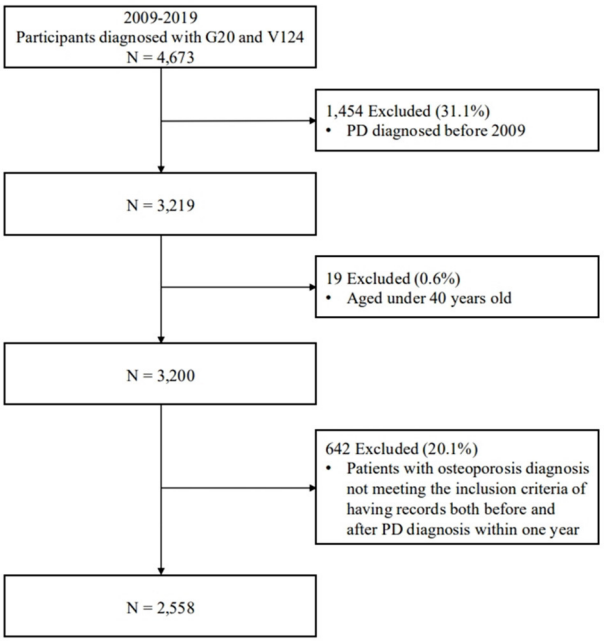

FIGURE 1
A flow diagram of the participant selection process. The diagram shows inclusion and exclusion criteria, along with the final number of participants categorized according to study requirements. PD, Parkinson's disease.

Using the ICD-10 (G20) and registration V-codes (V124), we identified study subjects registered in the claims database who were diagnosed with PD between January 1, 2009, and December 31, 2019. Patients diagnosed with PD prior to 2009 were excluded from the analysis. Figure 1 shows a flow diagram of the subject selection process.

The NHIS databases are de-identified and publicly available with approval from the National Health Insurance Big Data Department in South Korea, thus waiving the requirement for informed consent. The use of the data was approved by the NHIS Inquiry Commission and the Institutional Review Board (IRB) of Wonju Severance Christian Hospital (IRB number: CR321308). This study was also approved by the IRB of the Yonsei University Mirae Campus number: (IRB number: 1041849-202309-SB-171-01).

2.2 Operational definitions

We adopted the operational definitions of osteoporosis, hip fracture, and PD used in previous studies (Koo et al., 2023; Kim et al., 2022; Lee et al., 2018). The diagnosis of osteoporosis was determined by the presence of specific ICD-10 codes (M80, M81, and M82). Considering the nature of osteoporosis, which requires long-term follow up, and the characteristics of claims data, we defined patients with osteoporosis as those who had complete medical records for both pre- and postdiagnosis of osteoporosis

Abbreviations: BMD, bone mineral density; CCI, Charlson Comorbidity Index; CI, confidence intervals; ICD-10, International Classification of Diseases, 10th Edition; IRB, Institutional Review Board; NHIS-NSC, National Health Insurance Service–National Sample Cohort; PD, Parkinson's disease.

within 1 year of PD diagnosis. We defined hip fractures using ICD-10 codes (S72.0, S72.1, S72.2, S72.3, S72.4, S72.7, S72.8, and S72.9). Patients with a history of hip fracture prior to their osteoporosis or PD diagnosis were excluded. The NHIS databases provide information on the year and month of death (National Health Insurance Service, 2024). The date of death was determined based on events that occurred following the diagnosis of PD, and patients who died before the diagnosis of PD were excluded from the study cohort. Mortality status was categorized as "1," while survival was categorized as "0".

Demographic characteristics were used as covariates, including age at PD diagnosis, sex, the modified Charlson Comorbidity Index (CCI), and levodopa equivalent daily dose (LEDD). The modified CCI was determined using ICD-10 codes for diagnoses within 1 year before the diagnosis of PD and categorizing the number of comorbidities into three categories (0, 1, 2, or higher) (Quan et al., 2005). The LEDD was calculated at the time of enrollment and subsequently log-transformed to ensure a normal distribution and improve the precision of the mediation analysis.

2.3 Statistical analysis

The chi-square test and *t*-test were used to compare the characteristics of patients with PD with and without hip fractures. The Cox proportional hazards model was used to analyze time-to-event data and thus estimate the hazard ratios (HR) for the risk of osteoporosis related mortality in patients with PD. The model was adjusted for relevant covariates, including age, sex, and comorbidities. The estimates were expressed with HR and 95% confidence intervals (CI). Statistical significance was determined using a p-value threshold of 0.05.

Mediation analysis was performed to estimate the mediating effect of hip fractures on the association between osteoporosis and mortality by analyzing the covariates (Agler and De Boeck, 2017). In the mediation analysis, the independent variable was osteoporosis (X), the mediation variable was hip fractures (M), and the dependent variable was mortality (Y). A $p < 0.05$ was considered statistically significant. Data management and all statistical analyses were performed using SAS version 9.4 (SAS Institute Inc, 2013).

3 Results

3.1 Descriptive statistics

In total, 2,558 patients diagnosed with PD between January 1, 2009, and December 31, 2019, were enrolled in this study. Table 1 presents the descriptive statistics comparing patients with ($n = 474$; 18.5%) and without ($n = 2{,}084$; 81.5%) osteoporosis. Patients with osteoporosis had a higher percentage of hip fractures ($n = 46$, 9.7% vs. $n = 66$, 3.2%; $p < 0.0001$) and a higher proportion of women ($n = 431$, 90.9% vs. $n = 941$, 45.2%, $p < 0.0001$). Patients with osteoporosis showed a higher mean ± SD age at PD diagnosis than those without osteoporosis (74.6 years ± 6.9 vs. 70.2 years ± 9.9, $p < 0.0001$). However, PD severity assessed by LEDD, as well as mortality, did not differ significantly between the two groups.

3.2 Cox regression analysis

Table 2 presents the data on the Cox proportional hazards model examining the associations between risk factors and mortality in patients with PD. In Model 1, patients with osteoporosis showed a higher risk of mortality than those without (HR 1.295, 95% CI 1.109–1.512, $p = 0.0011$). In contrast, Model 2, which was adjusted for age, sex, and comorbidities, did not show a significant relationship between osteoporosis and mortality (HR 0.988, 95% CI 0.829–1.177, $p = 0.8913$).

3.3 Mediation analysis

Mediation analysis examined the unadjusted mediation effect of hip fractures on the association between osteoporosis and mortality (Supplementary Table 1). The direct (Path c) and total effects of osteoporosis and mortality were not statistically significant. However, osteoporosis was significantly associated with hip fractures (Path a: $\beta = 1.1897$, 95% CI 0.7991–1.5804, $p < 0.0001$), and hip fractures were significantly associated with increased mortality (Path b: $\beta = 0.1985$, 95% CI 0.1057–0.2913, $p < 0.0001$). Furthermore, the natural indirect effect, representing the mediation effect of hip fractures, was significant ($\beta = 0.0130$, 95% CI 0.0048–0.0212, $p = 0.0019$), indicating that hip fractures partially mediate the association between osteoporosis and mortality.

Figure 2 illustrates the mediation effect determined by the mediation analysis of hip fractures on the association between osteoporosis and mortality, in the model adjusted for sex, age group, and CCI. Furthermore, the direct and the total effects of osteoporosis and mortality were not significantly associated in the adjusted model (Figures 2A, B, respectively). Osteoporosis remained significantly associated with hip fractures (Path a: $\beta = 0.9527$, 95% CI 0.4947–1.4107, $p < 0.0001$), and hip fractures were significantly associated with increased mortality (Path b: $\beta = 0.1516$, 95% CI 0.0627–0.2404, $p = 0.0008$; Table 3). The natural indirect effect of hip fractures was significant ($\beta = 0.0061$, 95% CI 0.0009–0.0114, $p = 0.0223$), indicating that hip fractures partially mediate the relationship between osteoporosis and mortality, even after adjusting for covariates. These findings remained consistent after further adjustment for PD severity, as assessed by log-transformed LEDD values (Supplementary Table 2).

4 Discussion

This nationwide cohort study demonstrated the interrelationships among osteoporosis, hip fractures, and mortality in patients with PD. Specifically, our results indicate that hip fractures act as a full mediator in the relationship between osteoporosis and mortality in patients with PD. Thus, osteoporosis in PD is not directly associated with increased mortality but is linked to it only through hip fractures. Our study results can be used as reference in developing strategies aimed at reducing the risk factors for mortality in patients with PD, particularly by addressing the role of hip fractures in the relationship between osteoporosis and mortality.

TABLE 1 Descriptive statistics comparing patients with and without osteoporosis, *n* (%).

Variables	Full sample with PD; $N = 2,558$ (100%)	Osteoporosis		*p*
		Yes; $N = 474$ (18.5%)	No; $N = 2,084$ (81.5%)	
Hip fracture				<0.0001*
Yes	112 (4.4)	46 (9.7)	66 (3.2)	
No	2,446 (95.6)	428 (90.3)	2,018 (96.8)	
Age at PD diagnosis, mean (SD)	71.0 (9.6)	74.6 (6.9)	70.2 (9.9)	<0.0001*
Log-transformed LEDD, mean (SD)	3.3 (4.2)	3.5 (4.2)	3.3 (4.2)	0.3032
Age group				<0.0001*
40–59	319 (12.5)	12 (2.5)	307 (14.7)	
60–69	652 (25.5)	81 (17.1)	571 (27.4)	
70–79	1,107 (43.3)	268 (56.5)	839 (40.3)	
80+	480 (18.8)	113 (23.8)	367 (17.6)	
Observation period, monthly, mean (SD)	56.6 (35.5)	53.2 (31.7)	57.4 (36.2)	0.0201*
Sex				<0.0001*
Female	1,372 (53.6)	431 (90.9)	941 (45.2)	
Male	1,186 (46.4)	43 (9.1)	1,143 (54.9)	
CCI				<0.0001*
0	801 (31.3)	37 (7.8)	764 (36.7)	
1	479 (18.7)	82 (17.3)	397 (19.1)	
≥2	1,278 (50.0)	355 (74.9)	923 (44.3)	
Mortality				0.0772
Yes	1,004 (39.3)	203 (42.8)	801 (38.4)	
No	1,554 (60.8)	271 (57.2)	1,283 (61.6)	

CCI, Charlson comorbidity index; LEDD, levodopa equivalent daily dose; PD, Parkinson's disease; SD, standard deviation. *Statistically significant at an alpha level of 0.05.

The unadjusted Cox proportional hazards model revealed that osteoporosis was significantly associated with increased mortality rate in patients with PD (HR = 1.295, $p = 0.0011$). However, the association was no longer significant after adjusting for covariates, such as sex, age, and CCI, (HR = 0.988, $p = 0.8913$). Previous longitudinal studies have shown that male sex, older age at onset, and presence of comorbidities are associated with increased mortality risk (Pinter et al., 2015; Hoogland et al., 2019; Forsaa et al., 2010). Consistent with previous studies conducted in the general population, this study also demonstrated that although the prevalence of osteoporosis was markedly higher in women than in men, the risk of mortality associated with osteoporosis was notably higher in men (Zhang et al., 2024; Lee et al., 2013). They also reported that osteoporosis is not an independent major risk factor for mortality in patients with PD, indicating that interactions with other underlying factors may contribute more significantly to increased mortality (Pinter et al., 2015; Forsaa et al., 2010). Further studies should be conducted to clarify the causal relationship between osteoporosis and mortality in PD and the various associated factors.

Contrary to a previous study using a nationwide database, which reported that osteoporosis does not significantly increase the risk of hip fractures in patients with PD (Kim et al., 2022), our study found that hip fractures fully mediate the relationship between osteoporosis and mortality in PD. Thus, osteoporosis is not directly associated with mortality but is significantly linked to it only through hip fractures. Patients with PD are at high risk for both osteoporosis and hip fractures (Malochet-Guinamand et al., 2015). As PD progresses, various symptoms (e.g., mobility impairment, decreased hand–mouth coordination, dysphagia, and reduced gastrointestinal motility) can lead to malnutrition and sarcopenia. These secondary symptoms are also associated with an increased risk of osteoporosis and reduced BMD, leading to a higher risk of osteoporotic and hip fractures (Torsney et al., 2014; Pouwels et al., 2013). In particular, medication with levodopa in PD is associated with hyperhomocysteinemia, an independent risk factor for osteoporosis, as well as common deficiencies in vitamin B12 and folate (Figueroa and Rosen, 2020). Gao et al. (2015) found a negative correlation between daily levodopa dosage and BMD at the spine and hip in patients with PD. Some studies have shown that bisphosphonates, vitamin D, and calcium therapy can increase BMD and reduce fractures in patients with PD (van den Bos et al., 2012; Cummings et al., 2019).

Furthermore, mediation analysis revealed that hip fractures are significantly associated with increased mortality in PD. A retrospective cohort study among older Medicare beneficiaries in

TABLE 2 Cox proportional hazards model for mortality associated with osteoporosis in patients with PD.

Variables	Model 1		Model 2	
	HR (95% CI)	*p*	HR (95% CI)	*p*
Osteoporosis				
No	1		1	
Yes	1.295 (1.109–1.512)	0.0011*	0.988 (0.829–1.177)	0.8913
Sex				
Female			1	
Male			1.837 (1.601–2.107)	<0.0001*
Age group				
40–59			1	
60–69			1.559 (1.153–1.108)	0.0039*
70–79			2.600 (1.963–3.443)	<0.0001*
80+			5.011 (3.737–6.719)	<0.0001*
CCI				
0			1	
1			2.194 (1.801–2.673)	<0.0001*
≥2			2.669 (2.262–3.149)	<0.0001*

CCI, Charlson comorbidity index; CI, confidence interval; *Statistically significant at an alpha level of 0.05.

TABLE 3 Association between osteoporosis and mortality mediated by hip fracture in a covariate-adjusted model.

Path	*β*	95% CI		*p*
a*	0.9527	0.4947	1.4107	<0.0001
b†	0.1516	0.0627	0.2404	0.0008
c‡	0.0011	−0.0508	0.0529	0.9675
Total effect	0.0072	−0.0446	0.0590	0.7847
Natural direct effect (NDE)	0.0011	−0.0508	0.0529	0.9675
Natural indirect effect (NIE)	0.0061	0.0009	0.0114	0.0223

Adjusted for sex, age group, Charlson comorbidity index (CCI), confidence interval (CI).
*Path a: Association between osteoporosis (yes vs. no) and hip fracture (yes vs. no).
†Path b: Association between hip fracture (yes vs. no) and mortality (yes vs. no).
‡Path c: Association between osteoporosis (yes vs. no) and mortality (yes vs. no).

the United States found that patients with PD had a significantly higher adjusted mortality rate (HR = 2.41) after hip/pelvic fractures compared with patients without PD (Harris-Hayes et al., 2014). Nam et al. (2021) reported that patients with PD and hip fractures had twice the mortality rate compared with those without fractures. Another nationwide population-based study in Korea matched patients with and without PD and examined comorbidities associated with mortality in patients with PD (Yoon et al., 2021). In their study, no significant difference in mortality related to hip fractures was observed in patients aged <59 and <80 years. However, a significant association was found in the 60–79 age group. Our study reported results similar to those of previous studies on the increased risk of mortality associated with hip fractures after the onset of PD. Notably, subgroup analysis indicated that the relationship between hip fractures and mortality varied significantly with age (Yoon et al., 2021). These findings emphasize the need for age-specific interventions to reduce hip fracture-related mortality in patients with PD and indicate the necessity for further research to explore other factors influencing this relationship. To this end, interventions such as increasing calcium and vitamin D intake through dietary sources or supplementation in older adults, along with the implementation of fall prevention strategies, may be considered as potential approaches.

This study has several limitations. First, the diagnoses of PD, osteoporosis, hip fracture, and comorbidities were based on ICD codes of the NHIS-NSC database. Therefore, inaccuracies in the claims data may have resulted in disease misclassification. Second, because of the characteristics of claims data, clinical information, including the severity of PD symptoms and cognitive functions, was not included in the data analysis. In addition, clinical parameters such as disease stage, motor subtypes, fall history, nutritional status, and physical function were also unavailable, all of which may influence both fracture risk and post-fracture mortality. Future

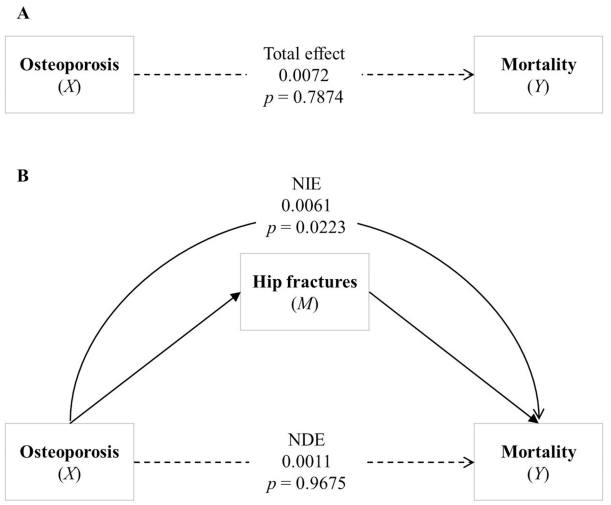

FIGURE 2
Analysis of the association between osteoporosis and mortality. **(A)** Shows the total effect of osteoporosis on mortality. **(B)** Illustrates the mediating effect of hip fracture between osteoporosis and mortality, highlighting the Natural Direct Effect (NDE) and the Natural Indirect Effect (NIE). Bold lines represent statistically significant paths, while dashed lines represent non-significant paths. NDE, Natural Direct Effect; NIE, Natural Indirect Effect.

prospective studies incorporating more granular clinical data are warranted to elucidate the relationship between hip fracture and mortality in patients with PD. The study population should include PD patients with osteoporosis, and regular follow-up assessments should systematically document potential confounding factors, including the severity of parkinsonism. To ensure more precise temporal assessment and stronger causal inference, future studies may need to incorporate regular bone mineral density evaluations, such as dual energy X-ray absorptiometry. Third, we only considered the initial hip fracture that occurred after the onset of PD and osteoporosis for analysis. We did not include subsequent fractures and thus did not analyze details regarding multiple fractures. Additionally, although we focused on hip fracture as the principal diagnosis to assess its mediating effect on mortality, we did not explicitly exclude individuals with co-existing vertebral fractures. Consequently, it is possible that some participants had both hip and vertebral fractures, which may have influenced the observed outcomes. This limits our ability to attribute the mediating effect solely to hip fractures. Future research should aim to analyze different types of osteoporotic fractures—such as hip and vertebral fractures—both independently and in combination, to better understand their respective and interactive contributions to mortality risk in patients with Parkinson's disease. Given that ICD-10 codes M80, M81, and M82 represent different subtypes of osteoporosis, which may reflect varying disease severity or underlying causes, future studies should consider analyzing these subgroups separately.

This study emphasizes that osteoporosis is associated with increased risk of hip fractures, highlighting the indirect role of hip fractures in the mortality of patients with PD and concurrent osteoporosis. For these patients, thus, interventions should include not only the prescription of medications to treat and prevent osteoporosis but also to the implementation of measures minimizing the risk of hip fractures. Our findings underscore the importance of managing the risk factors of osteoporosis related to disease progression and medication use in PD, emphasizing the need for proactive strategies for hip fracture prevention.

Data availability statement

The data analyzed in this study is subject to the following licenses/restrictions: the datasets presented in this article are not readily available because they are derived from medical claims provided by the South Korea National Health Insurance Service, and restrictions apply to their availability. Requests to access these datasets should be directed to National Health Insurance Service, https://nhiss.nhis.or.kr.

Ethics statement

The use of the data was approved by the NHIS Inquiry Commission and the Institutional Review Board (IRB) of Wonju Severance Christian Hospital (IRB number: CR321308). This study was also approved by the Yonsei University Mirae Campus (IRB number: 1041849-202309-SB-171-01). The studies were conducted in accordance with the local legislation and institutional requirements. Written informed consent for participation was not required from the participants or the participants' legal guardians/next of kin in accordance with the national legislation and institutional requirements.

Author contributions

YJ: Data curation, Formal analysis, Writing – original draft, Writing – review & editing. BC: Conceptualization, Methodology, Writing – original draft, Writing – review & editing. JL: Writing – review & editing. JH: Writing – review & editing. IH: Conceptualization, Formal analysis, Methodology, Supervision, Writing – review & editing. MB: Conceptualization, Funding acquisition, Project administration, Supervision, Writing – review & editing.

Funding

The author(s) declare that financial support was received for the research and/or publication of this article. This work was supported by the National Research Foundation of Korea (NRF) grant funded by the Ministry of Education (NRF2022R1C1C1012535) and by the Technology Innovation Program (20018182) funded by the Ministry of Trade, Industry and Energy (MOTIE, Korea).

Conflict of interest

The authors declare that the research was conducted in the absence of any commercial or financial relationships that could be construed as a potential conflict of interest.

Generative AI statement

The author(s) declare that no Gen AI was used in the creation of this manuscript.

Publisher's note

All claims expressed in this article are solely those of the authors and do not necessarily represent those of their affiliated organizations, or those of the publisher, the editors and the reviewers. Any product that may be evaluated in this article, or claim that may be made by its manufacturer, is not guaranteed or endorsed by the publisher.

Supplementary material

The Supplementary Material for this article can be found online at: https://www.frontiersin.org/articles/10.3389/fnagi.2025.1552381/full#supplementary-material

References

Agler, R., and De Boeck, P. (2017). On the interpretation and use of mediation: multiple perspectives on mediation analysis. *Front. Psychol.* 8:1984. doi: 10.3389/fpsyg.2017.01984

Cummings, S. R., Lui, L. Y., Eastell, R., and Allen, I. E. (2019). Association between drug treatments for patients with osteoporosis and overall mortality rates: a meta-analysis. *JAMA Intern. Med.* 179, 1491–1500. doi: 10.1001/jamainternmed.2019.2779

Figueroa, C. A., and Rosen, C. J. (2020). Parkinson's disease and osteoporosis: basic and clinical implications. *Expert Rev. Endocrinol. Metab.* 15, 185–193. doi: 10.1080/17446651.2020.1756772

Forsaa, E. B., Larsen, J. P., Wentzel-Larsen, T., and Alves, G. (2010). What predicts mortality in Parkinson disease? A prospective population-based long-term study. *Neurology* 75, 1270–1276. doi: 10.1212/WNL.0b013e3181f61311

Gao, H., Wei, X., Liao, J., Wang, R., Xu, J., Liu, X., et al. (2015). Lower bone mineral density in patients with Parkinson's disease: a cross-sectional study from Chinese Mainland. *Front. Aging Neurosci.* 7:203. doi: 10.3389/fnagi.2015.00203

Harris-Hayes, M., Willis, A. W., Klein, S. E., Czuppon, S., Crowner, B., and Racette, B. A. (2014). Relative mortality in U.S. Medicare beneficiaries with Parkinson disease and hip and pelvic fractures. *J. Bone Joint Surg. Am.* 96:e27. doi: 10.2106/JBJS.L.01317

Hoogland, J., Post, B., and de Bie, R. M. A. (2019). Overall and disease-related mortality in Parkinson's disease: a longitudinal cohort study. *J. Parkinsons. Dis.* 6, 39–45. doi: 10.3233/JPD-191652

Kim, H. K., Song, S. O., Noh, J., Jeong, I. K., and Lee, B. W. (2020). Data configuration and publication trends for the Korean National Health Insurance and Health Insurance Review and Assessment Database. *Diabetes Metab. J.* 44, 671–678. doi: 10.4093/dmj.2020.0207

Kim, T. L., Byun, S. J., Seong, M. Y., Oh, B. M., Park, S. J., and Seo, H. G. (2022). Fracture risk and impact of osteoporosis in patients with Parkinson's disease: a nationwide database study. *J. Bone Miner. Metab.* 40, 602–612. doi: 10.1007/s00774-022-01322-w

Koo, H. Y., Cho, E. B., Kong, S. H., Han, K., Lee, K. N., Yoo, J. E., et al. (2023). Fracture risk in Parkinson's disease according to its severity and duration. *Osteoporos. Int.* 34, 81–89. doi: 10.1007/s00198-022-06562-0

Lee, C. K., Choi, S. K., Shin, D. A., Yi, S., Kim, K. N., Kim, I., et al. (2018). Parkinson's disease and the risk of osteoporotic vertebral compression fracture: a nationwide population-based study. *Osteoporos. Int.* 29, 1117–1124. doi: 10.1007/s00198-018-4409-9

Lee, Y. K., Yoon, B. H., and Koo, K. H. (2013). Epidemiology of osteoporosis and osteoporotic fractures in South Korea. *Endocrinol. Metab.* 28, 90–93. doi: 10.3803/EnM.2013.28.2.90

Malochet-Guinamand, S., Durif, F., and Thomas, T. (2015). Parkinson's disease: a risk factor for osteoporosis. *Joint Bone Spine.* 82, 406–410. doi: 10.1016/j.jbspin.03, 009.

Mühlenfeld, N., Söhling, N., Marzi, I., Pieper, M., Paule, E., Reif, P. S., et al. (2021). Fractures in Parkinson's disease: injury patterns, hospitalization, and therapeutic aspects. *Eur. J. Trauma Emerg. Surg.* 47, 573–580. doi: 10.1007/s00068-019-01240-z

Nam, J. S., Kim, Y. W., Shin, J., Chang, J. S., and Yoon, S. Y. (2021). Hip fracture in patients with Parkinson's disease and related mortality: a population-based study in Korea. *Gerontology* 67, 544–553. doi: 10.1159/000513730

National Health Insurance Service (2024). Available online at: https://nhiss.nhis.or.kr/ (accessed July 5, 2024).

Park, S. J., Kwon, K. E., Choi, N. K., Park, K. H., and Woo, S. J. (2015). Prevalence and incidence of exudative age-related macular degeneration in South Korea: a nationwide population-based study. *Ophthalmology* 122, 2063–70.e1. doi: 10.1016/j.ophtha.2015.06.018

Pinter, B., Diem-Zangerl, A., Wenning, G. K., Scherfler, C., Oberaigner, W., Seppi, K., et al. (2015). Mortality in Parkinson's disease: a 38-year follow-up study. *Mov. Disord.* 30, 266–269. doi: 10.1002/mds.26060

Pouwels, S., Bazelier, M. T., de Boer, A., Weber, W. E., Neef, C. K., Cooper, C., et al. (2013). Five-year fracture risk estimation in patients with Parkinson's disease. *Bone* 56, 266–270. doi: 10.1016/j.bone.06, 018.

Quan, H., Sundararajan, V., Halfon, P., Fong, A., Burnand, B., Luthi, J. C., et al. (2005). Coding algorithms for defining comorbidities in ICD-9-CM and ICD-10 administrative data. *Med. Care.* 43, 1130–1139. doi: 10.1097/01.mlr.0000181983, 83.

Samii, A., Nutt, J. G., and Ransom, B. R. (2004). Parkinson's disease. *Lancet* 363, 1783–1793. doi: 10.1016/S0140-6736(04)16305-8

SAS Institute Inc (2013). *SAS Software, Version 9.4.* Cary, NC: SAS Institute Inc.

Schini, M., Vilaca, T., Poku, E., Harnan, S., Sutton, A., Allen, I. E., et al. (2020). The risk of hip and non-vertebral fractures in patients with Parkinson's disease and parkinsonism: a systematic review and meta-analysis. *Bone* 132:115173. doi: 10.1016/j.bone.2019.115173

Torsney, K. M., Noyce, A. J., Doherty, K. M., Bestwick, J. P., Dobson, R., and Lees, A. J. (2014). Bone health in Parkinson's disease: a systematic review and meta-analysis. *J. Neurol. Neurosurg. Psychiatr.* 85, 1159–1166. doi: 10.1136/jnnp-2013-307307

van den Bos, F., Speelman, A. D., Samson, M., Munneke, M., Bloem, B. R., and Verhaar, H. J. (2012). Parkinson's disease and osteoporosis. *Age Ageing.* 42, 156–162. doi: 10.1093/ageing/afs161

Yoon, S. Y., Shin, J., Kim, Y. W., Chang, J. S., and Won Kim, H. (2021). The mortality rate of Parkinson's disease and related comorbidities: a nationwide population-based matched cohort study in Korea. *Age Ageing.* 50, 1182–1188. doi: 10.1093/ageing/afaa250

Zhang, Y. Y., Xie, N., Sun, X. D., Nice, E. C., Liou, Y. C., Huang, C., et al. (2024). Insights and implications of sexual dimorphism in osteoporosis. *Bone Res.* 12:8. doi: 10.1038/s41413-023-00306-4

Frontiers in Endocrinology

Explores the endocrine system to find new therapies for key health issues

The second most-cited endocrinology and metabolism journal, which advances our understanding of the endocrine system. It uncovers new therapies for prevalent health issues such as obesity, diabetes, reproduction, and aging.

Discover the latest Research Topics

See more →

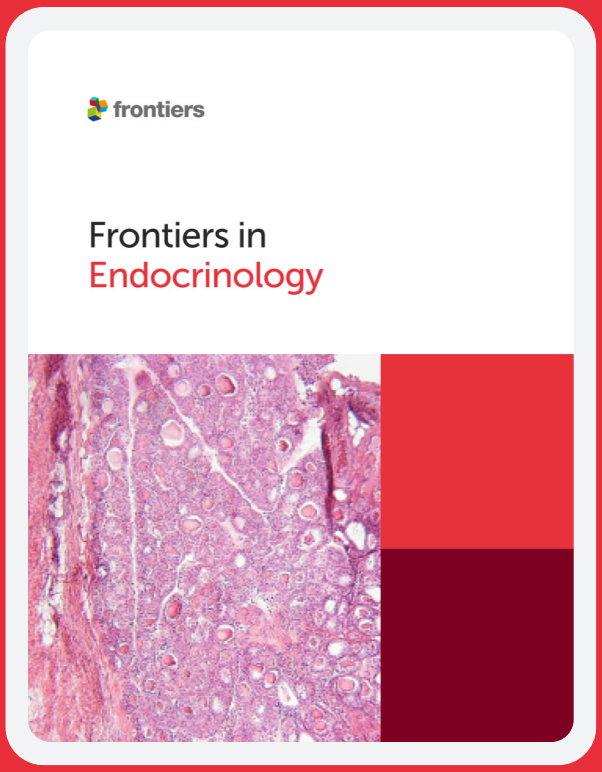

Frontiers

Avenue du Tribunal-Fédéral 34
1005 Lausanne, Switzerland
frontiersin.org

Contact us

+41 (0)21 510 17 00
frontiersin.org/about/contact